

Aus dem Institut für Physiologie und Pathophysiologie  
Geschäftsführender Direktor: Prof. Dr. Dominik Oliver  
des Fachbereichs Medizin der Philipps-Universität Marburg

**Molekulare Identifizierung und funktionelle Charakterisierung der  
K<sup>+</sup>-Kanal-Ausstattung auditorischer Haarsinneszellen**

Inaugural-Dissertation zur Erlangung  
des Doktorgrades der Naturwissenschaften  
dem Fachbereich Medizin der Philipps-Universität Marburg

vorgelegt von

**Marlen Dierich**

aus Kyritz, Deutschland

Marburg, 2020

Angenommen vom Fachbereich Medizin der Philipps-Universität Marburg  
am: 17.11.2020

Gedruckt mit Genehmigung des Fachbereichs.

Dekan i.V. der Prodekan: Prof. Dr. R. Müller

Referent: Prof. Dr. D. Oliver

1. Korreferent: Prof. Dr. I. Grgic

## ANMERKUNG

Die vorliegende Dissertation macht von der Möglichkeit Gebrauch, Publikationen als Dissertationsleistung anerkennen zu lassen (kumulative Promotion), wie es im §9 der „Promotionsordnung der Mathematisch-Naturwissenschaftlichen Fachbereiche und des Medizinischen Fachbereichs für seine mathematisch-naturwissenschaftlichen Fächer der Philipps-Universität Marburg vom 15.07.2009“ steht. Hierzu gehört eine Einleitung, eine Zusammenfassung der Ergebnisse und eine Diskussion der im Anhang angeführten Publikationen.

**Dierich M.**, Hartmann S., Dietrich N., Moeser P., Brede F., Chacko L.J., Tziridis K., Schilling A., Krauss P., Hessler S., Lehnert S., Karch S., Schrott-Fischer A., Blumer M., Birchmeier C., Oliver D., Moser T., Schulze H., Alzheimer C., Leitner M. G., Huth T. (2019).  $\beta$ -Secretase BACE1 Is Required for Normal Cochlear Function. *The Journal of Neuroscience*, 39(45):9013-9027. doi: 10.1523/JNEUROSCI.0028-19.2019

**Dierich M.**, Evers S., Wilke B. U., Leitner M. G. (2018). Inverse Modulation of Neuronal  $K_v12.1$  and  $K_v11.1$  Channels by 4-Aminopyridine and NS1643. *Frontiers in Molecular Neuroscience*, 11(January), 11:11. doi: 10.3389/fnmol.2018.00011

**Dierich M.**, & Leitner M. G. (2018).  $K_v12.1$  channels are not sensitive to  $G_q$ PCR-triggered activation of phospholipase  $C\beta$ . *Channels*, 12(1), 228-239. doi: 10.1080/19336950.2018.1475783

**Dierich M.**, van Ham W.B., Stary-Weinzinger A., Leitner M. G. (2019). Histidine at position 462 determines the low quinine sensitivity of ether-à-go-go channel superfamily member  $K_v12.1$ . *British Journal of Pharmacology*, 176(15): 2708-2723. doi: 10.1111/bph.14693

**Dierich M.**, Altoè A., Koppelman J., Evers S., Renigunta V., Schäfer M.K., Naumann R., Verhulst S., Oliver D., Leitner M. G. (2020). Optimized Tuning of Auditory Inner Hair Cells to Encode Complex Sound through Synergistic Activity of Six Independent  $K^+$  Current Entities. *Cell Reports* 32, 107869:1-e4. doi: 10.1016/j.celrep.2020.107869

# LITERATURVERZEICHNIS

Zusammenfassung

Summary

Abkürzungsverzeichnis

1. Einleitung .....	1
1.1 Das Gehör ist ein außerordentlich sensitives Sinnesorgan.....	1
1.2 Basolaterale $K^+$ -Ionenkanäle sind essentiell für die Funktion von Haarsinneszellen .....	3
1.3 Die Identität der meisten $K^+$ -Kanäle in Haarsinneszellen ist unbekannt.....	4
1.4 Fragestellung und Zielsetzung der Arbeit .....	5
2. Erklärung über den Eigenanteil an den vorliegenden Publikationen.....	7
3. Resultate.....	8
3.1 Die Rolle der Beta-Sekretase 1 (BACE1) im auditorischen System.....	8
3.1.1 Ist die Interaktion von BACE1 mit $K_v7.4$ -Kanaluntereinheiten die molekulare Grundlage für den Haarzellstrom $I_{K,n}$ ?.....	8
3.1.2 Sensorineuronaler Hörverlust aufgrund der Hypomyelinisierung von peripheren auditorischen Nervenfasern in BACE1 <sup>-/-</sup> Mäusen .....	9
3.2 Die molekulare Identität und physiologische Relevanz von $K^+$ -Kanälen innerer Haarsinneszellen.....	10
3.2.1 Identifizierung und Nachweis möglicher in Haarsinneszellen exprimierter Kandidatenkanäle .....	11
3.2.2 Elektrophysiologische und pharmakologische Charakterisierung der Kandidatenkanäle im heterologen Expressionssystem .....	12
3.2.3 $K_v1.8$ , $K_v11.1$ und $K_v12.1$ sind die molekulare Grundlage von $I_{K,s}$ in inneren Haarsinneszellen .....	14
3.2.4 Eine Kombination spannungsaktivierter $K^+$ -Ströme optimiert das Antwortverhalten von inneren Haarsinneszellen .....	14
4. Diskussion .....	16
4.1 BACE1-defiziente Mäuse zeigen sensorineuralen Hörverlust .....	16
4.2 Identifizierung der $I_{K,s}$ Komponente in inneren Haarsinneszellen.....	18
4.2.1 Die physiologische Relevanz der $K^+$ -Kanäle in Haarsinneszellen.....	20
4.3 Ausblick und Bedeutung meiner Arbeit.....	21
5. Literaturverzeichnis.....	22
6. Anhang .....	29
6.1 Eingereichte Publikationen	
6.2 Lebenslauf	
6.3 Verzeichnis der akademischen Lehrer/-innen	
6.4 Danksagung	
6.5 Ehrenwörtliche Erklärung	

## ZUSAMMENFASSUNG

**Hintergrund:** Die präzise Verarbeitung von auditiven Reizen wird durch äußere (ÄHZ) und innere Haarsinneszellen (IHZ) im Corti'schen Organ gewährleistet. Da die physiologischen Aufgaben (kochleäre Verstärkung und synaptische Übertragung) dieser Zellen vom Rezeptorpotential angetrieben werden, sind Form und Amplitude dieser Potentialänderungen essentiell für die Funktion der Sinneszellen. Die Charakteristika der Rezeptorpotentiale hängen dabei von der Aktivität der apikalen mechano-elektrischen Transduktionskanäle und von basolateralen  $K^+$ -Leitfähigkeiten ab. Diese Leitfähigkeiten wurden aufgrund ihrer biophysikalischen Eigenschaften als  $I_{K,f}$ ,  $I_{K,n}$  und  $I_{K,s}$  klassifiziert. Die Ionenkanäle und deren Interaktionspartner, die diese  $K^+$ -Leitfähigkeiten hervorbringen, sind weitestgehend unbekannt.

**Ziele der Arbeit:** Die Ziele dieser Doktorarbeit waren es, (I.) die Relevanz eines möglichen Interaktionspartners (das Enzym  $\beta$ -Sekretase 1; BACE1) der  $K^+$ -Kanäle in ÄHZ zu untersuchen, und (II.) die  $K^+$ -Kanaluntereinheiten, welche die  $I_{K,s}$  Komponente in IHZ von Mäusen ausmachen, zu entschlüsseln, sowie deren physiologische Aufgaben anhand von Computermodellen zu bestimmen.

**Ergebnisse zu BACE1:** Ich konnte zeigen, dass der signifikante Hörverlust der BACE1<sup>-/-</sup> Mäuse durch Desorganisation der synaptischen Verbindungen zwischen IHZ und auditorischen Nervenfasern und durch eine stark verringerte Myelinisierung dieser Nervenfasern hervorgerufen wird. Dabei ist BACE1 für die Entwicklung der kochleären Nervenfasern, nicht jedoch für die Aufrechterhaltung der Myelinisierung von Bedeutung. Außerdem konnte ich Neuregulin-1 als BACE1-Substrat identifizieren, das die Organisation der Nervenfasern in der Cochlea vermittelt. BACE1 ist also entgegen unserer Ausgangshypothese kein Interaktionspartner von  $K^+$ -Kanälen in Haarsinneszellen, jedoch unabkömmlich für sensitives Hören. Da die Inhibition von BACE1 ein populärer Ansatz zur Therapie der Alzheimer-Krankheit ist, war es wichtig zu prüfen, ob entsprechende Medikamente Auswirkungen auf die Hörleistung haben. Die Behandlung von Mäusen mit dem BACE1-Inhibitor NB-360 beeinträchtigte jedoch nicht das Hörvermögen der Tiere. Diese Ergebnisse lassen vermuten, dass Hörverlust keine Nebenwirkung der Therapie der Alzheimer-Krankheit darstellt.

**Ergebnisse zur  $K^+$ -Kanalausstattung der Haarsinneszellen:** In einem Hypothesen-basierten Kandidatenansatz ist es mir gelungen, die  $K^+$ -Kanalausstattung von IHZ zu entschlüsseln. Dafür habe ich aus publizierten Einzelzell-Transkriptom-Analysen von IHZ Kandidatenkanäle extrahiert und deren Expression in der Cochlea mittels molekularbiologischen und immunhistochemischen Techniken bestätigt. Mittels elektrophysiologischer Methoden konnte ich dann überprüfen, ob diese Kanäle in den IHZ aktiv sind. Für den funktionellen Nachweis konnte ich zum einen auf etablierte Protokolle zurückgreifen, andere Kandidatenkanäle musste ich erst im Expressionssystem eingehend charakterisieren und selbst geeignete Messprotokolle und ein pharmakologisches Profil zum Nachweis in nativem Gewebe entwickeln. Diese Untersuchungen zeigten, dass sich trotz enger phylogenetischer Verwandtschaft und darauf aufbauenden Ähnlichkeiten in der Gesamtarchitektur, die pharmakologischen Eigenschaften von  $K^+$ -Kanälen doch signifikant unterscheiden können. Aufbauend auf den Arbeiten im Expressionssystem konnte ich dann zeigen, dass  $K_v1.8$ -,  $K_v11.1$ - und  $K_v12.1$ -Kanäle in IHZ aktiv sind. Somit konnte ich  $K_v11.1$ -Kanälen erstmals eine Rolle im sensorischen System, und  $K_v1.8$ - und  $K_v12.1$ -Kanälen überhaupt erstmalig eine physiologische Bedeutung zuweisen. Die Relevanz dieser außergewöhnlichen Ausstattung aus fünf  $K^+$ -Kanaluntereinheiten in IHZ ( $K_v1.8$ -,  $K_v7.4$ -,  $K_v11.1$ -,  $K_v12.1$ - und  $BK_{Ca}$ -Kanäle) wurde dann anhand von Computermodellen eingehend untersucht. Diese Simulationen zeigten, dass alle Kanäle gemeinsam die Präzision der Schallverarbeitung in IHZ optimieren und die Verarbeitung komplexer Schallereignisse und somit sensitives Hören überhaupt erst ermöglichen, während IHZ mit vereinfachter Kanalzusammensetzung in der Verarbeitung von Schallreizen eingeschränkt sind.

## SUMMARY

**Background:** The precise processing of auditory stimuli is ensured by outer (OHC) and inner hair cells (IHC) in the organ of Corti. Since the physiological tasks (cochlear amplification and synaptic transmission) of these cells are driven by receptor potentials, the shape and the amplitude of these potential changes are essential for the function of the sensory cells. The characteristics of these receptor potentials depend on the activity of the apical mechano-electrical transduction channels and on basolateral (voltage-dependent)  $K^+$  conductances, which together define the biophysical membrane properties of the sensory cells. Due to their biophysical properties, the basolateral  $K^+$  currents were previously classified as  $I_{K,r}$ ,  $I_{K,n}$  and  $I_{K,s}$ . The underlying ion channels and their modulatory interaction partners are largely unknown.

**Aims of the thesis:** The goals of this doctoral thesis were (I.) to investigate the role of a potential interaction partner (the enzyme  $\beta$ -secretase 1; BACE1) for  $K^+$  channel function in hair cells, and (II.) to unravel the channel subunits that make up the  $K^+$  channel repertoire in IHCs, as well as to elucidate the physiological relevance of these  $K^+$  channels by using in-silico simulations.

**Results on BACE1:** I found that BACE1<sup>-/-</sup> mice exhibit significant hearing loss compared to wild-type mice, which is caused by disorganization of the synaptic connections between the IHC and the auditory nerve fibers and greatly reduced myelination of these nerve fibers. Noteworthy, BACE1 is important for the development of the cochlear nerve fibers, but not for the maintenance of their myelination in adulthood. I also identified Neuregulin-1 as the BACE1 substrate in the cochlea that is pivotal for normal organization and myelination of the cochlear nerve fibers. Contrary to our initial hypothesis, BACE1 thus is not an interaction partner of  $K^+$  channels in sensory hair cells. However, my results showed for the first time that BACE1 is indispensable for sensitive hearing. Because inhibiting BACE1 is considered a promising approach to treat Alzheimer's disease, it was important to determine whether such medication could affect hearing sensitivity. We did not detect any hearing impairment or abnormal changes in the cochlea of mice treated with the well-known BACE1 inhibitor NB-360. These results suggest that hearing loss may not be a side-effect of Alzheimer's disease therapy with BACE1 inhibitors.

**Results on the  $K^+$  channel repertoire of auditory hair cells:** In a hypothesis-driven candidate approach, I succeeded in deciphering the  $K^+$  channel repertoire of IHCs. First, I extracted candidate channels from published single cell transcriptome analyses of IHCs. Then I confirmed expression of these channels in the cochlea using molecular biological and immunohistochemical methods. I employed electrophysiological techniques to elucidate whether these candidate channels are active in IHCs. To develop an approach towards identification of channel subtypes by their biophysical properties, I established protocols in heterologous expression system to characterize the candidate channels in detail. Thus, I identified unique properties and suitable measurement protocols for subsequent detection in native tissue. Surprisingly, these studies showed that despite close phylogenetic relationship and similarities in the overall architecture, the pharmacological properties of  $K^+$  channels can differ significantly. Based on the work in the expression system, I was able to show that  $K_v1.8$ ,  $K_v11.1$  and  $K_v12.1$  channels are active in IHCs. Hence, for the first time I could assign a role in a sensory system to  $K_v11.1$  channels, and my results constitute the first demonstration of relevance of  $K_v1.8$  and  $K_v12.1$ . We then untangled the physiological importance of this extraordinary repertoire of five  $K^+$  channel subunits ( $K_v1.8$ ,  $K_v7.4$ ,  $K_v11.1$ ,  $K_v12.1$  and  $BK_{Ca}$  channels) in detail using in-silico simulations. These models showed that all channels together synergistically optimize the precision of sound processing in IHCs, while IHCs with fewer channel populations are limited in the processing of sound stimuli adequately. The channel repertoire thus represents an evolutionary adaptation, that enables the processing of complex sounds and sensitive hearing.

## ABKÜRZUNGSVERZEICHNIS

4-AP	4-Aminopyridin
ABR	Hirnstammaudiometrie ( <i>auditory brainstem responses</i> )
AC	phasisch-oszillierende Komponente ( <i>phasic component</i> )
ÄHZ	äußere Haarsinneszelle/n
APP	Amyloid-Precursor-Protein
AB	Beta-Amyloid-Peptid
BACE1	Beta-Sekretase 1 ( <i><math>\beta</math>-site of APP cleaving enzyme</i> )
CHL	Zelladhäsionsmolekül ( <i>close homolog of L1</i> )
CHO	<i>Chinese hamster ovary</i>
DC	anhaltende-depolarisierende Komponente ( <i>sustained component</i> )
DFNA2	autosomale dominante Taubheitsform 2 ( <i>deafness nonsyndromic autosomal dominant 2</i> )
E-4031	N-[4-[[1-[2-(6-Methyl-2-pyridinyl)ethyl]-4piperidinyl]carbonyl]phenyl] methanesulfonamide dihydrochloride
EAG	<i>ether-à-go-go</i>
IbTX	Iberiotoxin
IHZ	innere Haarsinneszelle/n
$I_{K,f}$	schnell ( <i>fast</i> ) aktivierender Kaliumstrom
$I_{K,n}$	negativ ( <i>negativ</i> ) aktivierender Kaliumstrom
$I_{K,s}$	langsam ( <i>slow</i> ) aktivierender Kaliumstrom
Kcnh2	Gen des spannungsabhängigen $K^+$ -Kanal $K_v11.1$
Kcnq4	Gen des spannungsabhängiger $K^+$ -Kanal $K_v7.4$
MBP	Basisches Myelinprotein ( <i>myelin basic protein</i> )
MET	mechano-elektrische Transduktionskanäle
NRG1	Neuregulin-1
NS1643	1,3-Bis-(2-hydroxy-5-trifluoromethyl-phenyl)-urea
OAE	otoakustische Emissionen
PI(4,5)P <sub>2</sub>	Phosphatidylinositol-(4,5)-bisphosphat
PSD95	<i>post-synaptic density protein 95</i>
RT-PCR	Reverse-Transkriptase-Polymerase-Kettenreaktion
SGN	Spiralganglionneuron
TEA	Tetraethylammonium
XE991	10,10-bis(4-Pyridinylmethyl)-9(10H)-anthracenone dihydrochloride

# EINLEITUNG

## 1. Einleitung

### 1.1 Das Gehör ist ein außerordentlich sensitives Sinnesorgan

Nicht nur wir Menschen, sondern auch die Tierwelt benutzt das Gehör, um sensorische Informationen aus der Umgebung zu gewinnen, die für das Überleben, die Orientierung und die Kommunikation essentiell sind. Dabei können Menschen Schallereignisse zwischen 20 und 20.000 Hz (Hertz) wahrnehmen und zwischen Tönen unterscheiden, deren Frequenzen sich nur um 0,3% unterscheiden (Dallos 1992; Fettiplace and Hackney 2006). Diese enorme Sensitivität wird durch schnelle und präzise Signalverarbeitung, sowie durch morphologische und funktionelle Besonderheiten im Corti'schen Organ in der Cochlea (Gehörschnecke) des Innenohres ermöglicht. Schallwellen versetzen dort zunächst die Basilarmembran in Schwingung, die zur Spitze (Apex) der Cochlea hin breiter, dünner und elastischer wird. Durch diese besonderen Eigenschaften bilden hohe Frequenzen ein Schwingmaximum am basalen Ende der Basilarmembran aus, während tiefe Frequenzen ein Maximum in der Nähe des Apex bilden (Békésy und Wever 1960). Auf diese Weise wird jeder Frequenz ein bestimmter Ort auf der Basilarmembran zugeordnet, ein Vorgang, der als Frequenz-Ortsabbildung oder Tonotopie bezeichnet wird. Diese schallinduzierten Schwingungen werden von auditorischen Haarsinneszellen, die in Reihen entlang des Corti'schen Organs auf der Basilarmembran angeordnet sind, in elektrische Signale des Nervensystems übersetzt (mechano-elektrische Transduktion).

Die Säugetierschnecke enthält zwei Klassen von Haarsinneszellen: Innere Haarsinneszellen (IHZ), von denen es in jeder menschlichen Cochlea 2.800-4.400 gibt, werden von der überwiegenden Mehrheit (90-95%) der afferenten Fasern des *Nervus cochlearis* innerviert. Sie sind die primären Schalldetektoren der Cochlea und übertragen die Schallinformation auf den Hörnerv. Die rund 11.200-16.000 äußeren Haarsinneszellen (ÄHZ) sind überwiegend efferent innerviert und erhöhen durch aktive Längenänderung die Frequenzdiskriminierung und die Empfindlichkeit der Cochlea gegenüber leisen Schallereignissen. Dieser Prozess wird als die von den ÄHZ-vermittelte kochleäre Verstärkung bezeichnet (Ryugo 1992).

Die Funktion aller Haarsinneszellen basiert auf der fein abgestimmten Expression und Funktion von Ionenkanälen, die als Poren in biologischen Membranen die passive Diffusion von Ionen entlang des bestehenden elektrochemischen Gradienten ermöglichen. Haarsinneszellen sind epitheliale Zellen, deren Membranpotential und insbesondere dessen Änderungen vom Wechselspiel zwischen apikalen mechano-elektrischen Transduktionskanälen (MET-Kanäle) und basolateralen (spannungsabhängigen)  $K^+$ -Kanälen abhängen. Die MET-Kanäle befinden sich im sogenannten Haarbündel am apikalen Zellpol, das in die Endolymphe mit einer für den Extrazellulärraum ungewöhnlich hohen  $K^+$ -Konzentration ragt (Schwander et al. 2010). Bei dem Haarbündel handelt es sich um miteinander über Proteinfäden (*Tip-links*) verbundene und mit Aktin gefüllte Ausstülpungen der Membran, den sogenannten Stereozilien, die in Reihen mit zunehmender Länge angeordnet sind. Wird das Haarbündel in Richtung des längsten Stereoziliums ausgelenkt, öffnen vermehrt MET-Kanäle, während eine Auslenkung in Gegenrichtung diese Kanäle schließt (Goutman et al. 2015; Schwander et al. 2010). Da  $K^+$ -Ionen über die MET-Kanäle in die Zellen einströmen, vermittelt das Haarbündel somit die Umwandlung der mechanischen Schallschwingung in ein elektrisches Signal, dem Rezeptorpotential der Haarsinneszellen. Sowohl in IHZ als auch in ÄHZ führt der  $K^+$ -Einstrom durch die MET-Kanäle zur Depolarisation des Membranpotentials (Beurg et al. 2009; Schwander et al. 2010). Das



## EINLEITUNG

Schließen der MET-Kanäle führt dementsprechend zur Hyperpolarisation des Membranpotentials der Sinneszellen. Somit bilden sich als Antwort auf Schallreize sinusförmige (abwechselnd de- und hyperpolarisierende) Rezeptorpotentiale, deren Amplitude mit der Auslenkung des Haarbündels und somit mit der Schallintensität zunimmt.

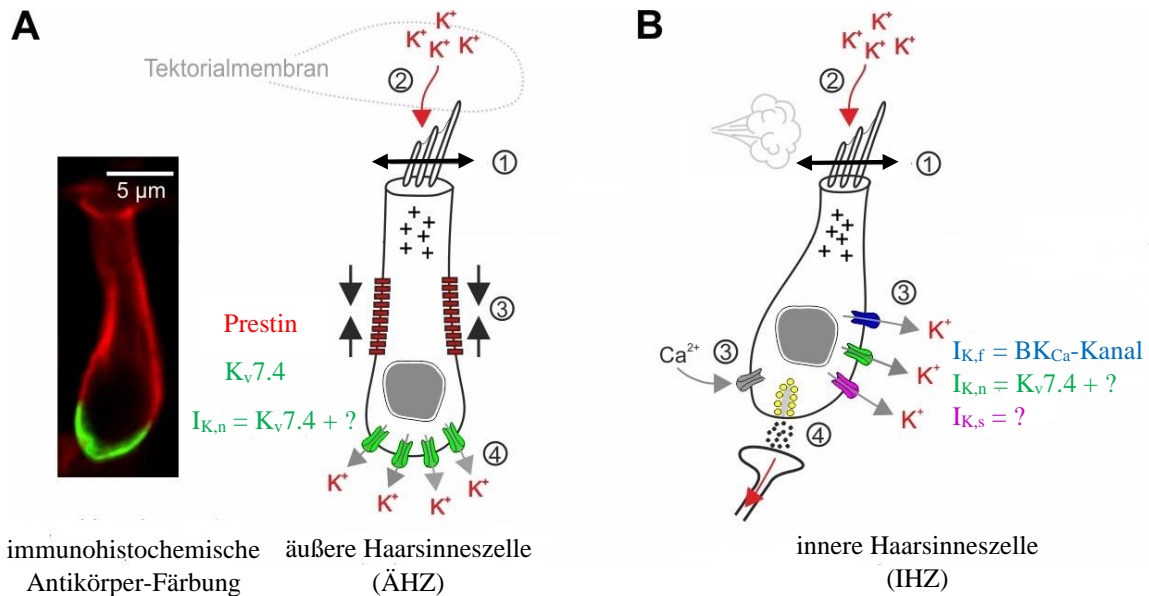


**Abb.1 Schematische Darstellung der Signalverarbeitung in Haarsinneszellen**

(A) Links: Immunohistochemische Färbung einer ÄHZ im nativen Gewebe der Cochlea mittels spezifischer Antikörper gegen Prestin (rot) und  $K_v7.4$  (grün). Rechts: Schematisch dargestellter Verstärkungsmechanismus von ÄHZ: ① Auslenkung der Stereozilien durch relative Scherbewegungen der Tektorialmembran zur Basilarmembran in ÄHZ. ② Öffnung der MET-Kanäle. Der Einstrom von  $K^+$  depolarisiert die Haarsinneszelle. ③ Spannungabhängige Längenveränderung (Prestin) der ÄHZ führt zur Verstärkung der Wanderwelle auf der Basilarmembran. ④  $K^+$ -Efflux über  $K_v7.4$ -Kanäle ( $I_{K,n}$ ). (B) Schematische Darstellung der Signalweiterleitung von IHZ auf Fasern des Hörnervs: Schritte ① und ② laufen ab wie bei ÄHZ, nur dass die Auslenkung der Stereozilien (kein Kontakt zur Tektorialmembran) durch den Fluss der Endolymphe ausgelöst wird. ③ Depolarisation des Membranpotentials öffnet spannungsabhängige  $Ca^{2+}$ -Kanäle ④ Eingeströmtes  $Ca^{2+}$  führt zur Ausschüttung von Glutamat aus IHZ, welches dann postsynaptische AMPA-Rezeptoren auf auditorischen Nervenfasern aktiviert. Generell entstehen in ÄHZ und IHZ durch die Auslenkung der Haarbündel Rezeptorpotentiale, deren Charakteristika durch die Aktivität der MET-Kanäle und der basolateralen  $K^+$ -Kanäle (ÄHZ:  $I_{K,n}$ ; IHZ:  $I_{K,n}$ ,  $I_{K,f}$ ,  $I_{K,s}$ ) moduliert werden.

Diese Rezeptorpotentiale lösen unterschiedliche Prozesse in ÄHZ (Abb.1A) und IHZ (Abb.1B) aus: In ÄHZ treiben die Rezeptorpotentiale spannungsabhängige Längenänderungen des Zellkörpers an, die die Grundlage des kochleären Verstärkers darstellen. Der molekulare Motor für diesen auch als Elektromotilität bezeichneten Vorgang ist das Protein Prestin in der lateralen Membran der ÄHZ, das Membranpotentialänderungen in zelluläre Kontraktionen umwandelt (Dallos and Fakler 2002; Zheng et al. 2002). Bei Depolarisation kommt es zur Verkürzung der ÄHZ, bei Hyperpolarisation zur Verlängerung. Die dabei entstehende Kraft wird in einer Rückkopplungsschleife in die Schwingung der Basilarmembran eingespeist und kann diese um das Tausendfache verstärken (Brownell et al. 1985; Dallos et al. 2009; Liberman et al. 2002; Zheng et al. 2002).

In IHZ dagegen aktivieren depolarisierende Rezeptorpotentiale spannungsabhängige Calciumkanäle ( $Ca_v1.3$ ) vom L-Typ (Brandt et al. 2003). Der resultierende  $Ca^{2+}$ -Einstrom führt

## EINLEITUNG

zur Freisetzung des Neurotransmitters L-Glutamat in den synaptischen Spalt aus den am basalen Zellpol liegenden Bändersynapsen (*ribbon synapse*). Glutamat steuert wiederum über die Bindung an AMPA-Rezeptoren die Generierung von Aktionspotentialen in den postsynaptischen Spiralganglionneuronen (SGN) und somit die Signalweiterleitung der Schallinformation in die höheren auditorischen Hirnareale. IHZ werden von mehreren afferenten Typ-1-SGN innerviert, wobei jedes SGN nur eine einzige IHZ kontaktiert (Glowatzki and Fuchs 2002; Moser and Lysakowski 2006).

### **1.2 Basolaterale K<sup>+</sup>-Ionenkanäle sind essentiell für die Funktion von Haarsinneszellen**

Da die physiologischen Aufgaben der ÄHZ (kochleäre Verstärkung) und IHZ (synaptische Übertragung) vom Rezeptorpotential angetrieben werden, sind Form und Amplitude dieser Potentialänderungen essentiell für die Funktion der Sinneszellen. Hierfür entscheidend ist einerseits die Aktivität der MET-Kanäle, über die schallinduzierte Rezeptorpotentiale in den Sinneszellen gebildet werden. Andererseits werden Form und Amplitude der Rezeptorpotentiale beeinflusst und moduliert durch die Aktivität von in den Haarsinneszellen exprimierten basolateralen spannungsabhängigen K<sup>+</sup>-Ionenkanälen, die die biophysikalischen Eigenschaften der Zellmembran (Ruhepotential, Zeitkonstante, etc.) maßgeblich bestimmen.

Diese Leitfähigkeiten werden nach ihren biophysikalischen Eigenschaften (siehe unten) als  $I_{K,f}$ ,  $I_{K,n}$  und  $I_{K,s}$  bezeichnet und sind in IHZ und ÄHZ differentiell ausgeprägt (Marcotti et al. 2003; Oliver et al. 2003). In ÄHZ kommen hauptsächlich der negativ aktivierende  $I_{K,n}$  und der schnell aktivierende  $I_{K,f}$  K<sup>+</sup>-Strom vor, wobei  $I_{K,n}$  den weitaus größten Stromanteil in diesen Sinneszellen stellt (Kharkovets et al. 2006; Kros et al. 1998; Mammano et al. 1995; Marcotti et al. 2003; Marcotti and Kros 1999).  $I_{K,n}$  ist charakterisiert durch eine Aktivierung bei außerordentlich negativer Membranspannung, was den ÄHZ eine komplette Aktivität im Bereich des Ruhemembranpotentials von -40 mV ermöglicht (Johnson et al. 2011; Mammano et al. 1995). Diese großen  $I_{K,n}$  Ströme nahe am Ruhemembranpotential reduzieren die Zeitkonstante der Zellmembran, wodurch schnelle Änderungen des Membranpotentials und somit die Prestin-vermittelte Elektromotilität ermöglicht wird (Johnson et al. 2011).  $I_{K,n}$  ist damit eine essentielle biophysikalische Voraussetzung für den kochleären Verstärkungsmechanismus und somit für die Sensitivität des Säugergehörs (Johnson et al. 2011).

Im Gegensatz zu ÄHZ kommt in IHZ neben  $I_{K,f}$  und  $I_{K,n}$  noch die langsam aktivierende Stromkomponente  $I_{K,s}$  vor (Marcotti et al. 2003). Bisher ist die physiologische Bedeutung der einzelnen Stromkomponenten zwar unklar, aber kürzlich konnte gezeigt werden, dass sich der relative Anteil der einzelnen Komponenten am Gesamtstrom der IHZ entlang der tonotopen Achse verändert. So bleibt die Größe des  $I_{K,f}$  Stroms zwar konstant entlang der tonotopen Achse, IHZ in der Basis der Cochlea weisen aber einen größeren  $I_{K,s}$  Strom und einen kleinen negativ aktivierenden  $I_{K,n}$  Strom auf. Apikale IHZ dagegen zeigen bei kleinem  $I_{K,s}$  einen großen  $I_{K,n}$  Strom (Johnson 2015). Außerdem zeichnen sich basale IHZ durch eine geringere Ruheaktivität der MET-Kanäle aus. Wohingegen apikale IHZ, welche niedrige Frequenzen verarbeiten, ein eher depolarisiertes Membranpotential ( $V_m = -55$  mV), eine größere Ruheleitfähigkeit und eine schnellere Membranzeitkonstante gegenüber der basalen IHZ ( $V_m = -65$  mV) zeigen (Johnson 2015). Das ermöglicht es den apikalen IHZ, Rezeptorpotentiale hervorzubringen, die mit einer schnellen phasisch-oszillierenden Komponente (AC) dem Schallreiz folgen (Glowatzki and Fuchs 2002; Johnson 2015), d.h. apikale IHZ können die Frequenz eines ankommenden

## EINLEITUNG

Schallereignisses genauer abbilden. Im Gegensatz dazu können die Rezeptorpotentiale von basalen IHZ hochfrequenten Stimuli aufgrund der Membraneigenschaften nicht mehr folgen, bringen aber für die Dauer des auditorischen Reizes eine anhaltende depolarisierende (DC)-Komponente hervor, auf der eine kleine AC-Komponente sitzt (Brandt et al. 2003). Dementsprechend können basale IHZ vornehmlich den Schalldruck eines Schallreizes abbilden (Johnson 2015). Die Ursache für diese Unterschiede liegt in der variierenden Aktivität der MET- Kanäle und der basolateralen  $K^+$ -Kanäle.

Zusammenfassend kann also gesagt werden, dass über Form und Amplitude der Rezeptorpotentiale apikale IHZ eher die Frequenz, basale IHZ eher die Intensität eines Schallreizes abbilden können. Die Charakteristika der Rezeptorpotentiale in den IHZ werden wiederum durch die biophysikalischen Eigenschaften der Zellmembran bedingt, die wiederum von  $K^+$ -Strömen bestimmt werden, deren Expression sich entlang der tonotopen Achse verändert.

### 1.3 Die Identität der meisten $K^+$ -Kanäle in Haarsinneszellen ist unbekannt

Trotz der enormen Relevanz der Kaliumströme für die Physiologie der Sinneszellen ist die molekulare Identität der Ionenkanäle, die  $I_{K,f}$ ,  $I_{K,n}$  und  $I_{K,s}$  hervorbringen, nicht völlig aufgeklärt. So konnte zwar mithilfe von Iberiotoxin (IbTX), Charybdotoxin und Tetraethylammonium (TEA) (Kros et al. 1998; Marcotti and Kros 1999) und durch Experimente an *knock-out* Mäusen (Pyott et al. 2007; Rüttiger et al. 2004; Thurm et al. 2005) eindeutig gezeigt werden, dass  $I_{K,f}$  in den Haarsinneszellen durch  $Ca^{2+}$ - und spannungsaktivierte BK-Kanäle ( $BK_{Ca}$ ) vermittelt wird, jedoch stimmen dessen biophysikalische Eigenschaften in IHZ nicht mit rekombinanten  $BK_{Ca}$ -Kanälen überein. In Haarsinneszellen aktivieren die Kanäle nämlich auch in Abwesenheit von  $Ca^{2+}$  bei negativen Membranpotentialen, was für heterolog exprimierte  $BK_{Ca}$ -Kanäle nicht der Fall ist (Thurm et al. 2005). Diese Unterschiede deuten darauf hin, dass Haarzell-spezifische Interaktionspartner diese besonderen Eigenschaften in den Sinneszellen bedingen. Tatsächlich konnte erst kürzlich gezeigt werden, dass diese Eigenschaften ( $Ca^{2+}$ -Unabhängigkeit und Aktivierung bei negativen Membranpotentialen) durch die regulatorische  $\gamma$ -Untereinheit LRRC52 determiniert wird, welche in den Sinneszellen prominent exprimiert ist (Lingle et al. 2019).

Ähnlich verhält es sich mit dem Ionenkanalkomplex, der  $I_{K,n}$  hervorbringt. So konnte zwar an Mäusen, in denen das *Kcnq4* Gen genetisch ausgeschaltet wurde, gezeigt werden, dass  $I_{K,n}$  in IHZ und ÄHZ fehlt, d.h.  $K_v7.4$ -Kanäle bringen  $I_{K,n}$  als essentielle Kanaluntereinheiten in den Sinneszellen hervor (Kharkovets et al. 2006). Jedoch können auch  $K_v7.4$ -Untereinheiten nicht alleine die biophysikalischen Eigenschaften des Haarzellstroms erklären. Während  $I_{K,n}$  bereits bei Spannungen um ca. -70 mV bis -80 mV halbmaximal aktiviert ist, aktivieren rekombinante  $K_v7.4$ -Kanäle erst bei um ungefähr +60 mV positiveren Potentialen (Mammano and Ashmore 1996; Sjøgaard et al. 2001). Darüber hinaus unterscheidet sich die Aktivierungskinetik, das pharmakologische Profil und die Phospholipid-Abhängigkeit von  $I_{K,n}$  deutlich von rekombinanten  $K_v7.4$ -Kanälen (Leitner et al. 2012; Leitner et al. 2011). Wahrscheinlich sind in Haarsinneszellen Interaktionspartner exprimiert, die  $I_{K,n}$  zusammen mit  $K_v7.4$  hervorbringen. Diese Interaktionspartner sind von besonderer physiologischer Bedeutung, weil sie die komplette Aktivierung von  $I_{K,n}$  beim Ruhepotential und somit die schnellen Rezeptorpotentialänderungen in ÄHZ gewährleisten. Somit ist diese Interaktion eine essentielle Voraussetzung für die Frequenzdiskriminierung und hohe Sensitivität des Säugergehørs (Johnson et al. 2011). Außerdem ist  $I_{K,n}/K_v7.4$  für das Überleben der ÄHZ unabdingbar, da die pharmakologische

## EINLEITUNG

Inhibition und die genetische Ablation von  $K_v7.4$ -Untereinheiten eine langsame Degeneration der ÄHZ zur Folge hat (Kharkovets et al. 2006; Nouvian et al. 2003). Klinisch von Bedeutung ist dies, da  $K_v7.4$ -Mutationen über analoge Mechanismen die autosomal dominante Taubheitsform DFNA2 im Menschen hervorrufen (Coucke et al. 1999; Kubisch et al. 1999). Somit ist  $I_{K,n}$  nicht nur wichtig für die Signalverarbeitung in Haarsinneszellen, sondern auch für den Erhalt der Sinneszellen. Die Interaktionspartner, die  $I_{K,n}$  zusammen mit  $K_v7.4$  ausbilden, sind bisher unbekannt.

Ebenso unbekannt sind auch die Ionenkanäle, die den langsam aktivierenden  $I_{K,s}$  in IHZ hervorbringen. Bekannt ist lediglich, dass der Strom teilweise durch den Kaliumkanalinhibitor 4-Aminopyridin (4-AP) gehemmt wird und sich die Stromkomponente in Mäusen etwa 12-19 Tage nach der Geburt entwickelt (Marcotti et al. 2003). Es ist also sehr gut möglich, dass sich der  $I_{K,s}$  in IHZ aus mehreren unabhängigen Ionenkanaluntereinheiten (4-AP-sensitive und nicht sensitive) zusammensetzt.

Demnach sind die Proteine, die  $I_{K,n}$  und  $I_{K,s}$  in auditorischen Haarsinneszellen hervorbringen bis heute unbekannt. Die Identifikation dieser Kanaluntereinheiten und der Interaktionspartner in Haarsinneszellen ermöglicht nicht nur ein besseres Verständnis der Hörphysiologie, sondern bietet auch neue Zielmoleküle für die therapeutische und pharmakologische Intervention bei Schwerhörigkeitsformen, die durch Verlust der Aktivität von  $K^+$ -Kanälen in Haarsinneszellen hervorgerufen werden (z.B. DFNA2, siehe oben). Allerdings gestaltet sich die Identifizierung der Kanaluntereinheiten und Interaktionspartner in den Sinneszellen als schwierig: so wurde erst 2019 und somit 29 Jahre nach der Erstbeschreibung des Stroms in IHZ (Kros and Crawford 1990) die regulatorische  $\gamma$ -Untereinheit LRRC52 (Lingle et al. 2019) der  $BK_{Ca}$ -vermittelten  $I_{K,f}$  Komponente in IHZ entdeckt. Dass die biophysikalischen und pharmakologischen Eigenschaften der Haarzellkanäle nicht nur durch akzessorische Untereinheiten, sondern auch durch Splice-Varianten, posttranslationale Modifikationen und die Bildung heteromerer Kanäle beeinflusst sein könnten, erschwert die Identifikation und Analyse der beteiligten Untereinheiten zusätzlich.

### 1.4 Fragestellung und Zielsetzung der Arbeit

Die vorliegende Arbeit hatte das Ziel, die in Haarsinneszellen exprimierten Kaliumkanäle, mögliche akzessorische Untereinheiten, sowie die Relevanz der vermittelten Ströme für die Physiologie der Sinneszellen zu ermitteln. Da klassische biochemische Methoden und Massenspektrometrie-Verfahren aufgrund der geringen zur Verfügung stehenden Gewebemenge (vgl. Corti'sches Organ) nur bedingt in Haarsinneszellen angewendet werden können, sollte hierfür zuerst eine Strategie zur Identifikation von in den Sinneszellen möglicherweise exprimierten Kandidatenkanälen etabliert werden. Die Kandidatenkanäle sollten dann im Expressionssystem eingehend charakterisiert und experimentelle Protokolle zum Nachweis ihrer Aktivität in Haarsinneszellen entwickelt werden. Diese Protokolle sollten dann angewendet werden, um zu prüfen, ob die Kanäle in Haarsinneszellen funktionell vorkommen. Abschließend wurde die Funktion und die biologische Bedeutung der identifizierten Ionenkanäle für die Sinneszellen anhand von Computersimulationen bestimmt. Die vorliegende Arbeit beschreibt meine Ergebnisse in zwei Abschnitten zu (I.) einem vielversprechenden Interaktionspartner von  $K_v7.4$ -Kanälen in ÄHZ und (II.) den  $K^+$ -Kanaluntereinheiten, die die  $K^+$ -Kanal-Ausstattung in IHZ ausmachen:

## EINLEITUNG

### I. Die Rolle der $\beta$ -Sekretase 1 (BACE1) im auditorischen System

Kürzlich konnte gezeigt werden, dass das Enzym  $\beta$ -Sekretase 1 (BACE1) eine akzessorische Untereinheit von  $K_v7$ -Kanälen ist (Agsten et al. 2015; Hessler et al. 2015; Lehnert et al. 2016). Im heterologen Expressionssystem und auch in zentralen Neuronen (Hippocampus) interagiert BACE1 direkt mit  $K_v7$ -Kanaluntereinheiten und erhöht dadurch deren Lokalisation in der Zellmembran, sowie deren Aktivität. Außerdem aktivieren  $K_v7$ -Kanäle (eingeschlossen  $K_v7.4$ ) in Zellen, die BACE1 ko-exprimieren, bei deutlich hyperpolarisierten Membranpotentialen (Hessler et al. 2015). In bis zum damaligen Zeitpunkt unveröffentlichten Vorarbeiten fanden Kollaborationspartner aus Erlangen und Göttingen heraus, dass BACE1<sup>-/-</sup> Mäuse einen signifikanten Hörverlust zeigen. Diese phänotypischen Gemeinsamkeiten zu *Kcnq4*<sup>-/-</sup> Mäusen, die einen ähnlichen Hörverlust entwickeln (Kharkovets et al. 2006), und die beschriebenen Auswirkungen der BACE1 Ko-expression auf  $K_v7.4$ -Kanaluntereinheiten (v.a. die Veränderung der Spannungsabhängigkeit von  $K_v7.4$  Kanälen durch BACE1) legten nahe, dass der Hörverlust in BACE1<sup>-/-</sup> Mäusen durch die Veränderung der Aktivität von  $K_v7.4$ -Kanälen hervorgerufen werden könnte. Das führte mich zu zwei zentralen Fragestellungen meiner Arbeit: 1. Könnte BACE1 der Interaktionspartner in ÄHZ sein, der  $I_{K,n}$  zusammen mit  $K_v7.4$ -Kanaluntereinheiten hervorbringt? 2. Was sind die molekularen und zellulären Ursachen für den Hörverlust in den BACE1<sup>-/-</sup> Mäusen (**Paper 1**)?

### II. Entschlüsselung des $K^+$ -Kanal-Ausstattung in Haarsinneszellen

Ein weiteres Ziel meiner Arbeit war es,  $K^+$ -Kanaluntereinheiten, die in Haarsinneszellen exprimiert sind, zu identifizieren und deren Bedeutung für die Physiologie der Sinneszellen aufzuklären. Um mögliche Kandidatenkanäle zu finden, sollten zunächst verfügbare Einzelzell-Transkriptome von IHZ analysiert werden (Liu et al. 2014), um Kanaluntereinheiten herauszuarbeiten, die möglicherweise in Haarsinneszellen exprimiert sein könnten. Dann sollte die Expression dieser Kandidaten in der Cochlea mittels molekularbiologischer und immunhistochemischer Methoden experimentell getestet (**Paper 5**) und elektrophysiologische Ansätze entwickelt werden (**Paper 2, 3 und 4**), die den funktionellen Nachweis der Kanäle in den Haarsinneszellen ermöglichen. Aufbauend auf dem funktionellen Nachweis der Kanäle sollten in Kollaboration mit Dr. Alessandro Altoè biophysikalische Modelle von Haarsinneszellen entwickelt werden, anhand derer die biologische Relevanz der einzelnen Kanalkomponenten ermittelt werden kann (**Paper 5**).

## 2. Erklärung über den Eigenanteil an den vorliegenden Publikationen

1. **Dierich M.**, Hartmann S., Dietrich N., Moeser P., Brede F., Chacko L.J., Tziridis K., Schilling A., Krauss P., Hessler S., Lehnert S., Karch S., Schrott-Fischer A., Blumer M., Birchmeier C., Oliver D., Moser T., Schulze H., Alzheimer C., Leitner M. G., Huth T. (2019).  $\beta$ -Secretase BACE1 Is Required for Normal Cochlear Function. *The Journal of Neuroscience*, 39(45):9013-9027. doi: 10.1523/JNEUROSCI.0028-19.2019

Alle immunhistochemischen Färbungen (Abb. 2, 3, 5, 6, 7, 8 E-H, 9,10) wurden von mir etabliert, durchgeführt und analysiert. Des Weiteren sind die Prestin-bezogenen Messungen in ÄHZ (Abb.4A1-A4) und die elektrophysiologische Charakterisierung der IHZ (Abb.4F-H) von mir geplant und durchgeführt worden. Ich war für die statistische Auswertung der Daten und die Zusammenstellung aller Abbildungen verantwortlich und habe maßgeblich an der schriftlichen Ausführung der Publikation mitgewirkt.

2. **\*Dierich M.**, \*Evers S., Wilke B. U., Leitner M. G. (2018). Inverse Modulation of Neuronal  $K_v12.1$  and  $K_v11.1$  Channels by 4-Aminopyridine and NS1643. *Frontiers in Molecular Neuroscience*, 11(January), 11:11. doi: 10.3389/fnmol.2018.00011

Ich habe alle elektrophysiologischen Messungen geplant, durchgeführt und ausgewertet, die in Abbildung 1, 3A-E, 4, 5 und 6 sowie im Supplement 2 C+F+I, 4 und 5 dargestellt sind. Ich habe das Manuskript zusammen mit Dr. Michael Leitner geschrieben und überarbeitet.

3. **Dierich M.** & Leitner M. G. (2018).  $K_v12.1$  channels are not sensitive to  $G_q$ PCR-triggered activation of phospholipase  $C\beta$ . *Channels*, 12(1), 228-239. doi: 10.1080/19336950.2018.1475783

Ich habe die Publikation zusammen mit Dr. Michael Leitner geschrieben und überarbeitet.

4. **Dierich M.**, van Ham W.B., Stary-Weinzinger A., Leitner M. G. (2019). Histidine at position 462 determines the low quinine sensitivity of ether-à-go-go channel superfamily member  $K_v12.1$ . *British Journal of Pharmacology*, 176(15): 2708-2723. doi: 10.1111/bph.14693

Alle elektrophysiologischen Messungen und molekularbiologischen Arbeiten (Mutagenese, PCR, etc.) wurden von mir geplant, durchgeführt und ausgewertet. Ich habe die Publikation zusammen mit Dr. Michael Leitner geschrieben und überarbeitet.

5. **\*Dierich M.**, \*Altoè A., Koppelman J., Evers S., Renigunta V., Schäfer M.K., Naumann R., Verhulst S., Oliver D., Leitner M. G. (2020). Optimized Tuning of Auditory Inner Hair Cells to Encode Complex Sound through Synergistic Activity of Six Independent  $K^+$  Current Entities. *Cell Reports* 32, 107869:1-e4. doi: 10.1016/j.celrep.2020.107869

Ich habe alle im Manuskript beschriebenen elektrophysiologischen Messungen, molekularbiologischen Arbeiten (RT-PCR) und immunhistochemischen Färbungen geplant, durchgeführt und ausgewertet und die Publikation zusammen mit Dr. Michael Leitner geschrieben und überarbeitet.

### \* Geteilte Erstautorenschaften

## RESULTATE

### 3. Resultate

#### 3.1 Die Rolle der Beta-Sekretase 1 (BACE1) im auditorischen System

Die Beta-Sekretase 1, auch BACE1 (für  *$\beta$ -site of APP cleaving enzyme*), Asp2 oder Memapsin genannt, ist eine Protease, die 1999 von fünf Gruppen unabhängig voneinander entdeckt worden ist (Hussain et al. 1999; Lin et al. 2000; Sinha et al. 1999; Vassar et al. 1999; Yan et al. 1999) und die Bildung des neurotoxischen Beta-Amyloid-Peptides (A $\beta$ ) initiiert. Dieser pathogenetische Mechanismus ist wahrscheinlich für die Entstehung und das Fortschreiten der Alzheimer-Krankheit verantwortlich, was die pharmakologische Inhibition des Enzyms zu einer vielversprechenden Strategie in der Therapie der Erkrankung macht (Haass and Selkoe 1993). Das Enzym hat aber natürlich auch weitere physiologische Aufgaben, was dadurch verdeutlicht wird, dass in den letzten Jahren über 60 BACE1-Substrate identifiziert werden konnten (Hemming et al. 2009). Somit kann die pharmakologische Inhibition des Enzyms zu ernstzunehmenden Nebenwirkungen bei der Therapie der Alzheimer-Krankheit führen. Um mögliche Nebenwirkungen der Behandlung abschätzen zu können, ist es daher wichtig, die physiologischen Funktionen von BACE1 zu kennen.

Auf der Suche nach neuen physiologischen Aufgaben von BACE1 haben unsere Kollaborationspartner (um Prof. Dr. Alzheimer und Dr. Huth) vom Institut für Physiologie und Pathophysiologie der Friedrich-Alexander-Universität in Erlangen die Hörleistung von Mäusen bestimmt, in denen BACE1 genetisch ausgeschaltet wurde (BACE1<sup>-/-</sup>) (Dominguez et al. 2005). Dies erfolgte zunächst anhand der Hirnstammaudiometrie (ABR), bei der mittels EEG-Elektroden das Antwortverhalten von neuronalen Strukturen entlang der auditorischen Bahn in Abhängigkeit definierter auditorischer Reize bestimmt wird. Dabei zeigen sich die synchronen Antworten neuronaler Strukturen entlang der Hörbahn als eine typische Abfolge von charakteristischen Potentialwellen (Welle 1-5/6). Diese Experimente ergaben eine deutliche Hörminderung in BACE1<sup>-/-</sup> Mäusen, die einerseits gekennzeichnet war durch eine erhöhte Hörschwelle von 20-40 dB im Frequenzbereich von 4 bis 32 kHz, und andererseits durch eine signifikante Verringerung der Amplitude und einer Verlängerung der Latenzzeit der Welle 1 (**Paper 1, Abb.1A-D**). Da Welle 1 die synchrone Aktivität im peripheren Anteil des Hirnnerven VIII widerspiegelt, liegt die Ursache für den Hörverlust der BACE1<sup>-/-</sup> Mäuse vermutlich an einer beeinträchtigten Informationsverarbeitung zwischen Haarsinneszellen und den auditorischen Nervenfasern im Corti'schen Organ. Dazu passend waren auch die erheblich reduzierten otoakustischen Emissionen (OAE) in den BACE1<sup>-/-</sup> Mäusen, welche direkt einen Funktionsverlust der ÄHZ anzeigten (**Paper 1, Abb.1E**).

##### 3.1.1 Ist die Interaktion von BACE1 mit K<sub>v</sub>7.4-Kanaluntereinheiten die molekulare Grundlage für den Haarzellstrom I<sub>K,n</sub>?

Umfangreiche histologische Analysen in der Cochlea ergaben keinerlei Hinweise auf strukturelle Veränderungen im Corti'schen Organ, sowie Verluste oder Schäden an Haarsinneszellen, die den Hörverlust von BACE1<sup>-/-</sup> Mäusen erklären könnten (**Paper 1, Abb.3A+B**). Deswegen habe ich anschließend untersucht, ob BACE1 essentiell für die Physiologie der Haarsinneszellen sein könnte. Mittels immunohistochemischen Färbungen konnte ich keinerlei Unterschiede in der Expression von K<sub>v</sub>7.4 in den ÄHZ zwischen Wildtyp und BACE1<sup>-/-</sup> Mäusen entdecken (**Paper 1, Abb.3E**). Elektrophysiologische Messungen zeigten, dass es in Hinsicht auf Zellmembrankapazität und Membranzeitkonstanten, sowie das Ruhemembranpotential keinerlei

## RESULTATE

Unterschiede zwischen IHZ bzw. ÄHZ von Wildtyp und BACE1<sup>-/-</sup> Mäusen gab (**Paper 1, Abb.4B-H**). Außerdem waren die biophysikalischen Eigenschaften von I<sub>K,n</sub> in den Haarsinneszellen der BACE1<sup>-/-</sup> Mäuse unverändert (**Paper 1, Abb.4B-D**). BACE1 ist also kein essentieller Interaktionspartner von K<sub>v</sub>7.4-Kanälen in Haarsinneszellen und dementsprechend nicht für die biophysikalischen Eigenschaften von I<sub>K,n</sub> verantwortlich.

Weiterführende Experimente zur Physiologie der Haarsinneszellen zeigten, dass in BACE1<sup>-/-</sup> Mäuse die Expression des Proteins Prestin in der lateralen Plasmamembran der ÄHZ (**Paper 1, Abb.3D**) und dessen Funktion (**Paper 1, Abb.4A**) vollkommen normal waren. Ebenso konnte ich mittels konfokaler Mikroskopie und der Applikation des lipophilen Styrylfarbstoffes FM1-43, der durch MET-Kanäle in Haarsinneszellen eindringt, keine Unterschiede in der Aktivität der MET-Kanäle in den BACE1<sup>-/-</sup> Mäusen feststellen (**Paper 1, Abb.3C**). Da die Physiologie von Haarsinneszellen in BACE1<sup>-/-</sup> Mäusen unverändert war, zeigen diese Ergebnisse, dass BACE1 für die Funktion der Sinneszellen nicht von Bedeutung ist. Dazu passt auch, dass ich in immunhistochemischen Experimenten keinerlei Hinweise auf die Expression von BACE1 in Haarsinneszellen finden konnte (**Paper 1, Abb.2C+D**). Dementsprechend ist es unwahrscheinlich, dass der Hörverlust in BACE1<sup>-/-</sup> Mäusen durch pathophysiologische Prozesse in den Haarsinneszellen hervorgerufen wird.

### 3.1.2 Sensorineuronaler Hörverlust aufgrund der Hypomyelinisierung von peripheren auditorischen Nervenfasern in BACE1<sup>-/-</sup> Mäusen

Stattdessen beobachtete ich, dass BACE1 stark in Nervenzellen der Cochlea exprimiert ist, nämlich in präsynaptischen Terminalen von efferenten olivo-kochleären Neuronen, sowie in primären auditorischen Nervenfasern, deren Zellkörper sich im Spiralganglion der Cochlea befindet (**Paper 1, Abb.2A-D**). Wegen der starken Expression von BACE1 in den Nervenzellen der Cochlea analysierte ich dann den Signalübertragungsweg von IHZ zu auditorischen Nervenfasern in den BACE1<sup>-/-</sup> Mäusen. In diesen Experimenten fand ich heraus, dass sich die Anzahl der präsynaptischen Bändersynapsen in den IHZ und der Cluster von postsynaptischen AMPA-Rezeptoren in den BACE1<sup>-/-</sup> Mäusen nicht von Wildtyp-Mäusen unterschieden, d.h. die morphologische Integrität der Synapsen war normal in den BACE1<sup>-/-</sup> Mäusen (**Paper 1, Abb.5**). In einem nächsten Schritt färbte ich die Nervenfasern mit Antikörpern, die gegen den neuronalen Marker NF-200, myelin *basic protein* (MBP; Darstellung der Myelinisierung) und *post synaptic density* Protein 95 (PSD95) gerichtet waren. Bei der Analyse der auditorischen Nervenfasern, die vom Spiralganglion zum Corti'schen Organ ziehen konnte ich zwei wesentliche Anomalien feststellen:

- 1) In BACE1<sup>-/-</sup> Mäusen waren die Nervenfasern im Bereich der IHZ unorganisiert, teilweise vergrößert und geschwollen. Außerdem war in diesen Mäusen PSD95 ektopisch überexprimiert und befand sich teilweise weit (d.h. mehrere µm) von der IHZ Synapse entfernt (**Paper 1, Abb.6**).
- 2) Die Myelinisierung der Nervenfasern in BACE1<sup>-/-</sup> Mäusen war extrem vermindert: Während in Wildtyp-Mäusen die Myelinisierung bis an die *Habenula perforata* nahe den IHZ heranreichte, endete diese in den BACE1<sup>-/-</sup> Mäusen, soweit überhaupt vorhanden, weit von den IHZ entfernt (**Paper 1, Abb.7A-C**). Transmissionselektronenmikroskopie bestätigte



## RESULTATE

die stark verringerte Myelinisierung der SGN in den BACE1<sup>-/-</sup> Mäusen (**Paper 1, Abb.7D+E**).

BACE1 ist also für eine normale Nervenfasearchitektur, Myelinisierung und organisierte synaptische Verbindungen zwischen IZH und den auditorischen Nervenfasern essentiell. Diese pathologischen Veränderungen können den Hörverlust in BACE1<sup>-/-</sup> Mäusen erklären, da in diesen Tieren eine normale Informationsübertragung auf den Hörnerv wahrscheinlich nicht möglich ist. In weiterführenden Experimenten suchte ich nach einem möglichen Substrat der enzymatischen Aktivität von BACE1 in der Cochlea, dessen Prozessierung für die Myelinisierung der Nervenfasern von Bedeutung sein könnte. Ein vielversprechender Kandidat war Neuregulin-1 (NRG1), das in SGN vorkommt (Hansen et al. 2001) und nach proteolytischer Spaltung durch BACE1 über ErbB-Rezeptoren die Myelinisierung von peripheren Nervenfasern vermittelt (Hu et al. 2006; Sherman and Brophy 2005; Willem et al. 2006; Wu et al. 2016). Tatsächlich zeigten heterozygote NRG1<sup>+/-</sup> Mäuse eine stark reduzierte Myelinisierung und eine Desorganisation von auditorischen Nervenfasern in der Cochlea (**Paper 1, Abb.10**). Da dieser Phänotyp, wenn auch in abgeschwächter Form, den Veränderungen in BACE1<sup>-/-</sup> Mäusen glich, deuteten diese Ergebnisse darauf hin, dass NRG1 tatsächlich ein für die Myelinisierung und die Organisation auditorischer Nervenfasern essentielles Substrat von BACE1 in der Cochlea darstellt.

Der Hörverlust in BACE1<sup>-/-</sup> Mäusen legt nahe, dass es bei der Behandlung von Alzheimer mit BACE1-Inhibitoren zu einer Verringerung der Hörleistung kommen könnte. Deswegen haben wir adulte Mäuse für sechs Wochen mit dem BACE1-Inhibitor NB-360 der Firma Novartis gefüttert (Neumann et al. 2015) und im Anschluss deren Hörleistung im Vergleich zu nicht behandelten Kontrolltieren untersucht. ABR-Messungen (**Paper 1, Abb.8D**) und immunohistochemischen Färbungen (**Paper 1, Abb.8E-H**) zeigten in diesen Tieren jedoch keine Hörminderung und auch keinerlei pathologische Veränderungen der kochleären Nervenfasern und synaptischen Strukturen. Des Weiteren verglich ich den zeitlichen Verlauf der Myelinisierung der Nervenfasern in Wildtyp-Mäusen mit der Entwicklung der Myelinisierung in BACE1<sup>-/-</sup> Mäusen zwischen fünf Tagen (P5) und 15 Tagen (P15) nach der Geburt der Tiere (**Paper 1, Abb.9A**). Bei Wildtyp-Mäusen war bereits an P5-P6 eine deutliche Myelinisierung der auditorischen Nervenfasern nachweisbar, ab P8 erstreckte sich die Myelinscheide in einigen Fasern distal bis zur *Habenula perforata* und erreichte am Ende der zweiten postnatalen Woche ein ausgereiftes Niveau. Im Gegensatz dazu zeigten BACE1<sup>-/-</sup> Mäuse erst am Ende der zweiten postnatalen Woche eine schwache und unvollständige Myelinisierung der SGN-Fasern (**Paper 1, Abb.9A**). Somit war die Entwicklung der Myelinisierung in der Cochlea von Mäusen mit BACE1-Mangel deutlich verzögert, und die axonale Umhüllung blieb auch im Erwachsenenalter unreif. Zusammenfassend zeigen diese Ergebnisse, dass eine therapeutische Inhibition der enzymatischen Aktivität der  $\beta$ -Sekretase BACE1 in Mäusen keinen Einfluss auf das Hörvermögen hat, da BACE1 für die Entwicklung und nicht für die Aufrechterhaltung der Myelinisierung und Organisation der auditorischer Nervenfasern im Erwachsenenalter essentiell ist.

### 3.2 Die molekulare Identität und physiologische Relevanz von K<sup>+</sup>-Kanälen innerer Haarsinneszellen

In einem weiteren Teil meiner Arbeit habe ich Expression und physiologische Relevanz von K<sup>+</sup>-Kanälen in Haarsinneszellen untersucht. Dazu war es in einem ersten Schritt notwendig,

## RESULTATE

mögliche Kandidatenkanäle zu identifizieren, die in Haarsinneszellen exprimiert sein könnten (**siehe 3.2.1**). In einem zweiten Schritt habe ich diese Kandidatenkanäle im Expressionssystem eingehend charakterisiert und experimentelle Protokolle zum Nachweis ihrer Aktivität in Haarsinneszellen entwickelt (**siehe 3.2.2**). Dann habe ich diese Strategien angewendet, um zu prüfen, ob die Kanäle in Haarsinneszellen funktionell sind (**siehe 3.2.3**). In Kollaboration mit Dr. Alexandro Altoè (*University of Southern California, Los Angeles*) haben wir anhand von Computersimulationen deren Rolle in Haarsinneszellen herausgearbeitet (**siehe 3.2.4**).

### **3.2.1 Identifizierung und Nachweis möglicher in Haarsinneszellen exprimierter Kandidatenkanäle**

Zunächst habe ich nach Möglichkeiten gesucht, Kanäle zu identifizieren, die in IHZ exprimiert sein könnten. Hierfür habe ich in der *SHIELD-Datenbank* zur Verfügung gestellte Expressionsdaten analysiert und aus einer Transkriptionsanalyse einzelner Haarsinneszellen (Liu et al. 2014; Shen et al. 2015) Kandidatenkanäle extrahiert. Als Schwellenwert habe ich hierbei die mRNA-Expression der  $K_v7.4$ -Untereinheit festgelegt, da diese in Sinneszellen vergleichsweise gering exprimiert ist, aber immerhin  $I_{K,n}$  in IHZ vermittelt (Oliver et al. 2003). Diese Analyse ergab mit  $K_v1.8$ ,  $K_v3.3$ ,  $K_v11.1$  und  $K_v12.1$  vier mögliche Kandidaten in IHZ (**Paper 5, Supplement 2**). Darunter befinden sich mit  $K_v11.1$  und  $K_v12.1$  zwei Mitglieder der *ether-à-gogo* (EAG)-Superfamilie. Im Gegensatz zu den  $K_v11.1$ -Kanälen, welche eine wichtige Rolle bei der Repolarisation von Aktionspotentialen im Herzen ( $I_{Kf}$ ) spielen (Curran et al. 1995; Sanguinetti et al. 1995) und auch im auditorischen Hirnstamm exprimiert sind (Hardman and Forsythe 2009), ist die physiologische Relevanz von  $K_v12.1$ -Kanälen bisher unbekannt. In auditorischen Haarsinneszellen sind beide bisher nicht untersucht worden. Ebenso wenig ist über die mögliche Rolle von  $K_v3.3$ - und  $K_v1.8$ -Untereinheiten in Haarsinneszellen bekannt. Immerhin konnte aber kürzlich gezeigt werden, dass  $K_v1.8$  *knock-out* Mäuse einen leichten Hörverlust entwickeln, was zumindest darauf hinweist, dass diese Kanäle wichtig für das auditorische System sein könnten (Lee et al. 2013). Um die Verlässlichkeit des Kandidatenansatzes zu überprüfen, sollte deswegen in einem ersten Schritt das Vorhandensein der Kanäle im Corti'schen Organ überprüft werden. Mittels der *Reverse-Transkriptase-Polymerase-Kettenreaktion* (RT PCR) konnte ich tatsächlich mRNA der Kandidatenkanäle  $K_v1.8$ ,  $K_v11.1$  und  $K_v12.1$  in Lysaten der gesamten Cochlea nachweisen (**Paper 5, Abb.2A, 3I, 4G**).

Immunhistochemische Untersuchungen mit spezifischen Antikörpern in Wildtyp-Mäusen und in Mäusen mit haarzellspezifischer Deletion des codierenden *Kcnh2* Gens (*Kcnh2<sup>HC/-</sup>* Mäuse) zeigten, dass  $K_v11.1$ -Untereinheiten tatsächlich stark in der Zellmembran von IHZ exprimiert sind (**Paper 5, Abb.2B**). Außerdem konnte ich in elektrophysiologischen Experimenten zeigen, dass  $K_v11.1$ -Kanäle in IHZ auch funktionell vorkommen: Denn die extrazelluläre Applikation von E 4031, einem spezifischen Antagonisten von  $K_v11$ -Kanälen (Trudeau et al. 1995), führte zu einer signifikanten Inhibition von  $K^+$ -Strömen in IHZ und zur Depolarisation des Membranpotentials (**Paper 5, Abb.2C+E**). Außerdem entsprachen die biophysikalischen Eigenschaften des E-4031-sensitiven Haarzellstroms exakt den Charakteristika von rekombinanten  $K_v11.1$ -Kanälen (**Paper 5, Abb.2F-I**). Da diese E-4031-sensitiven Ströme sowie auch die E-4031-abhängige Depolarisation in IHZ aus *Kcnh2<sup>HC/-</sup>* Mäusen komplett fehlten (**Paper 5, Abb.2D+E, Supplement 3C-F**), zeigen diese Daten, dass  $K_v11.1$ -Untereinheiten bedeutende Ströme in IHZ vermitteln.

### 3.2.2 Elektrophysiologische und pharmakologische Charakterisierung der Kandidatenkanäle im heterologen Expressionssystem

Da für die übrigen Kandidatenkanälen  $K_v1.8$  und  $K_v12.1$  keine spezifischen Antikörper erhältlich sind (vgl. **Paper 5, Supplement 5L**), konnte die Expression dieser Untereinheiten nicht mit immunhistochemischen Methoden untersucht werden. Außerdem sind bisher keine spezifischen Inhibitoren zur pharmakologischen Isolation möglicher  $K_v1.8$ - oder  $K_v12.1$ -vermittelter Ströme bekannt. Deswegen war es notwendig, eindeutige Eigenschaften dieser Kanäle zu identifizieren, über die sich Ströme in den Haarsinneszellen eindeutig diesen Kandidatenkanälen zuweisen lassen. Daher habe ich zunächst mittels *Whole-Cell-Patch-Clamp* die biophysikalischen und pharmakologischen Eigenschaften des  $K_v12.1$ -Kanals in „*Chinese hamster ovary cells*“ (CHO-Zellen) untersucht.

Das erste Augenmerk habe ich dabei auf die spannungsabhängige Aktivierung des  $K_v12.1$ -Kanals gelegt, die durch den sogenannten „*mode shift of activation*“ (auch *pre-pulse facilitation* oder *voltage-dependent potentiation* genannt (Dai and Zagotta 2017; Li et al. 2015)) bestimmt wird. Diese biophysikalische Eigenschaft ist durch eine Verschiebung der Spannungsabhängigkeit zu hyperpolarisierten Potentialen als Reaktion auf einen depolarisierten Vorpuls gekennzeichnet (Villalba-Galea 2017). Abhängig vom angelegten Haltepotential (*conditioning potential*) variiert somit die Spannungsabhängigkeit des Kanals. Um diese spezielle Eigenschaft von  $K_v12.1$ -Kanälen für den Nachweis in Haarsinneszellen nutzen zu können, war es daher notwendig, den *mode shift* von  $K_v12.1$ -Kanälen zunächst im Expressionssystem genau zu charakterisieren. Humane  $K_v12.1$ -Kanäle zeigten im heterologen Expressionssystem einen signifikanten spannungsabhängigen *mode shift* als Antwort auf ein depolarisierendes Haltepotential, der sich durch eine verlangsamte Kanaldeaktivierung und durch eine Verschiebung der Spannungsabhängigkeit zu hyperpolarisierten Potentialen manifestierte. Ein maximaler *mode shift* konnte unter Verwendung verschiedener Spannungsprotokolle (*mode shift*<sub>Max</sub>: Haltepotential: -60 mV und 0 mV) induziert werden, wobei das Ausmaß des *mode shift* mit der Dauer des angelegten depolarisierenden Potentials zwischen dem Haltepotential anstieg (**Paper 2, Abb.1**). Weitere Experimente zeigten, dass ein derartiges Verhalten keine exklusive Eigenschaft des  $K_v12.1$ -Kanals ist: Auch die anderen Kandidatenkanäle, der  $K_v11.1$  (**Paper 2, Abb.2B**) (Goodchild et al. 2015; Piper et al. 2003; Tan et al. 2012) und der  $K_v1.8$  (**Daten nicht veröffentlicht**), zeigten ebenfalls einen spannungsabhängigen *mode shift*.

Als Nächstes untersuchte ich die Regulation von  $K_v12.1$ -Kanälen durch Phosphatidylinositol-4,5-bisphosphat ( $PI(4,5)P_2$ ) (**Paper 3**), was ein essentieller Co-Faktor von vielen Ionenkanälen ist (Suh and Hille 2008). Diese Experimente zeigten, dass humane  $K_v12.1$ -Kanäle unempfindlich gegenüber Depletion von Phospholipiden waren (**Paper 3, Abb.2+3**), weswegen sich dessen Phospholipidabhängigkeit nicht dazu eignete,  $K_v12.1$ -vermittelte Ströme in Haarsinneszellen zu identifizieren. Der nächste Schritt war dann die Erstellung eines pharmakologischen Profils von  $K_v12.1$ . Dazu analysierte ich die Wirkung einer Reihe von nicht selektiven  $K^+$ -Kanal-Blockern (Tetraethylammonium (TEA); 4-Aminopyridin (4-AP); Chinin) und spezifischen Inhibitoren (E-4031; XE991) sowie Aktivatoren (NS1643) auf rekombinante  $K_v12.1$ -Kanäle (und die übrigen Kandidatenkanäle). Im Expressionssystem waren  $K_v12.1$ - (**Paper 2, Supplement 2; Paper 5, Supplement 5D+E+H**), wie auch  $K_v1.8$ -Kanäle (**Paper 5, Supplement 4D+E+I**) völlig insensitiv gegenüber TEA und XE991. Das ist von

## RESULTATE

Bedeutung, da TEA (5 mM) und XE991 (10  $\mu$ M) zur Inhibition der BK<sub>Ca</sub>-Kanal-vermittelten I<sub>K,f</sub> und der K<sub>v</sub>7.4-vermittelten I<sub>K,n</sub> Komponente in IHZ und damit zur Isolation von I<sub>K,s</sub> eingesetzt werden (Kros and Crawford 1990; Oliver et al. 2003).

Chinin wird als Antimalariamittel und Antiarrhythmikum eingesetzt und inhibiert K<sub>v</sub>11.1-Kanäle im mikromolaren Bereich (Sánchez-Chapula et al. 2003) (**Paper 4, Abb.2**). Da K<sub>v</sub>11.1, wie auch K<sub>v</sub>12.1-Kanäle, der EAG-Superfamilie zugeordnet werden, lag es nahe zu vermuten, dass auch K<sub>v</sub>12.1-Kanäle sensitiv gegenüber der Substanz sind. Ich konnte zeigen, dass Chinin zwar rekombinante K<sub>v</sub>12.1-Kanäle ebenso wie K<sub>v</sub>11.1-Kanäle hemmt, jedoch die Chinin-Affinität der K<sub>v</sub>12.1-Kanäle 10-fach niedriger als die von K<sub>v</sub>11.1 ist (**Paper 4, vgl. Abb.1A und Abb2A**). Im Gegensatz zu K<sub>v</sub>11.1 inhibierte Chinin K<sub>v</sub>12.1 weitgehend spannungsunabhängig und induzierte eine Kanalöffnung für K<sub>v</sub>12.1 bei depolarisierten Potentialen (**Paper 4, Abb.1D+I**). Diese Ergebnisse zeigten, dass sich die Sensitivität und die Wirkung von Chinin trotz der nahen Verwandtschaft zwischen K<sub>v</sub>11.1 und K<sub>v</sub>12.1 deutlich unterscheiden. Der Austausch eines Histidins (H) an Position 462 von K<sub>v</sub>12.1 mit einem Tyrosin (Y), wie es bei K<sub>v</sub>11.1-Kanälen an der entsprechenden Aminosäureposition (Y652) steht (**Paper 4, Abb. 3A**), führte zu einer drastischen Veränderung der Chinin-Sensitivität der mutierten K<sub>v</sub>12.1(H462Y)-Kanäle (**Paper 4, Abb.4**). Tatsächlich war die Sensitivität und die Wirkung von Chinin auf K<sub>v</sub>12.1(H462Y)-Kanäle fast identisch zu K<sub>v</sub>11.1, was zeigte, dass eben diese Aminosäureposition (462 in K<sub>v</sub>12.1 und 652 in K<sub>v</sub>11.1) die Chinin-Affinität und die molekularen Mechanismen der Chinin-abhängigen Inhibition in der EAG-Superfamilie bedingt. Die generelle Architektur dieser Kanäle ist dementsprechend zwar ähnlich, es bestehen aber doch bedeutende Unterschiede in den Bindetaschen für Inhibitoren (**Paper 4**).

In weiteren pharmakologischen Experimenten konnte ich darüber hinaus zeigen, dass sich das pharmakologische Profil der nahe verwandten K<sub>v</sub>11.1- und K<sub>v</sub>12.1-Kanäle noch bedeutender unterscheidet: NS1643, ein bekannter Agonist der K<sub>v</sub>11-Kanalfamilie (Casis et al. 2006) (**Paper 2, Abb.5A-C**), führte nämlich zu einer vollständigen Inhibition K<sub>v</sub>12.1-vermittelter Ströme (**Paper 2, Abb.5A-D; Paper 5, Supplement 5G+H**), sowie auch zur vollständigen Inhibition von K<sub>v</sub>1.8-Kanälen (**Paper 5, Supplement 4G+I**). Im Gegensatz dazu induzierte 4-AP, ein generell nicht-selektiver Inhibitor von K<sup>+</sup>-Kanälen, (für Inhibition von K<sub>v</sub>11.1 siehe **Paper 2, Supplement 3A-C** und für K<sub>v</sub>1.8 siehe (Lang et al. 2000) und **Paper 5, Supplement 4F+I**) eine signifikante Aktivierung von K<sub>v</sub>12.1-Kanälen (**Paper 2, Abb.3A-D; Paper 5, Supplement 5F+H+I**). Das bedeutet, dass es sich bei 4-AP um einen potenten Aktivator von K<sub>v</sub>12.1-Kanälen handelt. In diesen Experimenten ist es mir gelungen, charakteristische biophysikalische und pharmakologische Eigenschaften von K<sub>v</sub>12.1-Kanälen zu identifizieren; dazu zählen der spannungsabhängige *mode shift*, die 4-AP-induzierte Aktivierung und die NS1643-abhängige Inhibition dieser Kanäle. Diese charakteristischen Eigenschaften sollten sich dazu nutzen lassen, die potenzielle Aktivität von K<sub>v</sub>12.1-Kanälen in IHZ nachzuweisen. Um die Anwendbarkeit des Ansatzes im Expressionssystem zu überprüfen, habe ich zunächst eine Kombination neuronaler K<sup>+</sup>-Kanaluntereinheiten (K<sub>v</sub>11.1, K<sub>v</sub>7.2, K<sub>v</sub>7.3 und Kir2.1) in CHO-Zellen überexprimiert. In diesen Zellen konnte ich tatsächlich die etablierten K<sub>v</sub>12.1-typischen Eigenschaften klar darstellen und somit die Aktivität von K<sub>v</sub>12.1-Kanälen in diesem Mix von K<sup>+</sup>-Strömen eindeutig zeigen (**Paper 2, Abb.6**). Diese Experimente ermöglichten es mir, im nächsten Schritt zu untersuchen, ob K<sub>v</sub>12.1-Kanäle in auditorischen IHZ aktiv sind.

### 3.2.3 $K_v1.8$ , $K_v11.1$ und $K_v12.1$ sind die molekulare Grundlage von $I_{K,s}$ in inneren Haarsinneszellen

Um zu überprüfen, ob neben  $K_v11.1$ -Kanälen (**siehe 3.2.1**) auch die Kandidatenkanäle  $K_v1.8$  und  $K_v12.1$  in IHZ funktionell sind, habe ich elektrophysiologische Messungen an IHZ der Maus im *Whole-Cell-Patch-Clamp*-Modus durchgeführt. In diesen Experimenten fand ich eindeutige Hinweise darauf, dass sowohl  $K_v1.8$ - als auch  $K_v12.1$ -Kanäle in IHZ aktiv sind: Zum einen identifizierte ich eine Stromkomponente in IHZ, deren biophysikalische (Spannungsabhängigkeit) und pharmakologische (Inhibition durch 4-AP) Eigenschaften fast ident zu den Charakteristika heterolog exprimierter  $K_v1.8$ -Kanaluntereinheiten waren, deren genetische Information ich aus der Cochlea klonieren konnte (**Paper 5, Abb.3E-I; Supplement 4F+I**). Dies identifizierte eindeutig  $K_v1.8$ -Kanäle in IHZ; dafür spricht auch, dass kürzlich mittels eines  $\beta$ -Galaktosidase-Assays gezeigt wurde, dass diese Kanäle in IHZ und ÄHZ exprimiert sind (Lee et al. 2013).

Zum anderen führte die extrazelluläre Applikation von 4-AP, neben der Inhibition des durch  $K_v1.8$ -vermittelten Auswärtsstroms, zu einer signifikanten Hyperpolarisation des Membranpotentials (**Paper 5, Abb.4A+B**), und zur Aktivierung eines  $K^+$ -Stroms bei hyperpolarisierten Membranpotentialen (**Paper 5, Abb.4C**). Diese Eigenschaften stimmen mit den beschriebenen Charakteristika der rekombinanten  $K_v12.1$ -Kanäle überein (**siehe 3.2.2; Paper 2**). Dieselbe Stromkomponente wurde auch durch NS1643 inhibiert (**Paper 5, Supplement 6A-C**), d.h. auch die NS1643-Sensitivität dieses IHZ-Stroms spiegelt die besonderen Eigenschaften von rekombinanten  $K_v12.1$ -Kanälen wider. Ebenso ließ sich mit denselben Spannungsprotokollen, die ich im Expressionssystem entwickelt hatte (**siehe 3.2.2**), auch in IHZ ein *mode shift* von  $K^+$ -Kanälen nachweisen (**Paper 5, Abb.5D+E**). Die übereinstimmenden Eigenschaften der IHZ Stromkomponente zu den rekombinanten Kanälen lieferten demnach überzeugende Hinweise darauf, dass sowohl  $K_v1.8$ - wie auch  $K_v12.1$ -Kanäle in IHZ exprimiert und aktiv sind (**Paper 5**).

### 3.2.4 Eine Kombination spannungsaktivierter $K^+$ -Ströme optimiert das Antwortverhalten von inneren Haarsinneszellen

Meine Ergebnisse zeigen, dass IHZ neben den bereits bekannten  $K_v7.4$ - und  $BK_{Ca}$ -Kanälen noch funktionelle  $K_v1.8$ -,  $K_v11.1$ - und  $K_v12.1$ -Kanäle exprimieren und somit also mindestens fünf verschiedene  $K^+$ -Kanalkomponenten besitzen. Darüber hinaus konnte ich zeigen, dass in IHZ der Maus  $K_v7.4$ -Kanaluntereinheiten sogar zwei Stromkomponenten mit unterschiedlichen Eigenschaften in IHZ vermitteln (**Paper 5; Abb.1F+G**). Zum einen eine eher kleine negativ aktivierende Stromkomponente mit den Charakteristika von  $I_{K,n}$  (Marcotti et al. 2003; Oliver et al. 2003) und zum anderen eine größere Komponente, die bei eher positiveren Potentialen aktiviert und zuvor in apikalen IHZ von Rennmäusen (Gerbil) beschrieben wurde (Johnson 2015). Die physiologische Relevanz dieser IHZ- $K^+$ -Ströme analysierten wir in Kooperation mit Dr. Alexandro Altoè anhand von Computersimulationen. Hierzu hat Dr. Altoè ein kürzlich veröffentlichtes Computermodell von IHZ (Altoè et al. 2018) um die sechs  $K^+$ -Leitfähigkeiten erweitert, deren Eigenschaften ich in meinen Messungen ermitteln konnte (**Paper 5, Abb.6+7**). Dieses Modell erlaubte es uns, die Relevanz der  $K^+$ -Leitfähigkeiten für das Antwortverhalten, d.h. die Rezeptorpotentiale, der IHZ in Folge simulierter Schallstimulation (sinusoidale Auslenkung des Haarbündels) zu untersuchen. Hierzu verglichen wir das Antwortverhalten der

## RESULTATE

IHZ in einem „nativen Modell“ (einschließlich aller Leitfähigkeiten) mit Simulationen, in denen die spannungsabhängige Aktivität einzelner  $K^+$ -Ströme spezifisch entfernt werden konnten. Das native Modell ergab ein Ruhepotential von -53 mV (**Paper 5, Supplement 7D**) und eine Membranzeitkonstante von 0,24 ms, also Werte, die außerordentlich gut zu publizierten *in-vivo* Werten für IHZ passen (Johnson 2015; Johnson et al. 2011). Die Simulation zeigte weiterhin, dass alle  $K^+$ -Kanäle unter Ruhebedingungen und während der (Schall-) Stimulation aktiv sind und somit das elektrische Antwortverhalten der IHZ effektiv beeinflussen können (**Paper 5, Abb.6D-F**). Tatsächlich zeigten die Modelle, dass die Expression aller  $K^+$ -Kanäle zusammen (v.a.  $BK_{Ca}$ ,  $K_v1.8$  und die positiv aktivierende  $K_v7.4$ -Komponente) den Frequenzbereich, den das Rezeptorpotential einer IHZ abbilden kann, um eine Oktave erhöht (**Paper 5, Abb.7B+C**). Außerdem fanden wir anhand der Simulationen heraus, dass die Expression des nativen Repertoires aller sechs  $K^+$ -Leitfähigkeiten es IHZ ermöglicht, einen um etwa 20 dB größeren Lautstärkebereich zu kodieren (**Paper 5, Abb.7D+E**).

Zusammenfassend konnte also der beschriebene hypothesengetriebenen Kandidatenansatz zur Identifizierung der in IHZ exprimierten  $K^+$ -Kanäle genutzt werden, um daraus ein biophysikalisches Modell von IHZ zu entwickeln, welches es schlussendlich erlaubte, die physiologische Relevanz dieser Kanäle zu ermitteln. Unsere Ergebnisse zeigen, dass IHZ mindestens sechs unabhängige  $K^+$ -Leitfähigkeiten ( $I_{K,f}$  ( $BK_{Ca}$ ),  $I_{K,n}$  ( $K_v7.4$ ) und  $I_{K,s}$  ( $K_v1.8$ ,  $K_v11.1$ ,  $K_v12.1$  und positiv aktivierender  $K_v7.4$ )) mit unterschiedlichen biophysikalischen Eigenschaften exprimieren, welche die Kodierung (Verarbeitung) komplexer auditorischer Informationen (d.h. Frequenz und Lautstärke) in IHZ synergistisch optimieren. Im Gegensatz dazu sind IHZ mit weniger Kanalpopulation limitiert darin komplexe Schallereignisse zu verarbeiten und können nur Frequenz oder Lautstärke halbwegs präzise darstellen. Das  $K^+$ -Kanalrepertoire stellt also eine evolutionäre Anpassung dar, die sensitives Hören ermöglicht

## 4. Diskussion

### 4.1 BACE1-defiziente Mäuse zeigen sensorineuralen Hörverlust

BACE1 ist eine Protease die in der Alzheimer-Krankheit eine entscheidende Rolle bei der Bildung von neurotoxischen A $\beta$ -Plaques spielt, da sie den ersten Schritt der proteolytischen Spaltung des Amyloid-Vorläufer (*Precursor*)-Proteins (APP) vermittelt (Haass and Selkoe 1993). Die Hemmung von BACE1 und damit der A $\beta$ -Produktion stellt daher eine vielversprechende therapeutische Intervention gegen die Alzheimer-Krankheit dar. Unabhängig von der Rolle des Enzyms in der Entstehung der Erkrankung, sind mittlerweile über 60 natürliche Substrate von BACE1 bekannt (Hemming et al. 2009). Das legt nahe, dass die Hemmung von BACE1 bei der Behandlung zu schwerwiegenden Nebenwirkungen führen kann, da durch die pharmakologische Intervention auch die physiologischen Funktionen von BACE1 unterbunden werden. Tatsächlich mussten frühere klinische Studien mit BACE1-Inhibitoren wegen des Auftretens von toxischen Nebeneffekten in der Retina, der Leber und dem Gefäßsystems vorzeitig beendet werden, und die Gabe eines Inhibitors führte beunruhigender Weise sogar zur Verringerung des Gehirnvolumens in Patienten (Das and Yan 2019). Allein schon um die möglichen Nebenwirkungen der Therapie der Alzheimer-Erkrankung abschätzen zu können, ist es essentiell, die physiologischen Aufgaben von BACE1 zu kennen. Als besonders hilfreich haben sich bei der Suche nach physiologischen Funktionen des Enzyms BACE1<sup>-/-</sup> Mäuse erwiesen, in denen das Enzym genetisch ausgeschaltet worden ist (Dominguez et al. 2005).

In meiner Doktorarbeit ist es mir anhand dieses Mausmodells gelungen, erstmals zu zeigen, dass BACE1 essentiell für sensitives Hören ist. Wir konnten bei BACE1<sup>-/-</sup> Mäusen einen Hörverlust und eine verringerte Funktion des Corti'schen Organs des Innenohres nachweisen. Da kürzlich gezeigt wurde, dass BACE1 als  $\beta$ -Untereinheit die Funktion von K<sub>v</sub>7-Kanälen auf direkte, nicht-enzymatische Weise moduliert (Agsten et al. 2015; Hessler et al. 2015; Lehnert et al. 2016), vermuteten wir anfänglich, dass BACE1 in ÄHZ zusammen mit K<sub>v</sub>7.4 die besonderen Eigenschaften von I<sub>K,n</sub> hervorbringt. Daraus ergab sich auch die Arbeitshypothese, dass in Analogie zu *Kcnq4*<sup>-/-</sup> Mäusen, die genetische Deletion von BACE1 durch den Verlust des I<sub>K,n</sub> Stroms in den Haarsinneszellen zum Hörverlust führt. Diese Hypothese konnte ich jedoch aufgrund dreier Beobachtungen widerlegen: Erstens fand ich keine Hinweise auf eine Expression von BACE1 in Haarsinneszellen. Zweitens war die Expression von K<sub>v</sub>7.4-Kanälen in den ÄHZ von BACE1<sup>-/-</sup> Mäusen unverändert. Und drittens war die Physiologie von Haarsinneszellen in den BACE1<sup>-/-</sup> Mäusen völlig normal (Dierich et al. 2019 (a)).

In meiner Arbeit ist es mir aber gelungen, die Ursache für den Hörverlust der BACE1-defizienten Tieren zu identifizieren. Die Expression von BACE1 ist nämlich für eine normale Nervenfasearchitektur, Myelinisierung und organisierte synaptische Verbindungen zwischen IHZ und den auditorischen Nervenfasern, und somit für sensitives Hören essentiell. Aufgrund der Hypomyelinisierung und der desorganisierten synaptischen Verbindungen zwischen IHZ und den auditorischen Nervenfasern liegt der Grund für die Schwerhörigkeit der BACE1<sup>-/-</sup> Mäuse klar in der Cochlea. Hier kommt es direkt bei der ersten Verschaltung von Haarsinneszelle auf die Nervenfasern zu einer fehlerhaften Signalübertragung, was sich in der Verringerung der Amplitude und einer Verlängerung der Latenzzeit der Welle 1 in den ABR-Messungen widerspiegelt. Ausgeschlossen ist aber hiermit nicht, dass das Fehlen von BACE1 nicht auch Auswirkungen auf höhere Hirnareale hat und es dadurch zu einer fehlerhaften neuronalen

## DISKUSSION

Verarbeitung und schließlich Wahrnehmung des Reizes kommt, der Hörverlust entsteht aber auf jeden Fall bereits in der Cochlea (Dierich et al. 2019 (a)).

NRG1 ist ein bekanntes BACE1-Substrat, das bei der Myelinisierung von peripheren und zentralen Axonen, sowie bei dem korrekten Auswachsen von Neuriten eine wichtige Rolle spielt (Sherman and Brophy 2005; Wu et al. 2016). Nach der Spaltung von NRG1 bindet dessen N-Terminus an ErbB-Rezeptoren, was für die Myelinisierung peripherer Nervenzellen von Bedeutung ist (Hu et al. 2016). In der Cochlea ist NRG1 genauso wie BACE1 in SGN exprimiert (Hansen et al. 2001; Stankovic 2004) und steuert über ErbB-Rezeptoren der Schwannzellen die Entwicklung, die Aufrechterhaltung und möglicherweise die Regeneration des Hörnervs (Hansen et al. 2001). Ich konnte anhand von heterozygoten NRG1<sup>-/+</sup> Mäuse zeigen, die genauso wie BACE1<sup>-/-</sup> Mäuse eine reduzierte Myelinisierung und eine Desorganisation von auditorischen Nervenfasern in der Cochlea aufweisen, dass NRG1 wahrscheinlich ein wichtiges Substrat von BACE1 in der Cochlea darstellt. Somit ist die Beeinträchtigung dieses NRG1-ErbB-Signalwegs wahrscheinlich einer der hauptsächlichen Gründe für den Myelinisierungsdefekt in den BACE1<sup>-/-</sup> Mäusen (Dierich et al. 2019 (a)).

Ein weiteres interessantes Substrat von BACE1 ist das Zelladhäsionsmolekül *close homolog of LI* (CHL1), das beim Auswachsen von Neuriten eine Rolle spielt (Hitt et al. 2012). Tatsächlich konnten in CHL1-defizienten Mäusen unorganisierte und falsch ausgerichtete Axone im Hippocampus (Hitt et al. 2012; Ou-Yang et al. 2018) und im Riechkolben (*olfactory bulb*) (Cao et al. 2012; Rajapaksha et al. 2011) festgestellt werden, die stark an die axonalen Fehlbildungen und die vergrößerten Neuriten in der IHZ-Region von BACE1<sup>-/-</sup> Mäusen erinnern. So wie NRG1 wird auch CHL1 durch BACE1 prozessiert und aktiviert dann über eine nachgeschaltete Signalkaskade Semaphorin 3A (Barão et al. 2015), das für das Auswachsen und die Verzweigung von Neuriten kortikaler Neurone von Bedeutung ist (Barão et al. 2015). Da Semaphorin 3A auch maßgeblich an der Zielfindung von Axonen in der Cochlea beteiligt ist (Chilton and Guthrie 2003; Lu et al. 2011), könnte also CHL1 ebenfalls ein Substrat von BACE1 in der Cochlea darstellen. Die Relevanz des CHL1-Semaphorin 3A-Signalweges in der Cochlea muss aber erst näher untersucht werden.

Interessanterweise zeigten BACE1<sup>-/-</sup> Mäuse auch reduzierte OAE, was auf eine eingeschränkte Funktion der ÄHZ hinweist. Die Ursache hierfür konnten ich aber leider nicht aufklären, da die Physiologie dieser Sinneszellen *in-vitro* vollkommen normal war. Möglicherweise ist aber in den BACE1<sup>-/-</sup> Mäusen auch die Funktion von efferenten olivo-kochleären Neuronen verändert, in deren Nervenendigungen BACE1 ebenfalls stark exprimiert ist. So kann es hier durch den Verlust von BACE1 zur verstärkten efferenten Hemmung durch den olivo-kochleären Rückkopplungsmechanismus kommen, weswegen die Aktivität der ÄHZ zumindest *in-vivo* dauerhaft vermindert sein könnte. Für die Prüfung dieser Hypothese werden jedoch künftige Studien erforderlich sein.

Hinsichtlich der geplanten Verabreichung von BACE1-Inhibitoren zur Vorbeugung und Behandlung von Alzheimer, war es wichtig festzustellen, ob diese Medikamente Auswirkungen auf das Hörvermögen haben können. Daher fütterten wir Wildtyp-Mäuse mit dem BACE1-Inhibitor NB-360 in einer Dosierung und über einen Zeitraum, der für die Inhibition von BACE1 im Gehirn ausreicht (Keskin et al. 2017). Bei diesen Mäusen konnten wir keine Hördefizite oder neuropathologische Anomalien in der Cochlea feststellen. Das liegt wahrscheinlich daran, dass - wie meine Daten ebenfalls zeigen - BACE1 zumindest in Mäusen



## DISKUSSION

für die Entwicklung der Myelinisierung der auditorischen Nervenfasern, nicht aber für die Aufrechterhaltung der Myelinisierung im Erwachsenenalter essentiell ist. Somit hat die Inhibition der enzymatischen Aktivität von BACE1 in adulten Mäusen, in denen die Entwicklung abgeschlossen ist, offensichtlich keinerlei Auswirkungen mehr auf das Hörvermögen (Dierich et al. 2019 (a)). Ob sich diese Beobachtungen allerdings direkt auf den Menschen übertragen lassen, welche möglicherweise über Jahrzehnte medikamentös behandelt werden müssten, gilt es zu untersuchen. Bis diese Frage geklärt ist, sollten klinische Studien mit BACE1-Inhibitoren auf jeden Fall regelmäßige Hörtests in Betracht ziehen.

### 4.2 Identifizierung der $I_{K,s}$ Komponente in inneren Haarsinneszellen

IHZ wandeln schallinduzierte Schwingungen in Rezeptorpotentiale um, die die synaptische Übertragung antreiben und die Hörinformationen mit bemerkenswerter Geschwindigkeit und Präzision verlässlich an das Gehirn weiterleiten. Um die Schallqualitäten präzise zu kodieren, werden die Rezeptorpotentiale durch basolaterale  $K^+$ -Ströme moduliert, die die biophysikalischen Eigenschaften der Zellmembran determinieren; in IHZ sind das die drei spannungsabhängige  $K^+$ -Leitfähigkeiten  $I_{K,f}$ ,  $I_{K,n}$  und  $I_{K,s}$ . Trotz der enormen Relevanz der Kaliumströme für die Physiologie der Sinneszellen war die molekulare Identität der Ionenkanäle, die diese drei Haarzellströme hervorbringen, nicht völlig aufgeklärt. In meiner Arbeit konnte ich erstmalig zeigen, dass die  $I_{K,s}$  Komponente in IHZ von mindestens drei spannungsabhängigen  $K^+$ -Kanälen, nämlich von  $K_v11.1$ -,  $K_v1.8$ - und  $K_v12.1$ -Kanaluntereinheiten, hervorgebracht wird (Dierich et al. 2020).

Die Identifizierung dieser Ionenkanäle basierte auf der Auswahl von Kandidaten-Kanälen, die wir aus der *SHIELD-Datenbank* zur Transkriptionsanalyse einzelner Haarsinneszellen extrahieren konnten (Liu et al. 2014; Shen et al. 2015). Die Gangbarkeit dieser Kandidaten-Strategie wurde dadurch bestätigt, dass diese Datensätze auch die Expression von  $K_v7.4$ - und  $BK_{Ca}$ -Kanälen bestätigen, die bekanntermaßen die IHZ-Ströme  $I_{K,n}$  bzw.  $I_{K,f}$  vermitteln (Kharkovets et al. 2006; Rüttiger et al. 2004; Thurm et al. 2005). Ich validierte die Expression der Kandidaten in der Cochlea mittels PCR-Techniken und für  $K_v11.1$ -Kanäle auch mit spezifischen Antikörpern und Haarsinneszell-spezifischen *knock-out* Kontrollen. Im Gegensatz zu  $K_v1.8$ - und  $K_v12.1$ - sind  $K_v11.1$ -Kanäle biophysikalisch und pharmakologisch außerordentlich gut charakterisiert. Das liegt hauptsächlich an deren wichtiger Rolle bei der Repolarisation von Aktionspotentialen im Herzen ( $I_{K,r}$ ) sowie daran, dass Mutationen (Curran et al. 1995), wie auch die pharmakologische Hemmung (Sanguinetti et al. 1995; Trudeau et al. 1995) dieser Kanäle zu *Torsade-de-pointes*-Tachykardie führen, die sich als Kammerflimmern bis hin zum plötzlichen Herztod äußern können (Curran et al. 1995; Sanguinetti et al. 1995; Trudeau et al. 1995). Experimente mit dem spezifischen  $K_v11$ -Kanalantagonisten E-4031 (Trudeau et al. 1995) in IHZ von Wildtypen und Haarzell-spezifischen *Kcnh2 knock-out* Mäusen zeigten eindeutig, dass  $K_v11.1$ -Untereinheiten in IHZ funktionell exprimiert und beim Ruhepotential dieser Sinneszellen aktiv sind (Dierich et al. 2020). Der bereits erbrachte elektronenmikroskopische Nachweis von  $K_v11.1$ -Kanälen in Haarsinneszellen (Nie et al. 2005) bestätigt diese Ergebnisse.

Die mRNA von  $K_v1.8$ -Kanälen habe ich aus der Cochlea kloniert, um biophysikalische Charakteristika zu bestimmen und ein pharmakologisches Profil von rekombinanten  $K_v1.8$ -Kanälen zu erheben. Die Eigenschaften rekombinanter  $K_v1.8$ -Kanäle stimmen dabei (fast) exakt mit einer 4-AP-inhibierten Stromkomponente in IHZ überein. Zur Expression in IHZ passt

## DISKUSSION

auch, dass kürzlich gezeigt wurde, dass  $K_v1.8$ -defiziente Mäuse eine leicht erhöhte Hörschwelle (etwa 5-8 dB) und eine verlängerte Latenzzeit der Übertragung zwischen den IHZ und den SGN aufweisen (Lee et al. 2013). Zusammengenommen sind das starke Hinweise darauf, dass auch  $K_v1.8$ -Kanäle in IHZ exprimiert und aktiv sind.

$K_v12$ -Kanäle gehören wie  $K_v10$  und  $K_v11$  zur EAG-Superfamilie. Im Gegensatz zu den  $K_v11.1$ -Kanälen stehen jedoch nur wenig Informationen zur physiologischen Relevanz der drei  $K_v12.1$ - $K_v12.3$  Kanäle zur Verfügung (Engeland et al. 1998; Zou et al. 2003). Es ist zwar bekannt, dass  $K_v12.2$ -Kanäle die Erregbarkeit in pyramidalen Hippocampusneuronen von Mäusen regulieren (Zhang et al. 2010), bisher konnten jedoch  $K_v12.1$ - und  $K_v12.3$ -Untereinheiten aufgrund fehlender Mausmodelle und spezifischer pharmakologischer Hilfsmittel keine nativen Stromkomponenten zugeordnet werden. Der Nachweis möglicher  $K_v12.1$ -vermittelter Ströme in IHZ hing daher entscheidend von der Identifizierung eindeutiger biophysikalischer und pharmakologischer Eigenschaften ab. In Analogie konnten so zuvor beispielsweise die eng verwandten  $K_v10$ - und  $K_v11$ -Kanälen anhand ihrer einzigartigen Aktivierungskinetik (Meyer and Heinemann 1998) oder ihrer exklusiven  $Na^+$ -Sensitivität und Pharmakologie (Hardman and Forsythe 2009; Hirdes et al. 2005, 2009) in nativem Gewebe identifiziert werden.

In meiner Doktorarbeit habe ich zunächst nach Eigenschaften von rekombinanten  $K_v12.1$ -Kanälen gesucht, über die sich diese in IHZ nachweisen lassen (Dierich et al. 2018; Dierich et al. 2019 (b); Dierich and Leitner 2018). Obwohl die Gesamtarchitektur von  $K_v11.1$ - und  $K_v12.1$ -Kanälen ähnlich ist, konnte ich anhand des Antimalariamittels Chinin zeigen, dass es aufgrund einer einzelnen Änderung in der Aminosäureabfolge der Bindetaschen für Inhibitoren zu einer unterschiedlichen Sensitivität in den evolutionär konservierten Kanälen kommen kann (Dierich et al. 2019 (b)). Meine Ergebnisse unterstreichen daher die funktionelle und pharmakologische Vielfalt in dieser Gruppe von Ionenkanälen. Deswegen war es auch nicht verwunderlich, dass ich trotz der engen Verwandtschaft Unterschiede in pharmakologischen Charakteristika von  $K_v12.1$ - und  $K_v11.1$ -Kanälen feststellen konnte. So fand ich heraus, dass die Applikation von NS1643, einem etablierten Agonisten von  $K_v11$ -Kanälen (Casis et al. 2006; Hansen et al. 2006), zur vollständigen Inhibition von  $K_v12.1$ -vermittelten Strömen im Expressionssystem führt. Des Weiteren erwies sich der nicht selektive Inhibitor von  $K_v$ -Kanälen (und auch von  $K_v11.1$  Untereinheiten) 4-AP als potenter Aktivator von  $K_v12.1$ -Kanälen (Dierich et al. 2018). Diese einzigartigen pharmakologischen Charakteristika (Aktivierung durch 4-AP und Inhibition durch NS1643) konnte ich tatsächlich für eine Stromkomponente in IHZ nachweisen. Biophysikalisch zeichnen sich humane  $K_v12.1$ -Kanäle durch einen *mode shift of activation* aus (Dai and Zagotta 2017; Dierich et al. 2018; Li et al. 2015). Dabei handelt es sich um ein biophysikalisches Phänomen, das dazu führt, dass die Kanäle als Antwort auf anhaltende Depolarisation bei noch negativeren Membranpotentialen aktivieren; durch die Depolarisation werden die Kanäle also in einen Zustand der erhöhten Spannungssensitivität versetzt. In meiner Arbeit habe ich diesen spannungsabhängigen *mode shift* der  $K_v12.1$ -Kanäle erstmals eingehend charakterisiert und ideale Messprotokolle erstellt, um den *mode shift* zum funktionellen Nachweis von  $K_v12.1$  anzuwenden. Dabei fand ich heraus, dass dieser durch depolarisierte Haltepotentiale zwischen -60 mV und 0 mV maximal ausgeschöpft war und dass einige hundert Millisekunden konditionierende Depolarisation für die signifikante Änderungen der Spannungsabhängigkeit und Kinetik ausreichend waren (Dierich et al. 2018). Diese spezielle biophysikalische Eigenschaft konnte ich abschließend auch in IHZ mit den dafür etablierten Messprotokollen nachweisen.

## DISKUSSION

Außerdem konnte ich in IHZ sowohl die 4-AP-Aktivierung, wie auch die NS1643-Inhibition von  $K^+$ -Strömen zeigen. Die exklusive Kombination dieser unterschiedlichen Merkmale, zusammen mit der Tatsache, dass mRNA von  $K_v12.1$  in IHZ exprimiert wird, liefert sehr starke Hinweise auf die Expression von  $K_v12.1$ -Kanälen in IHZ. Somit exprimieren IHZ neben den bereits bekannten  $K_v7.4$ - und  $BK_{Ca}$ -Kanälen noch funktionelle  $K_v1.8$ -,  $K_v11.1$ - und  $K_v12.1$ -Kanäle und daher also mindestens fünf verschiedene  $K^+$ -Kanalkomponenten (Dierich et al. 2020).

Es ist nicht ausgeschlossen, dass es noch weitere spannungsabhängige  $K^+$ -Kanäle in IHZ gibt. Neben den hier identifizierten  $K_v1.8$ -,  $K_v11.1$ - und  $K_v12.1$ -Kanälen, zeigen auch  $K_v3.3$ -Kanäle eine (geringe) mRNA-Expression in IHZ (Liu et al. 2014), jedoch fanden wir keine Hinweise auf  $K_v3$ -vermittelte Ströme in diesen Zellen. Ein biophysikalisches Merkmal von  $K_v3$ -Kanälen ist eine schnelle spannungsabhängige Inaktivierung (Fernandez et al. 2003; Zhang et al. 2016), die ich jedoch bei keinem der  $K^+$ -Ströme nachweisen konnte. Des Weiteren sind  $K_v3.3$ -Kanäle sehr empfindlich gegenüber TEA und 4-AP (Fernandez et al. 2003; Zhang et al. 2016). In meinen Experimenten inhibierten jedoch TEA und der spezifische  $BK_{Ca}$ -Inhibitor IbTX genau im selben Maß die  $I_{K,f}$  Stromkomponente in IHZ. Außerdem waren alle 4-AP-sensitiven  $K^+$ -Ströme unempfindlich gegenüber TEA, wurden nicht schnell inaktiviert und aktivierten bei wesentlich negativeren Membranpotentialen als dies rekombinante  $K_v3.3$ -Kanäle tun, sodass es keine Hinweise auf eine zusätzliche  $K_v3.3$ -vermittelte Komponente in IHZ gibt (Dierich et al. 2020).

### 4.2.1 Die physiologische Relevanz der $K^+$ -Kanäle in Haarsinneszellen

Meine Arbeit liefert neue Einblicke in die Physiologie von Haarsinneszellen. Aus den Ergebnissen der biophysikalischen und funktionellen Eigenschaften der identifizierten Haarzellstromkomponenten ergaben sich unmittelbare weitere Fragestellungen. Unter dem Blickpunkt der Innenohr-Physiologie ist es vor allem interessant zu verstehen, warum IHZ diese fünf Kanalkomponenten exprimieren, die mindestens sechs verschiedene  $K^+$ -Leitfähigkeiten hervorbringen. Diese Fragestellung haben wir mittels Computermodellen zusammen mit Dr. Alexandro Altoè bearbeitet. Anhand der Modelle konnten wir die Relevanz der einzelnen Leitfähigkeiten für die Ausbildung der Rezeptorpotentiale in IHZ relativ einfach untersuchen. Zusammenfassend zeigen diese Simulationen, dass die native Kanalausstattung die Kodierung der Schallinformation durch Rezeptorpotentiale im Vergleich zu IHZ, die weniger Kanalkomponenten exprimieren, signifikant verbessert: So können IHZ, die alle  $K^+$ -Kanäle exprimieren, niedrigere Schallintensitäten verarbeiten, aber auch einen größeren dynamischen (Lautstärke-) Bereich innerhalb desselben Rezeptorpotentialbereiches kodieren und außerdem auch höhere Schallfrequenzen zeitlich präzise wiedergeben. Im Gegensatz dazu sind IHZ mit weniger  $K^+$ -Kanalkomponenten in der gleichzeitigen Verarbeitung von Frequenz und Intensität des ankommenden Schalls limitiert. Die natürliche Kanalausstattung der IHZ stellt also eine evolutionäre Anpassung dar, um komplexen Schall durch vielfältige Rezeptorpotentiale zu kodieren, während "einfachere" IHZ mit weniger Kanalpopulationen möglicherweise darauf beschränkt sind, nur bestimmte Aspekte (Frequenz oder Intensität) des eingehenden Tons abzubilden. Da Rezeptorpotentiale in IHZ die Freisetzung von Glutamat und somit die Aktivität der Fasern des Hörnervs steuern, erhöht die native Kanalausstattung der IHZ ebenfalls die Sensitivität und den Dynamikbereich des Hörnervs und ist daher eine Grundlage für das sensitive Hörvermögen von Säugetieren (Dierich et al. 2020). Des Weiteren zeigten morphologische, elektrophysiologische und funktionelle Untersuchungen von  $BK_{Ca}$ -defizienten Mäusen, welchen

## DISKUSSION

die dominierende  $BK_{Ca}$ -vermittelte  $I_{K,f}$  Stromkomponente fehlt, dass diese Kanäle zwar eine direkte Rolle bei der Entstehung von *noise-induced hearing loss* (NIHL, Lärmschwerhörigkeit) spielen, erstaunlicherweise aber nur moderate Änderungen in der Physiologie der Haarsinneszellen bewirken und somit keine essentielle Rolle für ein normales Hörvermögen haben (Oliver et al. 2007; Pyott et al. 2007; Maison et al. 2013). Ähnliche Ergebnisse zeigten sich auch bei  $K_v1.8$ -defizienten Mäusen (Lee et al. 2013). Diese offenbare Kompensation des Fehlens einzelner Ionenkanal-Typen in den genetischen Mausmodellen stützen unsere Computersimulation. Insbesondere legt dies nahe, dass die verschiedenen spannungsabhängigen  $K^+$ -Kanäle ein gewisses Maß an Redundanz aufweisen, welche eine schwerwiegende Hörbeeinträchtigung durch das Fehlen nur eines Kanals verhindert.

### 4.3 Ausblick und Bedeutung meiner Arbeit

Erstmals konnten  $K_v1.8$ - und  $K_v12.1$ -Kanälen native Stromkomponenten und damit eine physiologische Relevanz (nämlich für die Verarbeitung von Schallinformation) im Innenohr zugewiesen werden. Neben der Expression in Haarsinneszellen sind  $K_v12.1$ -Kanäle vorwiegend in Neuronen verschiedenster Hirnareale exprimiert (Engeland et al. 1998; Zou et al. 2003), wohingegen die Expression von  $K_v1.8$ -Kanälen sich vom Gehirn über die Aorta bis hin zur Niere und zum Herzen erstreckt (Lang et al. 2000; Tian et al. 2002; Yao et al. 2002). Meine ausführliche biophysikalische und pharmakologische Charakterisierung dieser beiden Kanäle bietet nun eine gute Grundlage für die Identifizierung weiterer nativer Stromkomponenten, die in den genannten Organen und Zelltypen durch diese Kanäle vermittelt werden könnten. Meine Arbeit kann somit dazu beitragen, die physiologische Relevanz dieser Kanäle in anderen Organsystemen besser zu verstehen. In meiner Arbeit konnte ich auch erstmals den spannungsabhängigen *mode shift* von  $K^+$ -Kanälen in IHZ darstellen. Meine Experimente lassen zwar keine Rückschlüsse darüber zu, ob dieses Phänomen in den Sinneszellen physiologisch relevant sein könnte, aber ich halte es für einen spannenden Mechanismus, über den möglicherweise die Eigenschaften der IHZ an anhaltende physiologische Depolarisation oder auch an eine pathophysiologisch erhöhte Erregbarkeit (z.B. nach Lärmexposition) speziell angepasst werden könnte. Es müssen aber auf jeden Fall anspruchsvolle Experimente geplant und durchgeführt werden, um diese Hypothese zu überprüfen.

Spannend bleibt auch weiterhin die Suche nach dem Interaktionspartner von  $K_v7.4$ , der die biophysikalischen Eigenschaften des Stroms  $I_{K,n}$  in ÄHZ bedingt. Trotz des erheblichen Einflusses von BACE1 auf die  $K_v7$ -Kanalfunktion in anderen Regionen des Nervensystems (Agsten et al. 2015; Hessler et al. 2015), halte ich aufgrund meiner Ergebnisse eine Wechselwirkung der Proteine in Haarsinneszellen der Cochlea für unwahrscheinlich. Letztendlich ist demnach weitere Arbeit notwendig, um die komplexen Mechanismen zu verstehen, welche die ultraschnelle und präzise Signalverarbeitung und die damit verbundene enorme Sensitivität des Corti'schen Organs gewährleisten

**5. Literaturverzeichnis**

- Agsten, Marianne, Sabine Hessler, Sandra Lehnert, Tilmann Volk, Andrea Rittger, Stephanie Hartmann, Christian Raab, Doo Yeon Kim, Teja W. Groemer, Michael Schwake, Christian Alzheimer, and Tobias Huth. 2015. "BACE1 Modulates Gating of KCNQ1 (K<sub>v</sub>7.1) and Cardiac Delayed Rectifier KCNQ1/KCNE1 (IKs)." *Journal of Molecular and Cellular Cardiology* 89:335–48.
- Altoè, Alessandro, Ville Pulkki, and Sarah Verhulst. 2018. "The Effects of the Activation of the Inner-Hair-Cell Basolateral K<sup>+</sup> Channels on Auditory Nerve Responses." *Hearing Research* 364:68–80.
- Barão, Soraia, Annette Gärtner, Eduardo Leyva-Díaz, Galina Demyanenko, Sebastian Munck, Tine Vanhoutvin, Lujia Zhou, Melitta Schachner, Guillermina López-Bendito, Patricia F. Maness, and Bart De Strooper. 2015. "Antagonistic Effects of BACE1 and APH1B- $\gamma$ -Secretase Control Axonal Guidance by Regulating Growth Cone Collapse." *Cell Reports* 12(9):1367–76.
- Békésy, Georg von. and Ernest Glen Wever. 1960. *Experiments in Hearing*. New York: McGraw-Hill.
- Beurg, Maryline, Robert Fettiplace, Jong-Hoon Nam, and Anthony J. Ricci. 2009. "Localization of Inner Hair Cell Mechanotransducer Channels Using High-Speed Calcium Imaging." *Nature Neuroscience* 12(5):553–58.
- Brandt, Andreas, Joerg Striessnig, and Tobias Moser. 2003. "CaV1.3 Channels Are Essential for Development and Presynaptic Activity of Cochlear Inner Hair Cells." *The Journal of Neuroscience* 23(34):10832–40.
- Brownell, William E., Charles R. Bader, Daniel Bertrand, and Yves De Ribaupierre. 1985. "Evoked Mechanical Responses of Isolated Cochlear Outer Hair Cells." *Science* 227(4683):194–96.
- Cao, Luxiang, Gregory T. Rickenbacher, Steve Rodriguez, Thomas W. Moulija, and Mark W. Albers. 2012. "The Precision of Axon Targeting of Mouse Olfactory Sensory Neurons Requires the BACE1 Protease." *Scientific Reports* 2:1–8.
- Casis, Oscar, Søren-peter Olesen, and Michael C. Sanguinetti. 2006. "Mechanism of Action of a Novel Human Ether-a-Go-Go-Related Gene Channel Activator." *Molecular Pharmacology* 69(2):658–65.
- Chilton, John K. and Sarah Guthrie. 2003. "Cranial Expression of Class 3 Secreted Semaphorins and Their Neuropilin Receptors." *Developmental Dynamics* 228(4):726–33.
- Coucke, Paul J., Peter Van Hauwe, Philip M. Kelley, Henricus Kunst, Isabelle Schatteman, Désirée Van Velzen, Johan Meyers, Robbert J. Ensink, Margriet Verstreken, Frank Declau, Henri Marres, Kumar Kastury, Shalender Bhasin, Wyman T. McGuirt, Richard J. H. Smith, Cor W. R. J. Cremers, Paul Van De Heyning, Patrick J. Willems, Shelley D. Smith, and Guy Van Camp. 1999. "Mutations in the KCNQ4 Gene Are Responsible for Autosomal Dominant Deafness in Four DFNA2 Families." *Human Molecular Genetics* 8(7):1321–28.
- Curran, M. E., I. Splawski, K. W. Timothy, G. M. Vincent, E. D. Green, and M. T. Keating. 1995. "A Molecular Basis for Cardiac Arrhythmia: HERG Mutations Cause Long QT Syndrome." *Cell* 80(5):795–803.
- Dai, Gucan and William N. Zagotta. 2017. "Molecular Mechanism of Voltage-Dependent Potentiation of KCNH Potassium Channels." *ELife* 6:1–18.
- Dallos, Peter. 1992. "The Active Cochlea." *The Journal of Neuroscience* 12(12):4575–85.
- Dallos, Peter and Bernd Fakler. 2002. "Prestin, a New Type of Motor Protein." *Nature Reviews Molecular Cell Biology* 3(2):104–11.
- Dallos, Peter, Xudong Wu, Mary Ann Cheatham, Jiangang Gao, Jing Zheng, T. Anderson, Shuping Jia, Xiang Wang, Wendy H. Y. Cheng, Soma Sengupta, and David. 2009. "Prestin-based outer hair cell motility is necessary for mammalian cochlear amplification" *Neuron* 58(3):333–39.

## LITERATURVERZEICHNIS

- Das, Brati and Riqiang Yan. 2019. "A Close Look at BACE1 Inhibitors for Alzheimer's Disease Treatment." *CNS Drugs* 33(3):251–63.
- Dierich, Marlen, Alessandro Altoe, Julia Koppelman, Sarah Verhulst, Dominik Oliver, and Michael G. Leitner. 2020. "Optimized Tuning of Auditory Inner Hair Cells to Encode Complex Sound through Synergistic Activity of Six Independent  $K^+$  Current Entities." *Cell Reports* 32 107869:1-e4
- Dierich, Marlen, Saskia Evers, Bettina U. Wilke, and Michael G. Leitner. 2018. "Inverse Modulation of Neuronal  $K_v12.1$  and  $K_v11.1$  Channels by 4-Aminopyridine and NS1643." *Frontiers in Molecular Neuroscience* 11(January):1–13.
- Dierich (a), Marlen, Stephanie Hartmann, Nadine Dietrich, Philip Moeser, Franziska Brede, Lejo Johnson Chacko, Konstantin Tziridis, Achim Schilling, Patrick Krauss, Sabine Hessler, Xsandra Karch, Anneliese Schrott-fischer, Michael Blumer, Carmen Birchmeier, Dominik Oliver, Tobias Moser, Holger Schulze, Christian Alzheimer, Michael G. Leitner, and Tobias Huth. 2019. " $\beta$ -Secretase BACE1 Is Required for Normal Cochlear Function." *The Journal of Neuroscience* 39(45):9013–27.
- Dierich (b), Marlen, Willem B. Van Ham, and Michael G. Leitner. 2019. "Histidine at Position 462 Determines the Low Quinine Sensitivity of Ether-à-Go-Go Channel Superfamily Member  $K_v12.1$ ." *2708 British Journal of Pharmacology* (January):2708–23.
- Dierich, Marlen and Michael G. Leitner. 2018. " $K_v12.1$  Channels Are Not Sensitive to  $G_q$ PCR-Triggered Activation of Phospholipase  $C\beta$ ." *Channels* 12(1):228–39.
- Dominguez, Diana, Jos Tournoy, Dieter Hartmann, Tobias Huth, Kim Cryns, Siska Deforce, Lutgarde Serneels, Ira Espuny Camacho, Els Marjaux, Katleen Craessaerts, Anton J. M. Roebroek, Michael Schwake, Rudi D'Hooge, Patricia Bach, Ulrich Kalinke, Dieder Moechars, Christian Alzheimer, Karina Reiss, Paul Saftig, and Bart De Strooper. 2005. "Phenotypic and Biochemical Analyses of BACE1-and BACE2-Deficient Mice." *Journal of Biological Chemistry* 280(35):30797–806.
- Engelard, Brigit, Axel Neu, Jost Ludwig, Jochen Roeper, and Olaf Pongs. 1998. "Cloning and Functional Expression of Rat Ether-a-Go-Go-like  $K^+$  Channel Genes." *Journal of Physiology* 513(3):647–54.
- Fernandez, Fernando R., Ezequiel Morales, Asim J. Rashid, Robert J. Dunn, and Ray W. Turner. 2003. "Inactivation of  $K_v3.3$  Potassium Channels in Heterologous Expression Systems." *Journal of Biological Chemistry* 278(42):40890–98.
- Fettiplace, Robert and Carole M. Hackney. 2006. "The Sensory and Motor Roles of Auditory Hair Cells." *Nature Review Neuroscience* 7(January):19–29.
- Glowatzki, Elisabeth and Paul A. Fuchs. 2002. "Transmitter Release at the Hair Cell Ribbon Synapse." *Nature Neuroscience* 5:147.
- Goodchild, Samuel J., Logan C. Macdonald, and David Fedida. 2015. "Sequence of Gating Charge Movement and Pore Gating in HERG Activation and Deactivation Pathways." *Biophysical Journal* 108(6):1435–47.
- Goutman, Juan D., A. Belén Elgoyhen, and María Eugenia Gómez-Casati. 2015. "Cochlear Hair Cells: The Sound-Sensing Machines." *FEBS Letters* 589(22):3354–61.
- Haass, Christian and Dennis J. Selkoe. 1993. "Cellular Processing of  $\beta$ -Amyloid Precursor Protein and the Genesis of Amyloid  $\beta$ -Peptide." *Cell* 75(6):1039–42.
- Hansen, Marlan R., Ulka Vijapurkar, John G. Koland, and Steven H. Green. 2001. "Reciprocal Signaling between Spiral Ganglion Neurons and Schwann Cells Involves Neuregulin and Neurotrophins." *Hearing Research* 161(1–2):87–98.
- Hansen, Rie Schultz, Thomas Goldin Diness, Torsten Christ, Joachim Demnitz, Ursula Ravens, and

## LITERATURVERZEICHNIS

- Morten Grunnet. 2006. "Activation of Human." *Perfusion* 69(1):266–77.
- Hardman, Rachael M. and Ian D. Forsythe. 2009. "Ether-à-Go-Go-Related Gene K<sup>+</sup> Channels Contribute to Threshold Excitability of Mouse Auditory Brainstem Neurons." *Journal of Physiology* 587(11):2487–97.
- Hemming, Matthew L., Joshua E. Elias, Steven P. Gygi, and Dennis J. Selkoe. 2009. "Identification of  $\beta$ -Secretase (BACE1) Substrates Using Quantitative Proteomics." *PLoS ONE* 4(12).
- Hessler, Sabine., Fang Zheng, Stephanie Hartmann, Andrea Rittger, Sandra Lehnert, Meike Volkel, Matthias Nissen, Elke Edelmann, Paul Saftig, Michael Schwake, Tobias. Huth, and Christian Alzheimer. 2015. "-Secretase BACE1 Regulates Hippocampal and Reconstituted M-Currents in a -Subunit-Like Fashion." *Journal of Neuroscience* 35(8):3298–3311.
- Hirdes, Wiebke, Nora Napp, Iris Wulfsen, Michaela Schweizer, Jürgen R. Schwarz, and Christiane K. Bauer. 2009. "Erg K<sup>+</sup> Currents Modulate Excitability in Mouse Mitral/Tufted Neurons." *Pflugers Archiv European Journal of Physiology* 459(1):55–70.
- Hirdes, Wiebke, Michaela Schweizer, Kristina S. Schuricht, Saskia S. Guddat, Iris Wulfsen, Christiane K. Bauer, and Jürgen R. Schwarz. 2005. "Fast Erg K<sup>+</sup> Currents in Rat Embryonic Serotonergic Neurons." *Journal of Physiology* 564(1):33–49.
- Hitt, Brian, Sean M. Riordan, Lokesh Kukreja, William A. Eimer, Tharinda W. Rajapaksha, and Robert Vassar. 2012. " $\beta$ -Site Amyloid Precursor Protein (APP)-Cleaving Enzyme 1 (BACE1)-Deficient Mice Exhibit a Close Homolog of L1 (CHL1) Loss-of-Function Phenotype Involving Axon Guidance Defects." *Journal of Biological Chemistry* 287(46):38408–25.
- Hu, Xiangyou, Qingyuan Fan, Hailong Hou, and Riqiang Yan. 2016. "Neurological Dysfunctions Associated with Altered BACE1-Dependent Neuregulin-1 Signaling." *Journal of Neurochemistry* 136(2):234–49.
- Hu, Xiangyou, Caitlin W. Hicks, Wanxia He, Philip Wong, Wendy B. Macklin, Bruce D. Trapp, and Riqiang Yan. 2006. "Bace1 Modulates Myelination in the Central and Peripheral Nervous System." *Nature Neuroscience* 9(12):1520–25.
- Hussain, Ishrut, David Powell, David R. Howlett, David G. Tew, Thomas D. Meek, Conrad Chapman, Israel S. Gloger, Kay E. Murphy, Christopher D. Southan, Dominic M. Ryan, Trudi S. Smith, David L. Simmons, Frank S. Walsh, Colin Dingwall, and Gary Christie. 1999. "Identification of a Novel Aspartic Protease (Asp 2) as  $\beta$ -Secretase." *Molecular and Cellular Neurosciences* 14(6):419–27.
- Johnson, Stuart L. 2015. "Membrane Properties Specialize Mammalian Inner Hair Cells for Frequency or Intensity Encoding." *ELife* 4(NOVEMBER2015):1–21.
- Johnson, Stuart L., Maryline Beurg, Walter Marcotti, and Robert Fettiplace. 2011. "Prestin-Driven Cochlear Amplification Is Not Limited by the Outer Hair Cell Membrane Time Constant." *Neuron* 70(6):1143–54.
- Keskin, Aylin D., Maja Kekuš, Helmuth Adelsberger, Ulf Neumann, Derya R. Shimshek, Beomjong Song, Benedikt Zott, Tingying Peng, Hans Förstl, Matthias Staufenbiel, Israel Nelken, Bert Sakmann, Arthur Konnerth, and Marc Aurel Busche. 2017. "BACE Inhibition-Dependent Repair of Alzheimer's Pathophysiology." *Proceedings of the National Academy of Sciences* 114(32):8631–36.
- Kharkovets, Tatjana, Karin Dedek, Hannes Maier, Michaela Schweizer, Darina Khimich, Régis Nouvian, Vitya Vardanyan, Rudolf Leuwer, Tobias Moser, and Thomas J. Jentsch. 2006. "Mice with Altered KCNQ4 K<sup>+</sup> Channels Implicate Sensory Outer Hair Cells in Human Progressive Deafness." *The EMBO Journal* 25(3):642–52.
- Kros, C. J. and A. C. Crawford. 1990. "Potassium Currents in Inner Hair Cells Isolated from the Guinea-Pig Cochlea." *J Physiol* 421:263–91.

## LITERATURVERZEICHNIS

- Kros, Corné J., J. Peter Ruppertsberg, and Alfons Rüsch. 1998. "Expression of a Potassium Current Inner Hair Cells during Development of Hearing in Mice." *Nature* 394(6690):281–84.
- Kubisch, Christian, Björn C. Schroeder, Thomas Friedrich, Björn Lütjohann, Aziz El-Amraoui, Sandrine Marlin, Christine Petit, and Thomas J. Jentsch. 1999. "KCNQ4, a Novel Potassium Channel Expressed in Sensory Outer Hair Cells, Is Mutated in Dominant Deafness." *Cell* 96(3):437–46.
- Lang, Rainer., G. Lee, W. Liu, S. Tian, H. Rafi, M. Orias, a S. Segal, and G. V Desir. 2000. "KCNA10: A Novel Ion Channel Functionally Related to Both Voltage-Gated Potassium and CNG Cation Channels." *American Journal of Physiology. Renal Physiology* 278(6):F1013–21.
- Lee, Sue I., Travis Conrad, Sherri M. Jones, Ayala Lagziel, Matthew F. Starost, Inna A. Belyantseva, Thomas B. Friedman, and Robert J. Morell. 2013. "A Null Mutation of Mouse Kcna10 Causes Significant Vestibular and Mild Hearing Dysfunction." *Hearing Research* 300:1–9.
- Lehnert, Sandra, Stephanie Hartmann, Sabine Hessler, Helmuth Adelsberger, Tobias Huth, and Christian Alzheimer. 2016. "Ion Channel Regulation by  $\beta$ -Secretase BACE1 – Enzymatic and Non-Enzymatic Effects beyond Alzheimer's Disease." *Channels* 10(5):365–78.
- Leitner, Michael G., Anja Feuer, Olga Ebers, Daniela N. Schreiber, Christian R. Halaszovich, and Dominik Oliver. 2012. "Restoration of Ion Channel Function in Deafness-Causing KCNQ4 Mutants by Synthetic Channel Openers." *British Journal of Pharmacology* 165(7):2244–59.
- Leitner, Michael G., Christian R. Halaszovich, and Dominik Oliver. 2011. "Aminoglycosides Inhibit KCNQ4 Channels in Cochlear Outer Hair Cells via Depletion of Phosphatidylinositol(4,5)Bisphosphate." *Molecular Pharmacology* 79:51–60.
- Li, Xiaofan, Andriy Anishkin, Hansi Liu, Damian B. van Rossum, Sree V Chintapalli, Jessica K. Sassic, David Gallegos, Kendra Pivaroff-Ward, and Timothy Jegla. 2015. "Bimodal Regulation of an Elk Subfamily  $K^+$  Channel by Phosphatidylinositol 4,5-Bisphosphate." *The Journal of General Physiology* 146(5):357–74.
- Lieberman, M. Charles, Jiangang Gao, David Z. Z. He, Xudong Wu, Shuping Jia, and Jian Zuo. 2002. "Prestin Is Required for Electromotility of the Outer Hair Cell and for the Cochlear Amplifier." *Nature* 419(6904):300–304.
- Lin, Xinli, Gerald Koelsch, Shili Wu, Debbie Downs, Azar Dashti and Jordan Tang 2000. "Human Aspartic Protease Memapsin 2 Cleaves the Beta-Secretase Site of Beta-Amyloid Precursor Protein." *Proceedings of the National Academy of Sciences of the United States of America* 97(4):1456–60.
- Lingle, Christopher J., Pedro L. Martinez-espinoza, Aizhen Yang-hood, Luis E. Boero, and Shelby Payne. 2019. "LRRC52 Regulates BK Channel Function and Localization in Mouse Cochlear Inner Hair Cells." *PNAS* 116(37):18397–403.
- Liu, Huizhan, Jason L. Pecka, Qian Zhang, Garrett A. Soukup, Kirk W. Beisel and David Z.Z. He. 2014. "Characterization of Transcriptomes of Cochlear Inner and Outer Hair Cells." *Journal of Neuroscience* 34(33):11085–95.
- Lu, Cindy C., Jessica M. Appler, E. Andres Houseman and Lisa V. Goodrich. 2011. "Developmental Profiling of Spiral Ganglion Neurons Reveals Insights into Auditory Circuit Assembly." *Journal of Neuroscience* 31(30):10903–18.
- Maison, S. F., S. J. Pyott, A. L. Meredith, and M. C. Liberman. 2013. "Olivocochlear Suppression of Outer Hair Cells in Vivo: Evidence for Combined Action of BK and SK2 Channels throughout the Cochlea." *Journal of Neurophysiology* 109(6):1525–34.
- Mammano, F. and J. F. Ashmore. 1996. "Differential Expression of Outer Hair Cell Potassium Currents in the Isolated Cochlea of the Guinea-Pig." *The Journal of Physiology* 496 (3):639–46.



## LITERATURVERZEICHNIS

- Mammano, Fabio, Corné J. Kros, and Jonathan F. Ashmore. 1995. "Patch Clamped Responses from Outer Hair Cells in the Intact Adult Organ of Corti." *Pflügers Archiv European Journal of Physiology* 430(5):745–50.
- Marcotti, Walter, Stuart L. Johnson, Matthew C. Holley, and Corné J. Kros. 2003. "Developmental Changes in the Expression of Potassium Currents of Embryonic, Neonatal and Mature Mouse Inner Hair Cells." *The Journal of Physiology* 548(Pt 2):383–400.
- Marcotti, Walter and Corn J. Kros. 1999. "Developmental Expression of the Potassium Current  $I_{K,n}$  Contributes to Maturation of Mouse Outer Hair Cells." *Journal of Physiology* 653–60.
- Meyer, Roman and Stefan H. Heinemann. 1998. "Characterization of an Eag-like Potassium Channel in Human Neuroblastoma Cells." *Journal of Physiology* 508(1):49–56.
- Moser, Tobias and Anna Lysakowski. 2006. "Hair cell ribbon synapses" *Cell Tissue Res* 326(2):347–59.
- Neumann, Ulf, Heinrich Rueeger, Rainer MacHauer, Siem Jacob Veenstra, Rainer M. Lueoend, Marina Tintelnot-Blomley, Grit Laue, Karen Beltz, Barbara Vogg, Peter Schmid, Wilfried Frieauff, Derya R. Shimshek, Matthias Staufenbiel, and Laura H. Jacobson. 2015. "A Novel BACE Inhibitor NB-360 Shows a Superior Pharmacological Profile and Robust Reduction of Amyloid- $\beta$  and Neuroinflammation in APP Transgenic Mice." *Molecular Neurodegeneration* 10(1):1–15.
- Nie, Liping, Michael Anne Gratton, Karen J. Mu, Judilee N. Dinglasan, Weihong Feng and Ebenezer N. Yamoah 2005. "Expression and Functional Phenotype of Mouse ERG  $K^+$  Channels in the Inner Ear: Potential Role in  $K^+$  Regulation in the Inner Ear." *Journal of Neuroscience* 25(38):8671–79.
- Nouvian, Régis, Jérôme Ruel, Jing Wang, Matthieu J. Guitton, Rémy Pujol, and Jean L. Puel. 2003. "Degeneration of Sensory Outer Hair Cells Following Pharmacological Blockade of Cochlear KCNQ Channels in the Adult Guinea Pig." *European Journal of Neuroscience* 17(12):2553–62.
- Oliver, Dominik., Marlies Knipper, Christian Derst, and Bernd Fakler. 2003. "Resting Potential and Submembrane Calcium Concentration of Inner Hair Cells in the Isolated Mouse Cochlea Are Set by KCNQ-Type Potassium Channels." *Journal of Neuroscience* 23(6):2141–49.
- Oliver, Dominik, Annette M. Taberner, Henrike Thurm, Matthias Sausbier, Peter Ruth, Bernd Fakler, and M. Charles Liberman. 2007. "The Role of  $BK_{Ca}$  Channels in Electrical Signal Encoding in the Mammalian Auditory Periphery." *Journal of Neuroscience* 26(23):6181–89.
- Ou-Yang, Ming-Hsuan, Jonathan E. Kurz, Toshihiro Nomura, Jelena Popovic, Tharinda W. Rajapaksha, Hongxin Dong, Anis Contractor, Dane M. Chetkovich, Warren G. Tourtellotte, and Robert Vassar. 2018. "Axonal Organization Defects in the Hippocampus of Adult Conditional BACE1 Knockout Mice." *Science Translational Medicine* 10(459):eaao5620.
- Piper, David R., Anthony Varghese, Michael C. Sanguinetti and Martin Tristani-Firouz. 2003. "Gating Currents Associated with Intramembrane Charge Displacement in HERG Potassium Channels." *Proceedings of the National Academy of Sciences* 100(18):10534–39.
- Pyott, Sonja J., Andrea L. Meredith, Anthony A. Fodor, Ana E. Vázquez, Ebenezer N. Yamoah, and Richard W. Aldrich. 2007. "Cochlear Function in Mice Lacking the BK Channel Alpha, Beta1, or Beta4 Subunits." *Journal of Biological Chemistry* 282(5):3312–24.
- Rajapaksha, Tharinda W., William A. Eimer, Thomas C. Bozza, and Robert Vassar. 2011. "The Alzheimer's -Secretase Enzyme BACE1 Is Required for Accurate Axon Guidance of Olfactory Sensory Neurons and Normal Glomerulus Formation in the Olfactory Bulb." *Molecular Neurodegeneration* 6(1):1–9.
- Rüttiger, Lukas, Matthias Sausbier, Ulrike Zimmermann, Harald Winter, Claudia Braig, Jutta Engel, Martina Knirsch, Claudia Arntz, Patricia Langer, Bernhard Hirt, Marcus Müller, Iris Köpschall, Markus Pfister, Stefan Münkner, Karin Rohbock, Imke Pfaff, Alfons Rüscher, Peter Ruth, and

## LITERATURVERZEICHNIS

- Marlies Knipper. 2004. "Deletion of the Ca<sup>2+</sup>-Activated Potassium (BK) Alpha-Subunit but Not the BKbeta1-Subunit Leads to Progressive Hearing Loss." *Proceedings of the National Academy of Sciences of the United States of America* 101(35):12922–27.
- Ryugo, David K. 1992. "The Auditory Nerve: Peripheral Innervation, Cell Body Morphology, and Central Projections." *Mammalian Auditory Pathway: Neuroanatomy* 23–65.
- Sánchez-Chapula, Jose A., Tania Ferrer, Ricardo A. Navarro-Polanco, and Michael C. Sanguinetti. 2003. "Voltage-Dependent Profile of Human Ether-a-Go-Go Related Gene Channel Block Is Influenced by a Single Residue in the S6 Transmembrane Domain." *Molecular Pharmacology* 63(5):1051 LP – 1058.
- Sanguinetti, Michael C., Changan Jiang, Mark E. Curran, and Mark T. Keating. 1995. "A Mechanistic Link between an Inherited and an Acquired Cardiac Arrhythmia: HERG Encodes the I<sub>Kr</sub> Potassium Channel." *Cell* 81(2):299–307.
- Schwander, Martin, Bechara Kachar, and Ulrich Müller. 2010. "The Cell Biology of Hearing." *Journal of Cell Biology* 190(1):9–20.
- Shen, Jun, Déborah I. Scheffer, Kelvin Y. Kwan, and David P. Corey. 2015. "SHIELD: An Integrative Gene Expression Database for Inner Ear Research." *Database* 2015:1–9.
- Sherman, Diane L. and Peter J. Brophy. 2005. "Mechanisms of Axon Ensheathment and Myelin Growth." *Nature Reviews Neuroscience* 6(9):683–90.
- Sinha, Sukanto, John P. Anderson, Robin Barbour, Guriqbal S. Basi, Russell Caccavello, David Davis, Minhtam Doan, Harry F. Dovey, Normand Frigon, Jin Hong, Kirsten Jacobson-Croak, Nancy Jewett, Pamela Keim, Jeroen Knops, Ivan Lieberburg, Michael Power, Hua Tan, Gwen Tatsuno, Jay Tung, Dale Schenk, Peter Seubert, Susanna M. Suomensaaari, Shuwen Wang, Donald Walker, Jun Zhao, Lisa McConlogue and Varghese John 1999. "Purification and Cloning of Amyloid Precursor Protein Beta-Secretase from Human Brain." *Nature* 402(6761):537–40.
- Søgaard, Rikke, Trine Ljungstrøm, Kamilla Angelo Pedersen, Søren-peter Olesen, and Bo Skaaning Jensen. 2001. "KCNQ4 Channels Expressed in Mammalian Cells: Functional Characteristics and Pharmacology." *Am J Physiol Cell Physiol* 859–66.
- Stankovic, Konstantina, Carlos Rio, Anping Xia, Mitsuru Sugawara, Joe C. Adams, Charles Liberman and Gabriel Corfas 2004. "Survival of Adult Spiral Ganglion Neurons Requires ErbB Receptor Signaling in the Inner Ear." *Journal of Neuroscience* 24(40):8651–61.
- Suh, Byung-Chang and Bertil Hille. 2008. "PIP2 Is a Necessary Cofactor for Ion Channel Function: How and Why?" *Annual Review of Biophysics* 37:175–95.
- Tan, Peter S., Matthew D. Perry, Chai Ann Ng, Jamie I. Vandenberg, and Adam P. Hill. 2012. "Voltage-Sensing Domain Mode Shift Is Coupled to the Activation Gate by the N-Terminal Tail of HERG Channels." *The Journal of General Physiology* 140(3):293–306.
- Thurm, Henrike, Bernd Fakler, and Dominik Oliver. 2005. "Ca<sup>2+</sup>-Independent Activation of BK Channels at Negative Potentials in Mammalian Inner Hair Cells." *Journal of Physiology* 569(1):137–51.
- Tian, Shulan, Weimin Liu, Yanling Wu, Hamid Rafi, Alan Segal, and Gary Desir. 2002. "Regulation of the Voltage-Gated K<sup>+</sup> Channel KCNA10 by KCNA4B, a Novel Beta-Subunit." *Am J Physiol Renal Physiol* 283(1):F142-149.
- Trudeau, Matthew, Jeffrey W. Warmke, Barry Ganetzky, Gail A. Robertson 1995. "HERG, a Human Inward Rectifier in the Voltage-Gated Potassium Channel Family." *Science* 269(5220):92–95.
- Vassar, Robert, Brian D. Bennett, Safura Babu-Khan, Steve Kahn, Elizabeth A. Mendiaz, Gary Rogers, and Martin Citron. 1999. "B-Secretase Cleavage of Alzheimer's Amyloid Precursor Protein by the Transmembrane Aspartic Protease BACE." *Science* 286(1999):735–41.

## LITERATURVERZEICHNIS

- Villalba-Galea, Carlos A. 2017. "Hysteresis in Voltage-Gated Channels." *Channels* 11(2):140–55.
- Willem, Michael, Alistair N. Garratt, Bozidar Novak, Martin Citron, Steve Kaufmann, Andrea Rittger, Bart DeStrooper, Paul Saftig, Carmen Birchmeier, and Christian Haass. 2006. "Control of Peripheral Nerve Myelination by the Beta-Secretase BACE1." *Science* 314(5799):664–66.
- Wu, S., B. Marie Lutz, X. Miao, L. Liang, K. Mo, Y. J. Chang, P. Du, P. Soteropoulos, B. Tian, A. G. Kaufman, A. Bekker, Y. Hu, and Y. X. Tao. 2016. "Dorsal Root Ganglion Transcriptome Analysis Following Peripheral Nerve Injury in Mice." *Molecular Pain* 12:1744806916629048.
- Yan, Riqlang, Michael J. Blenkowski, Mary E. Shuck, Hulyl Miao, Monica C. Tory, Adele M. Pauley, John R. Brashler, Nancy C. Stratman, W. Rodney Mathews, Allen E. Buhl, Donald B. Carter, Alfredo G. Tomasselli, Luis A. Parodl, Robert L. Helnrikson, and Mark E. Gurney. 1999. "Membrane-Anchored Aspartyl Protease with Alzheimer's Disease  $\beta$ -Secretase Activity." *Nature* 402(6761):533–37.
- Yao, Xiaoqiang, Shulan Tian, Ho Yu Chan, Daniel Biemesderfer, and Gary V. Desir. 2002. "Expression of KCNA10, a Voltage-Gated K Channel, in Glomerular Endothelium and at the Apical Membrane of the Renal Proximal Tubule." *Journal of the American Society of Nephrology* 13(12):2831–39.
- Zhang, Xiaofei, Federica Bertaso, Jong W. Yoo, Karsten Baumgärtel, Sinead M. Clancy, Van Lee, Cynthia Cienfuegos, Carly Wilmot, Jacqueline Avis, Truc Hunyh, Catherine Daguia, Christian Schmedt, Jeffrey Noebels, and Timothy Jegla. 2010. "Deletion of the Potassium Channel  $K_v12.2$  Causes Hippocampal Hyperexcitability and Epilepsy." *Nature Neuroscience* 13(9):1056–58.
- Zhang, Yalan, Xiao Feng Zhang, Matthew R. Fleming, Anahita Amiri, Lynda El-Hassar, Alexei A. Surguchev, Callen Hyland, David P. Jenkins, Rooma Desai, Maile R. Brown, Valeswara Rao Gazula, Michael F. Waters, Charles H. Large, Tamas L. Horvath, Dhasakumar Navaratnam, Flora M. Vaccarino, Paul Forscher, and Leonard K. Kaczmarek. 2016. " $K_v3.3$  Channels Bind Hax-1 and Arp2/3 to Assemble a Stable Local Actin Network That Regulates Channel Gating." *Cell* 165(2):434–48.
- Zheng, Jing, Laird Madison, Dominik Oliver, Bernd Fakler and Peter Dallos (2002). Prestin, the Motor Protein of Outer Hair Cells. *Audiology & Neuro-Otology*. 7(1):9–12.
- Zou, Anrour, Zhixin Lin, Margaret Humble, Christopher D. Creech, P. Kay Wagoner, Douglas Krafte, Timothy J. Jegla, and Alan D. Wickenden. 2003. "Distribution and Functional Properties of Human KCNH8 (Elk1) Potassium Channels." *American Journal of Physiology. Cell Physiology* 285(6):C1356-66.

## 6. Anhang

### 6.1 Eingereichte Publikationen

- A.  $\beta$ -Secretase BACE1 Is Required for Normal Cochlear Function. *The Journal of Neuroscience*, 2019 39(45):9013-9027.  
+ Cover vom Journal of Neuroscience
  
- B. Inverse Modulation of Neuronal  $K_v12.1$  and  $K_v11.1$  Channels by 4-Aminopyridine and NS1643. *Frontiers in Molecular Neuroscience*, 2018 11(January), 11:11.  
+ Supplemental Information
  
- C.  $K_v12.1$  channels are not sensitive to  $G_q$ PCR-triggered activation of phospholipase  $C\beta$ . *Channels*, 2018 12(1), 228-239.
  
- D. Histidine at position 462 determines the low quinine sensitivity of ether-à-go-go channel superfamily member  $K_v12.1$ . *British Journal of Pharmacology*, 2019 176(15): 2708-2723.  
+ Supplemental Information
  
- E. Optimized Tuning of Auditory Inner Hair Cells to Encode Complex Sound through Synergistic Activity of Six Independent  $K^+$  Current Entities. *Cell Reports* 2020 32, 107869:1-e4.  
+ Supplemental Information

# JNeurosci

THE JOURNAL OF NEUROSCIENCE

November 6, 2019 • Volume 39 Number 45 • www.jneurosci.org

The Journal of Neuroscience

November 6, 2019

Volume 39 Number 45

pages 8827-9040






## This Week in The Journal

- Non-Auditory Cortical Projections to Inferior Colliculus
- Congruent Visual Cortex Activation by Stories in Blind People

1969–2019



# $\beta$ -Secretase BACE1 Is Required for Normal Cochlear Function

Marlen Dierich,<sup>1</sup>  Stephanie Hartmann,<sup>2</sup> Nadine Dietrich,<sup>3</sup> Philip Moeser,<sup>2</sup> Franziska Brede,<sup>2</sup> Lejo Johnson Chacko,<sup>4</sup> Konstantin Tziridis,<sup>5</sup> Achim Schilling,<sup>5</sup> Patrick Krauss,<sup>5</sup> Sabine Hessler,<sup>2</sup>  Sandra Karch,<sup>2</sup> Anneliese Schrott-Fischer,<sup>4</sup> Michael Blumer,<sup>6</sup>  Carmen Birchmeier,<sup>7</sup> Dominik Oliver,<sup>1,8,9</sup> Tobias Moser,<sup>3</sup> Holger Schulze,<sup>5</sup> Christian Alzheimer,<sup>2\*</sup>  Michael G. Leitner,<sup>1,10\*</sup> and  Tobias Huth<sup>2\*</sup>

<sup>1</sup>Institute of Physiology and Pathophysiology, Department of Neurophysiology, Philipps-University Marburg, 35037 Marburg, Germany, <sup>2</sup>Institut für Physiologie und Pathophysiologie, Friedrich-Alexander-Universität Erlangen-Nürnberg, 91054 Erlangen, Germany, <sup>3</sup>Institute for Auditory Neuroscience and InnerEarLab, University Medical Center Göttingen, Göttingen, Germany, <sup>4</sup>Department of Otorhinolaryngology, Medical University of Innsbruck, 6020 Innsbruck, Austria, <sup>5</sup>Experimental Otolaryngology, Friedrich-Alexander-Universität Erlangen-Nürnberg, 91054 Erlangen, Germany, <sup>6</sup>Division Clinical and Functional Anatomy, Medical University of Innsbruck, 6020 Innsbruck, Austria, <sup>7</sup>Developmental Biology/Signal Transduction, Max-Delbrück-Center for Molecular Medicine, 13125 Berlin, Germany, <sup>8</sup>DFG Research Training Group, Membrane Plasticity in Tissue Development and Remodeling, GRK 2213, Philipps University, Germany, <sup>9</sup>Center for Mind, Brain and Behavior (CMBB), Universities of Marburg and Giessen, Germany, and <sup>10</sup>Institute of Physiology, Department of Physiology and Medical Physics, Medical University of Innsbruck, 6020 Innsbruck, Austria

Cleavage of amyloid precursor protein (APP) by  $\beta$ -secretase BACE1 initiates the production and accumulation of neurotoxic amyloid- $\beta$  peptides, which is widely considered an essential pathogenic mechanism in Alzheimer's disease (AD). Here, we report that BACE1 is essential for normal auditory function. Compared with wild-type littermates, BACE1<sup>-/-</sup> mice of either sex exhibit significant hearing deficits, as indicated by increased thresholds and reduced amplitudes in auditory brainstem responses (ABRs) and decreased distortion product otoacoustic emissions (DPOAEs). Immunohistochemistry revealed aberrant synaptic organization in the cochlea and hypomyelination of auditory nerve fibers as predominant neuropathological substrates of hearing loss in BACE1<sup>-/-</sup> mice. In particular, we found that fibers of spiral ganglion neurons (SGN) close to the organ of Corti are disorganized and abnormally swollen. BACE1 deficiency also engenders organization defects in the postsynaptic compartment of SGN fibers with ectopic overexpression of PSD95 far outside the synaptic region. During postnatal development, auditory fiber myelination in BACE1<sup>-/-</sup> mice lags behind dramatically and remains incomplete into adulthood. We relate the marked hypomyelination to the impaired processing of Neuregulin-1 when BACE1 is absent. To determine whether the cochlea of adult wild-type mice is susceptible to AD treatment-like suppression of BACE1, we administered the established BACE1 inhibitor NB-360 for 6 weeks. The drug suppressed BACE1 activity in the brain, but did not impair hearing performance and, upon neuropathological examination, did not produce the characteristic cochlear abnormalities of BACE1<sup>-/-</sup> mice. Together, these data strongly suggest that the hearing loss of BACE1 knock-out mice represents a developmental phenotype.

**Key words:** Alzheimer's disease; auditory function; BACE1; BACE1 inhibitor NB-360; BACE1 knock-out mice; Neuregulin-1

## Significance Statement

Given its crucial role in the pathogenesis of Alzheimer's disease (AD), BACE1 is a prime pharmacological target for AD prevention and therapy. However, the safe and long-term administration of BACE1-inhibitors as envisioned in AD requires a comprehensive understanding of the various physiological functions of BACE1. Here, we report that BACE1 is essential for the processing of auditory signals in the inner ear, as BACE1-deficient mice exhibit significant hearing loss. We relate this deficit to impaired myelination and aberrant synapse formation in the cochlea, which manifest during postnatal development. By contrast, prolonged pharmacological suppression of BACE1 activity in adult wild-type mice did not reproduce the hearing deficit or the cochlear abnormalities of BACE1 null mice.

## Introduction

The amyloid precursor protein (APP), a large type I membrane protein, can be processed along two major pathways, involving

sequential cleavage either at the  $\alpha$ - and  $\gamma$ -sites or at the  $\beta$ - and  $\gamma$ -sites of the protein. The latter pathway is initiated by the  $\beta$ -site APP-cleaving enzyme 1 (BACE1) and leads to the production of potentially neurotoxic amyloid  $\beta$ -peptides (A $\beta$ ). Since its first

Received Jan. 2, 2019; revised Aug. 30, 2019; accepted Sept. 4, 2019.

Author contributions: M.D., S. Hartmann, K.T., A.S., P.K., S.K., A.S.-F., M.B., C.B., D.O., T.M., H.S., C.A., M.G.L., and T.H. designed research; M.D., S. Hartmann, N.D., P.M., F.B., L.J.C., S. Hessler, D.O., and M.G.L. performed research;

M.D., S. Hartmann, N.D., P.M., F.B., L.J.C., A.S., S. Hessler, D.O., M.G.L., and T.H. analyzed data; M.D., M.G.L., and T.H. wrote the first draft of the paper; M.D., C.B., D.O., T.M., H.S., M.G.L., and T.H. edited the paper; C.A. wrote the paper.

identification in 1999, BACE1 has garnered ever-increasing attention, reflecting its pivotal role in the amyloidogenic pathway that has been closely linked to the pathogenesis of Alzheimer's disease (AD) (Vassar et al., 1999; Yan et al., 1999). Inhibition of BACE1 has therefore emerged as a prime therapeutic strategy to reduce the load of A $\beta$  in the brain (Cole and Vassar, 2007). Quite obviously, however, producing neurotoxic substances cannot be the main function of BACE1. In fact, BACE1 turned out to be important for the proteolytic processing of a plethora of proteins other than APP (Kuhn et al., 2012; Zhou et al., 2012). BACE1 knock-out mice have been—and still are—instrumental to decipher the numerous roles of BACE1 for the proper function of many tissues and organ systems. In general, BACE1-deficient mice show increased mortality after birth and decreased body weight as they mature (Dominguez et al., 2005). With respect to the PNS and CNS, BACE1<sup>-/-</sup> mice display a complex phenotype, which includes, at the behavioral level, increased locomotion and ataxia, spontaneous seizures, schizophrenia-like features and decreased thermal pain thresholds, and, at the network and cellular level, neuronal hyperexcitability, aberrant synaptic transmission, axon guidance defects and impaired axonal myelination (Kandalepas and Vassar, 2014; Weber et al., 2017). Importantly, BACE1 levels are high during neuronal development and, with few exceptions, decline with maturation (Willem et al., 2006). Thus, the phenotypes resulting from germline *Bace1* deletion might be, at least in part, attributable to the absence of BACE1 during critical developmental periods. An important implication of this notion for the pharmacological prevention and treatment of AD may be that the administration of BACE1 inhibitors in aged patients should not entail major side effects.

Here, we investigated whether BACE1 is required for normal auditory function. Our study was prompted by the finding that Neuregulin-1, a functionally important substrate of BACE1, is expressed in the cochlea (Morley, 1998), and by our previous finding that BACE1 interacts with KCNQ1 and KCNQ4 (Agsten et al., 2015; Hessler et al., 2015), two voltage-dependent K<sup>+</sup> channels which are essential for normal hearing (Jentsch, 2000; Maljevic et al., 2010). We found that BACE1<sup>-/-</sup> mice exhibit significant hearing loss and attribute the phenotype to aberrant synaptic organization in the cochlea and hypomyelination of auditory nerve fibers. We relate the hearing deficits and their neuropathological underpinnings primarily to the lack of BACE1 activity during auditory development, since, in wild-type mice, prolonged pharmacological suppression of BACE1 activity with the established inhibitor NB-360 did not engender hearing deficits or morphological changes.

We thank Dr. Ulf Neumann and Dr. Derya R. Shimshek, Novartis Institutes of BioMedical Research (NIBR), Neuroscience, Basel, for kind support and providing BACE inhibitor NB-360-containing food pellets. We are grateful to Iwona Izdorzyczyk for technical assistance. We also thank Dr. C. Vogl (Institute for Auditory Neuroscience, Göttingen) for insightful discussions and very helpful comments during development and progression of the project. Furthermore, we thank Dr. M. Schäfer (Institut für Anatomie und Zellbiologie, Marburg) for the great help with establishing research techniques. This work was funded by Research Grants of the University Medical Center Giessen und Marburg (UKGM 17/2013; UKGM 13/2016 to M.G.L.), by the German Research Foundation (DFG Priority Program 1608: "Ultrafast and temporally precise information processing: Normal and dysfunctional hearing", [LE 3600/1-1 to M.G.L.]), and by Tiroler Wissenschaftsförderung (TWF GZ UNI-0404/2381 to M.G.L.). T.M. acknowledges funding from the Collaborative Research Center 889, project A02. This work was supported by the Studienstiftung des deutschen Volkes to S. Hartmann and S.K.

The authors declare no competing financial interests. S. Hartmann became an employee of Novartis Pharma GmbH only after completion of her experimental contribution.

\*C.A., M.G.L., and T. H. contributed equally to this work and are all senior authors.

S. Hartmann's present address: Novartis Pharma GmbH, Roonstr. 25, 90429 Nürnberg, Germany.

Correspondence should be addressed to Michael G. Leitner at Michael.Leitner@i-med.ac.at or Tobias Huth at Tobias.Huth@fau.de.

<https://doi.org/10.1523/JNEUROSCI.0028-19.2019>

Copyright © 2019 the authors

## Materials and Methods

**Animals.** BACE1<sup>tm1Psa</sup> (BACE1<sup>-/-</sup>) mice were generated by insertion of a neomycin expression cassette from pMC1neoP into exon 1 of the *BACE1* gene, which introduces a premature translational stop codon into the open reading frame (Dominguez et al., 2005). This strain was crossed back on the C57BL/6J background for >10 generations. NRG1- $\beta$  mice carry a premature stop in exon 8 of Neuregulin-1 (*Nrg1*) which encodes the  $\beta$  variant of the EGF domain, whereas the  $\alpha$  variant remains intact. The type III  $\beta$  NRG1 variant is essential for Schwann cell development (Li, 2003). Homozygous *Nrg1*- $\beta$  mice die during embryogenesis and, therefore, only heterozygous animals were used for experiments. Mice had *ad libitum* access to food and water. Housing, feeding, breeding, and handling of the mice were according to federal/institutional guidelines with the approval of the local government. Mice of each sex were used for experiments.

**BACE1 inhibitor treatment.** Ten C57BL/6N mice (four weeks old) of either sex were fed with food pellets containing the preclinical BACE1 inhibitor NB-360 (Novartis, Neumann et al., 2015) at a concentration of 0.3 g/kg for 6 weeks. A cohort of 10 C57BL/6N mice served as controls and were fed with pellets of the same composition but without the BACE1 inhibitor. C57BL/6N mice exhibit identical hearing loss profiles as the C57BL/6J strain (Kane et al., 2012). Immediately after treatment, auditory brainstem responses (ABR) were recorded and brains and cochleae were harvested and processed for analysis with SDS-PAGE/Western blot and immunohistochemistry, respectively.

**Brain lysates.** After the ABR recordings, narcotized C57BL/6N mice (controls and NB-360-treated) were immediately decapitated and brains were dissected. Only one hemisphere was used for protein extraction. Per milligram tissue, 7  $\mu$ l of Synaptic Protein Extraction Reagent (Syn-PER; Thermo Fisher Scientific) supplemented with Complete Mini EDTA-free protease inhibitor mixture (Roche) were added and brains were homogenized. Homogenates were centrifuged at 1200  $\times$  g for 10 min at 4°C and cell debris was removed. Protein concentration was measured using the BCA Protein Assay Kit (Pierce). Samples were prepared in Syn-PER buffer, loading buffer (ProSieve ProTrack Dual Color Loading Buffer; Lonza), and 100 mM dithiothreitol (Sigma-Aldrich). 25  $\mu$ g of protein was loaded for SDS-PAGE/Western blot.

**SDS-PAGE and Western blot.** Samples were heated and maintained at 95°C for 5 min. Proteins were separated in 10% TGX stain-free precast gels (Bio-Rad) and transferred onto PVDF membranes (Bio-Rad) using a wet blotting system (Criterion Blotter, Bio-Rad). Membranes were blocked in 5% skim milk in TBS-T (10 mM Tris-HCl), 150 mM NaCl and 0.1% Tween 20) for 1 h at room temperature. Primary antibodies were diluted in TBS-T with 0.1% Na<sub>2</sub>S<sub>2</sub>O<sub>3</sub> and 1% BSA and incubated at 4°C overnight. After washing in TBS-T, secondary antibodies coupled to horseradish peroxidase (HRP) were incubated for 1 h at room temperature. Secondary antibodies were diluted in TBS-T with 5% skim milk. For detecting contactin2 (CNTN2), primary and secondary antibody solutions were prepared with 4% donkey serum instead of 1% BSA or 5% skim milk. The signal was visualized by enhanced chemiluminescence (ECL) using ECL Western Blotting Substrate (Bio-Rad) and imaged using the ChemoStar Imager (Intas). Membranes were stripped in 6 M guanidine-HCl, 20 mM Tris, 0.2% Triton X-100, pH 7.5, and 0.8%  $\beta$ -mercaptoethanol for 20 min at room temperature. After blocking in 5% skim milk in TBS-T, membranes were reblocked. The antibodies used for Western blots were goat-anti-CNTN2 (R&D Systems, AF4439), rabbit-anti-APP (C66, directed against the C terminus, Bhattacharyya et al., 2013), rabbit-anti-BACE1 (Abcam, ab108394), mouse-anti- $\beta$ -actin-HRP (Sigma-Aldrich, A3854), donkey-anti-goat-HRP (Jackson Laboratories, 705–035-147), and goat-anti-rabbit-HRP (Abcam, ab6721).

**Auditory brainstem responses (ABRs) and otoacoustic emissions.** ABRs were recorded in two different laboratories. In the first laboratory (see Fig. 1, lab 1) for recordings of ABR and distortion product otoacoustic emissions (DPOAE) mice were anesthetized with a combination of ketamine (125 mg/kg) and xylazine (2.5 mg/kg) intraperitoneally. The core temperature was maintained constant at 37°C using a heat blanket (Harvard Apparatus). For stimulus generation, presentation, and data acquisition, the TDT II System (Tucker Davis Technologies) run by BioSig

software (The MathWorks). Tone bursts (4/6/8/12/16/24/32 kHz, 10 ms plateau, 1 ms cos<sup>2</sup> rise/fall) or clicks of 0.03 ms were presented at 40 Hz (tone bursts) or 20 Hz (clicks) in the free field ipsilaterally using a JBL 2402 speaker. The difference potential between vertex and mastoid subdermal needles was amplified 50000 times, filtered (400–4000 Hz) and sampled at a rate of 50 kHz for 20 ms, 1300 times, to obtain two mean ABR traces for each sound intensity. Hearing threshold was determined with 10 dB precision as the lowest stimulus intensity that evoked a reproducible response waveform in both traces by visual inspection by two independent observers.

In the second independent laboratory (see Fig. 1, lab 2, and Fig. 8), ABR in anesthetized mice were recorded using a custom build recording setup consisting of a low noise amplifier (JHM NeuroAmp 401, J. Helbig Messtechnik; amplification 10.000; band-pass filter 400 Hz to 2000 Hz and 50 Hz notch filter) and an analog-digital converter card (National Instruments) with a sampling rate of 20 kHz. Hearing thresholds were determined objectively using an algorithm where data are fitted to a generalized logistic function that was extended by an additive term representing the measured background noise.

For recordings of DPOAEs, continuous primary tones (frequency  $f_2 = 1.2 \cdot f_1$ , intensity  $I_2 = I_1 - 10$  dB SPL, duration = 16 s) were delivered through the MF1 speaker system (Tucker Davis Technologies) and a custom-made probe containing an MKE-2 microphone (Sennheiser). The microphone signal was amplified (DMX 6Fire; Terratec) and the DPOAE amplitude at  $2 \cdot f_2 - f_1$  was analyzed by fast Fourier transformation using custom-written MATLAB version 3 (The MathWorks). Sound pressure levels (SPLs) are provided in decibels SPL root mean square (RMS, tonal stimuli) or decibels SPL peak equivalent (clicks).

**Immunohistochemistry.** Immunohistochemistry was performed on formaldehyde-fixed whole-mount preparations and on formaldehyde-fixed cochlear cryo-sections of the apical turn of the organ of Corti (if not stated otherwise). Tissue was isolated from wild-type, and BACE1<sup>-/-</sup> mice (between P35 and P45), as well as from C57BL/6N from mice fed with pellets containing BACE1 inhibitor NB-360 and the untreated C57BL/6N control mice (P68–P77, Neumann et al., 2015). All mice were killed through decapitation. Cochleae were removed from the temporal bone and, after introduction of a small hole in the apical part, cochleae were placed in 2% paraformaldehyde for 2 h at 4°C. For whole-mount immunostaining, the apical turn of the organ of Corti was dissected and separated from *modiolus*, *stria vascularis* and *tectorial membrane*. Specimens were mounted on Superfrost microscope slides (Thermo Scientific, 4951PLUS4). For cryo-sections, cochleae were decalcified in Rapid Bone Decalcifier (Thermo Scientific, 6764001) for 15 to 25 min at room temperature. After overnight incubation in 25% sucrose at 4°C, cochleae were embedded in O.C.T. compound (Sakura Finetek, 4583). 10–12  $\mu$ m cochlear cryo-sections were mounted on Superfrost microscope slides. Sections were stored at –80°C until further processing.

Samples were blocked and permeabilized for 1 h at room temperature in a buffer containing 10% normal goat serum (NGS), 0.3% Triton X-100, 20 mM phosphate buffer (PB), and 450 mM NaCl. Immunostaining was performed overnight at 4°C with the following primary antibodies (diluted in blocking solution): rabbit-anti-BACE1 (Abcam, ab108394; 1:50), guinea pig-anti-synapsin1,2 (Synaptic Systems, 106004; 1:500), rabbit-anti-KCNQ1 (K<sub>v</sub>7.1) (Abcam, ab135737; 1:200), goat-anti-prestin (N-20; Santa Cruz Biotechnology, sc-22692; 1:400), rabbit-anti-KCNQ4 (K<sub>v</sub>7.4) (H-130; Santa Cruz Biotechnology, sc-50417; 1:400), rabbit-anti-NF-200 (neurofilament heavy chain polypeptide, Sigma-Aldrich, N4142; 1:600) and chicken-anti-NF-H (neurofilament heavy chain polypeptide, Abcam, ab4680; 1:400), mouse-anti-CtBP2 (C-terminal binding protein; BD Bioscience, 612044; 1:200), rabbit-anti-GluR2/3 (Glutamate receptor subunits 2/3, Merck, ab1506; 1:200), rabbit-anti-PSD95 (postsynaptic density 95, Abcam, ab18258; 1:200), mouse-anti-MBP (myelin basic protein; F-6; Santa Cruz Biotechnology, sc-271524; 1:400), and rabbit-anti-B-FABP (brain-type fatty acid binding protein, Kurtz et al., 1994, 1:1000). The primary antibodies were labeled for 90 min at room temperature with species-appropriate secondary antibodies coupled to Alexa Fluor dyes (Thermo Scientific and Abcam). Alexa-Fluor488-coupled phalloidin (Abcam, ab176753) was used to visualize actin-containing stereocilia. Nuclei were stained with 2

$\mu$ g/ml 4',6-Diamidino-2'-phenylindole dihydrochloride (DAPI, Sigma-Aldrich, D9542).

**Confocal microscopy.** Confocal imaging was performed with an upright LSM 710 Axio Examiner Z1 microscope using W-Plan-Apochromat 63 $\times$ /1.0 M27 water-immersion objective (Carl Zeiss), as described previously (Wilke et al., 2014). Corresponding specimens of wild-type and BACE1<sup>-/-</sup> mice were imaged in parallel under identical experimental conditions (e.g., software and hardware settings). Fluorescent images represent maximum intensity projections of the  $x$ - $y$  plane generated from a minimum of five confocal planes (step size 1  $\mu$ m) with Zen2009 software (Carl Zeiss).

**Tissue preparation for transmission electron microscopy (TEM) analysis.** Twelve mice inner ear specimens (6 wild-type and 6 BACE1 knock-out animals) were fixed in 2.5% glutaraldehyde and 2% paraformaldehyde buffered in sodium cacodylate (0.1 M, pH = 7.4) overnight at 4°C. Tissue then was rinsed in sodium cacodylate buffer (SCB) and postfixed in 1% osmium tetroxide in sodium cacodylate buffer for 3–4 h at 4°C. Then samples were rinsed in SCB again and dehydrated in graded ethanol series and embedded in EPON resin. Ultrathin sections (90 nm) were cut on a Reichert Ultratrac S microtome (Leica Microsystems) with an ultra-diamond knife, mounted on dioxan-formvar-coated slot-grids (#G2500C, Christine Gröpl, Elektronenmikroskopie, Tulln, Austria) and stained 35 min with 0.5% (w/v) uranyl acetate, pH 4.4 and 10 min with 3% (w/v) lead citrate, pH 12 (Leica Ultrastainer, Leica Microsystems). The ultrathin sections were examined with a Philips CM 120 transmission electron microscope at 80 kV (FEI) equipped with a MORADA digital camera (Olympus SIS).

**Hair cell electrophysiology.** Hair cell electrophysiology was performed as previously reported (Leitner et al., 2011). In brief, apical turns of the organ of Corti of wild-type and BACE1<sup>-/-</sup> mice (for inner hair cells (IHCs): P39–P42; for outer hair cells (OHCs): P14–P16) were isolated in extracellular solution containing the following (in mM): 144 NaCl, 5.8 KCl, 1.3 CaCl<sub>2</sub>, 0.7 Na<sub>2</sub>HPO<sub>4</sub>, 0.9 MgCl<sub>2</sub>, 5.6 glucose, 10 HEPES, pH adjusted to 7.4 (NaOH) (305–310 mOsm/kg). For recordings, specimens were transferred to an experimental chamber and continuously perfused with extracellular solution. If necessary, supporting cells were carefully removed with gentle suction through a patch pipette (pulled to a wider tip diameter for cleaning) to get access to the basal pole of IHCs and OHCs of the outermost row. Whole-cell patch-clamp recordings were performed at room temperature (22–24°C) with an Axopatch 200B amplifier (Molecular Devices) or an HEKA EPC10 USB patch-clamp amplifier controlled with HEKA PatchMaster software (both HEKA electronics). Patch pipettes were pulled from borosilicate glass (Sutter Instruments) and had a resistance of 2–3.5 M $\Omega$  after filling with intracellular solution containing the following (in mM): 135 KCl, 3.5 MgCl<sub>2</sub>, 2.4 CaCl<sub>2</sub> (0.1 free Ca<sup>2+</sup>), 5 EGTA, 5 HEPES, and 2.5 Na<sub>2</sub>-ATP (pH adjusted with KOH to 7.3; 290–295 mOsm/kg) (Leitner et al., 2012). Voltage-clamp recordings were low-pass filtered at 2.5 kHz and sampled at 5 kHz. The series resistance ( $R_s$ ) was kept <6 M $\Omega$  and  $R_s$  was compensated throughout the recording (80–90%). Steady-state current amplitudes were normalized to cell capacitance (current density; pA/pF), and membrane potentials shown were not corrected for liquid junction potentials (approx. –4 mV). Steady-state current amplitudes were quantified at the end of an activating pulse. Time constants of current activation and deactivation were obtained from mono-exponential fits to the activating or deactivating current component. 10,10-bis(4-Pyridinylmethyl)-9(10H)-anthracenone dihydrochloride (XE991; Tocris Bioscience) was added to the extracellular solution at 20  $\mu$ M and was applied via a custom-made glass capillary pipette positioned in close proximity to the cell under investigation.

**Recordings of prestin-associated nonlinear capacitance (NLC).** Voltage-dependent NLC was recorded from OHCs of wild-type and BACE1<sup>-/-</sup> mice (P31–P44), as previously reported (Huang and Santos-Sacchi, 1993; Oliver and Fakler, 1999). In brief, NLC was measured using a stimulus stair-step protocol from –130 mV to +60 mV (5 ms duration, 10 mV increments). During recordings, OHCs were perfused with extracellular solution (see above) containing 20  $\mu$ M XE991 to inhibit predominant K<sub>v</sub>7 currents. Patch pipettes were filled with intracellular solution containing the following (in mM): 110 CsCl, 20 TEA-Cl, 3.5 MgCl<sub>2</sub>, 2.4



CaCl<sub>2</sub>, 2.5 Na<sub>2</sub>-ATP, 5 HEPES, 5 EGTA, pH 7.3 (KOH), 290–295 mOsm/kg. Currents were recorded with an EPC-10 patch-clamp amplifier and PatchMaster software (HEKA), low-pass filtered at 10 kHz and sampled at 100 kHz. Cell capacitance ( $C_m$ ) was not compensated in the whole-cell configuration and the time constant ( $\tau$ ) of current decay was calculated from mono-exponential fits to the current transients in response to each voltage step. The input resistance ( $R_{in}$ ) was calculated from voltage-dependent steady-state currents and integration of the current transients yielded the charge ( $Q$ ).  $C_m(i)$  at each voltage step was derived after correction of all voltages for  $R_s$  errors from the following formula:  $C_m(i) = (R_{in}/R_m)^{2*}(Q/V_c)$  where  $R_m$  is the membrane resistance and  $V_c$  is the holding potential.  $R_{in}$  and  $R_s$  were calculated as reported previously (Oliver and Fakler, 1999). The capacitance was fitted with a derivative of the

Boltzmann function:  $C(V) = C_{in} + \frac{Q_{max}}{\alpha * e^{-\frac{V-V_{1/2}}{\alpha}} * (1 + e^{-\frac{V-V_{1/2}}{\alpha}})^2}$  where

$C_{in}$  is the residual, noncompensated linear capacitance,  $V$  is the membrane potential,  $Q_{max}$  is the maximum voltage sensor charge moved through the membrane electrical field,  $V_{1/2}$  is the voltage at half-maximal charge transfer and  $\alpha$  is the slope factor of the voltage dependence.  $C_{in}$  was derived from the Boltzmann equation and reflected a measure for the surface membrane area of OHCs. As measure for prestin density in the OHC membrane,  $Q_{max}$  is presented as charge density ( $Q_{max}/C_{in}$ ). The nonlinear capacity (NLC) was normalized to  $C_{peak}$  that denotes maximal voltage-dependent capacitance at  $V_{1/2}$ .

**FM1-43 entry assay.** Organs of Corti of wild-type and BACE1<sup>-/-</sup> mice (P43–P45) were isolated in parallel and incubated for 45 s in extracellular solution containing 3  $\mu$ M FM1-43 (N-(3-(triethylammonium)propyl)-4-(4-(dibutylamino)styryl)pyridinium, Thermo Scientific, F35355). After repeated washing, specimens were fixed with 2% paraformaldehyde for 1 h at 4°C. After washing, organs were imaged on a LSM 710 Axio Examiner Z1 confocal microscope (Carl Zeiss) with identical experimental settings (FM1-43 entry assays were performed on 3 organ of Corti preparations from 3 mice per genotype).

**Data analysis.** Immunohistochemistry was analyzed with ImageJ, Zen2009 (Carl Zeiss) and IGOR Pro (Wavemetrics). Synapse counts (staining with antibodies directed against CtBP2, PSD95 or GluR2/3) were analyzed blinded for genotype by four to five independent researchers (see Figs. 5, 6, and 8). The spatial extension of NF-200-positive immunosignals extending from inner spiral plexus (ISP) close to IHCs toward the osseous spiral lamina (OSL) was analyzed manually using ImageJ and also blinded for genotype (see Fig. 7C). Electrophysiological recordings were analyzed with PatchMaster (HEKA) and IGOR Pro (Wavemetrics), as well as custom-made programs written in Python. Fiji software was used for densitometric analysis of Western blots (Schindelin et al., 2012) and data analysis was performed using Origin-Pro version 9.0 (OriginLab).

**Statistical analysis.** Statistical analysis was performed using two-tailed Student's *t* test or Wilcoxon–Mann–Whitney test. Significance was assigned at  $p \leq 0.05$  (\* $p \leq 0.05$ ; \*\* $p \leq 0.01$ ; \*\*\* $p \leq 0.001$ ). Data are presented as mean  $\pm$  SEM. In electrophysiological experiments,  $n$  represents the number of individual cells and accordingly the number of independent experiments.

## Results

### Deletion of *Bace1* causes hearing impairment in mice

To assess auditory function of BACE1<sup>-/-</sup> mice, we recorded ABRs and DPOAEs in 5- to 6-week-old mice compared with wild-type littermates of the same age. ABR recordings were performed independently in two different laboratories yielding qualitatively the same results (Fig. 1). ABR thresholds to tone bursts between 4 kHz and 32 kHz (Fig. 1A) and click stimulation (Fig. 1B,F) were significantly elevated by ~20 to 40 dB SPL in BACE1<sup>-/-</sup> mice. All ABR waves that report on synchronous activity in response to onset of sound (click stimulus) in spiral ganglia neurons (SGN; wave I) and in neurons of the auditory brainstem (waves II–V) were strongly reduced in amplitude in

BACE1<sup>-/-</sup> mice when compared with wild-type controls (Fig. 1B,C,F). The latencies of all ABR waves were increased concurrently, underscoring the auditory deficits in the mutant mice (Fig. 1B,D,G). In addition, DPOAE intensities were substantially reduced in BACE1<sup>-/-</sup> mice (Fig. 1E). Together, these data indicate a loss in auditory sensitivity due to impaired sound processing in the cochlea of BACE1<sup>-/-</sup> mice.

### BACE1 is expressed in SGN and olivocochlear efferent terminals

We therefore analyzed expression and distribution of BACE1 with immunohistochemistry using cochlear cryo-sections and whole-mount preparations of the organ of Corti. In 6 to 7 weeks old wild-type (BACE1<sup>+/+</sup>) mice, strong anti-BACE1 immunosignals were detected in cell bodies of neurons in the spiral ganglion (Fig. 2A), indicating expression of BACE1 in afferent auditory neurons. In the organ of Corti, anti-BACE1 immunosignals were found in small structures close to the basal pole of IHCs and OHCs, respectively (Fig. 2C). Strict colocalization with anti-synapsin1,2 immunofluorescence indicated that these BACE1-positive boutons are olivocochlear efferent terminals (Fig. 2C) (Vogl et al., 2015). Specific expression of BACE1 in these afferent and efferent structures was confirmed by strong reduction of the anti-BACE1 immunofluorescence in the spiral ganglion and the efferent terminals of BACE1<sup>-/-</sup> mice (Fig. 2B,D). In contrast, only faint and likely nonspecific anti-BACE1 immunosignals were present in the *stria vascularis* of wild-type and BACE1<sup>-/-</sup> mice (Fig. 2E), suggesting that BACE1 expression is either absent in the *stria vascularis* or below detection threshold. Expression of KCNQ1 (K<sub>v</sub>7.1) channels in marginal cells appeared identical in wild-type and knock-out mice (Fig. 2F).

### Integrity of hair cell structure and function in BACE1<sup>-/-</sup> mice

The *in vivo* electrophysiological data indicated that the hearing impairment of BACE1<sup>-/-</sup> mice originated from impaired signal processing in the auditory periphery, implicating a loss or dysfunction of hair cells, of synaptic transmission, or of signal propagation along auditory neurons. We therefore examined the structural integrity of the cochlea of mice matched to the age of mice analyzed in the ABR experiments with immunolabeling and confocal microscopy. We did not detect any structural changes in the organ of Corti or hair cell loss in BACE1<sup>-/-</sup> mice (Fig. 3A,B;  $n = 4$ ). When stained with fluorescently labeled phalloidin, hair bundles of IHCs and OHCs appeared normal in BACE1<sup>-/-</sup> mice (Fig. 3A,B). To analyze whether hair cell function was normal in BACE1<sup>-/-</sup> mice, we examined the physiology of hair cells *in vitro*. Function of the mechano-electrical transduction (MET) machinery was probed with the lipophilic styryl dye FM1-43 known to enter hair cells through functional MET channels (Gale et al., 2001; Meyers et al., 2003). Uptake of FM1-43 following brief 45 s application to acutely isolated explants of the organ of Corti was measured by confocal microscopy. FM1-43 accumulation in IHCs and OHCs was homogenous and indistinguishable between explants from wild-type and BACE1<sup>-/-</sup> mice consistent with a normal function of MET channels in the knock-out mice (Fig. 3C). Because reduced DPOAEs point toward OHC dysfunction, we evaluated the physiology of OHC in BACE1<sup>-/-</sup> mice by analyzing expression and function of two essential OHC proteins: prestin, underlying OHC electromotility, and voltage-gated K<sup>+</sup> channel K<sub>v</sub>7.4 (KCNQ4), known to dominate the basolateral OHC conductance (Kharkovets et al., 2006; Johnson et al., 2011). Immunohistochemistry showed that both, expres-

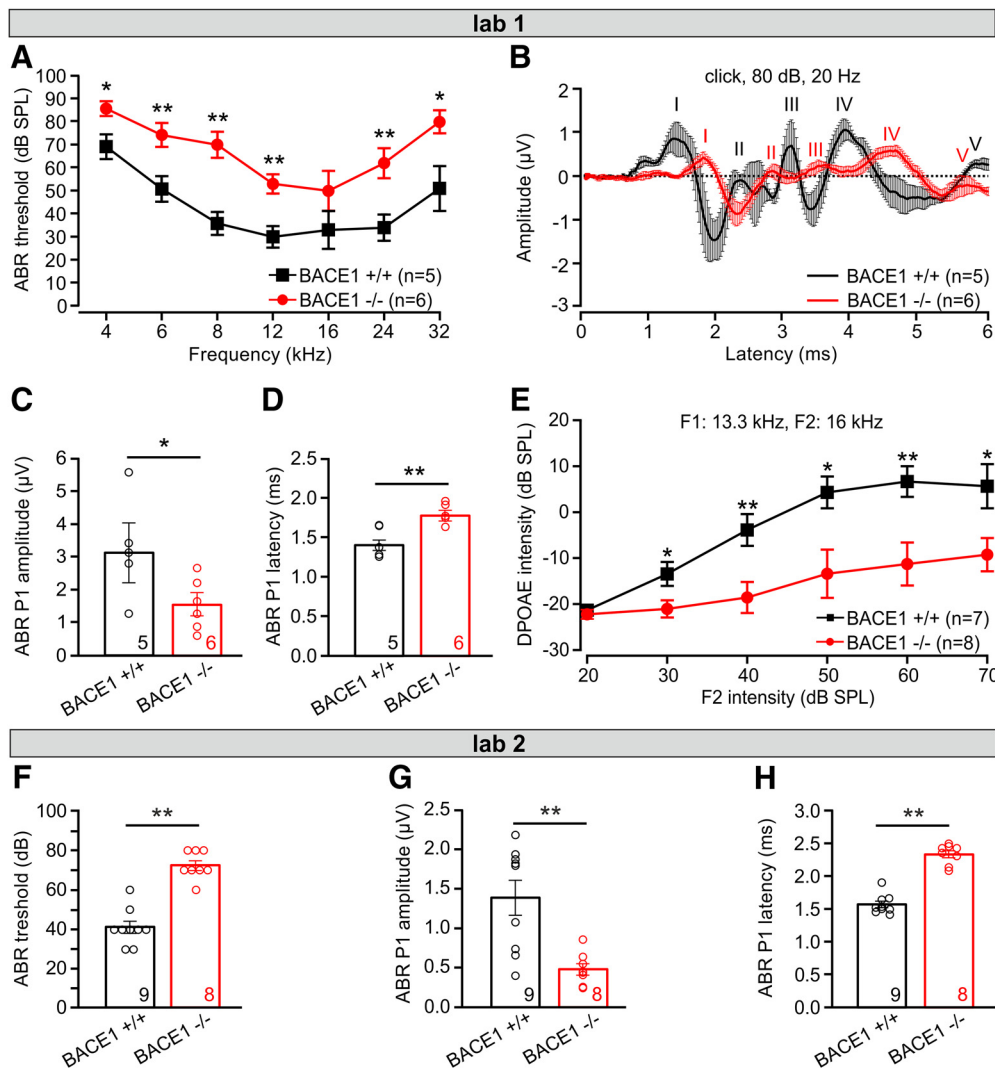


**Figure 1.** Deletion of BACE1 causes hearing impairment. **A**, ABR thresholds to tone bursts between 4 kHz and 32 kHz were significantly elevated by ~20 to 40 dB SPL in BACE1<sup>-/-</sup> mice (*n* = 6) compared with wild-type controls (*n* = 5). Note that there was no statistical difference between genotypes at 16 kHz in these experiments. **B–D**, In BACE1<sup>-/-</sup> mice, all ABR waves were reduced in amplitude and latencies were increased. **B**, Shows summarized ABR waveforms in response to click stimulation for BACE1<sup>-/-</sup> (red; *n* = 6) and wild-type (black; *n* = 5) mice (80 dB peak equivalent, 20 Hz stimulation rate). Matching the overall loss of sensitivity, ABR wave I showed (**C**) reduced amplitude and (**D**) increased latencies in BACE1<sup>-/-</sup> mice. Amplitudes and latencies were analyzed in recordings as shown in **B**, **E**, DPOAE intensities were also reduced in BACE1<sup>-/-</sup> mice (*n* = 8) compared with wild-type mice (*n* = 7) (F1 and F2 as indicated). Mice of both sexes were used 5–6 weeks after birth. **F–H**, Auditory brainstem responses following click stimulation were recorded in wild-type and BACE1<sup>-/-</sup> mice by a second independent laboratory (lab 2). Also in these recordings, in BACE1<sup>-/-</sup> mice, (**F**) the ABR thresholds were elevated, (**G**) the amplitude of ABR wave I (P1) was decreased and (**H**) the latency of wave I was increased compared with wild-type mice. Amplitude of ABR wave I was analyzed at 16 kHz (90 dB SPL) and wave I latency was quantified at 16 kHz (20 dB over threshold). Mice of both sexes were used 6–7 weeks after birth. *n* = 9 for wild-type and *n* = 8 for BACE1<sup>-/-</sup> mice. Note that ABR recordings with pure tones performed in an independent laboratory (lab 1) yielded essentially the same results (**A–E**). All data are represented as mean ± SEM, \**p* < 0.05, \*\**p* < 0.01 (*p*-values from two-tailed two-sample *t* test). Open symbols in **C**, **D**, and **F–H** show individual values for each animal.

sion levels and the characteristic subcellular distribution of prestin (Fig. 3D) and KCNQ4 (K<sub>v</sub>7.4) (Fig. 3E), appeared normal in OHCs of adult BACE1<sup>-/-</sup> mice (P35–P45). Functionally, amplitude and voltage-dependent features of prestin-mediated nonlinear capacitance were indistinguishable between OHCs from wild-type and BACE1<sup>-/-</sup> mice (Fig. 4A). Similarly, in OHCs KCNQ4-mediated currents quantified as the XE991-sensitive steady-state outward current at -60 mV (Oliver et al., 2003; Leitner et al., 2011) were indistinguishable between wild-type (33.6 ± 4.8 pA/pF; *n* = 6) and BACE1<sup>-/-</sup> mice (34.5 ± 5.1 pA/pF; *n* = 6; Fig. 4B). Other functional features of OHCs including resting membrane potential (Fig. 4C), kinetics of KCNQ4 currents (Fig. 4D) and cell capacitance (Fig. 4E) were unchanged in BACE1<sup>-/-</sup> mice. In summary, these experiments did not reveal major alterations of OHC physiology in BACE1<sup>-/-</sup> mice.

Similarly, in IHCs of BACE1<sup>-/-</sup> mice K<sup>+</sup> current amplitudes (Fig. 4F), cell capacitance (Fig. 4G), and resting membrane potential (Fig. 4H) were also the same as in wild-type.

**Normal organization of afferent ribbon synapses in BACE1<sup>-/-</sup> mice**

Given the apparent integrity of hair cells, we next analyzed the afferent synapses of IHCs. Structural alignment and integrity of the IHC-to-SGN synapse were assessed in wild-type and BACE1<sup>-/-</sup> mice by blinded counting of double-labeled presynaptic and postsynaptic structures in apical turns of the cochlea (Figs. 5, 6). Synapses were identified as juxtaposed presynaptic ribbons and postsynaptic AMPA receptor clusters characterized by staining with antibodies against CtBP2 and GluR2/3, respectively (Khimich et al., 2005). We found 11.8 ± 0.4 ribbons per

IHC and  $11.9 \pm 0.4$  GluR2/3 clusters in wild-type mice that importantly were located in close proximity ( $n = 41$  IHCs from 6 preparations of 3 mice; Fig. 5A, C), just as previously reported for wild-type mice (e.g., Vogl et al., 2017). Synapse counts were not altered in BACE1<sup>-/-</sup> mice, with  $11.7 \pm 0.4$  ribbons per IHC and  $11.8 \pm 0.4$  GluR2/3 clusters nearby ( $n = 57$ , IHCs from 6 preparations of 6 mice; Fig. 5B, C). GluR2/3 and CtBP2 immunofluorescent spots were juxtaposed in wild-type and BACE1<sup>-/-</sup> mice demonstrating identical counts of ribbon-occupied IHC synapses in both genotypes. Similarly, presynaptic ribbons in OHCs were also unchanged in number and morphology in BACE1<sup>-/-</sup> compared with wild-type mice (Fig. 5D).

### Disorganization of (afferent) SGN fibers and ectopic overexpression of PSD95 in BACE1<sup>-/-</sup> mice

We next examined the architecture of nerve fibers in the organ of Corti using an antibody directed against the spiral ganglion fiber marker neurofilament protein 200 kDa (NF-200). In doing so, we identified three distinct abnormalities in cochlea of BACE1<sup>-/-</sup> mice:

(1) Nerve fibers in the IHC region displayed higher anti-NF-200 immunofluorescence, appeared disorganized and enlarged, and occupied far more space in the synaptic area than in wild-type mice. Also, NF-200-stained fibers appeared somewhat thicker than in wild-type mice (Fig. 6A, B).

(2) To analyze the postsynaptic assembly in more detail, we stained presynaptic CtBP2 together with the postsynaptic scaffolding protein PSD95 and NF-H in acutely isolated organ of Corti explants. In wild-type mice, CtBP2- and PSD95-positive clusters precisely juxtaposed, i.e., PSD95 was exclusively localized in close proximity to the presynaptic region of IHCs (Fig. 6C, E). In contrast, in BACE1<sup>-/-</sup> mice the number of PSD95-positive clusters was significantly higher than in wild-type mice ( $p \leq 0.001$ ), by far exceeding the (unchanged) number of CtBP2-positive IHC ribbons ( $p \leq 0.001$ ; Fig. 6D, E). This increased number of PSD95 clusters indicated a mismatch of presynaptic and postsynaptic structures in BACE1<sup>-/-</sup> mice. The additional PSD95 clusters were preferentially located (far) outside the synaptic region and thus were not associated with presynaptic IHC ribbons (Fig. 6D, F). In BACE1<sup>-/-</sup> mice, the ectopic PSD95 clusters were distributed completely across the enlarged nerve fibers in the IHC region defined by NF-H reactivity (Fig. 6D, F). In contrast, in wild-type mice the PSD95 clusters were all located in close proximity to presynaptic IHCs (Fig. 6C, F). Thus, loss of BACE1 expression in the cochlea caused enlargement of SGN fibers and expression of PSD95 unmatched by CtBP2 reactivity. In contrast, expression

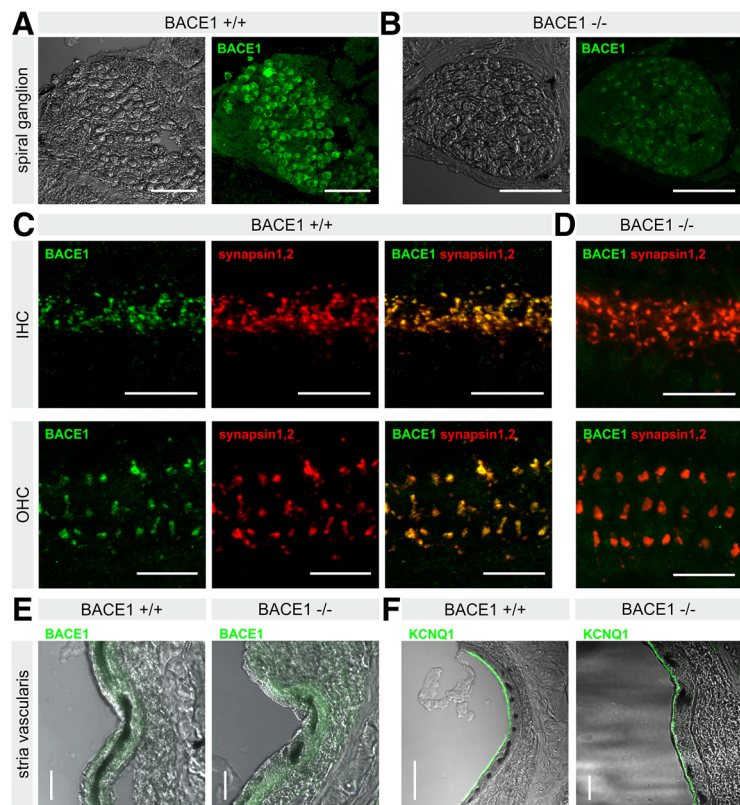


**Figure 2.** BACE1 is expressed in spiral ganglion neurons and olivocochlear terminals. Expression of BACE1 was analyzed with immunohistochemistry on (A, B, E) cochlear cryosections and (C, D) whole-mount preparations of the apical cochlear turn of the organ of Corti. All images are representative maximum intensity projections of confocal z-stacks (see material and methods for details). **A**, We detected strong anti-BACE1 immunosignals in cell bodies of SGN in BACE1<sup>+/+</sup> mice that (**B**) were strongly reduced in BACE1<sup>-/-</sup> mice. The panels (A + B) show representative transmitted light (left) and corresponding confocal images (right) of cryo-sections through the spiral ganglion stained with primary antibodies directed against BACE1 (green). **C**, In the organ of Corti of wild-type mice, we detected strong anti-BACE1 signals in synapsin1,2-positive structures that represent efferent olivocochlear terminals. **D**, These anti-BACE1 signals in efferent boutons were completely absent in the organ of Corti of BACE1<sup>-/-</sup> mice. **C** and **D** show confocal images of the organ of Corti in the IHC (top) or the OHC (bottom) region stained with primary antibodies against BACE1 (green) and synapsin1,2 (red). The right images in **C** and **D** show merged images of anti-BACE1 and the respective anti-synapsin1,2 staining. **E**, BACE1 expression was not detectable in the *stria vascularis*. We found comparable diffuse anti-BACE1-immunosignals in the *stria vascularis* of BACE1<sup>+/+</sup> (left) and BACE1<sup>-/-</sup> (right) mice. We thus consider these signals as caused by unspecific binding of the primary antibody. **F**, As demonstrated with antibodies directed against KCNQ1 channels (K<sub>v</sub>7.1), localization and expression of KCNQ1 channels (green) in the *stria vascularis* was indistinguishable between BACE1<sup>+/+</sup> (left) and BACE1<sup>-/-</sup> (right) mice. **E** and **F** show merged transmitted light and confocal images of cryo-sections through the *stria vascularis*. Scale bars, 20  $\mu$ m.

of GluR2/3 expression in the postsynapse appeared normal (cf. Fig. 5C).

(3) In BACE1<sup>-/-</sup> mice, NF-200-positive patches with high immunofluorescence appeared in the osseous spiral lamina (OSL) region between IHCs and the *modiolus* (Fig. 6B). These structures appeared as enlargements of the afferent fibers. As we did not detect anti-PSD95 immunosignals in these structures, we consider that these patches did not represent ectopically formed postsynaptic compartments (anti-PSD95 stainings not shown). These patches were entirely absent in wild-type cochleae (Fig. 6A, B).

### Demyelination of peripheral auditory nerve fibers in BACE1<sup>-/-</sup> mice

As the NF-200 antibody preferentially recognizes nonmyelinated segments of peripheral neurites (Kujawa and Liberman, 2009; Lin et al., 2011), we reasoned that the observed excessive NF-200 staining pattern may indicate altered myelination of auditory afferent nerve fibers. We thus examined myelination of SGN fi-

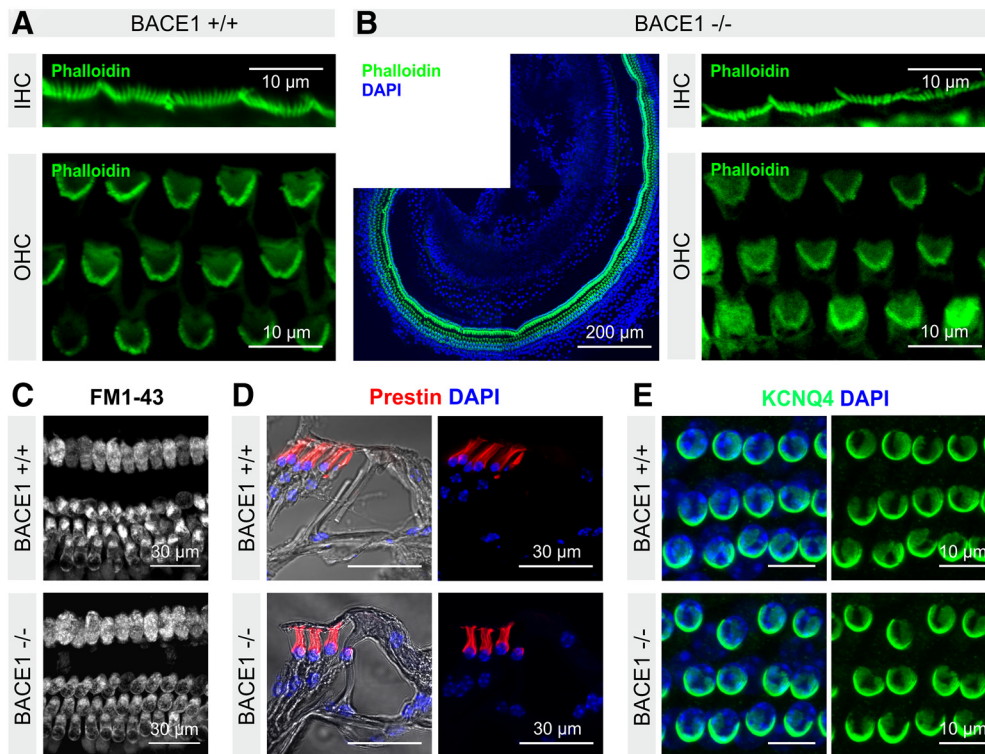


**Figure 3.** Normal hair cell function in  $BACE1^{-/-}$  mice. **A, B**, The images show representative confocal projections of whole-mount preparations of apical turns of the organ of Corti isolated from a (**A**) wild-type and (**B**)  $BACE1^{-/-}$  mice. Tissue was stained with fluorescently labeled phalloidin (green) and DAPI (blue) to visualize actin-containing stereocilia and the nuclei, respectively. We did not detect any signs of hair cell degeneration or altered hair bundle morphology in the organ of Corti of  $BACE1^{-/-}$  mice. (**C**) FM1–43 entry into IHCs and OHCs, as detected by comparing intensity of FM1–43-associated fluorescence in hair cells after 45 s exposure, was the same in  $BACE1^{+/+}$  (top) and  $BACE1^{-/-}$  mice (bottom). These experiments were performed on 3 organ of Corti preparations from three mice per genotype mice and did not reveal any difference of FM1–43 entry into hair cells of both genotypes. **D**, Cryosections of the cochlea stained with anti-prestin antibodies revealed that localization and expression of prestin (red) in the lateral membrane of OHCs was indistinguishable between wild-type (top) and  $BACE1^{-/-}$  (bottom) mice. The image depicts a representative section through the apical cochlear turn. **E**, Expression and localization of KCNQ4 ( $K_v7.4$ ) channels in OHCs was the same in wild-type and  $BACE1^{-/-}$  (whole-mount preparations of the organ of Corti stained with anti-KCNQ4 antibodies (green) and DAPI (blue)). **A–E** show representative confocal projections of z-stacks of tissue stained with the given primary antibodies in the apical turn of Corti. All tissue was isolated from mice of either sex at the age of P35–P45.

bers in whole-mount explants of the organ of Corti using an antibody directed against myelin basic protein (MBP). In wild-type mice, the anti-MBP-antibody strongly and homogeneously labeled most fibers in the OSL along their entire length, except for the most distal segment close to IHCs (Fig. 7A). This pattern is consistent with the fact that in the normal adult mouse cochlea, ~90% of the distal afferent nerve fibers are myelinated (Nayagam et al., 2011). Thus, we presume that most of these myelinated fibers recognized by the anti-MBP antibody are type I afferents. In cochleae from adult  $BACE1^{-/-}$  mice, the MBP staining was markedly reduced, as by far fewer fibers showed myelination at all and, if detectable, myelination did not extend all the way to the distal endings in the majority of those fibers (Fig. 7B). Indeed, when taking NF-200-positive immunostaining as measure for the traveling distance of fibers without myelination, we found that in wild-type mice the myelination of fibers traveling toward the hair cell region ended ~40  $\mu$ m away from IHCs in the OSL close to the habenula perforata (Fig. 7B,C). In contrast, in  $BACE1^{-/-}$  mice, NF-200-positive immunoreactivity extended approximately twice further from the inner spiral plexus (ISP) toward the spiral ganglion ( $p \leq 0.001$ ;  $n = 80$  fibers from 4 different animals per genotype; Fig. 7C). To substantiate our findings, we investigated ultrathin (90 nm) sections of the adult cochlea with transmission electron microscopy (TEM). In  $BACE1^{-/-}$  mice, the myelination of the SGN cell bodies and surrounding fibers was mostly absent (Fig. 7D, red arrows), and the thickness of the myelin layers of the nerve fibers in the OSL was substantially

reduced compared with the wild-type mice (Fig. 7E). Furthermore, in contrast to wild-type mice, many nerve fibers in the OSL were not myelinated (Fig. 7E, red asterisks). This supports the finding that myelination of the peripheral auditory fibers was decreased in  $BACE1^{-/-}$  mice.

Together, our data demonstrated severe disorganization of peripheral fibers of (type I) afferent neurons in  $BACE1^{-/-}$  mice, strongly enlarged endings, supernumerary postsynaptic sites, and impaired myelination. We therefore posit that BACE1 is essential to ensure normal architecture and, myelination of distal auditory fibers in the cochlea.

#### Treatment with BACE1 inhibitor does not cause hearing loss

Given that BACE1 is widely recognized as a prime drug target for the prevention and treatment of AD, we wondered whether chronic pharmacological suppression of BACE1 activity in normal mice would carry the risk of unwanted side effects in the auditory system. To address this translationally important question, we treated 1-month-old wild-type mice with the established blood–brain barrier permeable BACE1 inhibitor NB-360 (Neumann et al., 2015). The drug was administered for 6 weeks, which, in a mouse model of AD, proved sufficient to reduce A $\beta$  fibrils in cortical tissue and to rescue neuronal hyperactivity, impaired circuit function and memory deficits (Keskin et al., 2017). Suppression of BACE1 activity by NB-360 was indicated by the following findings. The fur of treated mice lost its homogeneous black color, thereby exhibiting more or less pronounced patches

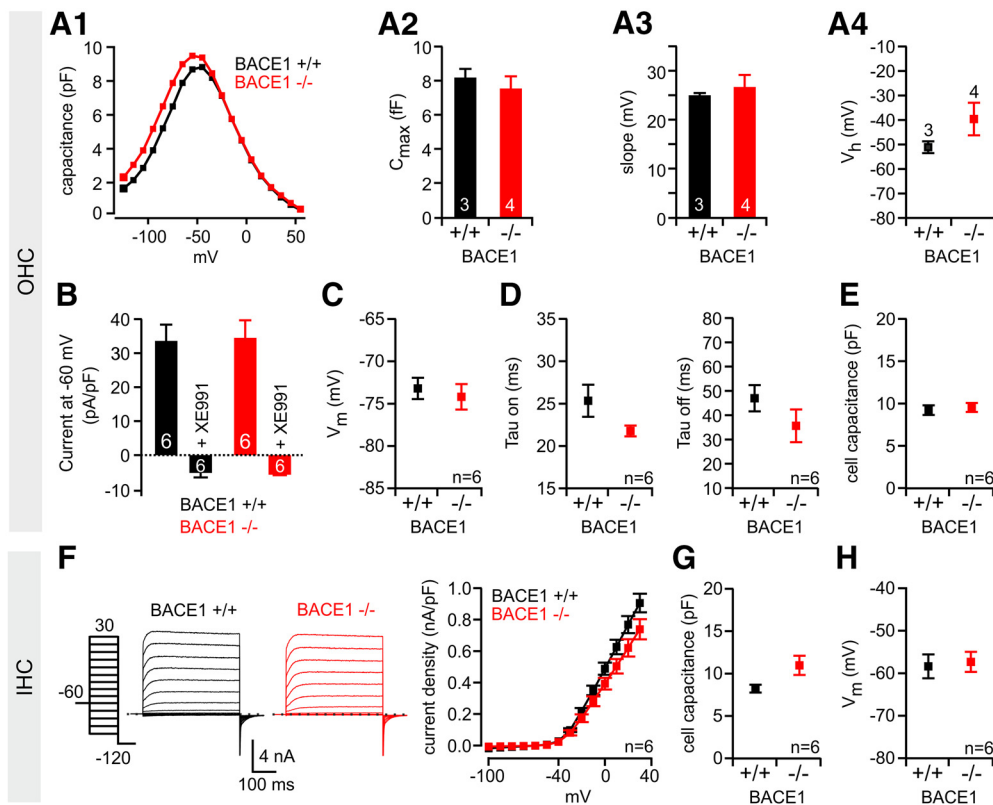


**Figure 4.** Normal biophysical properties of prestin and hair cell  $K^+$  currents in  $BACE1^{-/-}$  mice. We did not detect any differences in the properties of prestin or the  $K^+$  currents expressed in hair cells between wild-type and  $BACE1^{-/-}$  mice. **A–E** summarize for OHCs (**A1**, representative capacitance recordings; **A2**, summarized maximum capacitance  $C_{max}$  and voltage-dependent features of prestin-mediated nonlinear capacitance (**A3**, summarized slope; **A4**, summarized  $V_h$ ), (**B**)  $K_v7.4$ -mediated currents quantified as XE991-sensitive steady-state outward current at  $-60$  mV, (**C**) resting membrane potential, (**D**) activation (left) and deactivation (right) kinetics of XE991-sensitive currents and (**E**) cell capacitance. Note that all parameters were the same in OHCs of  $BACE1^{+/+}$  and  $BACE1^{-/-}$  mice. **F–H** show that also in IHCs (**F**) whole-cell current densities, (**G**) cell capacitance and (**H**) resting membrane potentials were the same in both genotypes. **F**, Representative current recordings. **F–H** summarize the recordings of IHCs isolated from mice of both genotypes ( $n = 6$  for each genotype). All tissue was isolated from mice at the age of P39–P42 (IHC) and P14–P16 (OHC). All hair cells were recorded from the apical turn of the organ of Corti.

of gray (Fig. 8A) (Shimshek et al., 2016; Hartmann et al., 2018). Western blot analysis of amyloid precursor protein (APP) and contactin-2 (CNTN2) (Gautam et al., 2014), two known BACE1 substrates, demonstrated a significant increase of the respective, unprocessed full-length protein (Fig. 8B,C), consistent with a previous report on NB-360 (Neumann et al., 2015). In stark contrast to the pronounced hearing impairment of  $BACE1^{-/-}$  mice, NB-360-treated wild-type mice performed just as well in ABR recordings as their drug-free counterparts (Fig. 8D). As almost predicted by the normal ABR results from the treated mice, NB-360 administration also did not produce the aberrant histological features in the cochlea that we had identified in  $BACE1^{-/-}$  mice. Thus, we did not observe differences between NB-360-treated and control mice at presynaptic or postsynaptic sites of the IHC-to-SGN synapse (Fig. 8E) and we observed no ectopically expressed PSD95 clusters as seen in  $BACE1^{-/-}$  mice (Fig. 8F). Also, staining against NF-200 and MBP showed that NB-360 did not affect axonal organization and myelination (Fig. 8G,H). It therefore appears safe to conclude that the auditory phenotype of  $BACE1$ -deficient mice including its neuropathological underpinnings is not reproduced by prolonged systemic NB-360 administration in wild-type mice.

#### BACE1 knock-out mice do not develop proper myelination in the cochlea

The lack of an auditory phenotype of NB-360-treated adult wild-type mice suggested to us that the hearing loss of the mutant line

might be of developmental origin. To explore the role of BACE1 in postnatal cochlear wiring, we compared the time course of myelination in the apical turn of the organ of Corti in wild-type and  $BACE1$ -deficient mice between postnatal days 5–15 (Fig. 9A), when cochlear BACE1 levels are invariably high (Shen et al., 2015). In wild-type mice, considerable proximal myelination was already present at P5–P6. At P8, the myelin sheath extended distally to the *habenula perforata* in some fibers, and myelination reached mature levels by the end of the second postnatal week (Fig. 9A, top; cf. Fig. 7A). In stark contrast,  $BACE1^{-/-}$  mice did not show any myelination in the cochlea at the end of the first postnatal week, and at P14, we detected only faint anti-MBP signals in proximal regions of SGN fibers (Fig. 9A, bottom). Thus, the developmental myelination in the cochlea of  $BACE1$ -deficient mice was markedly delayed, and axonal ensheathment remained immature even in adulthood (Fig. 7B). The observed enlargement and disorganization of fibers in adult  $BACE1^{-/-}$  mice (Fig. 7B) was not present until  $\sim$ P14 (Fig. 9A, arrows).

In the apical turn of the cochlea, the postsynaptic compartment appeared normal (Fig. 9A,B) until at least P14–P15 (Fig. 6B). However, in the base of the cochlea, SGN fiber terminals were already abnormally swollen around the same time point (Fig. 9B), indicating a progression of deterioration from the cochlear base to the apex that follows the sequence of tonotopic myelination in humans (Ray et al., 2005).

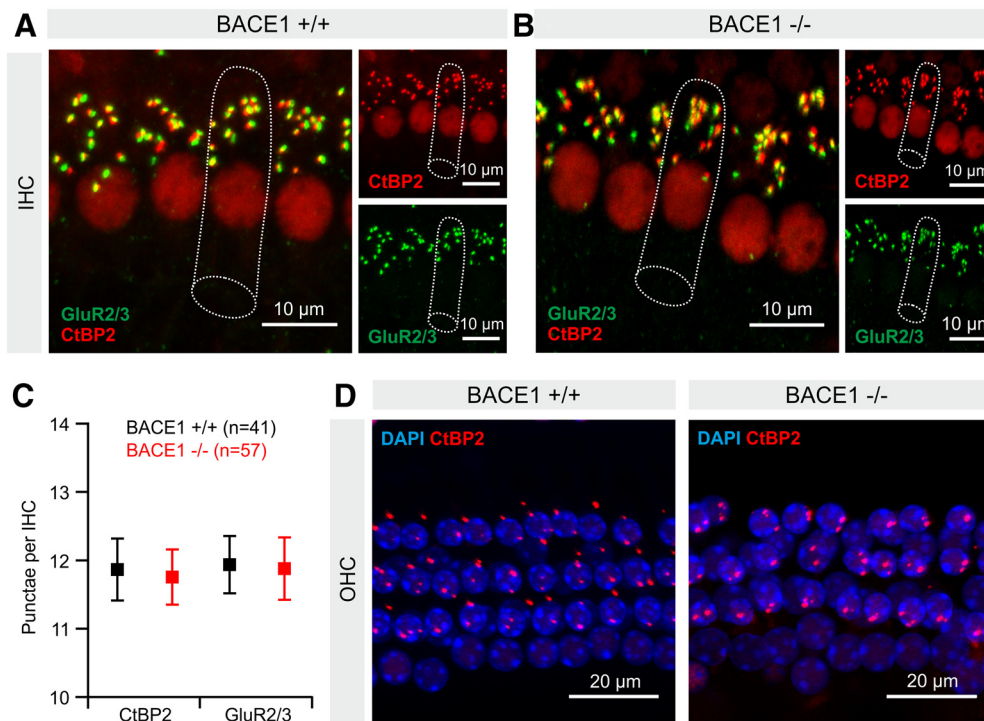


**Figure 5.** The architecture of ribbon synapses appears normal in BACE1<sup>-/-</sup> mice. **A, B**, Representative maximum intensity projections of confocal z-stacks from the IHC region in the organ of Corti of the apical turn of (**A**) wild-type and (**B**) BACE1<sup>-/-</sup> mice stained with antibodies directed against presynaptic CtBP2 (red) and postsynaptic GluR2/3 (green). Dotted lines visualize individual IHCs in the region. **C**, CtBP2 and GluR2/3 puncta were quantified by blinded counting of immunopositive clusters from images as shown in (**A** + **B**) in BACE1<sup>+/+</sup> ( $n = 41$  cells of 3 mice) and BACE1<sup>-/-</sup> mice ( $n = 57$  cells of 3 mice). There was no significant difference between genotypes. **D**, There was no obvious difference in the number of CtBP2-positive clusters in OHCs of BACE1<sup>+/+</sup> (left) and BACE1<sup>-/-</sup> (right) mice. **D**, Representative confocal projections through the OHC region in the apical turn of BACE1<sup>+/+</sup> (left) and BACE1<sup>-/-</sup> (right) mice stained with anti-CtBP2 antibodies (red) and DAPI (blue).

### Neuregulin signaling is impaired in BACE1 knock-out mice

NRG1 is an important substrate of BACE1. Upon BACE1 cleavage, its N-terminal region is released and binds to ErbB receptors (for review, see Hu et al., 2016). As a consequence of impaired NRG1-ErbB-signaling, myelination of peripheral nerves is compromised in BACE1<sup>-/-</sup> mice (Hu et al., 2006; Willem et al., 2006). In the cochlea, NRG1 is expressed in SGNs (Morley, 1998; Hansen et al., 2001; Stankovic et al., 2004) and signals to cochlear Schwann cells containing ErbB2 and ErbB3 receptors (Hansen et al., 2001). Activated NRG1 type III is a key regulator of myelin thickness in the peripheral nervous system (Taveggia et al., 2005; Velanac et al., 2012). Type-III NRG1<sup>+/-</sup> mice have slightly increased hearing thresholds at the age of 12 months (Jin et al., 2011). NRG1 is therefore a candidate BACE1 substrate in the cochlea that, when incompletely processed, might cause the observed hypomyelination. To substantiate this, we examined the cochlea of heterozygous *Nrg1*- $\beta$  allele mutant mice that carry only one intact copy of *Nrg1*. We restricted our analyses to heterozygous mice, as the homozygous *Nrg1*- $\beta$  mutation is lethal. We analyzed myelination of SGN fibers and nerve fiber architecture using anti-MBP and anti-NF-200-antibodies, respectively. Further, we used a B-FABP-antibody (brain-type fatty acid binding protein, Kurtz et al., 1994), that recognizes nonmyelinating glial cells and labels the synaptic region of inner hair cells devoid of myelin. In wild-type animals, the distal unmyelinated part of SGN fibers and the postsynaptic compartment was completely covered by FABP-positive glia cells (Fig. 10*A, B*). In BACE1<sup>-/-</sup> mice, the FABP-positive zone extended considerably more proximally covering a large part of unmyelinated axons and the enlarged postsynaptic region (Fig. 10*B*). *Nrg1*- $\beta$ -hetero-

zygous mice show a similar, but less pronounced phenotype exhibiting the same neuropathological hallmarks, namely enlarged and disorganized postsynaptic compartments (NF-200), fiber hypomyelination (MBP) and an extended axonal area covered by unmyelinated glia that stain for FABP (Fig. 10). The results strongly suggest that impaired NRG1-ErbB-signaling is responsible for the aberrant cochlear wiring in BACE1 knock-out mice.

### Discussion

Our study establishes hearing loss as a novel phenotype of BACE1-deficient mice. The high expression levels of BACE1 in neurons of the spiral ganglion and in olivocochlear terminals, together with the conspicuous neuropathology in the cochlea and the related abnormalities in the ABR recordings in the absence of BACE1 strongly argue for a peripheral origin of the hearing loss.

Compared with wild-type littermates, BACE1<sup>-/-</sup> mice displayed significantly increased ABR thresholds in response to pure tones over a wide range of frequencies (e.g.,  $\sim +40$  dB at 8 kHz in ABR recordings (Fig. 1*A*), and also after broad-band click stimulation (Fig. 1*F*). We link this finding to a sensorineural hearing loss, because amplitudes of all ABR waves, especially of wave I, were significantly decreased, and DPOAE thresholds were elevated in BACE1-null mice. This pattern of electrophysiological abnormalities is an unequivocal sign of diminished sound sensitivity in the cochlea. At present, we do not know the reasons for the observed reduction in DPOAE amplitude. Given the normal OHC morphology and *ex vivo* physiology one might speculate about a potential gain of efferent inhibition of OHCs in BACE1<sup>-/-</sup> mice, testing of which will require future studies.

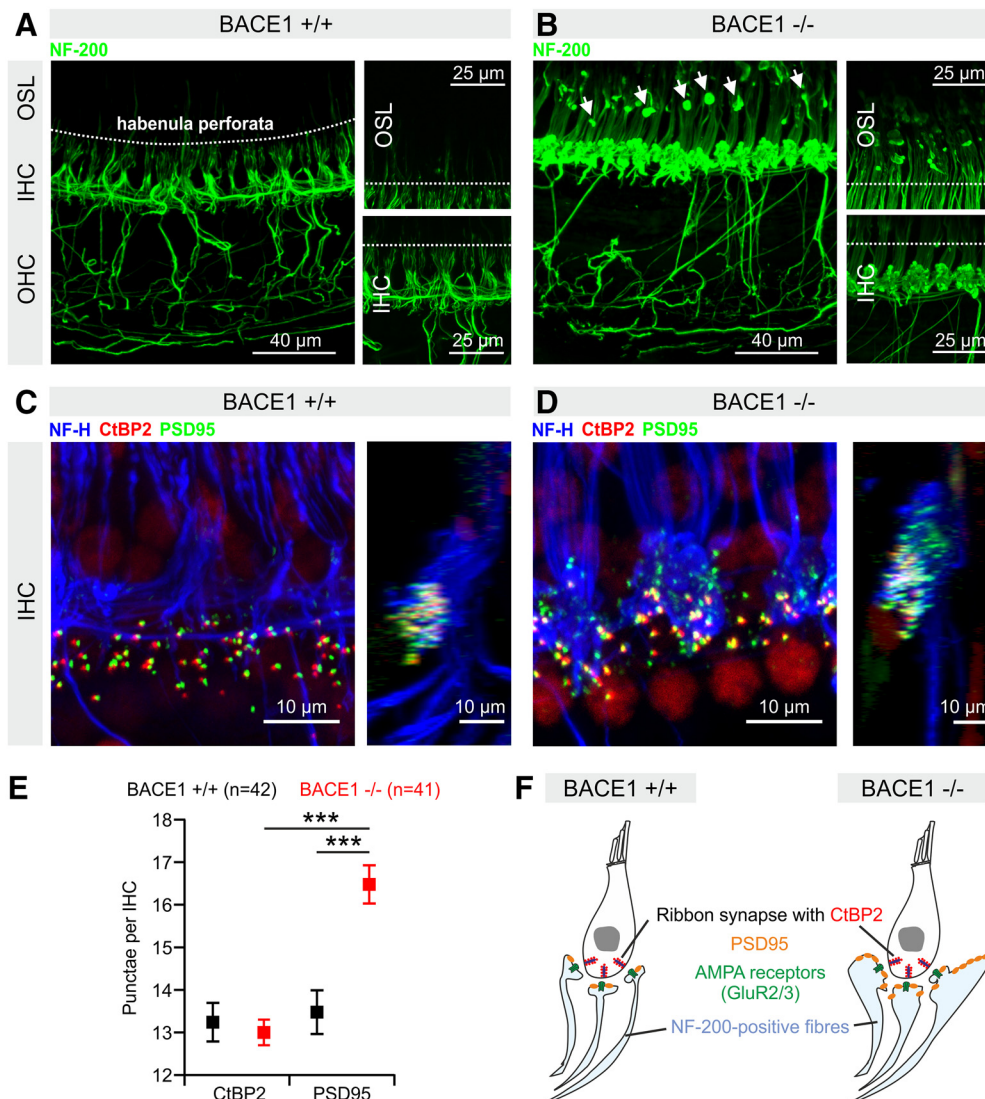


**Figure 6.** Disorganization of nerve fibers and ectopic overexpression of PSD95 in BACE1<sup>-/-</sup> mice. Auditory nerve fibers and the synaptic arrangement were analyzed in whole-mount organ of Corti preparations of the apical cochlear turn stained with primary antibodies targeted against neurofilament (NF-200 or NF-H, both are directed against neurofilament heavy chain polypeptide) and CtBP2 or PSD95, respectively. **A, B**, Auditory nerve fibers in the *osseus spiral lamina* (OSL) of BACE1<sup>-/-</sup> mice (in **B**; P48) showed more intense anti-NF-200 immunofluorescence, and appeared disorganized and swollen. In the OSL of BACE1<sup>-/-</sup> mice, we detected NF-200-positive patches with very high immunofluorescence (arrowheads in **B**) that were completely absent in wild-types. Dashed lines in **A** and **B** indicate the habenula perforata. Smaller images in **A** and **B** display magnifications of the OSL (top) and the IHC (bottom) region. **C, D**, Triple staining with antibodies directed against neurofilament (NF-H; blue), CtBP2 (presynaptic ribbon; red) and anti-PSD95 (postsynaptic density; green) showed that (**C**) in BACE1<sup>+/+</sup> mice the presynaptic and postsynaptic terminals were well aligned in close proximity. **D**, In BACE1<sup>-/-</sup> mice a substantial number of PSD95-positive clusters was located far outside the synaptic region and not aligned at all with presynaptic anti-CtBP2 signals. Maximum intensity projections of confocal z-stacks shown in the acquisition plane ( $x$ - $y$ , left) and in the orthogonal plane ( $z$ - $y$ , right). **E**, Blinded counting of CtBP2- and PSD95-positive signals revealed significantly more PSD95 clusters in BACE1<sup>-/-</sup> than in BACE1<sup>+/+</sup> mice ( $p < 0.001$ ). In BACE1<sup>-/-</sup> mice, postsynaptic PSD95 clusters significantly outnumbered presynaptic CtBP2 clusters ( $p < 0.001$ ). **F**, Schematic drawing summarizing our findings (neurofilament-positive fibers, blue; PSD95, orange; CtBP2, red; GluR2/3, green). (**A–D**) All images are representative confocal projections of the apical turn of the organ of Corti. Corresponding images (**A, B** and **C, D**) were taken in parallel under identical experimental conditions (See Materials and Methods). \*\*\* $p < 0.001$ .

Regardless of the precise mechanism, a reduction of cochlear amplification likely contributes to the hearing impairment of BACE1<sup>-/-</sup> mice.

It might appear surprising that, despite the many in-depth studies of BACE1-deficient mice at all levels of examination, the hearing loss escaped the attention so far. However, since the mice are not completely deaf, their hearing phenotype is not plainly obvious, but requires detailed audiometric analysis. In view of our findings, previous studies reporting deficits of BACE1<sup>-/-</sup> mice in behavioral paradigms that used acoustic stimuli such as prepulse inhibition (Savonenko et al., 2008) and acoustic startle responses (Weber et al., 2017) should be

discussed also in consideration of the hearing dysfunction of the mice described here.

#### BACE1 is essential for normal myelination of nerve fibers, axonal targeting and synapse formation in the cochlea

As morphological substrates of the hearing loss, we identified hypomyelination of auditory nerve fibers, as well as disorganization and enlargement of postsynaptic terminals close to the IHC synaptic region. Compared with the auditory impairment in other mouse models of peripheral myelination defects (Zhou et al., 1995; Wan and Corfas, 2017), BACE1 knock-out mice exhibit a more pronounced elevation of ABR thresholds suggesting that

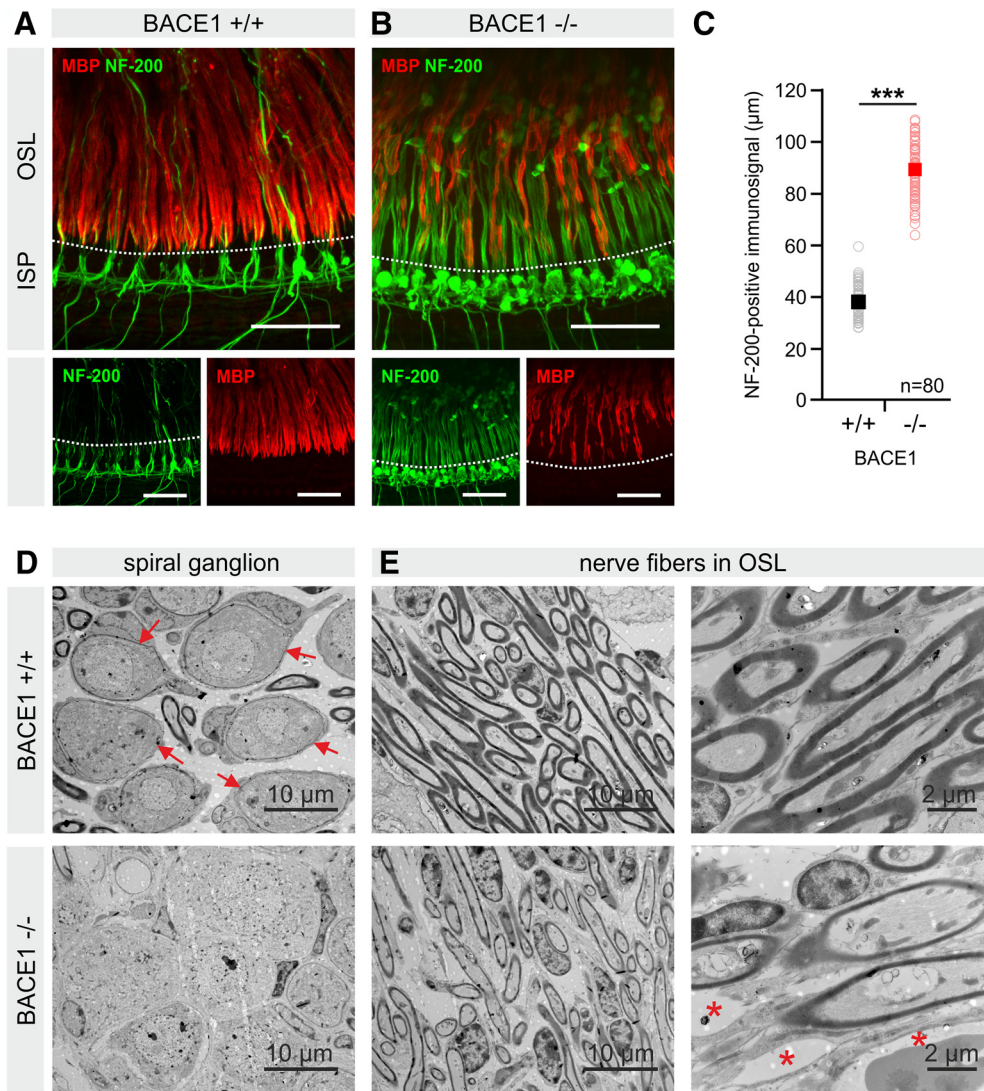


**Figure 7.** Deletion of BACE1 causes significant hypomyelination of auditory nerve fibers. **A, B**, Myelination of nerve fibers was largely reduced and fewer fibers showed myelination in BACE1<sup>-/-</sup> mice, as demonstrated by substantially reduced anti-MBP immunosignals in the apical turn of the organ of Corti. Whole-mount preparations of adult **(A)** BACE1<sup>+/+</sup> and **(B)** BACE1<sup>-/-</sup> mice were stained with antibodies directed against MBP (red) and NF-200 (green). Note that in wild types, but not in BACE1<sup>-/-</sup> mice, anti-MBP immunosignals extended completely toward the habenula perforata (indicated by the dashed line). The panels show representative confocal projections; all scale bars represent 40  $\mu$ m. **C**, As measure for the traveling distance of fibers without myelination, we quantified the distance of NF-200-positive immunostaining from the inner spiral plexus (ISP) close to IHCs toward the osseous spiral lamina. 80 nerve fibers of 4 animals per genotype were analyzed blinded to the analyst with ImageJ (\*\*\**p* ≤ 0.001; two-tailed two-sample *t* test). Note that NF-200 preferentially recognizes non-myelinated segments of nerve fibers. **D, E**, TEM analysis in ultrathin sections of the cochlea (basal turns; 90 nm) of **(D)** the cell bodies of SGN neurons in the ganglion and **(E)** of nerve fibers in the OSL of adult wild-type (top) and BACE1<sup>-/-</sup> mice (bottom). **D**, Cell bodies of SGN in the ganglion of wild-type mice were covered with myelin sheaths (c.f. red arrows) that were almost completely absent in BACE1<sup>-/-</sup> mice. **E**, In knock-out mice, myelin sheaths of nerve fibers in the OSL were thinner in general and some fibers were not myelinated (\*fibers in the OSL).

the synaptic abnormalities in their cochleae bear also functional relevance. In support of this notion, we found ectopically expressed PSD95 in these enlarged nodular structures. As the majority of myelinated fibers in the cochlea constitute type I fibers, loss of BACE1 affected the integrity of afferent SGN fibers carrying the auditory information from inner hair cells to brainstem nuclei as well as their postsynaptic compartments.

Disorganization of synaptic contact sites due to aberrant axonal targeting and hypomyelination of nerve fibers are not without precedent in BACE1-deficient mice (see Introduction and Results). In fact, NRG1 emerged as an important substrate of BACE1. NRG1 has multiple functions in myelination of peripheral axons and the induction of the muscle spindle, and depends on BACE1 cleavage to exert these roles (Michailov et al., 2004; Cheret et al., 2013). It was therefore plausible that in the auditory

periphery, as in other areas of the nervous system, the abrogated processing of NRG1 by BACE1 causes changes like hypomyelination. Heterozygous *Nrg1* knock-out mice display indeed an attenuated phenotype, i.e., hypomyelination and enlarged postsynaptic compartments (Fig. 10A). The fact that heterozygous loss of *Nrg1* produced a weaker auditory phenotype than complete disruption of *Bace1* might be attributable to higher levels of processed NRG1 in the former mice. Alternatively, there could be contribution of additional BACE1 substrates to normal cochlear function.

The extended FABP-positive area in NRG1<sup>+/-</sup> and BACE1<sup>-/-</sup> mice illustrates the enlarged synaptic compartment, and the abnormally thin and retracted myelin sheath. Interestingly, NRG1 overexpressing mice exhibit decreased PSD95 gene expression in SGN fibers (Jin et al., 2011), and terminal Schwann cell-mediated



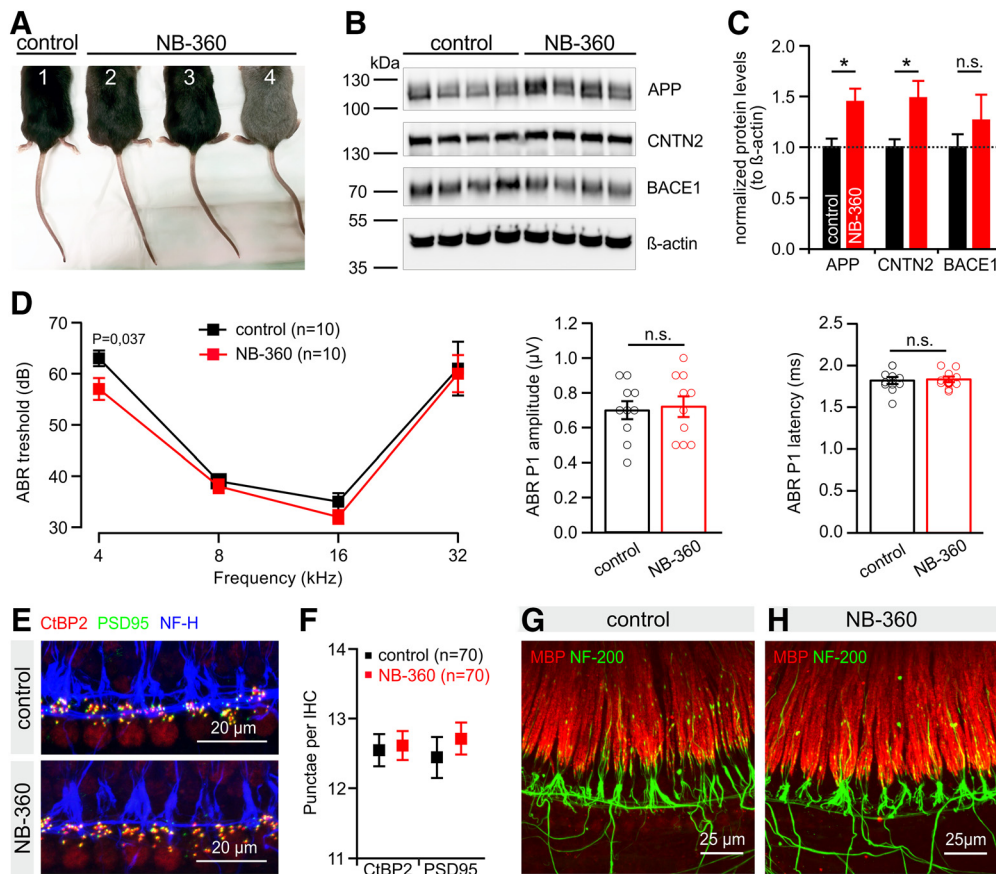


**Figure 8.** Treatment of mice with BACE inhibitor NB-360 does not cause hearing loss. **A**, Treatment of mice with NB-360 for 6 weeks led to significant changes of fur color ranging from the appearance of patches of gray hair (mouse 2, 3 versus control mouse 1) to general decolorization (mouse 4). **B**, **C**, Inhibition of BACE1 was evaluated by quantifying levels of APP, CNTN2 and BACE1 in brain lysates of four control and four NB-360-treated mice with Western blots. **C**, Levels of these proteins were densitometrically quantified in Western blots as shown in **B**, normalized to an internal standard to equalize between membranes, and normalized to the corresponding  $\beta$ -actin levels. Levels of untreated controls (black columns) were set to 1 for illustration. Red columns depict results for the BACE1 substrates CNTN2 and APP, as well as for BACE1 protein of NB-360-treated animals. The APP antibody is directed against the C terminus of APP (Bhattacharyya et al., 2013). The CNTN2 antibody is directed against GPI anchored full-length contactin-2 (Gautam et al., 2014) ( $n = 6$  for controls and  $n = 8$  for NB-360-fed mice,  $*p < 0.05$ , n.s., not significant, two-tailed two-sample  $t$  test). **D**, Feeding of mice with NB-360 for 6 weeks did not induce hearing loss, as ABR thresholds, ABR wave I amplitude and latency were indistinguishable between control (black) and NB-360-treated (red) mice. The panel shows summary of ABR thresholds in response to pure tones, and the quantification of wave I (P1) amplitude (16 kHz at 90 dB) and latency (16 kHz; 20 dB over threshold) ( $n = 10$  for both groups). **E**, **F**, Blinded counting of presynaptic CtBP2- (red) and postsynaptic PSD95-clusters (green) revealed no difference in synapse number and structure between control mice and mice fed with NB-360 (70 IHCs of 4 different animals per treatment group were analyzed; no significant difference). Organization and integrity of auditory nerve fibers, as visualized with antibodies directed against neurofilament (NF-H-immunoreactions, blue), was also the same in both groups. **G**, **H**, As demonstrated by anti-MBP immunoreactions (red), myelination of nerve fibers was indistinguishable between control mice and mice fed with NB-360. Also, anti-NF-200 signals were the same in both treatment groups and we did not detect any patches with high NF-200 immunofluorescence in the osseous spiral lamina (OSL) of mice fed with NB-360. **E**, **G**, and **H** show representative confocal projections of whole-mount explant cultures (apical cochlear turns) stained with primary antibodies against the indicated proteins.

synapse elimination of neuromuscular junctions depends on NRG1 (Lee et al., 2016). We therefore suggest that the converse phenotype, the increased number of PSD95-positive clusters around IHC synapses observed BACE1 null mice, is due to a lack of processed NRG1.

Analysis of the BACE1<sup>-/-</sup> mice demonstrated a pronounced delay of the onset of peripheral myelination in OSL fibers by ~10 d. In the cochlea of adult BACE1-deficient mice, myelination was still incomplete, demonstrating that the developmental deficit cannot be compensated over time. Together with the observation that the inhibition of BACE1 in adult mice did not impair cochlear function and morphology, these data suggest that the auditory phenotype of BACE1<sup>-/-</sup> mice represents predominantly a developmental disorder.

#### BACE1 is unlikely to interact with $K_v7$ channels in the cochlea

Two types of KCNQ ( $K_v7$ ) channels, KCNQ1/KCNE1 and KCNQ4, are essential for cochlear function. Mutations in either

channel gene produce hearing deficits of varying degrees up to deafness (for review, see Jentsch, 2000; Maljevic et al., 2010). While KCNQ1/KCNE1 channel complexes located in marginal cells of the *stria vascularis* serve to maintain the high  $K^+$  concentration of the endolymph, the prerequisite of the endocochlear potential, KCNQ4 provides the major  $K^+$  conductance of OHCs (Kharkovets et al., 2006). As we have reported previously BACE1 interacts with KCNQ channels including the subtypes present in the cochlea in a complex fashion, involving both enzymatic and nonenzymatic effects (Sachse et al., 2013; Agsten et al., 2015; Hessler et al., 2015; Lehnert et al., 2016). Thus, we wondered whether changes in KCNQ channel expression or function might contribute to the hearing deficit of BACE1<sup>-/-</sup> mice. Our evidence against an appreciable role of these channels is the following. First, in whole-cell voltage-clamp recordings of  $K^+$  currents from OHCs of wild-type and mutant mice, we did not detect any significant difference, consistent with the lacking BACE1 staining of hair cells in immunohistochemical preparations of wild-type mice. Further support for the absence of

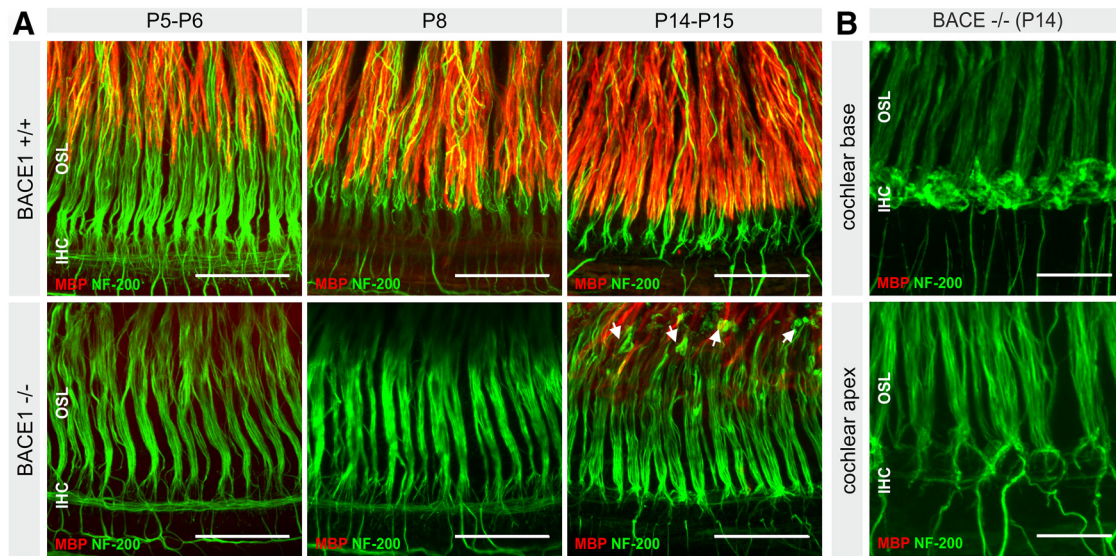


**Figure 9.** Postnatal myelination of SGN fibers is delayed in  $BACE1^{-/-}$  mice. **A**, Compared with age-matched wild-type animals (top), onset of SGN fiber myelination was substantially delayed in  $BACE1$  knock-out mice (bottom), and myelination was highly incomplete at P14–P15. Two weeks after birth, nodule patches with high NF-200 immunofluorescence appeared in the OSL of  $BACE1^{-/-}$  mice (white arrows). Note that NF-200 preferentially recognizes unmyelinated segments of nerve fibers. The panels show representative confocal z-stack projections of whole-mount preparations of the apical turn of the organ of Corti at indicated age; scale bars, 50  $\mu\text{m}$ . Three animals were analyzed per age group. **B**, Two weeks after birth, SGN fiber terminals were disorganized at the cochlear base, whereas fiber architecture in the cochlear apex was normal. At least three animals were analyzed per age group. In **A** and **B**, myelination was visualized in whole-mount preparations of the apical turn of the organ of Corti using antibodies directed against MBP (red), SGN fibers were visualized with NF-200 (green). The postnatal day is indicated above the images. Scale bars, 20  $\mu\text{m}$ .

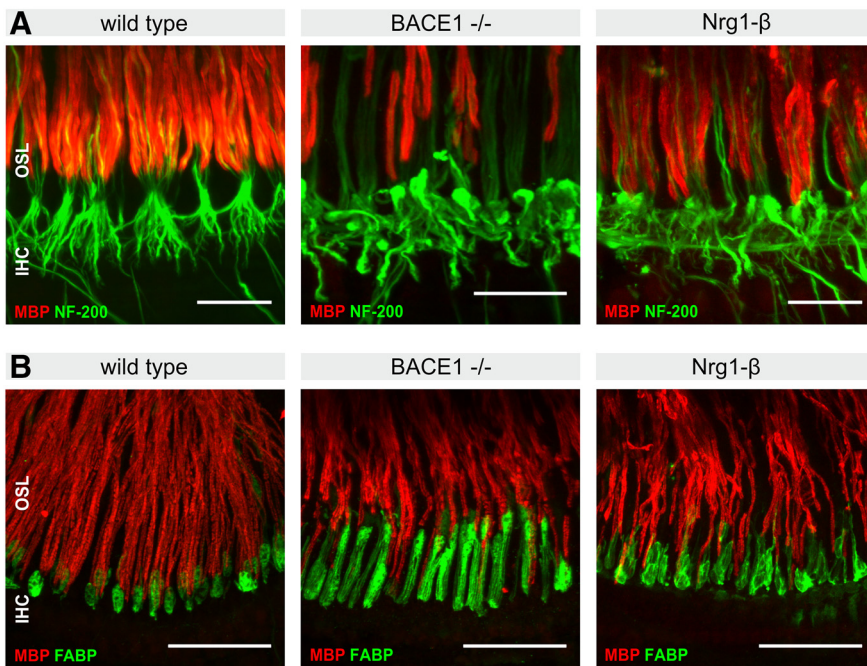


**Figure 10.**  $NRG1^{-/-}$  mice display reduced myelination and abnormal fiber configuration. **A**, Heterozygous  $NRG1^{-/+}$  mice ( $Nrg1-\beta$ , right) display hypomyelination, disorganization and abnormal enlargement of the synaptic region of SGN fibers in the cochlea 4 weeks after birth. Compared with  $BACE1^{-/-}$  mice (middle), the reported abnormalities are similar albeit less pronounced. Scale bars represent 20  $\mu\text{m}$ . **B**, Visualization of nonmyelinated glia cells in the synaptic region of the cochlea with antibodies directed against FABP (brain-type fatty acid binding protein, green) in wild-type (left),  $BACE1^{-/-}$  (middle), and  $NRG1^{-/+}$  mice ( $Nrg1-\beta$ ; right). In both  $BACE1^{-/-}$  and  $NRG1^{-/+}$  mice, the nonmyelinated synaptic region was extended compared with wild-type mice. Scale bars represent 50  $\mu\text{m}$ . **A** and **B** show representative maximum intensity projections of confocal z-stacks of the apical turn of the cochlea stained with the indicated antibodies. Four animals were examined per genotype.

$BACE1$  from hair cells comes from expression analyses made available through the SHIELD database (Shen et al., 2015). Second, immunostaining of marginal cells of the *stria vascularis* did not reveal expression of  $BACE1$  in wild-type mice (Fig. 9A), and expression of  $KCNQ1$  in these cells appeared unchanged in  $BACE1$  knock-out mice (Fig. 2F). Finally, rodents with impaired peripheral myelination uniformly display elevated ABR thresholds, reduced ABR amplitudes and prolonged ABR latencies (for review, see Long et al., 2018). Thus, the auditory phenotype of  $BACE1$  null mice can be fully explained based on the neuropathological aberrations in their cochlea, without considering a decrease in  $KCNQ$  currents.

We therefore conclude that, whereas  $BACE1$  has considerable impact on  $KCNQ$  channel function in other regions of the nervous system and elsewhere in the body, such an interaction is unlikely to occur in marginal and hair cells of the cochlea, probably owing to the lack of sufficient expression of  $BACE1$  in cells with significant  $KCNQ$  currents.

**Would BACE1 inhibitors worsen hearing function in AD?**

A recent study on auditory function in a mouse model of AD reported reduced

acoustic startle response and peripheral hearing loss (O'Leary et al., 2017). These AD mice showed increased ABR thresholds at 13–14 months of age and a significant higher loss of IHCs and OHCs in the cochlea at 15–16 months of age compared with age-matched wild-type mice (O'Leary et al., 2017). In a similar vein, clinical studies found a positive correlation between hearing loss and dementia, particularly in AD patients (Lin et al., 2013; Fritze et al., 2016).

The interdependence between cognitive decline and progressive hearing impairment, together with our data on an essential role of BACE1 for hearing, raises concerns regarding the envisaged chronic administration of BACE1 inhibitors to prevent and treat AD. Such reservations appear the more justified as evidence is growing that the influence of BACE1 on synaptic morphology and function as well as on axon guidance is not restricted to development, but continues into adulthood, at least in brain regions rich in BACE1. For example, *Bace1* gene deletion in the adult mouse brain leads to axon guidance defects and disorganization of the mossy fiber tract in the hippocampus (Ou-Yang et al., 2018). Moreover, in a pre-clinical study with 3–4 months old mice, a three-week administration of the orally available and blood–brain barrier permeable BACE1 inhibitor NB-360 reduced spine density of hippocampal pyramidal neurons and impaired synaptic long-term potentiation (Zhu et al., 2018). Similarly, inhibition of BACE1 in adulthood impairs muscle spindle morphology and function (Cheret et al., 2013). Thus, BACE1 functions are not restricted to development, but rather BACE1 is needed in adulthood.

To extrapolate possible side effects of chronic pharmacological BACE1 inhibition in the auditory system of patients, we treated wild-type animals with NB-360 at a dosage and over a time period (6 weeks) that proved sufficient to repair AD pathophysiology in a mouse model (Keskin et al., 2017). Although BACE1 is highly expressed in SGNs and olivocochlear efferent terminals in the cochlea, we did not detect hearing deficits or neuropathological abnormalities in the treated group. Therefore, systemic delivery of this BACE1-inhibitor in adulthood does not compromise hearing. Nevertheless, some caveats must be expressed when translating this finding to the clinical setting. One important issue that remains to be addressed relates to the function of the high levels of BACE1 expression in parts of the mature cochlea. It seems conceivable that BACE1 is important for the long-term maintenance or regeneration of axonal myelination and of proper synaptic function in the cochlea and might be in particular demand in the elderly to slow age-dependent hearing decline. We cannot rule out that such favorable properties of BACE1 might have remained undetected with our treatment protocol or will become only apparent in the inner ear of humans. While the oral route of NB-360 application proved effective in our hands to inhibit BACE1 activity in the mouse brain, indicating good blood–brain barrier permeability, it remains to be determined whether the drug is equally well permeable across the blood–labyrinth barrier, and if so, whether the pharmacokinetic profile is comparable to that in the human cochlea. Until these questions are resolved, clinical trials with BACE1 inhibitors would be well advised to consider regular hearing tests.

## References

Agsten M, Hessler S, Lehnert S, Volk T, Rittger A, Hartmann S, Raab C, Kim DY, Groemer TW, Schwake M, Alzheimer C, Huth T (2015) BACE1 modulates gating of KCNQ1 (Kv7.1) and cardiac delayed rectifier KCNQ1/KCNE1 (IKs). *J Mol Cell Cardiol* 89:335–348.

Bhattacharyya R, Barren C, Kovacs DM (2013) Palmitoylation of amyloid

precursor protein regulates amyloidogenic processing in lipid rafts. *J Neurosci* 33:11169–11183.

Cheret C, Willem M, Fricker FR, Wende H, Wulf-Goldenberg A, Tahirovic S, Nave KA, Saftig P, Haass C, Garratt AN, Bennett DL, Birchmeier C (2013) Bace1 and neuregulin-1 cooperate to control formation and maintenance of muscle spindles. *EMBO J* 32:2015–2028.

Cole SL, Vassar R (2007) The basic biology of BACE1: a key therapeutic target for Alzheimer's disease. *Curr Genomics* 8:509–530.

Dominguez D, Tournoy J, Hartmann D, Huth T, Cryns K, Deforce S, Serneels L, Camacho IE, Marjaux E, Craessaerts K, Roebroek AJ, Schwake M, D'Hooge R, Bach P, Kalinke U, Moechars D, Alzheimer C, Reiss K, Saftig P, De Strooper B (2005) Phenotypic and biochemical analyses of BACE1- and BACE2-deficient mice. *J Biol Chem* 280:30797–30806.

Fritze T, Teipel S, Óvári A, Kilimann I, Witt G, Doblhammer G (2016) Hearing impairment affects dementia incidence: an analysis based on longitudinal health claims data in germany. *PLoS One* 11:e0156876.

Gale JE, Marcotti W, Kennedy HJ, Kros CJ, Richardson GP (2001) FM1–43 dye behaves as a permeant blocker of the hair-cell mechanotransducer channel. *J Neurosci* 21:7013–7025.

Gautam V, D'Avanzo C, Hebisch M, Kovacs DM, Kim DY (2014) BACE1 activity regulates cell surface contactin-2 levels. *Mol Neurodegener* 9:4.

Hansen MR, Vijapurkar U, Koland JG, Green SH (2001) Reciprocal signaling between spiral ganglion neurons and schwann cells involves neuregulin and neurotrophins. *Hear Res* 161:87–98.

Hartmann S, Zheng F, Kyncl MC, Karch S, Voelkl K, Zott B, D'Avanzo C, Lomoio S, Tesco G, Kim DY, Alzheimer C, Huth T (2018)  $\beta$ -secretase BACE1 promotes surface expression and function of Kv3.4 at hippocampal mossy fiber synapses. *J Neurosci* 38:3480–3494.

Hessler S, Zheng F, Hartmann S, Rittger A, Lehnert S, Völkel M, Nissen M, Edelmann E, Saftig P, Schwake M, Huth T, Alzheimer C (2015)  $\beta$ -secretase BACE1 regulates hippocampal and reconstituted M-currents in a  $\beta$ -subunit-like fashion. *J Neurosci* 35:3298–3311.

Huang G, Santos-Sacchi J (1993) Mapping the distribution of the outer hair cell motility voltage sensor by electrical amputation. *Biophys J* 65:2228–2236.

Hu X, Hicks CW, He W, Wong P, Macklin WB, Trapp BD, Yan R (2006) Bace1 modulates myelination in the central and peripheral nervous system. *Nat Neurosci* 9:1520–1525.

Hu X, Fan Q, Hou H, Yan R (2016) Neurological dysfunctions associated with altered BACE1-dependent neuregulin-1 signaling. *J Neurochem* 136:234–249.

Jentsch TJ (2000) Neuronal KCNQ potassium channels: physiology and role in disease. *Nat Rev Neurosci* 1:21–30.

Jin D, Ohlemiller KK, Lei D, Dong E, Role L, Ryugo DK, Bao J (2011) Age-related neuronal loss in the cochlea is not delayed by synaptic modulation. *Neurobiol Aging* 32:2321.e13–e23.

Johnson SL, Beurig M, Marcotti W, Fettiplace R (2011) Prestin-driven cochlear amplification is not limited by the outer hair cell membrane time constant. *Neuron* 70:1143–1154.

Kandalepas PC, Vassar R (2014) The normal and pathologic roles of the Alzheimer's  $\beta$ -secretase, BACE1. *Curr Alzheimer Res* 11:441–449.

Kane KL, Longo-Guess CM, Gagnon LH, Ding D, Salvi RJ, Johnson KR (2012) Genetic background effects on age-related hearing loss associated with *Cdh23* variants in mice. *Hear Res* 283:80–88.

Keskin AD, Kekuš M, Adelsberger H, Neumann U, Shimshek DR, Song B, Zott B, Peng T, Förstl H, Staufienbiel M, Nelken I, Sakmann B, Konnerth A, Busche MA (2017) BACE inhibition-dependent repair of Alzheimer's pathophysiology. *Proc Natl Acad Sci U S A* 114:8631–8636.

Kharkovets T, Dedek K, Maier H, Schweizer M, Khimich D, Nouvian R, Vardanyan V, Leuwer R, Moser T, Jentsch TJ (2006) Mice with altered KCNQ4 K<sup>+</sup> channels implicate sensory outer hair cells in human progressive deafness. *EMBO J* 25:642–652.

Khimich D, Nouvian R, Pujol R, Tom Dieck S, Egner A, Gundelfinger ED, Moser T (2005) Hair cell synaptic ribbons are essential for synchronous auditory signalling. *Nature* 434:889–894.

Kuhn PH, Koroniak K, Hogg S, Colombo A, Zeitschel U, Willem M, Volbracht C, Schepers U, Imhof A, Hoffmeister A, Haass C, Roßner S, Bräse S, Lichtenthaler SF (2012) Secretome protein enrichment identifies physiological BACE1 protease substrates in neurons. *EMBO J* 31:3157–3168.

Kujawa SG, Liberman MC (2009) Adding insult to injury: cochlear nerve degeneration after “temporary” noise-induced hearing loss. *J Neurosci* 29:14077–14085.

- Kurtz A, Zimmer A, Schnütgen F, Brüning G, Spener F, Müller T (1994) The expression pattern of a novel gene encoding brain-fatty acid binding protein correlates with neuronal and glial cell development. *Development* 120:2637–2649.
- Lee YI, Li Y, Mikesch M, Smith I, Nave KA, Schwab MH, Thompson WJ (2016) Neuregulin1 displayed on motor axons regulates terminal schwann cell-mediated synapse elimination at developing neuromuscular junctions. *Proc Natl Acad Sci U S A* 113:E479–E487.
- Lehnert S, Hartmann S, Hessler S, Adelsberger H, Huth T, Alzheimer C (2016) Ion channel regulation by  $\beta$ -secretase BACE1 - enzymatic and non-enzymatic effects beyond Alzheimer's disease. *Channels* 10:365–378.
- Leitner MG, Halaszovich CR, Oliver D (2011) Aminoglycosides inhibit KCNQ4 channels in cochlear outer hair cells via depletion of phosphatidylinositol(4,5)bisphosphate. *Mol Pharmacol* 79:51–60.
- Leitner MG, Feuer A, Ebers O, Schreiber DN, Halaszovich CR, Oliver D (2012) Restoration of ion channel function in deafness-causing KCNQ4 mutants by synthetic channel openers. *Br J Pharmacol* 165:2244–2259.
- Li L (2003) Isoform-specific knock-out of the Neuregulin-1 gene. Inaugural-Dissertation zur Erlangung des Doktorgrades der Mathematisch-Naturwissenschaftlichen Fakultät der Universität zu Köln. Available at [https://pdfs.semanticscholar.org/f9f6/625ce08de27edf1251a8c304a4823c1ff175.pdf?\\_ga=2.261360073.592192026.1572018637-1974222216.1552652373](https://pdfs.semanticscholar.org/f9f6/625ce08de27edf1251a8c304a4823c1ff175.pdf?_ga=2.261360073.592192026.1572018637-1974222216.1552652373).
- Lin FR, Ph MDD, Yaffe K, Xia J, Xue QL, Ph D, Harris TB, Purchase-Helzner E, Satterfield S, Ayonayon HN, Ferrucci L, Simonsick EM (2013) Hearing loss and cognitive decline in older adults. *JAMA Intern Med* 173:293–299.
- Lin HW, Furman AC, Kujawa SG, Liberman MC (2011) Primary neural degeneration in the guinea pig cochlea after reversible noise-induced threshold shift. *J Assoc Res Otolaryngol* 12:605–616.
- Long P, Wan G, Roberts MT, Corfas G (2018) Myelin development, plasticity, and pathology in the auditory system. *Dev Neurobiol* 78:80–92.
- Maljevic S, Wuttke TV, Seebohm G, Lerche H (2010) KV7 channelopathies. *Pflugers Arch* 460:277–288.
- Meyers JR, MacDonald RB, Duggan A, Lenzi D, Standaert DG, Corwin JT, Corey DP (2003) Lighting up the senses: FM1–43 loading of sensory cells through nonselective ion channels. *J Neurosci* 23:4054–4065.
- Michailov GV, Sereda MW, Brinkmann BG, Fischer TM, Haug B, Birchmeier C, Role L, Lai C, Schwab MH, Nave KA (2004) Axonal neuregulin-1 regulates myelin sheath thickness. *Science* 304:700–703.
- Morley BJ (1998) ARIA is heavily expressed in rat peripheral auditory and vestibular ganglia. *Brain Res Mol Brain Res* 54:170–174.
- Nayagam BA, Muniak MA, Ryugo DK (2011) The spiral ganglion: connecting the peripheral and central auditory systems. *Hear Res* 278:2–20.
- Neumann U, Rueeger H, Machauer R, Veenstra SJ, Lueoend RM, Tintnot-Blomley M, Laue G, Beltz K, Vogt B, Schmid P, Friauff W, Shimshek DR, Staufenberg M, Jacobson LH (2015) A novel BACE inhibitor NB-360 shows a superior pharmacological profile and robust reduction of amyloid- $\beta$  and neuroinflammation in APP transgenic mice. *Mol Neurodegener* 10:44.
- O'Leary TP, Shin S, Fertan E, Dingle RN, Almklass A, Gunn RK, Yu Z, Wang J, Brown RE (2017) Reduced acoustic startle response and peripheral hearing loss in the 5xFAD mouse model of Alzheimer's disease. *Genes Brain Behav* 16:554–563.
- Oliver D, Fakler B (1999) Expression density and functional characteristics of the outer hair cell motor protein are regulated during postnatal development in rat. *J Physiol* 519:791–800.
- Oliver D, Knipper M, Derst C, Fakler B (2003) Resting potential and submembrane calcium concentration of inner hair cells in the isolated mouse cochlea are set by KCNQ-type potassium channels. *J Neurosci* 23:2141–2149.
- Ou-Yang MH, Kurz JE, Nomura T, Popovic J, Rajapaksha TW, Dong H, Contractor A, Chetkovich DM, Tourtellotte WG, Vassar R (2018) Axonal organization defects in the hippocampus of adult conditional BACE1 knockout mice. *Sci Transl Med* 10:eaa05620.
- Ray B, Roy TS, Wadhwa S, Roy KK (2005) Development of the human fetal cochlear nerve: a morphometric study. *Hear Res* 202:74–86.
- Sachse CC, Kim YH, Agsten M, Huth T, Alzheimer C, Kovacs DM, Kim DY (2013) BACE1 and presenilin/ $\gamma$ -secretase regulate proteolytic processing of KCNE1 and 2, auxiliary subunits of voltage-gated potassium channels. *FASEB J* 27:2458–2467.
- Savonenko AV, Melnikova T, Laird FM, Stewart KA, Price DL, Wong PC (2008) Alteration of BACE1-dependent NRG1/ErbB4 signaling and schizophrenia-like phenotypes in BACE1-null mice. *Proc Natl Acad Sci U S A* 105:5585–5590.
- Schindelin J, Arganda-Carreras I, Frise E, Kaynig V, Longair M, Pietzsch T, Preibisch S, Rueden C, Saalfeld S, Schmid B, Tinevez JY, White DJ, Hartenstein V, Eliceiri K, Tomancak P, Cardona A (2012) Fiji: an open-source platform for biological-image analysis. *Nat Methods* 9:676–682.
- Shen J, Scheffer DI, Kwan KY, Corey DP (2015) SHIELD: an integrative gene expression database for inner ear research. *Database (Oxford)* 2015:bav071.
- Shimshek DR, Jacobson LH, Kolly C, Zamurovic N, Balavenkatraman KK, Morawiec L, Kreutzer R, Schelle J, Jucker M, Bertschi B, Theil D, Heier A, Bigot K, Beltz K, Machauer R, Brzak I, Perrot L, Neumann U (2016) Pharmacological BACE1 and BACE2 inhibition induces hair depigmentation by inhibiting PMEL17 processing in mice. *Sci Rep* 6:21917.
- Stankovic K, Rio C, Xia A, Sugawara M, Adams JC, Liberman MC, Corfas G (2004) Survival of adult spiral ganglion neurons requires erbB receptor signaling in the inner ear. *J Neurosci* 24:8651–8661.
- Taveggia C, Zanazzi G, Petrylak A, Yano H, Rosenbluth J, Einheber S, Xu X, Esper RM, Loeb JA, Shrager P, Chao MV, Falls DL, Role L, Salzer JL (2005) Neuregulin-1 type III determines the ensheathment fate of axons. *Neuron* 47:681–694.
- Vassar R, Bennett BD, Babu-Khan S, Kahn S, Mendiaz EA, Denis P, Teplow DB, Ross S, Amarante P, Loeloff R, Luo Y, Fisher S, Fuller J, Edenson S, Lile J, Jarosinski MA, Biere AL, Curran E, Burgess T, Louis JC et al. (1999) Beta-secretase cleavage of Alzheimer's amyloid precursor protein by the transmembrane aspartic protease BACE. *Science* 286:735–741.
- Velanac V, Unterbarnscheidt T, Hinrichs W, Gummert MN, Fischer TM, Rossner MJ, Trimarco A, Brivio V, Taveggia C, Willem M, Haass C, Möbius W, Nave KA, Schwab MH (2012) Bace1 processing of NRG1 type III produces a myelin-inducing signal but is not essential for the stimulation of myelination. *Glia* 60:203–217.
- Vogl C, Cooper BH, Neef J, Wojcik SM, Reim K, Reisinger E, Brose N, Rhee JS, Moser T, Wichmann C (2015) Unconventional molecular regulation of synaptic vesicle replenishment in cochlear inner hair cells. *J Cell Sci* 128:638–644.
- Vogl C, Butola T, Haag N, Hausrat TJ, Leitner MG, Moutschen M, Lefebvre PP, Speckmann C, Garrett L, Becker L, Fuchs H, Hrabe de Angelis M, Nietzsche S, Kessels MM, Oliver D, Kneussel M, Kilimann MW, Strenzke N (2017) The BEACH protein LRBA is required for hair bundle maintenance in cochlear hair cells and for hearing. *EMBO Rep* 18:2015–2029.
- Wan G, Corfas G (2017) Transient auditory nerve demyelination as a new mechanism for hidden hearing loss. *Nat Commun* 8:14487.
- Weber M, Wu T, Meilandt WJ, Dominguez SL, Solanoy HO, Maloney JA, Ngu H, Baca M, Kung C, Lima L, Earr TK, Fleck D, Shields SD, Forrest WF, Foreman O, Warming S, Watts RJ, Scarce-Lewis K (2017) BACE1 across species: a comparison of the in vivo consequences of BACE1 deletion in mice and rats. *Sci Rep* 7:44249.
- Wilke BU, Lindner M, Greifenberg L, Albus A, Kronimus Y, Bünemann M, Leitner MG, Oliver D (2014) Diacylglycerol mediates regulation of TASK potassium channels by Gq-coupled receptors. *Nat Commun* 5:5540.
- Willem M, Garratt AN, Novak B, Citron M, Kaufmann S, Rittger A, DeStrooper B, Saftig P, Birchmeier C, Haass C (2006) Control of peripheral nerve myelination by the beta-secretase BACE1. *Science* 314:664–666.
- Yan R, Bienkowski MJ, Shuck ME, Miao H, Tory MC, Pauley AM, Brashier JR, Stratman NC, Mathews WR, Buhl AE, Carter DB, Tomasselli AG, Parodi LA, Heinrikson RG, Gurney ME (1999) Membrane-anchored aspartyl protease with Alzheimer's disease beta-secretase activity. *Nature* 402:533–537.
- Zhou L, Barão S, Laga M, Bockstael K, Borgers M, Gijzen H, Annaert W, Moechars D, Mercken M, Gevaert K, Gevaert K, De Strooper B (2012) The neural cell adhesion molecules L1 and CHL1 are cleaved by BACE1 protease in vivo. *J Biol Chem* 287:25927–25940.
- Zhou R, Assouline JG, Abbas PJ, Messing A, Gantz BJ (1995) Anatomical and physiological measures of auditory system in mice with peripheral myelin deficiency. *Hear Res* 88:87–97.
- Zhu K, Xiang X, Filser S, Marinković P, Dorostkar MM, Crux S, Neumann U, Shimshek DR, Rammes G, Haass C, Lichtenthaler SF, Gunnarsen JM, Herms J (2018) Beta-site amyloid precursor protein cleaving enzyme 1 inhibition impairs synaptic plasticity via seizure protein 6. *Biol Psychiatry* 83:428–437.



# Inverse Modulation of Neuronal $K_v12.1$ and $K_v11.1$ Channels by 4-Aminopyridine and NS1643

Marlen Dierich<sup>1†</sup>, Saskia Evers<sup>1†</sup>, Bettina U. Wilke<sup>1</sup> and Michael G. Leitner<sup>1,2\*</sup>

<sup>1</sup> Department of Neurophysiology, Institute of Physiology and Pathophysiology, Philipps University of Marburg, Marburg, Germany, <sup>2</sup> Division of Physiology, Department of Physiology and Medical Physics, Innsbruck Medical University, Innsbruck, Austria

## OPEN ACCESS

### Edited by:

Alexandre Mouro, Université Pierre et Marie Curie, France

### Reviewed by:

Marco Martina, Northwestern University, United States  
Norelle Christine Wildburger, Washington University in St. Louis, United States

### \*Correspondence:

Michael G. Leitner  
Michael.Leitner@i-med.ac.at

<sup>†</sup>These authors have contributed equally to this work.

**Received:** 10 November 2017

**Accepted:** 09 January 2018

**Published:** 30 January 2018

### Citation:

Dierich M, Evers S, Wilke BU and Leitner MG (2018) Inverse Modulation of Neuronal  $K_v12.1$  and  $K_v11.1$  Channels by 4-Aminopyridine and NS1643. *Front. Mol. Neurosci.* 11:11. doi: 10.3389/fnmol.2018.00011

The three members of the *ether-à-go-go-gene*-like (Elk;  $K_v12.1$ - $K_v12.3$ ) family of voltage-gated  $K^+$  channels are predominantly expressed in neurons, but only little information is available on their physiological relevance. It was shown that  $K_v12.2$  channels modulate excitability of hippocampal neurons, but no native current could be attributed to  $K_v12.1$  and  $K_v12.3$  subunits yet. This may appear somewhat surprising, given high expression of their mRNA transcripts in several brain areas. Native  $K_v12$  currents may have been overlooked so far due to limited knowledge on their biophysical properties and lack of specific pharmacology. Except for  $K_v12.2$ , appropriate genetically modified mouse models have not been described; therefore, identification of  $K_v12$ -mediated currents in native cell types must rely on characterization of unique properties of the channels. We focused on recombinant human  $K_v12.1$  to identify distinct properties of these channels. We found that  $K_v12.1$  channels exhibited significant mode shift of activation, i.e., stabilization of the voltage sensor domain in a “relaxed” open state after prolonged channel activation. This mode shift manifested by a slowing of deactivation and, most prominently, a significant shift of voltage dependence to hyperpolarized potentials. In contrast to related  $K_v11.1$ , mode shift was not sensitive to extracellular  $Na^+$ , which allowed for discrimination between these isoforms. Sensitivity of  $K_v12.1$  and  $K_v11.1$  to the broad-spectrum  $K^+$  antagonist 4-aminopyridine was similar. However, 4-AP strongly activated  $K_v12.1$  channels, but it was an inhibitor of  $K_v11$  channels. Interestingly, the agonist of  $K_v11$  channels NS1643 also differentially modulated the activity of these channels, i.e., NS1643 activated  $K_v11.1$ , but strongly inhibited  $K_v12.1$  channels. Thus, these closely related channels are distinguished by inverse pharmacological profiles. In summary, we identified unique biophysical and pharmacological properties of  $K_v12.1$  channels and established straightforward experimental protocols to characterize  $K_v12.1$ -mediated currents. Identification of currents in native cell types with mode shift that are activated through 4-AP and inhibited by NS1643 can provide strong evidence for contribution of  $K_v12.1$  to whole cell currents.

**Keywords:**  $K_v10$ ,  $K_v11$ ,  $K_v12$ , HERG, mode shift, voltage-dependent potentiation, 4-aminopyridine, NS1643

## INTRODUCTION

The ether-à-go-go (Eag) superfamily of voltage-gated  $K^+$  channels comprises three evolutionary conserved families that share high sequence homology: Ether-à-go-go (Eag;  $K_v10$ ), ether-à-go-go-related-gene (Erg;  $K_v11$ ) and ether-à-go-go-gene-like (Elk;  $K_v12$ ) channels (Bauer and Schwarz, 2001). The best-studied member,  $K_v11.1$  (the human isoform is referred to as HERG channel) mediates rapidly activating  $K^+$  current  $I_{Kr}$  in cardiac myocytes determining heart action potential duration (Sanguinetti et al., 1995). Accordingly, loss of  $K_v11.1$  channel function through mutations or drug treatment causes cardiac arrhythmia and sudden death in humans (Curran et al., 1995; Sanguinetti et al., 1995; Trudeau et al., 1995).  $K_v11$  channels also mediate important  $K^+$  currents in neurons of the auditory brainstem (Hardman and Forsythe, 2009), the olfactory bulb (Hirdes et al., 2009) and the midbrain (Ji et al., 2012).  $K_v10.1$  channels regulate cell cycle progression and proliferation (Sanchez et al., 2016; Urrego et al., 2016), and are frequently overexpressed in human cancers with poor prognosis (Pardo and Stuhmer, 2014).  $K_v10.1$  channel mutations cause developmental disorders and epilepsy (Kortum et al., 2015; Simons et al., 2015).

In contrast to  $K_v10$  and  $K_v11$  channels, only little information on physiological relevance is available for the three members of the  $K_v12$  family that are expressed predominantly in neurons (Engeland et al., 1998; Shi et al., 1998; Miyake et al., 1999; Trudeau et al., 1999; Saganich et al., 2001; Zou et al., 2003).  $K_v12.2$  channels regulate excitability in pyramidal neurons of hippocampus in mice (Zhang et al., 2010), but no native current component could be attributed to  $K_v12.1$  and  $K_v12.3$  subunits despite expression of their mRNA transcripts in several brain areas (Shi et al., 1998; Miyake et al., 1999; Saganich et al., 2001; Zou et al., 2003). We consider that  $K_v12.1/K_v12.3$ -mediated currents in neurons were overlooked so far due to insufficient knowledge on biophysical properties and lack of specific pharmacological tools.

Recently, it was shown that  $K_v12.1$  channels exhibit mode shift of activation (also termed pre-pulse facilitation or voltage-dependent potentiation) (Li et al., 2015; Dai and Zagotta, 2017). Mode shift denotes time-dependent stabilization of the voltage sensor domain in a “relaxed” open state after prolonged channel activation through depolarized (conditioning) membrane potentials (Bezanilla et al., 1982; Villalba-Galea et al., 2008). It manifests by slowing of deactivation and a shift of voltage dependence to hyperpolarized potentials (Li et al., 2015; Dai and Zagotta, 2017). Accordingly, when measured with routine voltage clamp protocols (e.g., holding potentials of  $-60$  mV) human  $K_v12.1$  channels mediate “conventional”  $K^+$  currents that activate similar to many other  $K_v$  channels with voltages at half-maximal activation of around  $-30$  mV (c.f. **Figure 1**) (Li et al., 2015). These currents could easily go unnoticed in cell types expressing different endogenous  $K^+$  currents. Taking into account their mode shift, appropriate voltage protocols (e.g., depolarized holding potentials) may uncover  $K_v12$ -mediated currents. However, it remains to be explored whether mode shift can be detected in cells expressing various  $K^+$  currents and whether it may be employed to

identify native  $K_v12.1$  channels. Mode shift is not an exclusive feature of  $K_v12.1$  channels, but has been demonstrated also for voltage-gated  $Na^+$  channels (Bezanilla et al., 1982), HCN (Mannikko et al., 2005; Bruening-Wright and Larsson, 2007), *Shaker* (Olcese et al., 1997; Tilegenova et al., 2017), and  $K_v11.1$  (Erg1) channels (Piper et al., 2003; Tan et al., 2012; Goodchild et al., 2015). Nevertheless, it may constitute a prominent hallmark to distinguish  $K_v12$  channels from other  $K^+$  current components in native tissue.

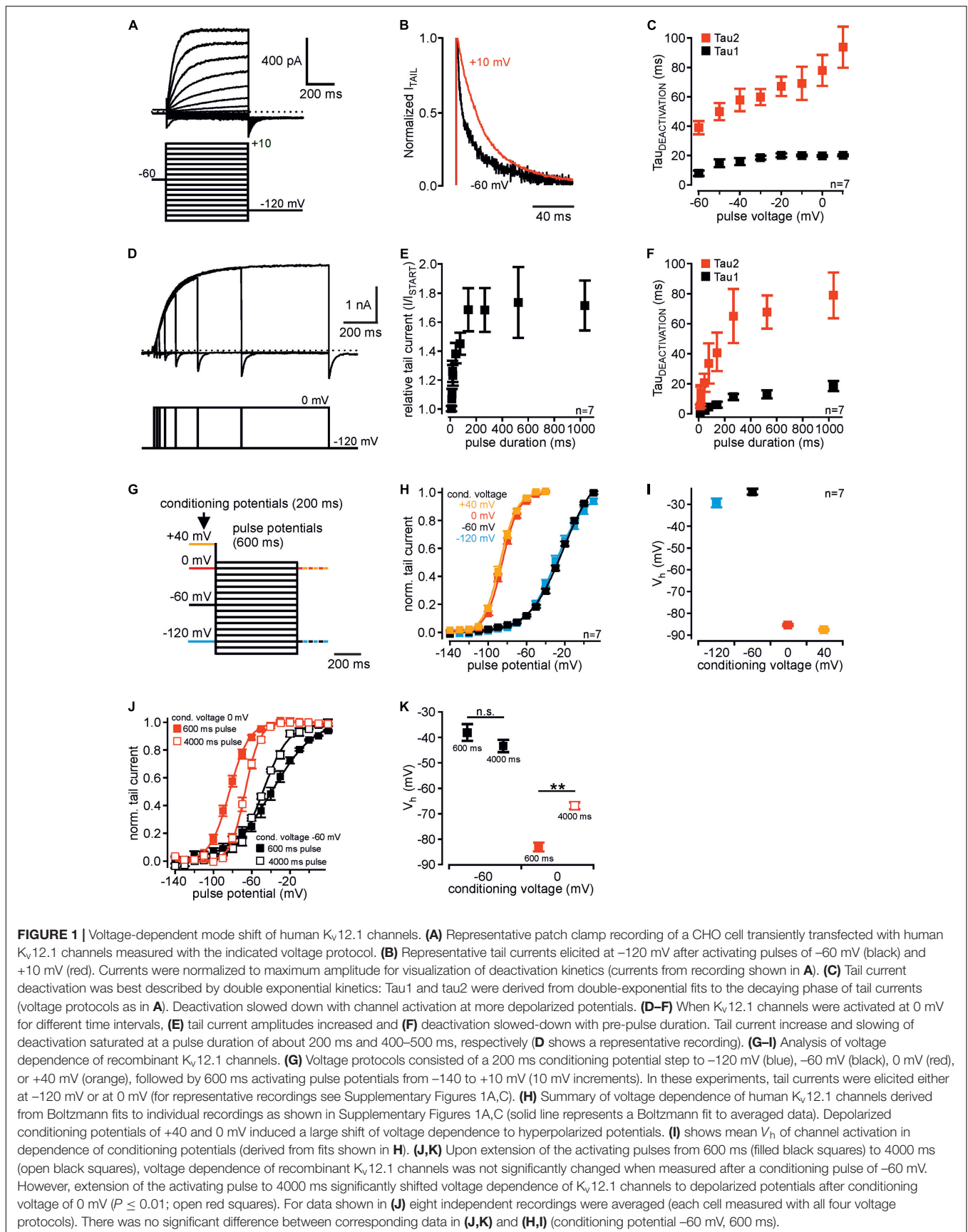
Here we describe biophysical and pharmacological properties of  $K_v12.1$  channels and demonstrate straightforward experimental protocols that may be employed to identify  $K_v12$  currents in neurons. We show, that these properties allowed detection of  $K_v12.1$ -mediated currents in cells expressing a variety of different  $K^+$  channels. Our findings may be utilized to identify physiological roles of  $K_v12.1$  channels.

## RESULTS

### Voltage-Dependent Mode Shift of Human $K_v12.1$ Channels

Mode shift of human  $K_v12.1$  channels was recently demonstrated (Li et al., 2015), but a detailed characterization is currently not available. In order to identify exclusive properties of human  $K_v12.1$  channels, we thus set out with detailed biophysical analysis of these channels in an overexpression system. In CHO cells, activation of  $K_v12.1$  channels through depolarizing voltage steps produced robust outwardly rectifying currents (**Figure 1A**) (Zou et al., 2003; Li et al., 2015; Dai and Zagotta, 2017). Channel deactivation at hyperpolarized potentials was best described by double exponential kinetics, and deactivation slowed down with more depolarized pre-potentials (**Figures 1B,C**). When we activated  $K_v12.1$  channels at  $0$  mV for different time intervals, tail current amplitudes increased (**Figures 1D,E**) and deactivation slowed down with the duration of the pre-pulse (**Figure 1F**). Tail current increase and slowing of deactivation saturated at a pulse duration of about  $200$  ms and  $400$ – $500$  ms, respectively.

We then analyzed voltage dependence of human  $K_v12.1$  channels with voltage protocols established previously to study mode shift of related  $K_v11.1$  (Tan et al., 2012). We applied depolarizing holding potentials (conditioning potentials;  $200$  ms) before a series of activating voltage steps (pulse potentials from  $-140$  mV to  $+10$  mV;  $600$  ms) (**Figure 1G** and Supplementary Figures 1A–C). To minimize time intervals at hyperpolarized potentials that may counteract mode shift (c.f. Villalba-Galea, 2017), we at start recorded tail currents at correspondingly depolarized potentials (**Figures 1G–I**). In these experiments, amplitudes of  $K_v12.1$ -mediated outward currents were similar irrespective of conditioning potentials. This indicated that comparable steady-state channel activation was reached with all voltage protocols (Supplementary Figures 1A–C). After a conditioning potential of  $-60$  mV, voltage dependence of  $K_v12.1$  channels also did not change relevantly upon extension of the activating steps to  $4000$  ms (**Figures 1J,K**). This additionally demonstrated that steady-state activation of  $K_v12.1$  channels was already reached by activating pulses as short as  $600$  ms.



For 600 ms activating pulses, half-maximal voltages of activation ( $V_h$ ) were  $-29.3 \pm 2.3$  mV and  $-24.1 \pm 1.6$  mV for negative conditioning potentials of  $-120$  mV or  $-60$  mV, respectively ( $n = 7$ ; 600 ms activating pulses; **Figures 1H,I**). When cells were held at depolarized conditioning pulses of  $0$  mV or  $+40$  mV,  $V_h$  was  $-85.3 \pm 0.9$  mV and  $-87.6 \pm 0.8$  mV, respectively (**Figures 1H,I**; 600 ms activating pulses). In these experiments, slope factors derived from Boltzmann fits to the recordings changed from  $-15.7 \pm 0.7$  mV (conditioning pulse of  $-120$  mV) and  $-16.4 \pm 0.9$  mV ( $-60$  mV) to  $-8.6 \pm 0.1$  mV ( $0$  mV) and  $-8.9 \pm 0.6$  ( $+40$  mV) ( $n = 7$ ; Supplementary Figure 1D; 600 ms activating pulses). Accordingly, depolarizing conditioning potentials induced a large shift of voltage dependence by about  $-60$  mV, and the full shift occurred across a potential range of  $60$  mV (between holding potentials of  $-60$  and  $0$  mV). In analogous experiments, the same conditioning voltages shifted  $V_h$  of related  $K_v11.1$  channels from  $-6.8 \pm 4.4$  mV (conditioning voltage  $-60$  mV) to  $-62.4 \pm 1.5$  (conditioning voltage  $+40$  mV;  $n = 7$ ; **Figures 2A,B**), consistent with a previous report (Tan et al., 2012).

We next tested whether mode shift was sensitive to the employed voltage protocol. Therefore, we again applied 200 ms depolarized conditioning pulses, but this time we extended the activating pulses to 4000 ms (**Figures 1J,K**). When in these experiments cells were held at conditioning pulses of  $-60$  and  $0$  mV,  $V_h$  was  $-43.3 \pm 2.5$  mV and  $-66.8 \pm 1.5$  mV, respectively (**Figures 1J,K**). Thus, mode shift of  $K_v12.1$  channels was readily induced also when activating the channels for 4000 ms. However, the extent of mode shift was significantly reduced in these experiments compared to experiments with 600 ms activating pulses (**Figure 1K**;  $P \geq 0.01$ ), i.e., increased time intervals at hyperpolarized holding potentials during these protocols presumably counteracted development of mode shift. Similarly, the extent of mode shift was reduced when we activated channels for 600 ms after conditioning pulses of  $-60$  and  $0$  mV, but recorded tail currents at hyperpolarized holding potentials ( $-120$  mV; Supplementary Figures 1E,F), i.e., we introduced additional hyperpolarizing potentials after every activating pulse. Thus, also in these experiments hyperpolarizing holding potentials between the conditioning pulses reduced the expression of mode shift.

Taken together, human  $K_v12.1$  channels exhibited significant voltage-dependent mode shift that in response to depolarized holding potentials manifested by slowed channel deactivation and by a large hyperpolarizing shift of voltage dependence. This mode shift of  $K_v12.1$  channels can be induced robustly employing different voltage protocols, but the extent of mode shift significantly varies with duration of hyperpolarized holding potentials.

## In Contrast to $K_v11.1$ , $K_v12.1$ Channels Are Insensitive to Extracellular $Na^+$

Inhibition of  $K_v11$  channels by extracellular  $Na^+$  is well established (Numaguchi et al., 2000; Sturm et al., 2005) and a hallmark used to identify  $K_v11$ -mediated currents in neurons (e.g., Hardman and Forsythe, 2009). In control

experiments, replacement of extracellular  $Na^+$  with NMDG without altering extracellular  $K^+$  concentration slightly increased  $K_v11.1$ -mediated outward currents (**Figure 2A**), as previously reported (Numaguchi et al., 2000). Upon removal of extracellular  $Na^+$ , activation voltage range of  $K_v11.1$  channels conditioned at  $-60$  and  $+40$  mV shifted to hyperpolarized potentials by  $-24.4 \pm 1.5$  mV and  $-13.9 \pm 0.7$  mV, respectively ( $n = 7$ ; **Figures 2B,C**). Accordingly, overall mode shift of voltage dependence was attenuated from  $-55.7 \pm 4.4$  mV under control conditions to  $-45.1 \pm 3.5$  mV in absence of extracellular  $Na^+$  ( $n = 7$ ;  $P \leq 0.05$ ). We then tested whether related  $K_v12.1$  channels also exhibited such  $Na^+$  sensitivity. We found that neither current amplitudes nor voltage dependence of  $K_v12.1$  channels were affected by removal of extracellular  $Na^+$  (**Figures 2D–F**). Consequently, the extent of mode shift was also insensitive to changes of the  $Na^+$  concentration. To conclude, despite the high similarity in mode shift behavior, the absence of  $Na^+$  sensitivity in  $K_v12.1$  channels distinguishes  $K_v11.1$ -mediated currents from  $K_v12.1$ .

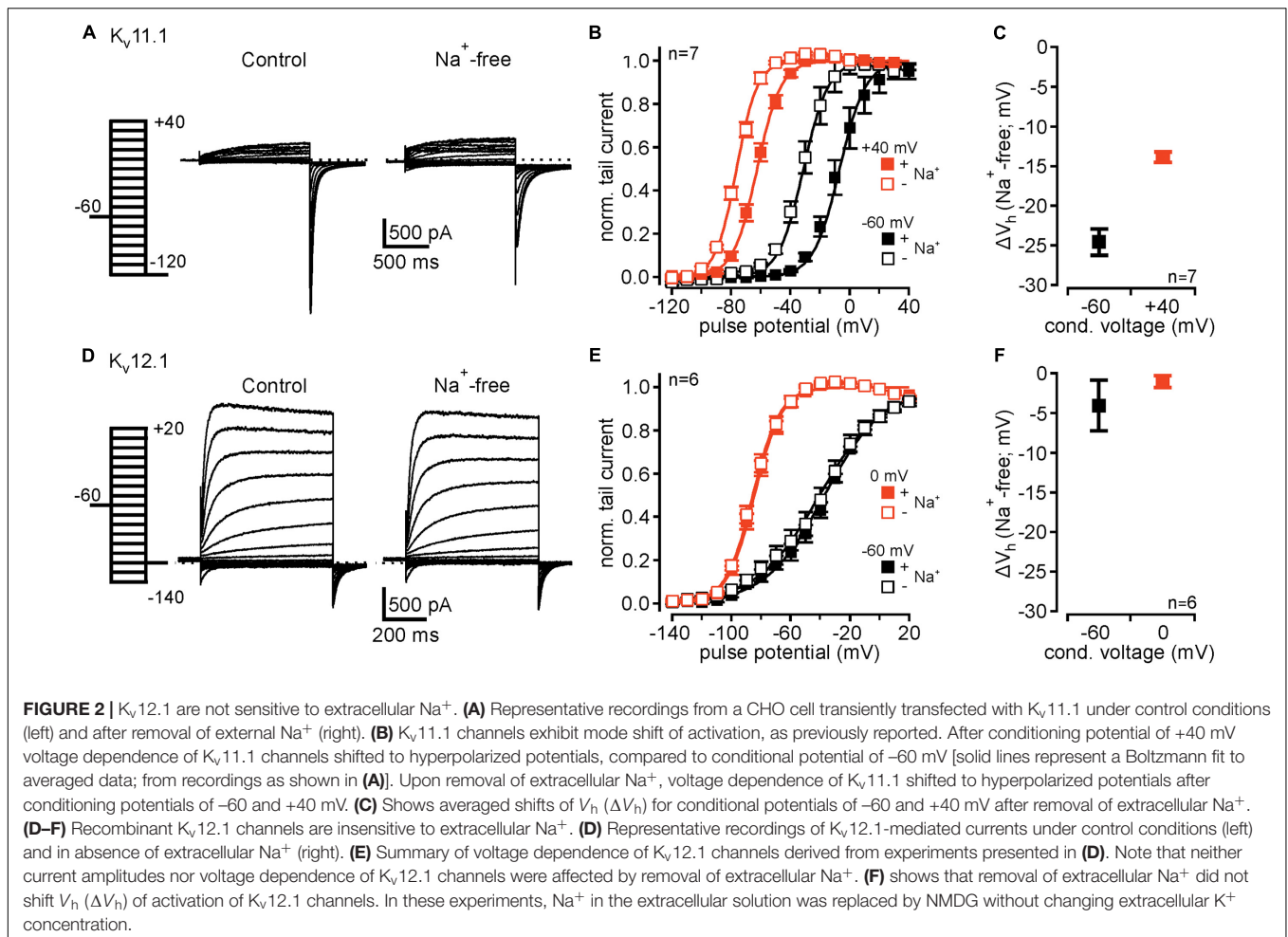
## $K_v12.1$ Channels Are Not Sensitive to $K_v$ Channel Blockers E-4031, XE991, and TEA

We then evaluated whether  $K_v12.1$  channels were sensitive to channel inhibitors that are widely used to attribute neuronal  $K^+$  currents to particular channel families. At concentrations generally applied to inhibit established target channels, human  $K_v12.1$  channels were insensitive to both E-4031 ( $20 \mu\text{M}$ ), a specific inhibitor of  $K_v11$  channels (Supplementary Figures 2A,B) (Trudeau et al., 1995), and XE991 ( $10 \mu\text{M}$ ), a specific antagonist of neuronal  $K_v7$  (KCNQ) channels (Supplementary Figures 2D,E) (Wang et al., 1998).  $K_v12.1$ -mediated currents were also insensitive to E-4031 and XE991 concentrations up to  $100 \mu\text{M}$  (Supplementary Figures 2C,F).  $K_v12.1$  channels also were not affected by the broad-spectrum  $K^+$  channel inhibitor tetraethylammonium (TEA) at a concentration that completely inhibited  $K_v7.2$  channels ( $5 \text{ mM}$ ; Supplementary Figures 2G,H) (Hadley et al., 2000). However,  $K_v12.1$  channels were slightly inhibited by  $50$  and  $100 \text{ mM}$  TEA ( $I_{50\text{mM TEA}}/I_{\text{Start}} = 0.90 \pm 0.01$ ;  $I_{100\text{mM TEA}}/I_{\text{Start}} = 0.83 \pm 0.01$ ;  $n = 9$ ; Supplementary Figure 2I). Of note, low sensitivity of  $K_v12.1$  channels to E-4031 and TEA has been shown in an early report (Shi et al., 1998). In summary, E-4031, XE991 and TEA cannot be used to inhibit  $K_v12.1$  channels in native tissue, but may be used to isolate  $K_v12.1$  channel activity through inhibition of other  $K^+$  channels.

## The Broad-Spectrum $K^+$ Channel Antagonist 4-Aminopyridine (4-AP) Activates $K_v12.1$

We then tested whether human  $K_v12.1$  channels were sensitive to 4-AP, another established antagonist of several  $K_v$  families (Gutman et al., 2005). Surprisingly, 4-AP at a concentration well in the range often used to isolate neuronal  $K^+$  currents ( $3 \text{ mM}$ ; e.g., Marcotti et al., 2003) increased  $K_v12.1$ -mediated steady-state and tail currents within seconds (**Figures 3A–C**). Current potentiation was the same for conditioning pulses of  $-60$  and





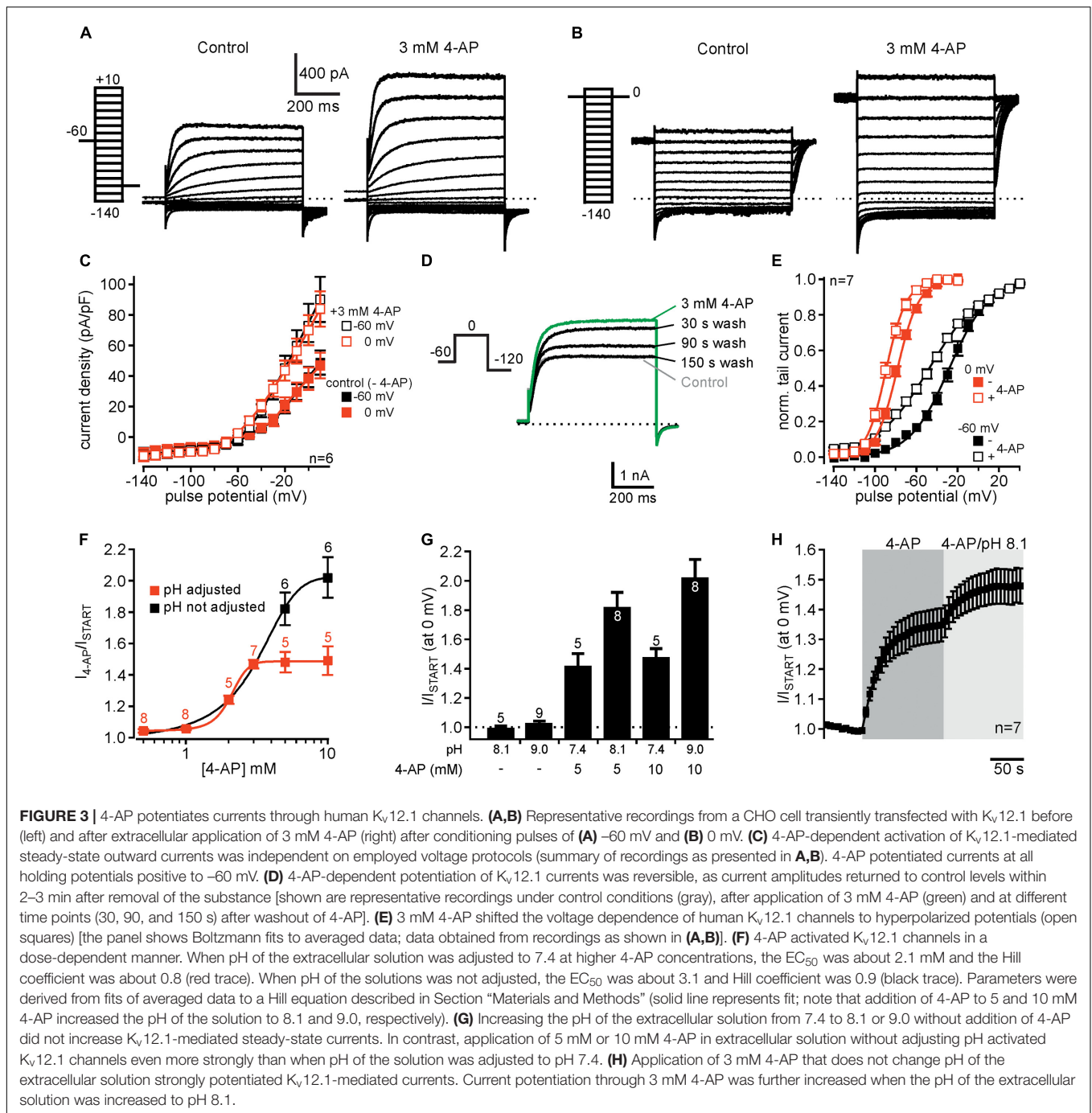
0 mV, and 4-AP potentiated currents at all holding potentials positive to -60 mV (**Figure 3C**). 4-AP-dependent current increase was reversible within 2–3 min after washout of the drug (**Figure 3D**). 4-AP (3 mM) not only potentiated  $K_v12.1$ -mediated currents, but also significantly shifted the voltage dependence of  $K_v12.1$  channels to hyperpolarized potentials (**Figure 3E**). Compared to control recordings measured before application of the substance, 3 mM 4-AP shifted  $V_h$  by  $-19.7 \pm 1.7$  mV ( $n = 7$ ;  $P \leq 0.001$ ) and by  $-10.4 \pm 1.5$  mV ( $n = 7$ ;  $P \leq 0.001$ ) after condition voltage pulses of -60 and 0 mV, respectively. Thus, the shift of  $V_h$  was significantly more pronounced for currents conditioned at -60 mV ( $P \leq 0.01$ ; c.f. **Figure 3E**).

We then analyzed the dose-response relationship of 4-AP action on  $K_v12.1$  channels. As 5 and 10 mM 4-AP increased pH of the solution to about 8.1 and 9.0, respectively, we adjusted pH of these solutions to 7.4 after addition of 4-AP. Of note, 3 mM 4-AP or lower 4-AP concentrations did not alter the pH of the solution relevantly and thus no adjustment of pH was necessary. Under these experimental conditions, 4-AP potentiated  $K_v12.1$  currents in a concentration-dependent manner with an  $EC_{50}$  of about 2.1 and a Hill coefficient of about 0.8 (**Figure 3F**, red trace). In contrast,  $K_v11.1$  channels were inhibited by 4-AP with an  $IC_{50}$  of approximately 2.6 mM and a Hill coefficient

of about 0.7 (Supplementary Figure 3), consistent with previous reports (e.g., Ridley et al., 2003). Thus, despite inverse effects of 4-AP on  $K_v12.1$  and  $K_v11.1$ , the sensitivity of both channels to 4-AP was quite similar. When we applied 5 mM or 10 mM 4-AP without adjusting pH, we found that these concentrations activated  $K_v12.1$  channel even stronger than at physiological pH (**Figures 3F,G**). Without adjusting pH at higher concentrations, the  $EC_{50}$  was about 3.1 and the Hill coefficient was 0.9 (**Figure 3F**, black trace). As in line with a previous study (Kazmierczak et al., 2013) increasing pH of the extracellular solution from 7.4 to 8.1 or 9.0 without addition of 4-AP did not potentiate  $K_v12.1$ -mediated steady-state currents (**Figure 3G**), these data suggested that 4-AP activated  $K_v12.1$  channels more efficiently at more alkaline pH. Indeed, increasing pH of the extracellular solution containing 3 mM 4-AP to 8.1 further increased  $K_v12.1$ -mediated steady-state outward currents (**Figure 3H**).

### $K_v12.1$ Channels Are Also Activated by Isomeric Aminopyridines

Several other aminopyridines have been shown to inhibit voltage-gated  $K^+$  channels, albeit antagonistic efficiency of these substances was lower than that of 4-AP (Robertson

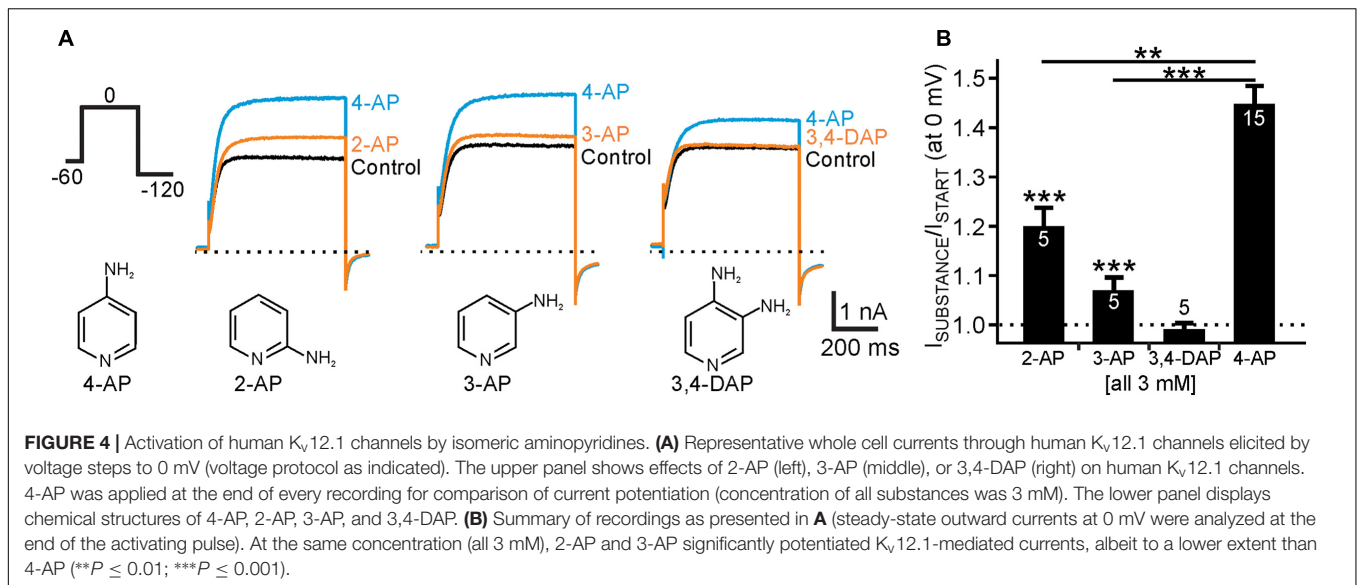


and Nelson, 1994; Sedehizadeh et al., 2012; Strupp et al., 2017). We thus wondered whether we could identify isomeric aminopyridines that activated  $K_v12.1$ , at best without affecting other  $K^+$  channels. We found that 2-aminopyridine (2-AP) and 3-aminopyridine (3-AP) potentiated  $K_v12.1$ -mediated currents at a concentration close to the  $EC_{50}$  of 4-AP (3 mM) by about 20% ( $P \leq 0.001$ ) and 7% ( $P \leq 0.001$ ), respectively (Figure 4). At the same concentration 3,4-diaminopyridine (3,4-DAP; 3 mM) was ineffective. Hence, 2-AP ( $P \leq 0.01$ ) and 3-AP ( $P \leq 0.001$ ) activated  $K_v12.1$  channels significantly less than 4-AP mirroring

efficacy of inhibition of other  $K^+$  channels by these substances (Robertson and Nelson, 1994; Sedehizadeh et al., 2012; Strupp et al., 2017).

### NS1643, an Activator of $K_v11$ Channels, Inhibits $K_v12.1$ Channels

We then turned to NS1643, a partial agonist of the  $K_v11$  channel family (Casis et al., 2006). As shown earlier (c.f. Hansen et al., 2006), NS1643 (30  $\mu$ M) slowed channel deactivation and



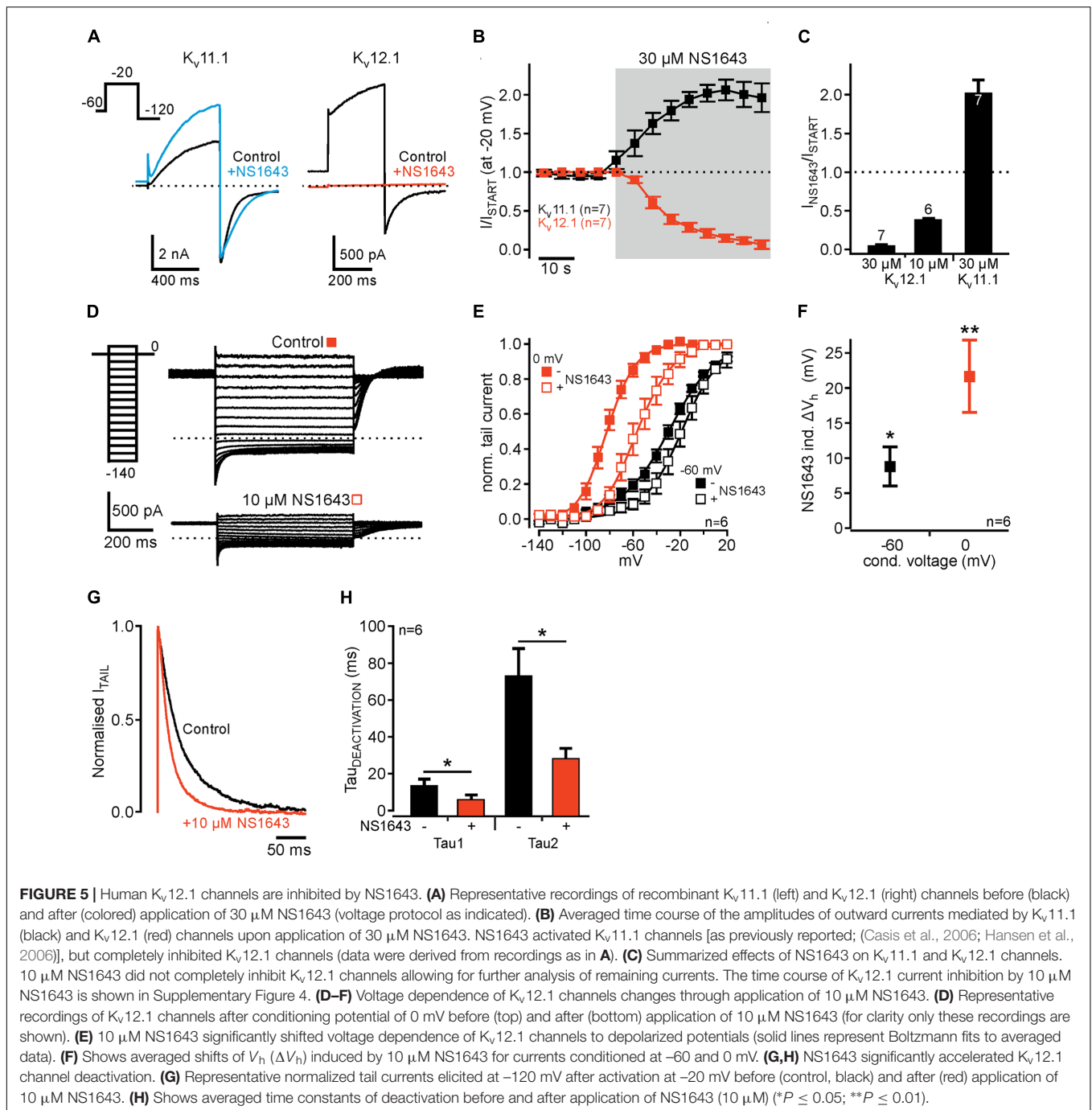
potentiated  $K_v11.1$ -mediated outward currents (Figures 5A–C). In contrast, the same concentration of NS1643 (30  $\mu$ M) completely inhibited  $K_v12.1$  channels with a time constant of  $16.8 \pm 2.6$  s ( $n = 7$ ; Figures 5A–C). When we applied only 10  $\mu$ M NS1643, a concentration close to the reported  $EC_{50}$  of NS1643 for activation of  $K_v11.1$  channels (Casis et al., 2006),  $K_v12.1$ -mediated currents were reduced to  $37.1 \pm 4.1\%$  of initial current amplitudes. Inhibition of currents by 10  $\mu$ M was much slower than when 30  $\mu$ M NS1643 was applied ( $n = 6$ ; compare Figure 5B and Supplementary Figure 4). We then analyzed voltage dependence of residual  $K_v12.1$  currents in the presence of 10  $\mu$ M NS1643 (Figures 5D–F): Application of NS1643 (10  $\mu$ M) shifted  $V_h$  by  $+8.8 \pm 2.9$  mV ( $n = 6$ ;  $P \leq 0.05$ ) and by  $+21.7 \pm 5.2$  mV ( $n = 6$ ;  $P \leq 0.01$ ) after conditioning voltage pulses of  $-60$  and  $0$  mV, respectively (Figures 5D–F). At the same time, slope factors changed by  $+8.0 \pm 1.5$  mV (conditioning pulse of  $-60$  mV;  $n = 6$ ;  $P \leq 0.05$ ) and  $-1.8 \pm 0.9$  mV (conditioning pulse  $0$  mV;  $n = 6$ ;  $P \leq 0.01$ ). Furthermore, NS1643 (10  $\mu$ M) significantly accelerated deactivation of  $K_v12.1$  channels at hyperpolarized potentials (Figures 5G,H;  $P \leq 0.05$ ;  $n = 6$ ).

## Identification of $K_v12.1$ Currents in Cells Expressing Different $K^+$ Currents

Our results suggested that voltage-clamp protocols designed to detect mode shift in combination with pharmacology using 4-AP or NS1643 should provide a robust approach for isolation of  $K_v12.1$ -mediated currents in native cell types. As proof of principle, we sought to isolate  $K_v12.1$  channel activity in cells expressing different  $K^+$  channels (Figure 6). To this end, we co-expressed  $K_v12.1$  channels together with  $K_v11.1$  and typical neuronal  $K^+$  channels ( $K_v7.2$ ,  $K_v7.3$  and  $Kir2.1$ ). In these experiments, CHO cells were transiently transfected with equal amounts of plasmid DNA encoding the channel subunits (see section “Materials and Methods” for details). We first analyzed whether we could isolate  $Kir2.1$ - and  $K_v7$ -mediated currents in those cells. In all cells tested, we found large inward currents at

hyperpolarized potentials and XE991-sensitive outward currents at depolarized potentials demonstrating expression of functional  $Kir2.1$  and  $K_v7$  channels, respectively (Supplementary Figure 5). As measure for abundance of  $K_v11.1$  and  $K_v12.1$  channels, we then tested whether we could detect mode shift of voltage dependence in the mix of  $K^+$  currents. As determined from whole cell currents,  $V_h$  was  $-6.7 \pm 1.3$  mV and  $-80.0 \pm 2.1$  mV after conditioning potentials of  $-60$  and  $0$  mV, respectively ( $n = 7$ ; Figures 6A–C). Thus, mode shift of channels expressed in these cells ( $K_v11.1$  and  $K_v12.1$  channels) was readily detectable even among a complement of different voltage-dependent  $K^+$  channels. We next attempted to isolate  $K_v12.1$ -mediated currents among the mixture of  $K^+$  channel by making use of the pharmacological profile established above. 4-AP (3 mM) shifted the voltage dependence of whole cell currents by  $-8.5 \pm 0.9$  mV ( $n = 7$ ;  $P \leq 0.001$ ) and by  $-12.3 \pm 2.3$  mV ( $n = 7$ ;  $P \leq 0.05$ ) to hyperpolarized potentials after conditioning voltages of  $-60$  and  $0$  mV, respectively (Figures 6B,C). Thus, although being less pronounced than for  $K_v12.1$  channels alone (Figure 6C), the 4-AP-induced shift of voltage dependence was readily detectable in the mixed  $K^+$  current situation. At the same time, 4-AP (3 mM) potentiated whole cell currents elicited at  $-60$  and  $0$  mV to about 210% and 140% of baseline amplitudes, respectively (Figures 6A,D–F). Finally, we applied 30  $\mu$ M NS1643 (on top of 4-AP) to the same cells and found that the substance inhibited outward currents and inward tail currents (Figures 6A,D,E). NS1643 also slowed deactivation kinetics of remaining currents (c.f. Figure 6A) indicating that NS1643-sensitive and functional  $K_v11.1$  channels were expressed in these cells.

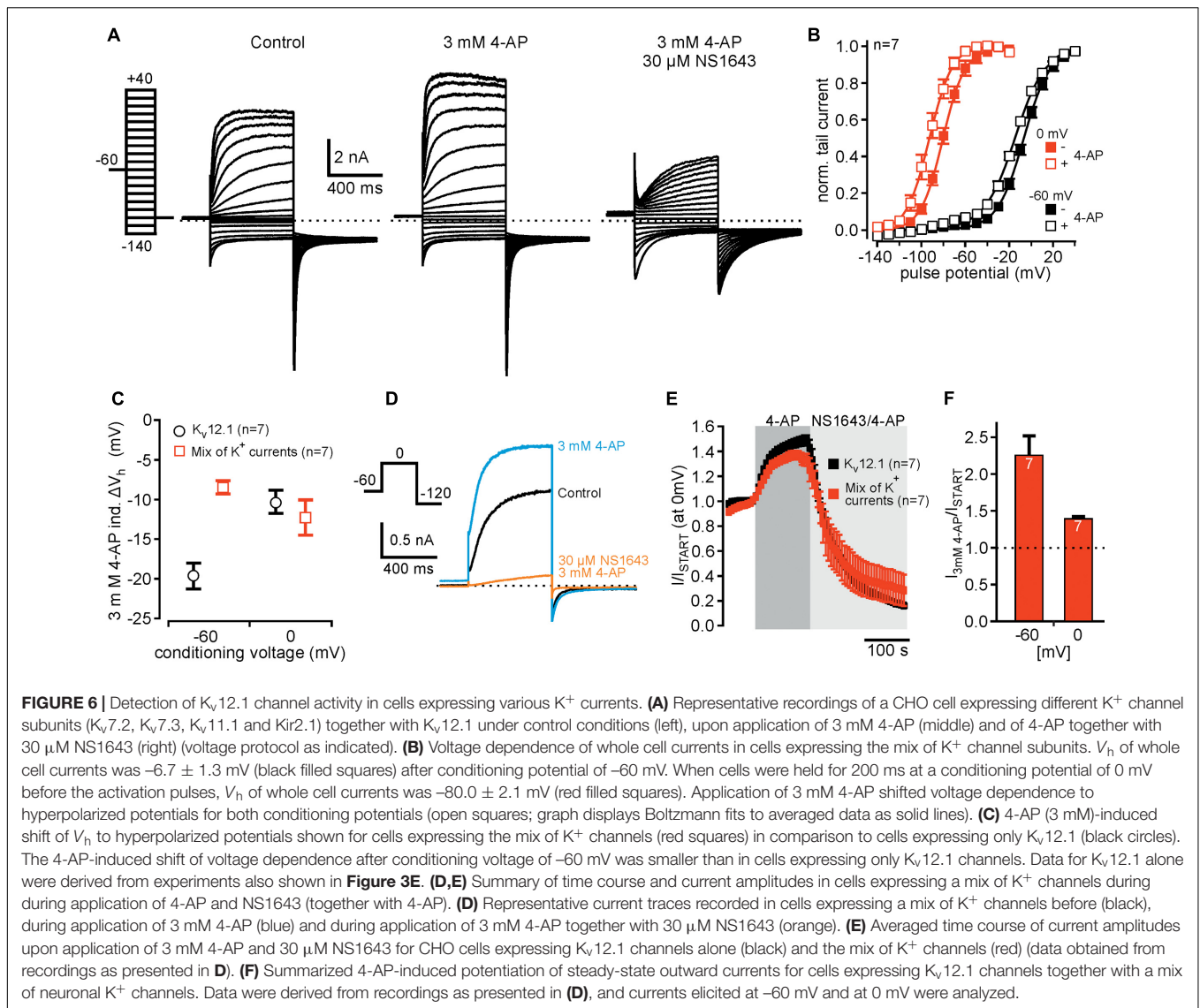
Taken together, using abovementioned experimental protocols we could unequivocally identify properties of  $K_v12.1$  channels (mode shift, 4-AP and NS1643 sensitivity) among a mixture of  $K^+$  currents. These results therefore suggest that the same protocols may be used to assign  $K^+$  current components to  $K_v12.1$  channels in complex (native) cellular/neuronal settings.



## DISCUSSION

The three members of the *ether-à-go-go*-like channel family of voltage-gated  $K^+$  channels ( $K_v12.1$ - $K_v12.3$ ) are predominantly expressed in neurons, as shown by mRNA transcripts in several brain areas including cerebral cortex and hippocampus (Miyake et al., 1999; Trudeau et al., 1999; Saganich et al., 2001; Zou et al., 2003), as well as in sympathetic ganglia (Shi et al., 1998). However, neuronal current components and their physiological relevance have been resolved for

$K_v12.2$  subunits exclusively: as demonstrated by application of a selective inhibitor,  $K_v12.2$  activity controls resting membrane potential and spontaneous firing of pyramidal neurons in hippocampus (Zhang et al., 2010). Also, in  $K_v12.2$  knock-out mice it was shown that  $K_v12.2$  channels regulate hippocampal excitability (Zhang et al., 2010) and may be important for processing of spatial working memory (Miyake et al., 2009). However, it is not known whether  $K_v12$  channels mediate relevant currents in any other physiological system.



Here, we focused on recombinant human  $K_v12.1$  to identify distinct biophysical and pharmacological properties allowing for attribution of native currents to these channels.

## Human $K_v12.1$ Channels Exhibit Mode Shift of Activation

Mode shift of activation was recently demonstrated for  $K_v12.1$  channel isoforms of humans and zebrafish heterologously expressed in *Xenopus laevis* oocytes (Li et al., 2015; Dai and Zagotta, 2017). However, mode shift of these channels has not been characterized in mammalian cells in detail yet. We found that mode shift of human  $K_v12.1$  was readily induced by depolarized holding potentials between  $-60$  and 0 mV and that it manifested by slowed channel deactivation and a striking shift of voltage dependence to hyperpolarized potentials. Deceleration of deactivation is generally considered a biophysical hallmark of mode shift, as channels undergo additional (time-consuming) transitions from this “relaxed” (metastable) open state into

deactivation (Bezannila et al., 1982; Villalba-Galea et al., 2008; Corbin-Leftwich et al., 2016; Villalba-Galea, 2017). Similar to  $K_v11.1$  (Tan et al., 2012) and zebrafish  $K_v12.1$  (Dai and Zagotta, 2017), mode shift of human  $K_v12.1$  channels manifested by a striking  $-60$  mV shift of voltage dependence. Thus, mode shift-dependent hyperpolarizing shifts of voltage dependence were qualitatively and quantitatively comparable for these three ion channels. Of note, mode shift of  $K_v12.1$  channels was readily induced using different voltage protocols, albeit the extent of the hyperpolarizing shift of activation potentials varied considerably with duration of hyperpolarized voltage steps. This demonstrated high sensitivity of  $K_v12.1$  channels to the holding potential, but also highlighted that voltage dependence of native  $K_v12.1$  currents might also vary with the used voltage protocols. In contrast to zebrafish  $K_v12.1$  (Dai and Zagotta, 2017), activation of human  $K_v12.1$  channels did not exhibit prominent double exponential kinetics that might indicate transition into a more stable open conformation. However, human  $K_v11.1$  channels that

beyond doubt exhibit mode shift do not display such kinetics neither (Tan et al., 2012; Goodchild et al., 2015). This indicates that either kinetics were masked by channel inactivation, or transition was too fast in the human channel isoforms.

Time course of transition into the relaxed state varies considerably between channels requiring depolarization for minutes in  $Na_v$  (Bezanilla et al., 1982), seconds in *Shaker* (Olcese et al., 1997) and some hundreds of milliseconds in  $K_v11.1$  channels (Piper et al., 2003). For human  $K_v12.1$ , we found that also some hundreds of milliseconds of conditioning depolarization was sufficient for significant alterations of voltage dependence and kinetics. Thus, time course of development of  $K_v12.1$  mode shift was well in the range of that published for  $K_v11.1$  channels (Piper et al., 2003). As  $K_v12.1$  channels are highly sensitive to changes of the holding potential, voltage dependence of the channels strongly depends on the employed voltage protocols. In fact, such protocol differences could account for considerable variations in voltage dependence of  $K_v12.1$  channels reported in different studies ( $V_h$  close to 0 mV in Shi et al., 1998;  $V_h$  of about  $-60$  mV in Zou et al., 2003).

### **$K_v12.1$ Channels Are Activated by 4-AP, an Established $K_v$ Channel Inhibitor**

4-AP is a rather selective blocker of voltage-gated  $K^+$  channels: At micromolar concentrations, it reversibly inhibits activity of  $K_v1$  and  $K_v3$  family members, but at higher concentrations (in the millimolar range) 4-AP also blocks other  $K_v$  channels (e.g.,  $K_v11$ ) (Gutman et al., 2005; Alexander et al., 2015). Thus, it was somewhat surprising to find that 4-AP activates  $K_v12.1$  channels. As an early study mentioned potentiation of  $K_v12.3$  through 4-AP without, however, showing any recordings (named rELK1; Engeland et al., 1998), such 4-AP sensitivity may constitute a general feature of the  $K_v12$  family.

Earlier, it was shown that currents through  $K_v2.1$  channels that are normally inhibited by 4-AP were potentiated by the substance, but only when  $K_v6.4$  subunits were co-expressed (Stas et al., 2015). As  $K_v2.1$  and  $K_v6.4$  co-assemble into functional channels (reviewed in Bocksteins, 2016), this suggested that  $K_v6.4$  largely determined altered 4-AP sensitivity of the resulting heteromeric channels. 4-AP suppressed closed state inactivation of  $K_v2.1/K_v6.4$  resulting in exclusive current potentiation of currents through those heteromers (Stas et al., 2015). In contrast,  $K_v12.1$  channels did not inactivate in our experiments, and thus 4-AP probably does not potentiate  $K_v12.1$ -mediated currents through a similar mechanism. As 4-AP, in contrast to  $K_v2.1/K_v6.4$  heteromers, also modulated voltage dependence of  $K_v12.1$ , actions of 4-AP are probably even more complex for these channels. Interestingly, a recent study demonstrated 4-AP-dependent activation of  $K_v7.4$  channels (Khammy et al., 2017) indicating that 4-AP-dependent activation of voltage-gated  $K^+$  channels may constitute a more frequent phenomenon than expected. However, further work is needed to elucidate whether other members of the  $K_v$  channel superfamily also exhibit this special 4-AP sensitivity.

Yet, we do not know whether 4-AP directly activates  $K_v12.1$  channels or whether an auxiliary subunit endogenously expressed

in CHO cells confers 4-AP activation to  $K_v12.1$ . Unfortunately, at present nothing is known about physiologically relevant interaction partners of  $K_v12.1$  channels. As  $K_v$  channels (with  $K_v2.1$  as exception) normally do not form functional channels with members of other  $K_v$  families, heteromerization of  $K_v12.1$  channels with another pore forming  $\alpha$  subunit apart from  $K_v12.2$  or  $K_v12.3$  is quite unlikely (Zou et al., 2003). Accordingly, a mechanism as shown for  $K_v2.1$  is rather implausible, and it is hard to imagine how a non-pore-forming auxiliary subunit could reverse 4-AP sensitivity from inhibition to activation. Furthermore, any endogenously expressed auxiliary subunit would need to be expressed at high abundance to saturate overexpressed  $K_v12.1$  channels. Hence, a straightforward model proposes direct activation of  $K_v12.1$  channels through 4-AP. However, we want to point-out that we cannot exclude indirect actions on the channels at the moment.

### **NS1643, a “Specific” Activator of $K_v11$ Channels, Inhibits $K_v12.1$**

NS1643 is a well-characterized partial agonist of  $K_v11$  channels that slows deactivation, increases tail-current amplitude, and shifts voltage dependence of activation to hyperpolarized potentials and voltage dependence of C-type inactivation to depolarized potentials (Casis et al., 2006; Hansen et al., 2006). At the same time, NS1643 exhibits weak antagonistic effects on  $K_v11$  channels as evident by an attenuation of drug-induced current increase at higher concentrations (Casis et al., 2006; Schuster et al., 2011).  $K_v11.3$  channels are even inhibited by higher concentrations of NS1643. For  $K_v12.1$  channels, NS1643 accelerated deactivation, inhibited outward and tail currents and shifted voltage dependence of activation to depolarized potentials (c.f. Figure 5). Thus, NS1643 affected  $K_v11$  and  $K_v12.1$  channels exactly in opposite directions. Similar to  $K_v11.3$  channels, NS1643 increased slope factor of voltage dependence of  $K_v12.1$  channels, even though already at lower concentrations. This suggests that NS1643 similarly affects  $K_v11$  and  $K_v12.1$  channels, but antagonistic effects might dominate over activation for  $K_v12.1$ . In line, the concentration range of NS1643 effects was similar for these channel isoforms (Casis et al., 2006). However, so far we cannot tell whether NS1643 also exhibits weak agonistic effects on  $K_v12.1$  channels or whether NS1643 binds to homologous regions in  $K_v11$  and  $K_v12.1$  channels.

### **Conclusion and Outlook**

As pharmacological tools and appropriate mouse models are currently missing, identification of native  $K_v12.1$ -mediated currents critically depends on identification of unique biophysical and pharmacological properties. Indeed, native currents were successfully attributed to related  $K_v10$  and  $K_v11$  channels by exploiting their unique activation kinetics (c.f. Cole-Moore shift; e.g., Meyer and Heinemann, 1998) or exclusive  $Na^+$  sensitivity and pharmacology (Hirdes et al., 2005, 2009; Hardman and Forsythe, 2009), respectively. Here, we present distinctive pharmacological properties, and straightforward experimental protocols that may be employed to isolate  $K_v12.1$  channel activity in native tissue. As mode shift readily manifested in

cells expressing various neuronal  $K^+$  currents, this experimental protocol may be used to demonstrate expression of channels with mode shift in native cell types. In neurons expressing various  $K^+$  current components, such changes of voltage dependence may be easier to detect than associated changes of deactivation kinetics. Such experiments may not provide definite proof for  $K_v12$  channel expression. However, expression of mode shift may be employed together with expression analyses,  $Na^+$  sensitivity, activation through 4-AP and inhibition by NS1643 to narrow down (or exclude) contribution of  $K_v12.1$  channels to whole cell currents. Identification of the combination of these properties would provide strong evidence for expression and thus potential physiological relevance of  $K_v12.1$  channels.

## MATERIALS AND METHODS

### Cell Culture and Transfection

Chinese hamster ovary (CHO) dhFR<sup>-</sup> cells were maintained as previously reported (Leitner et al., 2016). Cells were kept in MEM Alpha Medium supplemented with 10% fetal calf serum (FCS) and 1% penicillin/streptomycin (pen/strep) (all Invitrogen GmbH, Darmstadt, Germany) in a humidified atmosphere at 5% CO<sub>2</sub> and 37°C. Transient transfection of cells was done with jetPEI transfection reagent (Polyplus Transfection, Illkirch, France). All experiments were performed 24–48 h after transfection at room temperature (22–25°C). The expression vectors used were:  $K_v7.2$ -pBK-CMV (gene: human KCNQ2; UniProt accession number: O43526),  $K_v7.3$ -pBK-CMV (human KCNQ3; O43525),  $K_v7.4$ -pBK-CMV (human KCNQ4; P56696)  $K_v11.1$  (Erg1)-pcDNA3.1 (rat KCNH2; O08962),  $K_v12.1$ (Elk1)-pcDNA3.1-IRESeGFP (human KCNH8; Q96L42), Kir2.1-pBK-CMV (human KCNJ2; P63252), and pEGFP-C1 (Addgene, Teddington, United Kingdom). For recordings presented in **Figure 6** and Supplementary Figure 5, CHO cells were transiently transfected with identical amounts of plasmids encoding  $K_v7.2$ ,  $K_v7.3$ ,  $K_v11.1$ ,  $K_v12.1$ , and Kir2.1 (0.6 μg of plasmid DNA for every subunit).

### Electrophysiological Recordings

Electrophysiological recordings were performed in the whole cell configuration with an Axopatch 200B amplifier (Molecular Devices, Union City, CA, United States) or an HEKA EPC10 USB patch clamp amplifier HEKA (Elektronik, Lambrecht, Germany) in voltage-clamp mode (Leitner et al., 2011). All recordings were low-pass filtered at 2 kHz and sampled at 5 kHz. Currents were elicited by voltage protocols indicated in the figures. Dashed lines in representative recordings highlight zero current. Borosilicate glass patch pipettes (Sutter Instrument Company, Novato, CA, United States) were used with an open pipette resistance of 2–3 MΩ after back-filling with intracellular solution. Liquid junction potentials were not compensated (approximately –4 mV). Series resistance ( $R_s$ ) typically was below 6 MΩ and compensated throughout the recordings (80–90%). Whole cell currents are presented normalized to the cell capacitance (current density; pA/pF) or as normalized to

baseline current amplitude ( $I/I_{Start}$ ). Extracellular solutions for most experiments contained (mM) 144 NaCl, 5.8 KCl, 1.3 CaCl<sub>2</sub>, 0.9 MgCl<sub>2</sub>, 0.7 NaH<sub>2</sub>PO<sub>4</sub>, 10 HEPES and 5.6 D-glucose, pH 7.4 (with NaOH), 305–310 mOsm/kg. In some experiments, NaCl in the extracellular solution was substituted by *N*-methyl-D-glucamine (NMDG; Sigma–Aldrich) (c.f. **Figure 2**). The standard intracellular solution contained (mM) 135 KCl, 2.41 CaCl<sub>2</sub> (100 nM free Ca<sup>2+</sup>), 3.5 MgCl<sub>2</sub>, 5 HEPES, 5 EGTA, 2.5 Na<sub>2</sub>ATP, pH 7.3 (with KOH), 290–295 mOsm/kg (Wilke et al., 2014).

### Substances

Tetraethylammonium (TEA, Sigma), NMDG (Sigma), 4-aminopyridine (≥99%; Sigma and Tocris Bioscience, Bristol, United Kingdom), 2-aminopyridine (2-AP; Sigma), 3-aminopyridine (3-AP; Sigma), 3,4-diaminopyridine (3,4-DAP; Sigma), 1,3-Bis-(2-hydroxy-5-trifluoromethyl-phenyl)-urea (NS 1643, Tocris), 10,10-*bis*-(4-Pyridinylmethyl)-9(10*H*)-anthracenone dihydrochloride (XE991, Tocris), and *N*-[4-[[1-[2-(6-Methyl-2-pyridinyl)ethyl]-4-piperidinyl]carbonyl]phenyl]methanesulfonamide dihydrochloride (E-4031, Tocris) were diluted in extracellular solution to concentrations indicated in “Results.” All substances were applied locally via a glass capillary through a custom-made application system.

### Note on 4-AP Solutions

4-AP did not significantly change the pH of the extracellular solution at concentrations below 3 mM. After dilution of the substance, pH of the extracellular solution containing 5 mM or 10 mM 4-AP typically was about 8.1 or 9.0, respectively. As indicated in “Results,” in some experiments the pH of solutions containing 5 and 10 mM 4-AP was adjusted to 7.4 after dilution of 4-AP. At the concentration applied in the present study (3 mM), isomeric aminopyridines did not change pH of the extracellular solution (c.f. **Figure 4**).

### Data Analysis

Patch clamp recordings were analyzed with PatchMaster (HEKA) and IgorPro (Wavemetrics, Lake Oswego, OR, United States). Voltage dependence of activation was derived from tail current amplitudes using voltage protocols indicated: Tail currents were fitted with a two-state Boltzmann function with  $I = I_{min} + (I_{max} - I_{min}) / (1 + \exp((V - V_h)/s))$ , where  $I$  is current,  $V$  is the membrane voltage,  $V_h$  is the voltage at half maximal activation, and  $s$  describes the steepness of the curve. Results are shown as conductance-voltage curves, obtained by normalizing to  $(I_{max} - I_{min})$ , obtained from fits to data of individual experiments. Time constants of deactivation were derived from double-exponential fits to deactivating current components at indicated potentials. For dose-response relations, current potentiation at 0 mV (normalized to baseline) was fitted to a Hill equation with  $I/I_b = I_b + (I_{max} - I_b) / (1 + (EC_{50}/[S])^{n_H})$ , where  $I$  is the (normalized) current,  $I_b$  and  $I_{max}$  denote minimal and maximal currents at low and high drug concentrations,  $EC_{50}$  is the concentration at the half maximal effect,  $[S]$  is the drug concentration and  $n_H$  is the Hill coefficient (Leitner et al., 2012).

## Statistical Analysis

Isolated cells under investigation were randomly assigned to different treatment groups. Data recordings and analysis for experiments presented were not performed in a blinded manner. For some experiments, single recordings were normalized to base line values individually to account for baseline variations between cells. Statistical analysis was performed using two-tailed Student's *t*-test/Wilcoxon–Mann–Whitney test, and when appropriate comparisons between multiple groups were performed with ANOVA followed by Dunnett test. Significance was assigned at  $P \leq 0.05$  ( $*P \leq 0.05$ ,  $**P \leq 0.01$ ,  $***P \leq 0.001$ ). Data subjected to statistical analysis have *n* over 5 per group and data are presented as mean  $\pm$  SEM. In electrophysiological experiments, *n* represents the number of individual cells and accordingly the number of independent experiments (no pseudo-replication).

## AUTHOR CONTRIBUTIONS

MD, SE, BW, and ML planned and performed the experiments and analyzed the data. ML conceived study, designed the experiments, and wrote the paper together with MD. All authors revised and approved the final version of the manuscript. All experiments were conducted at the Institute of Physiology and Pathophysiology at the Philipps-University Marburg (Germany).

## REFERENCES

- Alexander, S. P., Catterall, W. A., Kelly, E., Marrion, N., Peters, J. A., Benson, H. E., et al. (2015). The concise guide to PHARMACOLOGY 2015/16: voltage-gated ion channels. *Br. J. Pharmacol.* 172, 5904–5941. doi: 10.1111/bph.13349
- Bauer, C. K., and Schwarz, J. R. (2001). Physiology of EAG K<sup>+</sup> channels. *J. Membr. Biol.* 182, 1–15. doi: 10.1007/s00232-001-0031-3
- Bezanilla, F., Taylor, R. E., and Fernandez, J. M. (1982). Distribution and kinetics of membrane dielectric polarization. 1. Long-term inactivation of gating currents. *J. Gen. Physiol.* 79, 21–40. doi: 10.1085/jgp.79.1.21
- Bocksteins, E. (2016). Kv5, Kv6, Kv8, and Kv9 subunits: no simple silent bystanders. *J. Gen. Physiol.* 147, 105–125. doi: 10.1085/jgp.201511507
- Bruening-Wright, A., and Larsson, H. P. (2007). Slow conformational changes of the voltage sensor during the mode shift in hyperpolarization-activated cyclic-nucleotide-gated channels. *J. Neurosci.* 27, 270–278. doi: 10.1523/JNEUROSCI.3801-06.2007
- Casis, O., Olesen, S. P., and Sanguinetti, M. C. (2006). Mechanism of action of a novel human ether-a-go-go-related gene channel activator. *Mol. Pharmacol.* 69, 658–665. doi: 10.1124/mol.105.019943
- Corbin-Leftwich, A., Mossadeq, S. M., Ha, J., Ruchala, I., Le, A. H., and Villalba-Galea, C. A. (2016). Retigabine holds KV7 channels open and stabilizes the resting potential. *J. Gen. Physiol.* 147, 229–241. doi: 10.1085/jgp.201511517
- Curran, M. E., Splawski, I., Timothy, K. W., Vincent, G. M., Green, E. D., and Keating, M. T. (1995). A molecular basis for cardiac arrhythmia: HERG mutations cause long QT syndrome. *Cell* 80, 795–803. doi: 10.1016/0092-8674(95)90358-5
- Dai, G., and Zagotta, W. N. (2017). Molecular mechanism of voltage-dependent potentiation of KCNH potassium channels. *Elife* 6:e26355. doi: 10.7554/eLife.26355
- Engelard, B., Neu, A., Ludwig, J., Roeper, J., and Pongs, O. (1998). Cloning and functional expression of rat ether-a-go-go-like K<sup>+</sup> channel genes. *J. Physiol.* 513(Pt 3), 647–654.
- Goodchild, S. J., Macdonald, L. C., and Fedida, D. (2015). Sequence of gating charge movement and pore gating in HERG activation and deactivation pathways. *Biophys. J.* 108, 1435–1447. doi: 10.1016/j.bpj.2015.02.014

## FUNDING

This work was funded by Research Grants of the University Medical Center Giessen und Marburg (UKGM 17/2013; UKGM 13/2016 to ML) and by the German Research Foundation (DFG Priority Program 1608: “Ultrafast and temporally precise information processing: normal and dysfunctional hearing,” [LE 3600/1-1 to ML]).

## ACKNOWLEDGMENTS

The authors acknowledge the kind gift of plasmids for  $K_v7$  (KCNQ) channels from Dr. T. Jentsch,  $K_v12.1$  (Elk) from Dr. T. Jegla, and  $K_v11.1$  (Erg) from Dr. C. Bauer. They thank Olga Ebers and Neslihan Özen for superb technical assistance and Dr. Dominik Oliver (Marburg) for helpful comments and discussion.

## SUPPLEMENTARY MATERIAL

The Supplementary Material for this article can be found online at: <https://www.frontiersin.org/articles/10.3389/fnmol.2018.00011/full#supplementary-material>

- Gutman, G. A., Chandy, K. G., Grissmer, S., Lazdunski, M., Mckinnon, D., Pardo, L. A., et al. (2005). International union of pharmacology. LIII. Nomenclature and molecular relationships of voltage-gated potassium channels. *Pharmacol. Rev.* 57, 473–508. doi: 10.1124/pr.57.4.10
- Hadley, J. K., Noda, M., Selyanko, A. A., Wood, I. C., Abogadie, F. C., and Brown, D. A. (2000). Differential tetraethylammonium sensitivity of KCNQ1-4 potassium channels. *Br. J. Pharmacol.* 129, 413–415. doi: 10.1038/sj.bjp.0703086
- Hansen, R. S., Diness, T. G., Christ, T., Demnitz, J., Ravens, U., Olesen, S. P., et al. (2006). Activation of human ether-a-go-go-related gene potassium channels by the diphenylurea 1,3-bis-(2-hydroxy-5-trifluoromethyl-phenyl)-urea (NS1643). *Mol. Pharmacol.* 69, 266–277.
- Hardman, R. M., and Forsythe, I. D. (2009). Ether-a-go-go-related gene K<sup>+</sup> channels contribute to threshold excitability of mouse auditory brainstem neurons. *J. Physiol.* 587, 2487–2497. doi: 10.1113/jphysiol.2009.170548
- Hirdes, W., Napp, N., Wulfsen, I., Schweizer, M., Schwarz, J. R., and Bauer, C. K. (2009). Erg K<sup>+</sup> currents modulate excitability in mouse mitral/tufted neurons. *Pflugers. Arch.* 459, 55–70. doi: 10.1007/s00424-009-0709-4
- Hirdes, W., Schweizer, M., Schuricht, K. S., Guddat, S. S., Wulfsen, I., Bauer, C. K., et al. (2005). Fast erg K<sup>+</sup> currents in rat embryonic serotonergic neurons. *J. Physiol.* 564, 33–49. doi: 10.1113/jphysiol.2004.082123
- Ji, H., Tucker, K. R., Putzier, I., Huertas, M. A., Horn, J. P., Canavier, C. C., et al. (2012). Functional characterization of ether-a-go-go-related gene potassium channels in midbrain dopamine neurons - implications for a role in depolarization block. *Eur. J. Neurosci.* 36, 2906–2916. doi: 10.1111/j.1460-9568.2012.08190.x
- Kazmierczak, M., Zhang, X., Chen, B., Mulkey, D. K., Shi, Y., Wagner, P. G., et al. (2013). External pH modulates EAG superfamily K<sup>+</sup> channels through EAG-specific acidic residues in the voltage sensor. *J. Gen. Physiol.* 141, 721–735. doi: 10.1085/jgp.201210938
- Khammy, M. M., Kim, S., Bentzen, B. H., Lee, S., Choi, I., Aalkjaer, C., et al. (2017). 4-aminopyridine: a pan Kv channel inhibitor that enhances Kv7.4 currents and inhibits noradrenaline-mediated contraction of rat mesenteric small arteries. *Br. J. Pharmacol.* doi: 10.1111/bph.14097 [Epub ahead of print].
- Kortum, F., Caputo, V., Bauer, C. K., Stella, L., Ciolfi, A., Alawi, M., et al. (2015). Mutations in KCNH1 and ATP6V1B2 cause zimmermann-laband syndrome. *Nat. Genet.* 47, 661–667. doi: 10.1038/ng.3282



- Leitner, M. G., Feuer, A., Ebers, O., Schreiber, D. N., Halaszovich, C. R., and Oliver, D. (2012). Restoration of ion channel function in deafness-causing KCNQ4 mutants by synthetic channel openers. *Br. J. Pharmacol.* 165, 2244–2259. doi: 10.1111/j.1476-5381.2011.01697.x
- Leitner, M. G., Halaszovich, C. R., and Oliver, D. (2011). Aminoglycosides inhibit KCNQ4 channels in cochlear outer hair cells via depletion of phosphatidylinositol(4,5)bisphosphate. *Mol. Pharmacol.* 79, 51–60. doi: 10.1124/mol.110.068130
- Leitner, M. G., Michel, N., Behrendt, M., Dierich, M., Dembla, S., Wilke, B. U., et al. (2016). Direct modulation of TRPM4 and TRPM3 channels by the phospholipase C inhibitor U73122. *Br. J. Pharmacol.* 173, 2555–2569. doi: 10.1111/bph.13538
- Li, X., Anishkin, A., Liu, H., Van Rossum, D. B., Chintapalli, S. V., Sassic, J. K., et al. (2015). Bimodal regulation of an Elk subfamily K<sup>+</sup> channel by phosphatidylinositol 4,5-bisphosphate. *J. Gen. Physiol.* 146, 357–374. doi: 10.1085/jgp.201511491
- Mannikko, R., Pandey, S., Larsson, H. P., and Elinder, F. (2005). Hysteresis in the voltage dependence of HCN channels: conversion between two modes affects pacemaker properties. *J. Gen. Physiol.* 125, 305–326. doi: 10.1085/jgp.200409130
- Marcotti, W., Johnson, S. L., Holley, M. C., and Kros, C. J. (2003). Developmental changes in the expression of potassium currents of embryonic, neonatal and mature mouse inner hair cells. *J. Physiol.* 548, 383–400. doi: 10.1113/jphysiol.2002.034801
- Meyer, R., and Heinemann, S. H. (1998). Characterization of an eag-like potassium channel in human neuroblastoma cells. *J. Physiol.* 508(Pt 1), 49–56. doi: 10.1111/j.1469-7793.1998.049br.x
- Miyake, A., Mochizuki, S., Yokoi, H., Kohda, M., and Furuichi, K. (1999). New ether-a-go-go K(+) channel family members localized in human telencephalon. *J. Biol. Chem.* 274, 25018–25025. doi: 10.1074/jbc.274.35.25018
- Miyake, A., Takahashi, S., Nakamura, Y., Inamura, K., Matsumoto, S., Mochizuki, S., et al. (2009). Disruption of the ether-a-go-go K<sup>+</sup> channel gene BEC1/KCNH3 enhances cognitive function. *J. Neurosci.* 29, 14637–14645. doi: 10.1523/JNEUROSCI.0901-09.2009
- Numaguchi, H., Johnson, J. P. Jr., Petersen, C. I., and Balsler, J. R. (2000). A sensitive mechanism for cation modulation of potassium current. *Nat. Neurosci.* 3, 429–430. doi: 10.1038/74793
- Olcese, R., Latorre, R., Toro, L., Bezanilla, F., and Stefani, E. (1997). Correlation between charge movement and ionic current during slow inactivation in Shaker K<sup>+</sup> channels. *J. Gen. Physiol.* 110, 579–589. doi: 10.1085/jgp.110.5.579
- Pardo, L. A., and Stuhmer, W. (2014). The roles of K(+) channels in cancer. *Nat. Rev. Cancer* 14, 39–48. doi: 10.1038/nrc3635
- Piper, D. R., Varghese, A., Sanguinetti, M. C., and Tristani-Firouzi, M. (2003). Gating currents associated with intramembrane charge displacement in HERG potassium channels. *Proc. Natl. Acad. Sci. U.S.A.* 100, 10534–10539. doi: 10.1073/pnas.1832721100
- Ridley, J. M., Milnes, J. T., Zhang, Y. H., Witchel, H. J., and Hancox, J. C. (2003). Inhibition of HERG K<sup>+</sup> current and prolongation of the guinea-pig ventricular action potential by 4-aminopyridine. *J. Physiol.* 549, 667–672. doi: 10.1113/jphysiol.2003.043976
- Robertson, B. E., and Nelson, M. T. (1994). Aminopyridine inhibition and voltage dependence of K<sup>+</sup> currents in smooth muscle cells from cerebral arteries. *Am. J. Physiol.* 267, C1589–C1597. doi: 10.1152/ajpcell.1994.267.6.C1589
- Saganich, M. J., Machado, E., and Rudy, B. (2001). Differential expression of genes encoding subthreshold-operating voltage-gated K<sup>+</sup> channels in brain. *J. Neurosci.* 21, 4609–4624.
- Sanchez, A., Urrego, D., and Pardo, L. A. (2016). Cyclic expression of the voltage-gated potassium channel KV10.1 promotes disassembly of the primary cilium. *EMBO Rep.* 17, 708–723. doi: 10.15252/embr.201541082
- Sanguinetti, M. C., Jiang, C., Curran, M. E., and Keating, M. T. (1995). A mechanistic link between an inherited and an acquired cardiac arrhythmia: HERG encodes the IKr potassium channel. *Cell* 81, 299–307. doi: 10.1016/0092-8674(95)90340-2
- Schuster, A. M., Glassmeier, G., and Bauer, C. K. (2011). Strong activation of ether-a-go-go-related gene 1 K<sup>+</sup> channel isoforms by NS1643 in human embryonic kidney 293 and Chinese hamster ovary cells. *Mol. Pharmacol.* 80, 930–942. doi: 10.1124/mol.111.071621
- Sedehizadeh, S., Keogh, M., and Maddison, P. (2012). The use of aminopyridines in neurological disorders. *Clin. Neuropharmacol.* 35, 191–200. doi: 10.1097/WNF.0b013e31825a68c5
- Shi, W., Wang, H. S., Pan, Z., Wymore, R. S., Cohen, I. S., Mckinnon, D., et al. (1998). Cloning of a mammalian elk potassium channel gene and EAG mRNA distribution in rat sympathetic ganglia. *J. Physiol.* 511(Pt 3), 675–682.
- Simons, C., Rash, L. D., Crawford, J., Ma, L., Cristofori-Armstrong, B., Miller, D., et al. (2015). Mutations in the voltage-gated potassium channel gene KCNH1 cause Temple-Baraitser syndrome and epilepsy. *Nat. Genet.* 47, 73–77. doi: 10.1038/ng.3153
- Stas, J. I., Bocksteins, E., Labro, A. J., and Snyder, D. J. (2015). Modulation of closed-state inactivation in Kv2.1/Kv6.4 heterotetramers as mechanism for 4-AP induced potentiation. *PLOS ONE* 10:e0141349. doi: 10.1371/journal.pone.0141349
- Strupp, M., Teufel, J., Zwergal, A., Schniepp, R., Khodakhah, K., and Feil, K. (2017). Aminopyridines for the treatment of neurologic disorders. *Neurol. Clin. Pract.* 7, 65–76. doi: 10.1212/CPJ.0000000000000321
- Sturm, P., Wimmers, S., Schwarz, J. R., and Bauer, C. K. (2005). Extracellular potassium effects are conserved within the rat erg K<sup>+</sup> channel family. *J. Physiol.* 564, 329–345. doi: 10.1113/jphysiol.2004.078840
- Tan, P. S., Perry, M. D., Ng, C. A., Vandenberg, J. I., and Hill, A. P. (2012). Voltage-sensing domain mode shift is coupled to the activation gate by the N-terminal tail of hERG channels. *J. Gen. Physiol.* 140, 293–306. doi: 10.1085/jgp.201110761
- Tilegenova, C., Cortes, D. M., and Cuello, L. G. (2017). Hysteresis of KcsA potassium channel's activation- deactivation gating is caused by structural changes at the channel's selectivity filter. *Proc. Natl. Acad. Sci. U.S.A.* 114, 3234–3239. doi: 10.1073/pnas.1618101114
- Trudeau, M. C., Titus, S. A., Branchaw, J. L., Ganetzky, B., and Robertson, G. A. (1999). Functional analysis of a mouse brain Elk-type K<sup>+</sup> channel. *J. Neurosci.* 19, 2906–2918.
- Trudeau, M. C., Warmke, J. W., Ganetzky, B., and Robertson, G. A. (1995). HERG, a human inward rectifier in the voltage-gated potassium channel family. *Science* 269, 92–95. doi: 10.1126/science.7604285
- Urrego, D., Movsisyan, N., Ufartes, R., and Pardo, L. A. (2016). Periodic expression of Kv10.1 driven by pRb/E2F1 contributes to G2/M progression of cancer and non-transformed cells. *Cell Cycle* 15, 799–811. doi: 10.1080/15384101.2016.1138187
- Villalba-Galea, C. A. (2017). Hysteresis in voltage-gated channels. *Channels* 11, 140–155. doi: 10.1080/19336950.2016.1243190
- Villalba-Galea, C. A., Sandtner, W., Starace, D. M., and Bezanilla, F. (2008). S4-based voltage sensors have three major conformations. *Proc. Natl. Acad. Sci. U.S.A.* 105, 17600–17607. doi: 10.1073/pnas.0807387105
- Wang, H. S., Pan, Z., Shi, W., Brown, B. S., Wymore, R. S., Cohen, I. S., et al. (1998). KCNQ2 and KCNQ3 potassium channel subunits: molecular correlates of the M-channel. *Science* 282, 1890–1893. doi: 10.1126/science.282.5395.1890
- Wilke, B. U., Lindner, M., Greifenberg, L., Albus, A., Kronimus, Y., Bunemann, M., et al. (2014). Diacylglycerol mediates regulation of TASK potassium channels by Gq-coupled receptors. *Nat. Commun.* 5:5540. doi: 10.1038/ncomms6540
- Zhang, X., Bertaso, F., Yoo, J. W., Baumgartel, K., Clancy, S. M., Lee, V., et al. (2010). Deletion of the potassium channel Kv12.2 causes hippocampal hyperexcitability and epilepsy. *Nat. Neurosci.* 13, 1056–1058. doi: 10.1038/nn.2610
- Zou, A., Lin, Z., Humble, M., Creech, C. D., Wagoner, P. K., Krafte, D., et al. (2003). Distribution and functional properties of human KCNH8 (Elk1) potassium channels. *Am. J. Physiol. Cell Physiol.* 285, C1356–C1366. doi: 10.1152/ajpcell.00179.2003

**Conflict of Interest Statement:** The authors declare that the research was conducted in the absence of any commercial or financial relationships that could be construed as a potential conflict of interest.

Copyright © 2018 Dierich, Evers, Wilke and Leitner. This is an open-access article distributed under the terms of the Creative Commons Attribution License (CC BY). The use, distribution or reproduction in other forums is permitted, provided the original author(s) and the copyright owner are credited and that the original publication in this journal is cited, in accordance with accepted academic practice. No use, distribution or reproduction is permitted which does not comply with these terms.

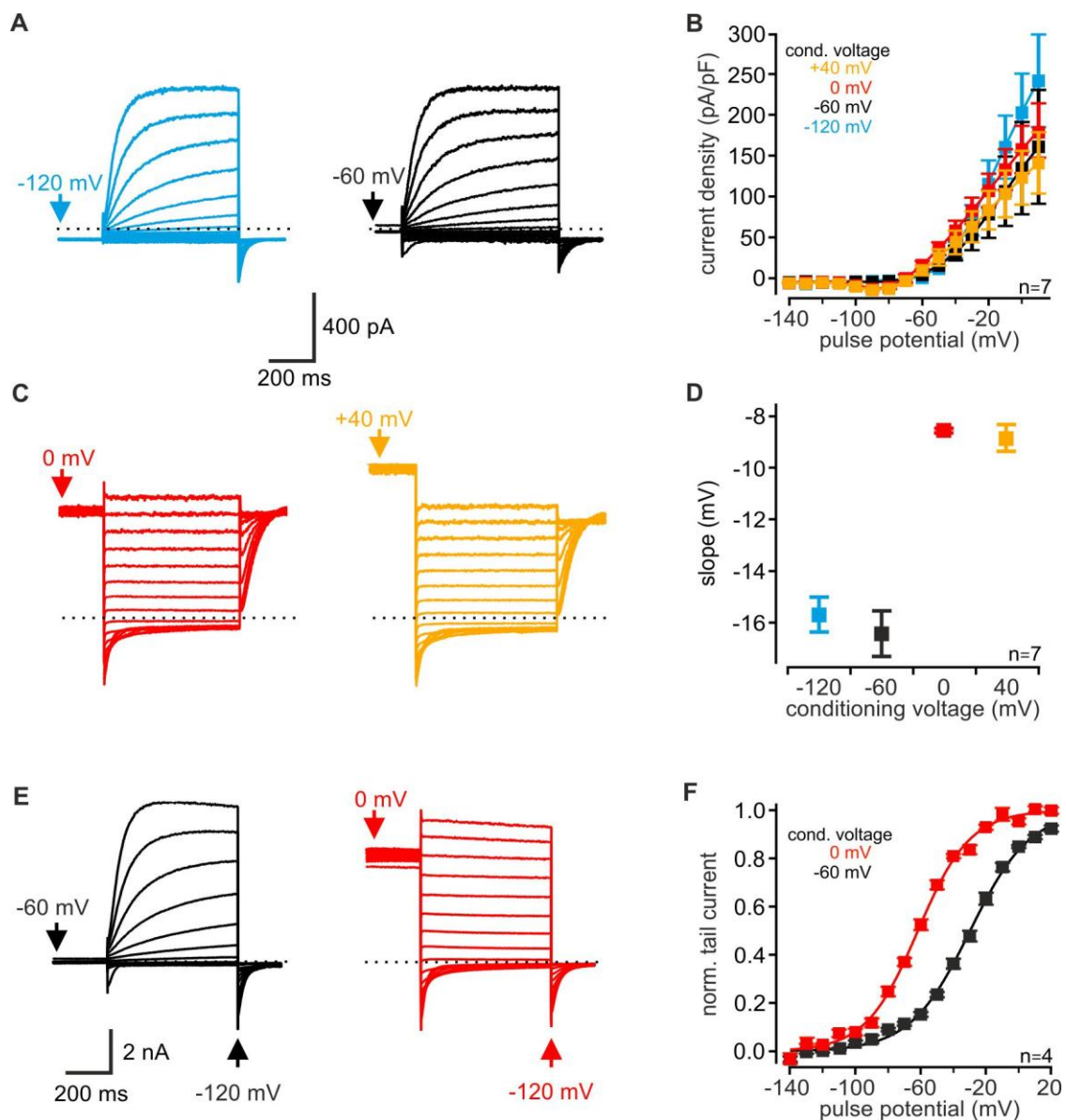


*Supplementary Material*

**Inverse modulation of neuronal  $K_v12.1$  and  $K_v11.1$  channels by 4-aminopyridine and NS1643**

Marlen Dierich, Saskia Evers, Bettina U. Wilke, and \*Michael G. Leitner

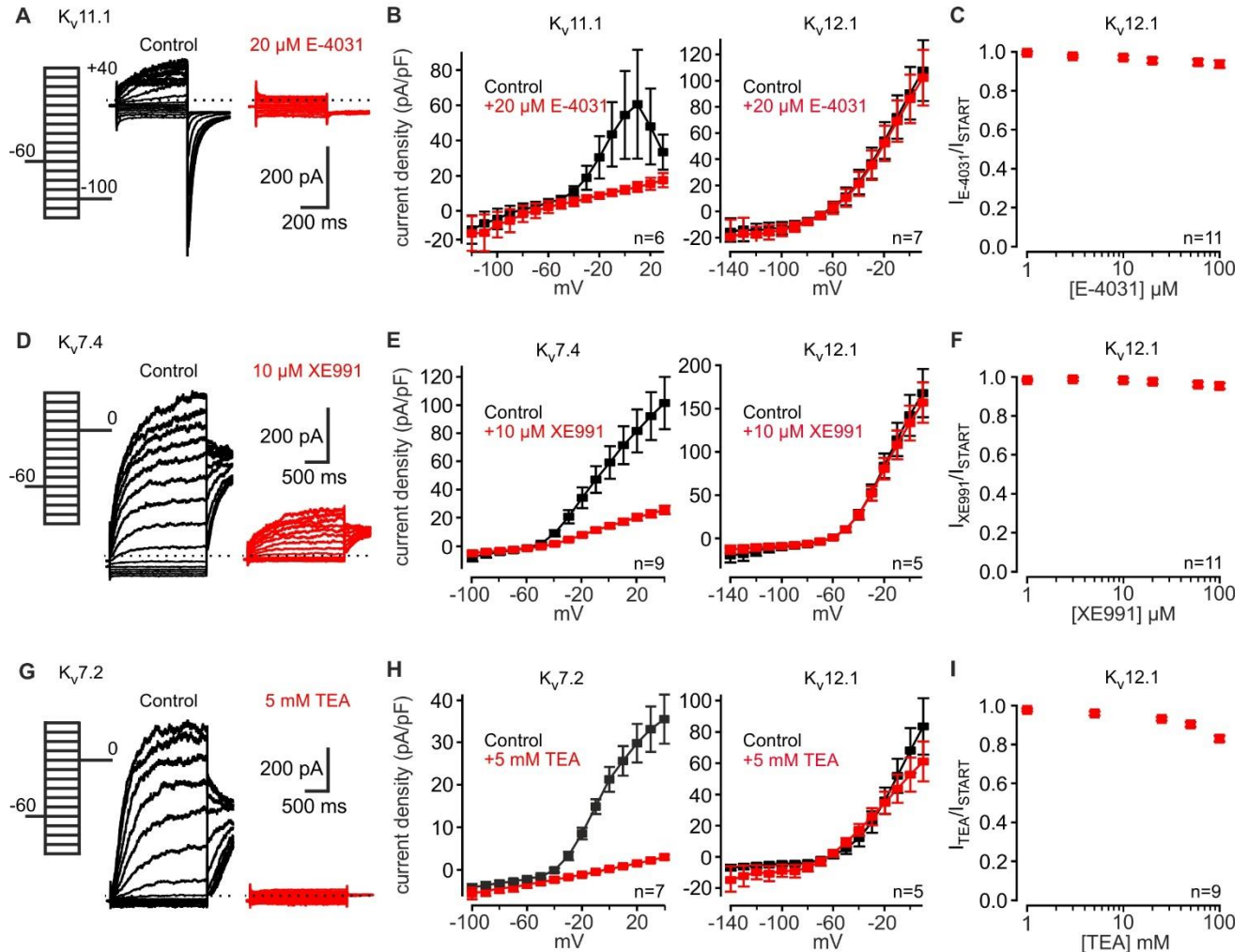
\*Correspondence: Dr. Michael G. Leitner: leitnerm@staff.uni-marburg.de



**Supplementary Figure 1. Measuring activity of human  $K_v12.1$  channels in CHO cells.**

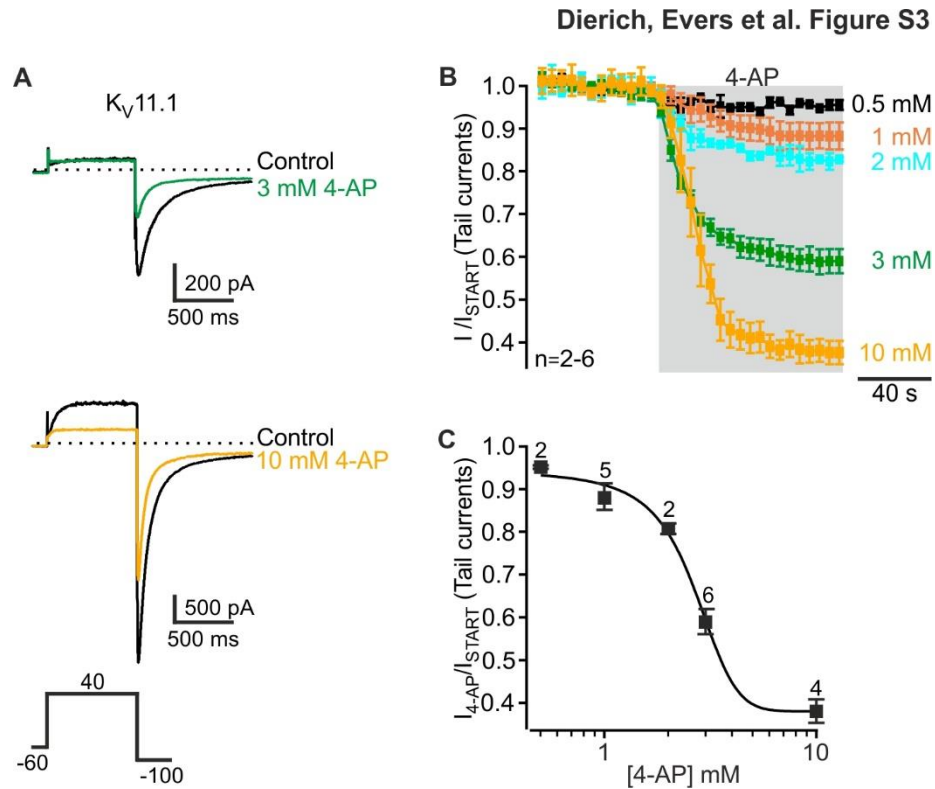
**Supplementary Figure 1. Measuring activity of human K<sub>v</sub>12.1 channels in CHO cells.**

(A+C) Representative recordings of human K<sub>v</sub>12.1 channels transiently expressed in CHO cells measured with the following voltage protocols (c.f. **Figure 1G**): a 200 ms conditioning potential step to -120 mV (*blue*), -60 mV (*black*), 0 mV (*red*), or +40 mV (*orange*) was followed by 600 ms activating pulses at potentials from -140 mV to +10 mV (+10 mV increments). Tail currents were elicited at potentials that corresponded to conditioning pulses (-120 mV or 0 mV). Current traces for conditioning potential of -60 mV are also as shown in **Figure 1A**. **(B)** Summary of steady-state outward currents obtained from recordings as presented in (A). Amplitudes of outward currents were the same for all protocols indicating that channels were comparably activated with all voltage protocols. **(D)** Slope factors derived from Boltzmann fits to the recordings changed with conditioning potentials. Slope factors were derived from recordings as shown here in (A+C) and in **Figure 1G-I**. **(E+F)** Mode shift of human K<sub>v</sub>12.1 channels was sensitive to the employed voltage protocol: In these experiments, tail currents were measured at hyperpolarized potentials (-120 mV) after 600 ms activating pulses from -140 mV to +20 mV (10 mV increments) and 200 ms conditioning potentials of -60 mV or 0 mV. **(E)** shows representative recordings of human K<sub>v</sub>12.1 channels measured with these protocols and **(F)** shows the summary of voltage dependence of human K<sub>v</sub>12.1 channels (solid line represents a Boltzmann fit to averaged data). Depolarized conditioning potentials of 0 mV induced a large shift of voltage dependence to hyperpolarized potentials also in these experiments. In these experiments, V<sub>h</sub> was  $-29.8 \pm 1.3$  mV and  $-61.8 \pm 1.1$  mV after conditioning pulses of -60 mV and 0 mV, respectively (n=4, data derived from fits shown in (F) and recordings shown in (E)).



### Supplementary Figure 2. $K_v12.1$ channels are not sensitive to E-4031, XE991, and TEA.

(A, D, G) Representative recordings of CHO cells transiently transfected with (A)  $K_v11.1$ , (D)  $K_v7.4$  and (G)  $K_v7.2$  before (*black*) and after (*red*) application of (A) E-4031, (D) XE991 and (G) TEA (voltage protocols as indicated). These channels are well established targets of the respective  $K^+$  channel inhibitor. (B) Effect of E-4031 at a concentration generally applied to inhibit native  $K_v11$  channels (20  $\mu\text{M}$ ) on steady-state outward currents mediated by  $K_v11.1$  (*left*) and  $K_v12.1$  (*right*). (C)  $K_v12.1$  channels were insensitive to E-4031 applied at concentrations between 1  $\mu\text{M}$  and 100  $\mu\text{M}$ . (E) Averaged steady-state outward currents through  $K_v7.4$  (*left*) and  $K_v12.1$  (*right*) channels before and after application of 10  $\mu\text{M}$  XE991, a concentration typically used to inhibit native  $K_v7$  channels. (F)  $K_v12.1$ -mediated currents were not affected by XE991 at concentrations between 1  $\mu\text{M}$  and 100  $\mu\text{M}$ . (H) Steady-state outward currents mediated by  $K_v7.2$  (*left*) and  $K_v12.1$  (*right*) before and after application of TEA (5 mM). In contrast to  $K_v7.2$ ,  $K_v12.1$  channels were insensitive to TEA at this concentration. (I) Dose-response experiments revealed that  $K_v12.1$  channels were slightly inhibited by high TEA concentrations. When we applied 50 mM or 100 mM TEA,  $K_v12.1$  channels were inhibited by approximately 10% and 17% (NaCl was substituted with TEA-Cl in these recordings).

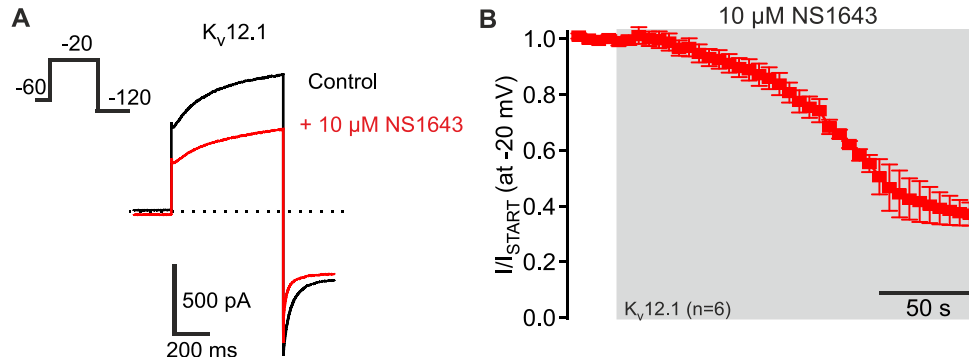


### Supplementary Figure 3. Inhibition of recombinant $K_v11.1$ channels by 4-AP.

(A) Representative recordings of currents through  $K_v11.1$  channels before (*black*) and after application of 3 mM 4-AP (*green*, upper panel) or 10 mM 4-AP (*yellow*; lower panel). Voltage protocol was as indicated. (B) Averaged time course of tail current amplitudes upon application of increasing concentrations of 4-AP (concentrations as indicated). (C) 4-AP inhibited  $K_v11.1$  channels in a dose-dependent manner with an  $IC_{50}$  of about 2.6 mM and a Hill coefficient of about 0.7, in line with a previous report (Ridley et al., 2003). Parameters were derived from fits of averaged data to a Hill equation described in *Methods* (solid line represents this fit) (pH adjusted).

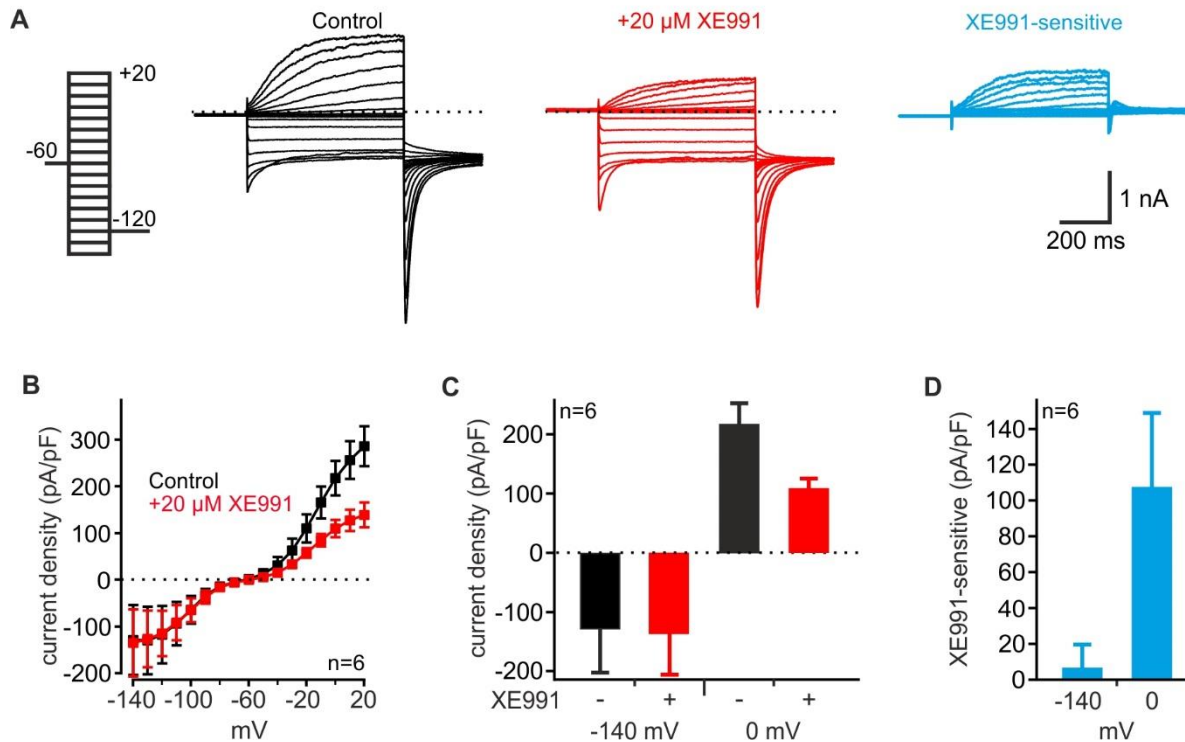
### Reference

Ridley, J.M., Milnes, J.T., Zhang, Y.H., Witchel, H.J., and Hancox, J.C. (2003). Inhibition of HERG  $K^+$  current and prolongation of the guinea-pig ventricular action potential by 4-aminopyridine. *J Physiol* 549, 667-672.



**Supplementary Figure 4. Slow and incomplete inhibition of  $K_v12.1$  channels by  $10 \mu\text{M}$  NS1643.** (A) Representative recordings from CHO cell transiently transfected with  $K_v12.1$  before (*black*) and after (*red*) extracellular application of  $10 \mu\text{M}$  NS1643 (Voltage protocol as indicated). (B) Averaged time course of  $K_v12.1$ -mediated currents upon application of  $10 \mu\text{M}$  NS1643 (currents measured at  $-20 \text{ mV}$  in recordings as presented in (A)). Note that  $10 \mu\text{M}$  NS1643 did not completely inhibit  $K_v12.1$  currents and that time course of inhibition was much slower than inhibition induced by  $30 \mu\text{M}$  NS1643 (c.f. **Figure 5B** in main text).

## Dierich, Evers et al. Figure S5



**Supplementary Figure 5. CHO cells transfected with plasmids encoding five different  $K^+$  channel subunits express large Kir2.1- and  $K_v7$ -mediated currents.**

In these experiments, CHO cells were transfected with equal amounts of plasmid DNA encoding  $K_v7.2$ ,  $K_v7.3$ ,  $K_v11.1$ ,  $K_v12.1$  and Kir2.1. This figure shows analysis of Kir2.1- and  $K_v7$ -mediated current components in these cells. For identification of  $K_v11.1$  and  $K_v12.1$ , currents see **Figure 6** in the main text. **(A)** Representative recordings of  $K^+$  currents in CHO cells transfected with the mix of  $K^+$  channel subunits before (black; left) and after (red; middle) application of the  $K_v7$ -specific antagonist XE991. XE991-sensitive currents (blue; right) were calculated by subtracting currents after XE991 from control currents (voltage protocol as indicated). **(B-D)** Analysis of steady-state currents. **(B)** Summary of steady-state currents elicited by voltage steps between -140 mV and +20 mV before and after application of XE991 (20  $\mu$ M). CHO cells transfected with the mix of  $K^+$  channels showed large inward and outward currents at hyperpolarized and depolarized potentials, respectively. Inward currents demonstrated expression of functional Kir2.1 channels, and application of XE991 (20  $\mu$ M) selectively inhibited outward currents demonstrating functional expression of  $K_v7$  channels in these cells. Steady-state current amplitudes were analyzed at the end of the activating pulse from recordings as shown in **(A)**. **(C)** Summary of steady-state inward currents elicited at -140 mV and outward currents at 0 mV before and after application of XE991 (20  $\mu$ M). **(D)** Summary of XE991-sensitive currents at -140 mV and 0 mV (derived from recordings as shown in **(A)**).



## K<sub>v</sub>12.1 channels are not sensitive to G<sub>q</sub>PCR-triggered activation of phospholipase C $\beta$

Marlen Dierich<sup>a</sup> and Michael G. Leitner <sup>a,b</sup>

<sup>a</sup>Department of Neurophysiology, Institute of Physiology and Pathophysiology, Philipps-University Marburg, Marburg, Germany; <sup>b</sup>Division of Physiology, Department of Physiology and Medical Physics, Medical University of Innsbruck, Innsbruck, Austria

### ABSTRACT

K<sub>v</sub>12.1 K<sup>+</sup> channels are expressed in several brain areas, but no physiological function could be attributed to these subunits so far. As genetically-modified animal models are not available, identification of native K<sub>v</sub>12.1 currents must rely on characterization of distinct channel properties. Recently, it was shown in *Xenopus laevis* oocytes that K<sub>v</sub>12.1 channels were modulated by membrane PI(4,5)P<sub>2</sub>. However, it is not known whether these channels are also sensitive to physiologically-relevant PI(4,5)P<sub>2</sub> dynamics. We thus studied whether K<sub>v</sub>12.1 channels were modulated by activation of phospholipase C  $\beta$  (PLC $\beta$ ) and found that they were insensitive to receptor-triggered depletion of PI(4,5)P<sub>2</sub>. Thus, K<sub>v</sub>12.1 channels add to the growing list of K<sup>+</sup> channels that are insensitive to PLC $\beta$  signaling, although modulated by PI(4,5)P<sub>2</sub> in *Xenopus laevis* oocytes.

### ARTICLE HISTORY

Received 19 February 2018  
Accepted 30 April 2018

### KEYWORDS

K<sub>v</sub>12; K<sub>v</sub>7; KCNQ; M current; mode shift; PI(4,5)P<sub>2</sub>; K<sub>v</sub>7; PI(3,4,5)P<sub>3</sub>; phospholipase C; G<sub>q</sub>PCR; Ci-VSP

## Introduction

The ether-à-go-go-gene-like (Elk; K<sub>v</sub>12) family of voltage-gated potassium (K<sub>v</sub>) channels comprises three members (K<sub>v</sub>12.1–K<sub>v</sub>12.3) that are predominantly expressed in neurons of various brain regions [1–6]. Despite recent significant progress in understanding biophysical properties and characteristics of these channels [7–10], at present only little information is available on physiological functions of the family members. Genetic deletion and pharmacological inhibition revealed that K<sub>v</sub>12.2 channels constitute sub-threshold K<sup>+</sup> conductance regulating excitability of pyramidal neurons in hippocampus [11], but no native physiological relevance could be attributed to K<sub>v</sub>12.1 and K<sub>v</sub>12.3 subunits so far. As K<sub>v</sub>12.1 channels activate at hyperpolarized membrane potentials [7,8,10], it is reasonable to assume that these channels also modulate neuronal excitability.

A prominent and characteristic feature of K<sub>v</sub>12.1 channels is a mode shift of activation (also referred to as pre-pulse facilitation or voltage-dependent potentiation) [7,8,12]. This biophysical phenomenon describes hysteresis of voltage-dependent channel activation that most probably is caused by time-dependent stabilization of the channel's voltage

sensor in a “relaxed” open state in response to depolarized (conditioning) holding potentials [13,14]. It was shown recently that prolonged depolarization of the membrane potential induces slow rearrangement of a structural interaction between domains in the C- and N-terminus of K<sub>v</sub>12.1 channels [8]. This rearrangement apparently is coupled to channel gating and necessary for transition of K<sub>v</sub>12.1 channels into the more stable gating mode that favors channel opening [8]. Accordingly, conditioning depolarisation of the membrane potential causes a large shift in voltage dependence of activation to hyperpolarized potentials and a slowing of deactivation of K<sub>v</sub>12.1 channels [7,8,10]. This mode shift may constitute a biophysical adaption to dampen excitability of neurons upon ongoing stimulation possibly also to prevent hyperexcitability in nervous tissue. Analogous mode shift of related K<sub>v</sub>11.1 channels might contribute to repolarization of cardiac action potentials through slowing of channel deactivation [15,16], but to our knowledge physiological relevance of this mode shift in neurons has not been demonstrated.

Recently, it was shown that K<sub>v</sub>12.1 channel activity was regulated through membrane-associated phosphatidylinositol-4,5-bisphosphate (PI(4,5)P<sub>2</sub>)

[7] that is a minor component of the inner leaflet of the plasma membrane and a well-known co-factor of many ion channels [17–19]. Li and colleagues showed that loss of phosphoinositides (PI) induced by excision of membrane patches from *Xenopus laevis* oocytes caused acceleration of  $K_v12.1$  channel activation and deactivation and a potentiation of steady-state  $K^+$  currents. Furthermore, excision of membrane patches expressing  $K_v12.1$  channels caused a shift of voltage dependence of channel activation to hyperpolarized potentials and almost completely eliminated voltage-dependent mode shift [7]. As application of a water soluble  $PI(4,5)P_2$  analogue restored  $K_v12.1$  channel kinetics as well as voltage dependence, and partially brought-back mode shift, the authors consistently concluded that  $PI(4,5)P_2$  in a bimodal way of action stabilized the open state, but at the same time inhibited voltage dependent activation of  $K_v12.1$  channels [7]. Accordingly, variations of membrane  $PI(4,5)P_2$  levels might control excitability of neurons through modulating  $K_v12.1$  channel activity. Most interestingly, impact of  $PI(4,5)P_2$  level changes on neuronal excitability might vary considerably with the general excitation status of the neuron, as the extent of mode shift apparently also was PI-dependent [7]. Unfortunately, it has not been shown yet whether  $K_v12.1$  channels were sensitive to physiologically-relevant  $PI(4,5)P_2$  depletion at all. As activation of phospholipase C  $\beta$  (PLC $\beta$ ) through  $G_q$  protein-coupled receptors ( $G_q$ PCR) constitutes an important signaling pathway to deplete  $PI(4,5)P_2$  in neurons [20,21], we studied whether  $K_v12.1$  channels were modulated by activation of  $G_q$  protein-coupled muscarinic receptors.

## Results

### Analyzing voltage-dependent mode shift of $K_v12.1$ channels

We analyzed sensitivity to  $G_q$ PCR signaling of human  $K_v12.1$  channels heterologously expressed in CHO cells. To be able to analyze whether voltage-dependent activation of  $K_v12.1$  channels was sensitive to activation of the  $G_q$ PCR pathway, we first established appropriate voltage protocols to study voltage dependence of these channels. As recently reported [10], we applied depolarizing

holding potentials (conditioning voltage; 200 ms) before a series of activating voltage steps (pulse potentials from  $-140$  mV to  $+10$  mV; 600 ms) (Figure 1(A,B)). We activated  $K_v12.1$  channels for as short as 600 ms, as we previously found that 600 ms allowed for steady-state activation of  $K_v12.1$  channels, whereas longer activating pulses attenuated mode shift due to longer time intervals at hyperpolarized potentials [10]. Accordingly, we also recorded tail currents at correspondingly depolarized potentials to minimize time at hyperpolarized voltages (Figure 1(B)). These voltage protocols elicited robust, outwardly-rectifying and voltage-dependent  $K_v12.1$  currents in CHO cells (Figure 1(A)). For conditioning voltages of  $-60$  mV, half-maximal voltage ( $V_h$ ) and slope factor of  $K_v12.1$  channel activation were  $-21.3 \pm 2.1$  mV and  $-14.6 \pm 1.3$  mV, respectively ( $n = 6$ ; Figure 1(C–E)). When cells were held at a depolarized conditioning potential of 0 mV,  $V_h$  of channel activation was  $-68.2 \pm 5.2$  mV and the slope factor was  $-8.1 \pm 0.8$  mV ( $n = 6$ ; Figure 1(C–E)). Accordingly, as reported by us and others [7,8,10] depolarizing conditioning potentials induced a large shift of voltage dependence to hyperpolarized potentials by about  $-50$  mV. This shift of voltage dependence in response to depolarized holding potentials is generally referred to as mode shift of activation [12].

### $K_v12.1$ channels are insensitive to physiological $PI(4,5)P_2$ depletion through PLC $\beta$

Recently, it was shown that activity of  $K_v12.1$  channels was modulated by PI in membrane patches excised from *Xenopus laevis* oocytes [7,8]. We thus set out to analyze in CHO cells whether these channels were also sensitive to stimulation of  $G_q$ PCR signaling that physiologically leads to depletion of membrane  $PI(4,5)P_2$  through activation of PLC $\beta$ . To this end, we overexpressed  $G_q$ -coupled muscarinic receptor type 1 (m1R) in CHO cells and activated the receptor by extracellular application of oxotremorine-M (Oxo-M;  $10 \mu\text{M}$ ). In this expression system, activation of recombinant m1R reconstitutes  $G_q$ PCR signaling and induces depletion of  $PI(4,5)P_2$  through endogenous PLC $\beta$  thereby producing second messengers diacylglycerol (DAG) and inositol-1,4,5-

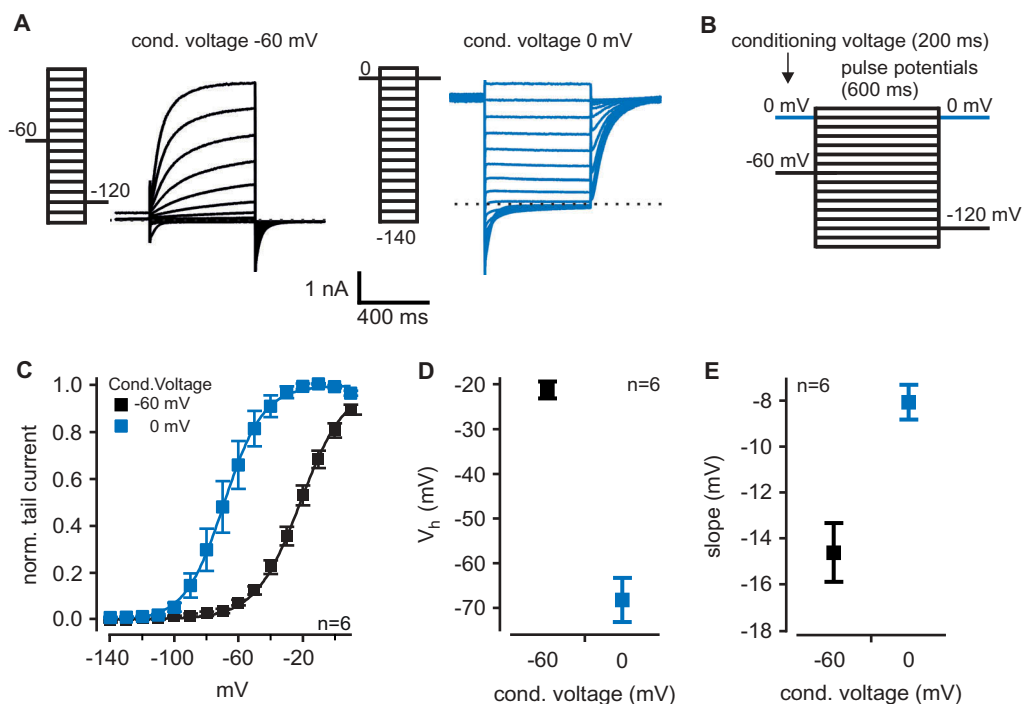


**Figure 1.** Mode shift of recombinant human Kv12.1 channels.

(A) Representative patch clamp recording of a CHO cell transiently transfected with human Kv12.1 channels activated by the voltage steps as indicated. (B) Voltage protocols consisted of a 200 ms conditioning potential step to  $-60$  mV (black) or  $0$  mV (blue) followed by 600 ms activating pulse potentials from  $-140$  mV to  $+10$  mV (10 mV increments). Tail currents were elicited either at  $-120$  mV or at  $0$  mV to minimize time at hyperpolarized membrane potentials (voltage protocols were established in a recent publication [10]). (C-E) Summary of voltage dependence of human Kv12.1 channels. (C) Voltage dependence was analyzed with Boltzmann fits to individual recordings as shown in (A). Solid lines in (C) represent Boltzmann fits to averaged data. Depolarized conditioning potential of  $0$  mV induced a large shift of voltage dependence to hyperpolarized potentials, as recently reported [10]. (D) shows mean  $V_h$  and (E) displays mean slope factor of channel activation in dependence of conditioning potentials of  $-60$  mV and  $0$  mV (values were derived from Boltzmann fits shown in (C)).

triphosphate (I(1,4,5)P<sub>3</sub>) [e.g. 20,22–25]. At start, we co-expressed *bona fide* PI(4,5)P<sub>2</sub>-sensitive homomeric Kv7.4 or Kv7.3 channels together with m1R. We utilized Kv7.3 channels carrying a A315T mutation in the pore region to increase whole cell currents without however affecting the channel's sensitivity to PI(4,5)P<sub>2</sub> depletion (Kv7.3<sup>T</sup> [26,27]). We found that stimulation of m1R strongly reduced Kv7.4- and Kv7.3<sup>T</sup>-mediated currents (Figure 2(A,B)). It is well established that m1R-dependent inhibition of Kv7 channels mainly depends on PLCβ-dependent depletion of PI(4,5)P<sub>2</sub> [22,23,28,29] and that degree of inhibition corresponds to PI(4,5)P<sub>2</sub> affinity of the respective Kv7 isoform [30]. In line, activation of m1R caused stronger inhibition of Kv7.4 that exhibit lower PI(4,5)P<sub>2</sub> affinity than Kv7.3<sup>T</sup> channels [29–31]. These recordings demonstrated robust activation

of G<sub>q</sub>PCR signaling and substantial PLCβ-dependent PI(4,5)P<sub>2</sub> depletion in CHO cells upon stimulation of m1R. In contrast, Kv12.1-mediated steady-state currents elicited by voltages between  $-140$  mV and  $+10$  mV were not affected by stimulation of m1R through Oxo-M (Figure 2(A–E)). G<sub>q</sub>PCR-dependent activation of PLCβ also did not change kinetics of activation (Figure 2(F)) and deactivation (Figure 2(G)) of human Kv12.1 channels in CHO cells. After 60 s of application of Oxo-M (10 μM),  $V_h$  of activation was  $-23.7 \pm 2.1$  mV and  $-67.3 \pm 5.6$  mV for conditioning voltages of  $-60$  mV and  $0$  mV, respectively (Figure 2(H,I)). Thus, also voltage dependence of human Kv12.1 channels was not affected by stimulation of PLCβ demonstrating that mode shift of Kv12.1 channels was not sensitive to activation of the pathway in CHO cells. To rule out that for

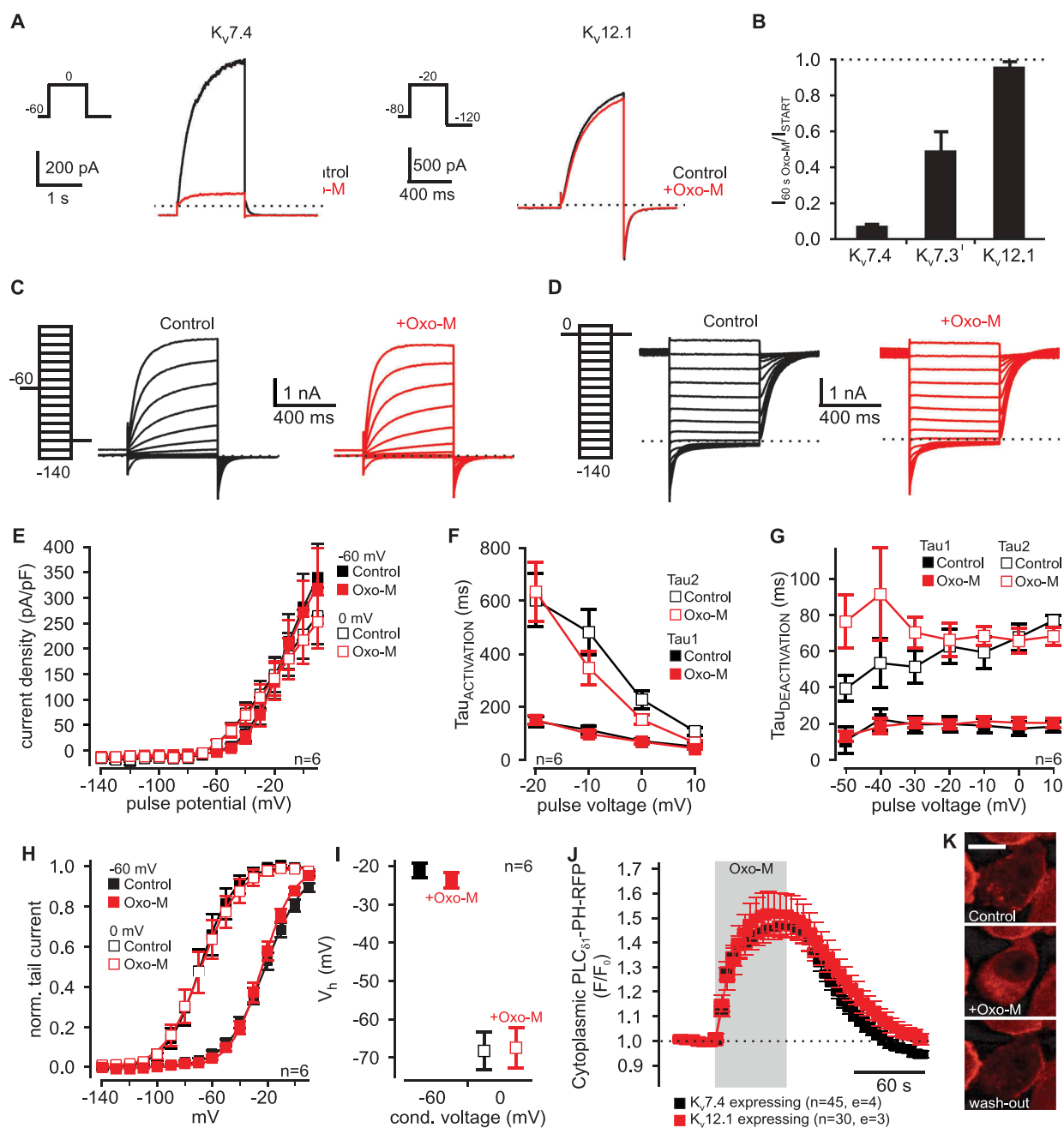


**Figure 2.** Human  $K_v12.1$  channels are insensitive to  $G_q$ PCR/PLC $\beta$  signaling.

(A + B) Activation of muscarinic  $G_q$  protein-coupled receptor type 1 (m1R) by Oxo-M ( $10 \mu\text{M}$ ) strongly inhibited *bona fide* PI(4,5) $P_2$ -sensitive  $K_v7.4$  and  $K_v7.3^T$  channels. In contrast,  $K_v12.1$ -mediated currents were resistant to stimulation of m1R. (A) shows representative  $K_v7.4$ - and  $K_v12.1$ -mediated whole cell currents before (*black*) and at the end of a 60 s application of  $10 \mu\text{M}$  Oxo-M (*red*) (voltage protocol and scale bars as indicated). (B) shows a summary of recordings as presented in (A). (C–E) Steady-state  $K_v12.1$  currents elicited by voltage steps between  $-140$  mV and  $+10$  mV were not sensitive to activation of m1R through Oxo-M ( $10 \mu\text{M}$ ). (F) Neither activating kinetics nor (G) deactivating kinetics of  $K_v12.1$  channels were altered upon activation of m1R (time constants were calculated from double-exponential fits to the activating current component and to deactivating tail currents). (C + D) show representative whole cell  $K_v12.1$  currents elicited by the voltage protocols indicated. To induce voltage-dependent mode shift of  $K_v12.1$  channels, voltage protocols consisted of a 200 ms conditioning potential step to (C)  $-60$  mV or (D)  $0$  mV followed by 600 ms activating pulse potentials from  $-140$  mV to  $+10$  mV ( $10$  mV increments). (H + I) Oxo-M-dependent activation of m1R did not change voltage-dependence or mode-shift of  $K_v12.1$  channels expressed in CHO cells. (H) shows a summary of the voltage dependence of human  $K_v12.1$  channels and (I) displays mean  $V_h$  derived from Boltzmann fits to individual recordings as shown in (C) and (D) (solid lines in (H) represent Boltzmann fits to averaged data; Data with Oxo-M were analyzed at the end of 60 s Oxo-M application; control recordings are also shown in Figure 1). (J + K) In CHO cells coexpressing m1R together with  $K_v7.4$ , application of Oxo-M ( $10 \mu\text{M}$ ) induced robust and reversible translocation of the optical PI(4,5) $P_2$ /l(1,4,5) $P_3$  biosensor  $\text{PLC}_{\beta 1}\text{-PH-RFP}$  from the membrane to the cytoplasm.  $\text{PLC}_{\beta 1}\text{-PH-RFP}$  translocation was indistinguishable between cells coexpressing  $K_v12.1$  or  $K_v7.4$  channels together with m1R. Thus, PLC $\beta$  activation was comparable in cells expressing  $K_v7.4$  or  $K_v12.1$ . (J) shows mean RFP fluorescence intensities measured in confocal sections averaged over a region of interest in the cytoplasm of CHO cells coexpressing  $\text{PLC}_{\beta 1}\text{-PH-RFP}$  together with either  $K_v12.1$  or  $K_v7.4$ . (K) shows representative images of a CHO cell expressing  $K_v12.1$  together with m1R before (*top*), after 60 s application of Oxo-M (*middle*) and after wash-out of the agonist (*bottom*). The scale bar represents  $10 \mu\text{m}$ .

some reason depletion of PI(4,5)P<sub>2</sub> was reduced in CHO cells expressing K<sub>v</sub>12.1 channels, we then directly assessed activity of PLCβ under our experimental conditions. We quantified putative PLCβ activity using pleckstrin homology (PH) domain of PLC<sub>δ1</sub> fused to RFP (PLC<sub>δ1</sub>-PH-RFP) as genetically-encoded, optical biosensor that binds to membrane PI(4,5)P<sub>2</sub>, but also to cytoplasmic I(1,4,5)P<sub>3</sub> [32]. PLC<sub>δ1</sub>-PH-RFP associates to the plasma membrane, when resting PI(4,5)P<sub>2</sub> levels are high, and translocates into the cytoplasm in response to PLCβ-dependent decrease of membrane PI(4,5)P<sub>2</sub> and a corresponding increase of cytoplasmic I(1,4,5)P<sub>3</sub> [32,33]. Accordingly, changes of the fluorescence intensity at the membrane or in the cytoplasm are a measure for the activity of PLCβ during stimulation of G<sub>q</sub>PCR [17,34]. Here, we used confocal imaging to monitor translocation of PLC<sub>δ1</sub>-PH-RFP from membrane to the cytoplasm of transiently transfected CHO cells during application of Oxo-M (10 μM). In cells, coexpressing m1R together with PLC<sub>δ1</sub>-PH-RFP and K<sub>v</sub>7.4 channels, RFP-associated fluorescence in the cytoplasm strongly increased during activation of the G<sub>q</sub>PCR. This increase of fluorescence indicated translocation of the sensor from membrane into cytoplasm and thus PLCβ-mediated PI(4,5)P<sub>2</sub> depletion (Figure 2(J)). Upon wash-out of Oxo-M, the signal recovered within a couple of minutes demonstrating reversibility of PI(4,5)P<sub>2</sub> depletion. When we activated m1R in cells coexpressing K<sub>v</sub>12.1 channels, sensor translocation into the cytoplasm and its return to the plasma membrane were indistinguishable from cells expressing K<sub>v</sub>7.4 (Figure 2(J,K)). These experiments demonstrated that PLCβ was strongly activated under our experimental conditions and that PLCβ activity and thus PI(4,5)P<sub>2</sub> depletion were the same in cells expressing K<sub>v</sub>7.4 and K<sub>v</sub>12.1 channels. Taking together these data showed that human K<sub>v</sub>12.1 channels were not sensitive to activation of G<sub>q</sub>PCR signaling and more importantly PLCβ-mediated PI(4,5)P<sub>2</sub> depletion in CHO cells.

### **Recombinant K<sub>v</sub>12.1 channels are insensitive to Ci-VSP-dependent PI(4,5)P<sub>2</sub> depletion**

To assess in more detail whether K<sub>v</sub>12.1 channels were sensitive to PI(4,5)P<sub>2</sub> depletion in CHO cells,

we utilized voltage-sensitive PI 5-phosphatase from *Ciona intestinalis* (Ci-VSP). Upon depolarization of the membrane potential, Ci-VSP rapidly removes PI(4,5)P<sub>2</sub> and PI(3,4,5)P<sub>3</sub> from the membrane by dephosphorylation to PI(4)P and PI(3,4)P<sub>2</sub>, respectively [35–39]. In these experiments, we selected cells for clear membrane localization of Ci-VSP-RFP-associated fluorescence and recorded K<sub>v</sub>7 and K<sub>v</sub>12.1 currents activated by depolarizing voltage steps from the holding potential of –80 mV to 0 mV or –20 mV, respectively (Figure 3(A)). After recording stable control current amplitudes for at least 30 s, the holding potential was depolarized for another 30 s to +80 mV to activate Ci-VSP. As shown in Figure 3(A,B), currents through homomeric K<sub>v</sub>7.2 and K<sub>v</sub>7.3<sup>T</sup> channels were strongly inhibited by activation of Ci-VSP. After 30 s of Ci-VSP activation at +80 mV, K<sub>v</sub>7.2 and K<sub>v</sub>7.3<sup>T</sup> currents were reduced to 27.8 ± 4.6% and 40.6 ± 1.9% of baseline current amplitudes, respectively (Figure 3(A,B)). This inhibition of K<sub>v</sub>7-mediated currents, especially inhibition of K<sub>v</sub>7.3<sup>T</sup> channels that exhibit higher PI(4,5)P<sub>2</sub> affinity than K<sub>v</sub>7.2, demonstrated substantial depletion of membrane PI(4,5)P<sub>2</sub> upon activation of Ci-VSP, in line with many previous reports [e.g. 29, 38]. In these experiments, K<sub>v</sub>7 currents returned to baseline within a minute after deactivation of Ci-VSP at hyperpolarized potentials demonstrating reversible PI(4,5)P<sub>2</sub> depletion and its resynthesis through endogenous PI kinases (Figure 3(B)) [38]. Interestingly after deactivation of Ci-VSP, K<sub>v</sub>7.2-mediated currents transiently over-recovered before returning to baseline amplitudes indicating some kind of over-recovery of PI(4,5)P<sub>2</sub> levels possibly stimulated by Ci-VSP-induced PI(4,5)P<sub>2</sub> depletion [c.f. 38].

In contrast to K<sub>v</sub>7 currents, K<sub>v</sub>12.1 channels were almost completely resistant to activation of co-expressed Ci-VSP utilizing the same voltage protocol to activate the phosphatase. After 30 s at +80 mV, K<sub>v</sub>12.1 current amplitudes were 92.7 ± 1.3% of control currents before voltage-dependent activation of Ci-VSP (n = 5; Figure 3(A,B)). In three out of five cells tested, we detected slight acceleration of the activating kinetics of K<sub>v</sub>12.1 channels in response to stimulation of Ci-VSP (Figure 3(C)). As these changes of kinetics were small and not detectable in all cells, we did not examine the phenomenon any further.

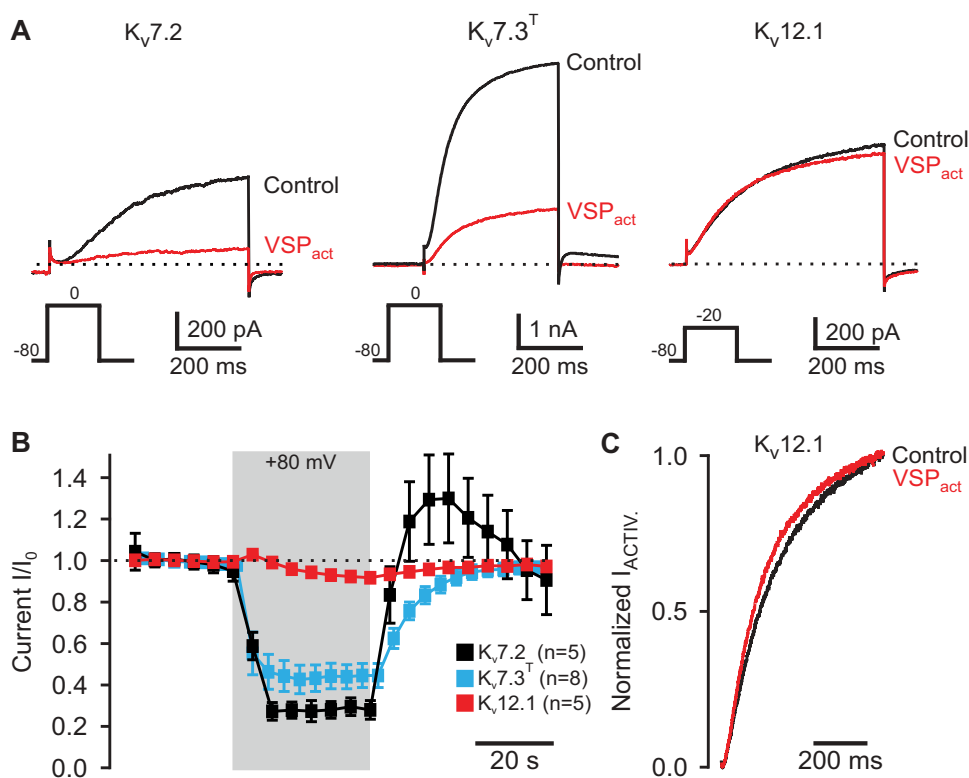


**Figure 3.** In CHO cells, human  $K_v12.1$  channels are insensitive to activation of a voltage-sensitive  $PI(4,5)P_2/PI(3,4,5)P_3$  5-phosphatase from *ciona intestinalis*.

**(A + B)** Activation of Ci-VSP through 30 s depolarization of the holding potential to +80 mV reversibly inhibited recombinant  $K_v7.2$  and  $K_v7.3^T$  channels. In contrast,  $K_v12.1$ -mediated current amplitudes were largely insensitive to voltage-dependent activation of Ci-VSP. **(A)** shows representative recordings of  $K_v7.2$ ,  $K_v7.3^T$  or  $K_v12.1$  currents before (*black*) and at the end of Ci-VSP activation for 30 s (*red*) (voltage steps to activate  $K^+$  channel were applied every 5 s; Ci-VSP was activated by depolarization to +80 mV between these voltage steps). **(B)** displays averaged time course of recordings as shown in **(A)**. **(C)** In only three out of five cells, we found slight acceleration of  $K_v12.1$  activating kinetics upon voltage-dependent activation of Ci-VSP. **(C)** shows exemplary normalized  $K_v12.1$  currents activating upon a voltage step from  $-80$  mV to  $-20$  mV before (*black*) and after activation of Ci-VSP at +80 mV for 30 s (*red*).

In summary,  $K_v12.1$  channels were not affected by Ci-VSP-dependent depletion of  $PI(4,5)P_2$  in CHO cells. Thus, we conclude that  $K_v12.1$  channels are not relevantly modulated by membrane  $PI(4,5)P_2$  in this cell line. As Ci-VSP stoichiometrically converts  $PI(4,5)P_2$  into  $PI(4)P$  thereby substantially increasing  $PI(4)P$  levels in the membrane [39], these data also demonstrated that  $K_v12.1$  channels are not modulated by membrane-associated  $PI(4)P$ .

## Discussion

Activation of  $PLC\beta$  through  $G_{q/11}$ -coupled receptors is an important intercellular signaling pathway that induces  $PI$  dynamics in neurons [17,18,21]. Although  $PLC\beta$  possibly also hydrolyses  $PI(4)P$  [20,40,41], it is well known that  $PI$

$(4,5)P_2$  is the prime substrate of its enzymatic activity in living cells [21]. Whereas actual changes in membrane-associated  $PI(4,5)P_2$  might vary significantly depending on the receptor type, as well as on the activity of  $PLC\beta$  and  $PI(4,5)P_2$  resynthesis pathways, it is generally believed that the signaling cascade affects cellular physiology also through depletion of  $PI(4,5)P_2$  [20,21,32]. Thus, as  $PI(4,5)P_2$  is an important cofactor for many ion channels, activation of  $PLC\beta$  is directly linked to neuronal excitability through  $PI(4,5)P_2$  depletion and  $PI(4,5)P_2$ -dependent modulation of ion channel activity. As one prominent example, stimulation of endogenous  $G_q$ -coupled muscarinic receptors induces significant depolarization of neuronal membrane potentials through  $PI(4,5)P_2$ -dependent inhibition of  $K_v7$  potassium channels [22,23,42].

Here, we evaluated whether human  $K_v12.1$  channels were sensitive to physiological changes of  $PI(4,5)P_2$  for two reasons: (i) As no physiological function could be assigned to  $K_v12.1$  channels yet, novel properties of these channels might be useful to identify native  $K_v12.1$ -mediated currents in neurons [c.f. 10]. We thus considered  $PLC\beta$  sensitivity of  $K_v12.1$  channels a potentially interesting feature fostering future attribution of neuronal  $K^+$  currents to  $K_v12.1$  channels. And (ii), recently it was shown for  $K_v12.1$  channels that excision of membrane patches from *Xenopus laevis* oocytes speeded activation and deactivation, shifted voltage dependence to hyperpolarized potentials and significantly attenuated mode shift [7]. Importantly, such excision of membrane patches into solution without ATP causes depletion of  $PI(4,5)P_2$  (and possibly other PI species) through irreversible activation of phosphatases [19,24,28,31,43,44]. As application of a water-soluble  $PI(4,5)P_2$  analogue restored  $K_v12.1$  channel properties in the excised inside-out patches, these findings demonstrated  $PI(4,5)P_2$  sensitivity of  $K_v12.1$  channels [7]. We considered this  $PI(4,5)P_2$  sensitivity especially interesting, as by attenuating mode shift and by affecting voltage dependence of these channels, impact of  $PLC\beta$  activation on the excitability of  $K_v12.1$  expressing neurons might significantly vary depending on synaptic input and thus excitation status of the respective neuron. Utilizing m1R as G protein-coupled receptor to activate  $PLC\beta$  in an expression system, we studied sensitivity of human  $K_v12.1$  channels to  $G_qPCR$  signaling. It has been shown in many studies that overexpression of a  $G_qPCR$  (such as m1R) adequately reconstitutes  $PLC\beta$  signaling in expression systems (including CHO cells used in our report). Through activation of endogenous  $PLC\beta$ , stimulation of recombinant m1R substantially depletes  $PI(4,5)P_2$  [20,22,23,24,25,30,34], produces reasonable amounts of DAG and  $I(1,4,5)P_3$ , induces  $I(1,4,5)P_3$ -dependent  $Ca^{2+}$  release and activates downstream effectors of the cascade (e.g. protein kinase C, PKC) [20,22,30,34,45,46]. This has been used successfully to explore sensitivity of ion channels to physiological  $PI(4,5)P_2$

depletion [20,22,29,30,47], but also the modulation of ion channels through second messengers downstream of  $PLC\beta$  activation [48–51]. Importantly, heterologous systems can even be utilized to dissect  $PI(4,5)P_2$  dependence of ion channels from their sensitivity to second messengers produced during activation of  $PLC\beta$  [47,49,52]. Heterologous expression systems accordingly constitute a well-accepted model to study the  $G_qPCR$  pathway and  $PI(4,5)P_2$  dependence of ion channels [17,18]. The stimulation of  $PLC\beta$  as well as voltage-dependent activation of Ci-VSP strongly inhibited *bonafide*  $PI(4,5)P_2$ -dependent  $K_v7$  channels (c.f. Figures 2 and 3). Especially, the significant inhibition of  $K_v7.3^T$  channels that exhibit considerably higher  $PI(4,5)P_2$  affinity than  $K_v7.2$  or  $K_v7.4$  channels [29,30,38] demonstrated substantial  $PI(4,5)P_2$  depletion under our experimental conditions. Translocation of the optical  $PI(4,5)P_2$  biosensor  $PLC_{\delta 1}$ -PH-RFP from the membrane during stimulation of m1R additionally showed strong reduction of  $PI(4,5)P_2$  levels in these experiments. However,  $K_v12.1$  channels were not sensitive to this  $PLC\beta$ -mediated  $PI(4,5)P_2$  depletion at all. Theoretically, a rise in DAG,  $I(1,4,5)P_3$  and intracellular  $Ca^{2+}$  or activation of PKC could stimulate  $K_v12.1$ , which might counterbalance PI depletion thereby masking  $PI(4,5)P_2$  sensitivity of these channels. However, although we consider such a mechanism rather unlikely, we want to point out that we cannot exclude sensitivity of  $K_v12.1$  to these second messengers completely at present.  $K_v7$ -mediated currents are indeed reduced by PKC-dependent phosphorylation [48] and  $Ca^{2+}$ /calmodulin signaling [53], but importantly  $G_qPCR$ -dependent inhibition of these channels almost exclusively depends on  $PI(4,5)P_2$  depletion and not on messengers produced by  $PLC\beta$  [23,29]. Based on these considerations, we conclude that  $K_v12.1$  channels are resistant to stimulation of  $G_qPCR$  and importantly insensitive to physiologically-relevant  $PI(4,5)P_2$  dynamics. This insensitivity of  $K_v12.1$  channels to stimulation of  $PLC\beta$  is not surprising, as several other  $K^+$  channels, including members of the  $K_v1$ ,  $K_v2$ ,  $K_v3$ , and  $K_v4$  families, have been described to be not affected by stimulation of

the PLC $\beta$  pathway and of Ci-VSP [24,25]. However, it is surprising that for some of these K<sub>v</sub> channels (K<sub>v</sub>1.1, K<sub>v</sub>1.4, K<sub>v</sub>1.5, K<sub>v</sub>3.4), just as for K<sub>v</sub>12.1 channels, PI(4,5)P<sub>2</sub> sensitivity was reported using excised patches from *Xenopus laevis* oocytes as experimental model [54,55]. Importantly however, like K<sub>v</sub>12.1 these channels were resistant to activation of m1R and Ci-VSP in mammalian cell lines [24,25]. As comprehensively discussed by the Hille group [24,25], we do not think that our findings represent a discrepancy to results obtained in the frog oocytes (presented by Li and colleagues [7]). First, upon excision of inside-out patches levels of membrane PI(4,5)P<sub>2</sub> might fall well below levels reached by physiological stimulation of PLC $\beta$  (and possibly even by activation of Ci-VSP) and other PI species may also be depleted during the patch excision. Conversely, perfusion of membrane patches with water soluble PI analogues might introduce super-physiological PI(4,5)P<sub>2</sub> levels within or close to the membrane [25]. Therefore, on the one hand PI sensitivity of ion channels might be overestimated upon PI(4,5)P<sub>2</sub> depletion through patch excision and subsequent application of exogenous PI(4,5)P<sub>2</sub>. On the other hand, the degree of PLC $\beta$ -dependent PI(4,5)P<sub>2</sub> depletion might be just too low to induce relevant modulation of K<sub>v</sub>12.1 channel activity. And second, as comprehensively discussed and pointed-out by Li and colleagues [7], K<sub>v</sub>12.1 channels might exhibit low PI affinity and low selectivity between different PI species. This conclusion is supported by the fact that not only PI(4,5)P<sub>2</sub> but probably also other PI species might be depleted after excision of the membrane patches from oocytes. This depletion of several PI species upon patch excision might affect ion channels with unselective PI specificity even stronger than a highly selective channel that recognizes only a certain PI species. Supporting this notion, in membrane patches excised from *Xenopus* oocytes mode shift of K<sub>v</sub>12.1 channels was sensitive to application of PI(4)P, PI(4,5)P<sub>2</sub> and PI(3,4,5)P<sub>3</sub> [7]. This strongly indicated that K<sub>v</sub>12.1 channels (in contrast to e.g. K<sub>v</sub>7 channels) do not exhibit highly selective binding to

a certain PI species, but rather general electrostatic interactions with several PI [7]. Completely in line, K<sub>v</sub>12.1 channels were resistant to activation of Ci-VSP in CHO cells, which stoichiometrically converts PI(4,5)P<sub>2</sub> and PI(3,4,5)P<sub>3</sub> into PI(4)P and PI(3,4)P<sub>2</sub>, respectively [35–37,39]. Whilst depleting PI(4,5)P<sub>2</sub> from the membrane, activation of Ci-VSP thus leaves constant the total PI concentration in the plasma membrane. At the same time however, Ci-VSP substantially increases PI(4)P levels [38,39], which revealed that activity of K<sub>v</sub>12.1 channels is not relevantly modulated by PI(4)P. This low sensitivity to Ci-VSP activation (and PLC $\beta$  signaling) may as well point to lack of selectivity towards PI(4,5)P<sub>2</sub> thereby indicating a rather general PI sensitivity of K<sub>v</sub>12.1 channels. In line, EC<sub>50</sub> values of K<sub>v</sub>12.1 channels for application of exogenous PI(4,5)P<sub>2</sub> expressed in *Xenopus* oocytes (approx. 10  $\mu$ M [7]) were well in the range previously demonstrated for K<sub>v</sub>7.3 channels [28]. However, most probably due to high PI(4,5)P<sub>2</sub> specificity and selectivity, K<sub>v</sub>7.3 channels are readily inhibited by activation of m1R and Ci-VSP, whereas K<sub>v</sub>12.1 channels are not. In line, sensitivity of K<sup>+</sup> channels to activation of Ci-VSP generally correlates well with their sensitivity towards receptor-triggered activation of PLC [29], which apparently is also true for K<sub>v</sub>12.1 channels.

Thus, in summary, human K<sub>v</sub>12.1 channels most probably exhibit unselective PI sensitivity thereby adding to the growing list of K<sub>v</sub> channels resistant to stimulation of G<sub>q</sub>PCR/PLC $\beta$ -signaling and Ci-VSP-dependent PI(4,5)P<sub>2</sub> depletion [c.f. 24, 25].

## Methods

### Cell culture and transfection

Chinese hamster ovary (CHO) dhFR<sup>-</sup> cells were maintained as previously reported [56]. In brief, cells were kept in MEM Alpha Medium supplemented with 10% fetal calf serum (FCS) and 1% penicillin/streptomycin (pen/strep) (all Invitrogen GmbH, Darmstadt, Germany) in a humidified atmosphere at 5% CO<sub>2</sub> and 37°C. Transient transfection of CHO cells in culture was done with jetPEI



transfection reagent (Polyplus Transfection, Illkirch, France) and all experiments were performed at room temperature (22°C–25°C) approx. 24–48 h after transfection. The following vectors for transient expression in CHO cells were used: K<sub>v</sub>7.2-pBK-CMV (gene: human KCNQ2; UniProt accession number: O43526), K<sub>v</sub>7.3(A315T)-pBK-CMV (human KCNQ3(A315T); O43525), K<sub>v</sub>7.4-pBK-CMV (human KCNQ4; P56696), K<sub>v</sub>12.1(Elk1)-pcDNA3.1-IRES-eGFP (human KCNH8; Q96L42), human muscarinic receptor 1 (human M1R)-pSGHV0 (Q96RH1), Ci-VSP-mRFP-C1 (Q4W8A1), PLC<sub>δ1</sub>-PH-mRFP-C1 (amino acids 1–70; P51178) and pEGFP-C1 (transfection control; Addgene, Teddington, UK).

### Electrophysiological recordings

Electrophysiological recordings (in the whole cell configuration) were performed with an Axopatch 200B amplifier (Molecular Devices, Union City, CA) in voltage-clamp mode [57]. Recordings were low-pass filtered at 2 kHz and sampled at 5 kHz. In the figures, voltage protocols are indicated and the dashed lines highlight zero current. Borosilicate glass patch pipettes (Sutter Instrument Company, Novato, CA, USA) used had an open pipette resistance of 2–3 MΩ after back-filling with intracellular solution containing (in mM) 135 KCl, 2.41 CaCl<sub>2</sub> (100 nM free Ca<sup>2+</sup>), 3.5 MgCl<sub>2</sub>, 5 HEPES, 5 EGTA, 2.5 Na<sub>2</sub>ATP, 0.1 Na<sub>3</sub>GTP, pH 7.3 (with KOH), 290–295 mOsm/kg. Series resistance (R<sub>s</sub>) typically was below 6 MΩ and compensated throughout the recordings (80–90%), and liquid junction potentials were not compensated (approx. –4 mV). For presentation whole cell currents were normalized to the cell capacitance (current density; pA/pF) or to baseline current amplitude (I/I<sub>0</sub>). The extracellular solution contained (in mM) 144 NaCl, 5.8 KCl, 1.3 CaCl<sub>2</sub>, 0.9 MgCl<sub>2</sub>, 0.7 NaH<sub>2</sub>PO<sub>4</sub>, 10 HEPES and 5.6 D-glucose, pH 7.4 (with NaOH), 305–310 mOsm/kg.

### Voltage-dependent activation of Ci-VSP

For coexpression of ion channels with Ci-VSP-RFP, cells were selected for clear membrane localization of RFP (attached to Ci-VSP). K<sub>v</sub> channel-mediated currents were elicited every 5 s with the voltage protocol indicated in the figure and Ci-

VSP was activated in between those voltage steps by depolarizing the holding potential to +80 mV for a total of 30 s, as previously reported [47].

### Confocal microscopy

Confocal imaging was performed with an upright LSM 710 – Axio Examiner.Z1 microscope equipped with a W Plan/Apochromat 20x/1.0 DIC M27 75 mm water immersion objective (Zeiss, Jena, Germany) [58]. Red fluorescent protein (RFP) was excited at 561 nm with a DPSS 561–10 laser (Zeiss) and fluorescence emission was sampled at 582–754 nm. Green fluorescent protein (GFP) was excited at 488 nm with an argon laser and fluorescence emission was recorded at 493–597 nm. The sample interval for time series was 5 s. In these experiments, K<sub>v</sub>7.4 or K<sub>v</sub>12.1 expressing cells were identified through coexpression of GFP or the GFP expression associated with the pcDNA3.1-IRES-eGFP plasmid, respectively.

### Solutions and substances

Oxotremorine-M (Oxo-M) was purchased from Biotrend Chemikalien GmbH (Cologne, Germany) and was diluted to a concentration of 10 μM in extracellular solution. Oxo-M was applied locally through a custom-made application system via a glass capillary brought into close proximity to cells under investigation.

### Data analysis

Patch clamp recordings were analyzed with IgorPro (Wavemetrics, Lake Oswego, OR) and the PatchMaster (HEKA) software. Voltage dependence of activation was derived from tail current amplitudes using voltage protocols indicated: Tail currents were fitted with a two-state Boltzmann function with  $I = I_{min} + (I_{max} - I_{min}) / (1 + \exp((V - V_h) / s))$ , where  $I$  is current,  $V$  is the membrane voltage,  $V_h$  is the voltage at half maximal activation, and  $s$  describes the steepness of the curve [59]. Results are shown as conductance-voltage curves, obtained by normalizing to  $(I_{max} - I_{min})$ , obtained from fits to data of individual experiments. Time constants of activation and deactivation were

derived from double-exponential fits to deactivating current components at indicated potentials. Imaging time series were analyzed measured with confocal microscopy with Zen2009 (Zeiss) and IgorPro (Wavemetrics). PLC $_{\delta 1}$ -PH-mRFP fluorescent intensities were derived after background subtraction from averages over a region of interest (ROI) in the cytoplasm of transfected cells and are presented as cytoplasmic F/F $_0$ .

### Data presentation

In electrophysiological experiments,  $n$  represents the number of individual cells and accordingly the number of independent experiments (no pseudo-replication). In imaging experiments (c.f. Figure 2(J)),  $n$  represents the number of individual cells and  $e$  denotes the number of independent experiments.

### Acknowledgments

The authors thank Dr. T. Jegla for constructive comments on the manuscript and helpful discussion of data. We acknowledge the kind gift of plasmids for K $_v$ 7 channels from Dr T. Jentsch, K $_v$ 12.1 (Elk) from Dr T. Jegla, Ci-VSP from Dr Y. Okamura, and PLC $_{\delta 1}$ -PH from Dr T. Meyer. We thank Olga Ebers and Neslihan Özen for superb technical assistance.

### Disclosure statement

No potential conflict of interest was reported by the authors.

### Funding

This work was funded by Research Grants of the University Medical Center Giessen and Marburg (UKGM 17/2013; UKGM 13/2016 to M.G.L.) and by the German Research Foundation (DFG Priority Program 1608: "Ultrafast and temporally precise information processing: Normal and dysfunctional hearing", [LE 3600/1-1 to MGL]).

### ORCID

Michael G. Leitner  <http://orcid.org/0000-0002-3259-6481>

### References

- [1] Engeland B, Neu A, Ludwig J, et al. Cloning and functional expression of rat ether-a-go-go-like K $^+$  channel genes. *J Physiol.* 1998 Dec 15;513(Pt 3):647–654.
- [2] Miyake A, Mochizuki S, Yokoi H, et al. New ether-a-go-go K(+) channel family members localized in human telencephalon. *J Biol Chem.* 1999 Aug 27;274(35):25018–25025.
- [3] Shi W, Wang HS, Pan Z, et al. Cloning of a mammalian elk potassium channel gene and EAG mRNA distribution in rat sympathetic ganglia. *J Physiol.* 1998 Sep 15;511(Pt 3):675–682.
- [4] Zou A, Lin Z, Humble M, et al. Distribution and functional properties of human KCNH8 (Elk1) potassium channels. *Am J Physiol Cell Physiol.* 2003 Dec;285(6):C1356–66.
- [5] Trudeau MC, Titus SA, Branchaw JL, et al. Functional analysis of a mouse brain Elk-type K $^+$  channel. *J Neurosci.* 1999 Apr 15;19(8):2906–2918.
- [6] Saganich MJ, Machado E, Rudy B. Differential expression of genes encoding subthreshold-operating voltage-gated K $^+$  channels in brain. *J Neurosci.* 2001 Jul 1; 21(13):4609–4624.
- [7] Li X, Anishkin A, Liu H, et al. Bimodal regulation of an Elk subfamily K $^+$  channel by phosphatidylinositol 4,5-bisphosphate. *J Gen Physiol.* 2015 Nov;146(5):357–374.
- [8] Dai G, Zagotta WN. Molecular mechanism of voltage-dependent potentiation of KCNH potassium channels. *eLife.* 2017 Apr 27;6 . DOI:10.7554/eLife.26355
- [9] Kazmierczak M, Zhang X, Chen B, et al. External pH modulates EAG superfamily K $^+$  channels through EAG-specific acidic residues in the voltage sensor. *J Gen Physiol.* 2013 Jun;141(6):721–735.
- [10] Dierich M, Evers S, Wilke BU, et al. Inverse modulation of neuronal Kv12.1 and Kv11.1 channels by 4-aminopyridine and NS1643. *Front Neurosci.* 2018;11:11.
- [11] Zhang X, Bertaso F, Yoo JW, et al. Deletion of the potassium channel Kv12.2 causes hippocampal hyperexcitability and epilepsy. *Nat Neurosci.* 2010 Sep;13(9):1056–1058.
- [12] Villalba-Galea CA. Hysteresis in voltage-gated channels. *Channels (Austin).* 2017 Mar 4;11(2):140–155.
- [13] Bezanilla F, Taylor RE, Fernandez JM. Distribution and kinetics of membrane dielectric polarization. 1. Long-term inactivation of gating currents. *J Gen Physiol.* 1982 Jan;79(1):21–40.
- [14] Villalba-Galea CA, Sandtner W, Starace DM, et al. S4-based voltage sensors have three major conformations. *Proc Natl Acad Sci U S A.* 2008 Nov 18;105(46):17600–17607.
- [15] Trudeau MC, Warmke JW, Ganetzky B, et al. HERG, a human inward rectifier in the voltage-gated potassium channel family. *Science.* 1995 Jul 7;269(5220):92–95.
- [16] Sanguinetti MC, Jiang C, Curran ME, et al. A mechanistic link between an inherited and an acquired cardiac arrhythmia: HERG encodes the IKr potassium channel. *Cell.* 1995 Apr 21;81(2):299–307.
- [17] Leitner MG, Halaszovich CR, Ivanova O, et al. Phosphoinositide dynamics in the postsynaptic membrane compartment: mechanisms and experimental approach. *Eur J Cell Biol.* 2015 Jul-Sep;94(7–9):401–414.
- [18] Balla T. Phosphoinositides: tiny lipids with giant impact on cell regulation. *Physiol Rev.* 2013 Jul;93(3):1019–1137.

- [19] Suh BC, Hille B. PIP2 is a necessary cofactor for ion channel function: how and why? *Annu Rev Biophys.* 2008;37:175–195.
- [20] Horowitz LF, Hirdes W, Suh BC, et al. Phospholipase C in living cells: activation, inhibition, Ca<sup>2+</sup> requirement, and regulation of M current. *J Gen Physiol.* 2005 Sep;126(3):243–262.
- [21] Kadamur G, Ross EM. Mammalian phospholipase C. *Annu Rev Physiol.* 2013;75:127–154.
- [22] Shapiro MS, Roche JP, Kaftan EJ, et al. Reconstitution of muscarinic modulation of the KCNQ2/KCNQ3 K(+) channels that underlie the neuronal M current. *J Neurosci.* 2000 Mar 1;20(5):1710–1721.
- [23] Gomez-Posada JC, Etxeberria A, Roura-Ferrer M, et al. A pore residue of the KCNQ3 potassium M-channel subunit controls surface expression. *J Neurosci.* 2010 Jul 7;30(27):9316–9323.
- [24] Shapiro MS, Roche JP, Kaftan EJ, et al. Reconstitution of muscarinic modulation of the KCNQ2/KCNQ3 K(+) channels that underlie the neuronal M current. *J Neurosci.* 2000 Mar 1;20(5):1710–1721.
- [25] Suh BC, Hille B. Recovery from muscarinic modulation of M current channels requires phosphatidylinositol 4,5-bisphosphate synthesis. *Neuron.* 2002 Aug 1; 35(3):507–520. S0896627302007900 [pii].
- [26] Zhang H, Craciun LC, Mirshahi T, et al. PIP(2) activates KCNQ channels, and its hydrolysis underlies receptor-mediated inhibition of M currents. *Neuron.* 2003 Mar 27;37(6):963–975.
- [27] Rjasanow A, Leitner MG, Thallmair V, et al. Ion channel regulation by phosphoinositides analyzed with VSPs-PI(4,5)P2 affinity, phosphoinositide selectivity, and PI(4,5)P2 pool accessibility. *Front Pharmacol.* 2015;6:127.
- [28] Hernandez CC, Falkenburger B, Shapiro MS. Affinity for phosphatidylinositol 4,5-bisphosphate determines muscarinic agonist sensitivity of Kv7 K<sup>+</sup> channels. *J Gen Physiol.* 2009 Nov;134(5):437–448.
- [29] Li Y, Gamper N, Hilgemann DW, et al. Regulation of Kv7 (KCNQ) K<sup>+</sup> channel open probability by phosphatidylinositol 4,5-bisphosphate. *J Neurosci.* 2005 Oct 26;25(43):9825–9835.
- [30] Stauffer TP, Ahn S, Meyer T. Receptor-induced transient reduction in plasma membrane PtdIns(4,5)P2 concentration monitored in living cells. *Curr Biol.* 1998 Mar 12;8(6):343–346.
- [31] Hirose K, Kadowaki S, Tanabe M, et al. Spatiotemporal dynamics of inositol 1,4,5-trisphosphate that underlies complex Ca<sup>2+</sup> mobilization patterns. *Science.* 1999 May 28;284(5419):1527–1530.
- [32] Varnai P, Balla T. Live cell imaging of phosphoinositide dynamics with fluorescent protein domains. *Biochim Biophys Acta.* 2006 Aug;1761(8):957–967.
- [33] Murata Y, Iwasaki H, Sasaki M, et al. Phosphoinositide phosphatase activity coupled to an intrinsic voltage sensor. *Nature.* 2005 Jun 30;435(7046):1239–1243.
- [34] Murata Y, Okamura Y. Depolarization activates the phosphoinositide phosphatase Ci-VSP, as detected in *Xenopus* oocytes coexpressing sensors of PIP2. *J Physiol.* 2007 Sep 15;583(Pt 3):875–889.
- [35] Iwasaki H, Murata Y, Kim Y, et al. A voltage-sensing phosphatase, Ci-VSP, which shares sequence identity with PTEN, dephosphorylates phosphatidylinositol 4,5-bisphosphate. *Proc Natl Acad Sci U S A.* 2008 Jun 10;105(23):7970–7975.
- [36] Falkenburger BH, Jensen JB, Hille B. Kinetics of PIP2 metabolism and KCNQ2/3 channel regulation studied with a voltage-sensitive phosphatase in living cells. *J Gen Physiol.* 2010 Feb;135(2):99–114.
- [37] Halaszovich CR, Schreiber DN, Oliver D. Ci-VSP is a depolarization-activated phosphatidylinositol-4,5-bisphosphate and phosphatidylinositol-3,4,5-trisphosphate 5 $\alpha$ -phosphatase. *J Biol Chem.* 2009 Jan 23; 284(4):2106–2113.
- [38] Wilson DB, Bross TE, Hofmann SL, et al. Hydrolysis of polyphosphoinositides by purified sheep seminal vesicle phospholipase C enzymes. *J Biol Chem.* 1984 Oct 10;259(19):11718–11724.
- [39] Ryu SH, Cho KS, Lee KY, et al. Purification and characterization of two immunologically distinct phosphoinositide-specific phospholipases C from bovine brain. *J Biol Chem.* 1987 Sep 15; 262(26):12511–12518.
- [40] Brown DA, Adams PR. Muscarinic suppression of a novel voltage-sensitive K<sup>+</sup> current in a vertebrate neuron. *Nature.* 1980 Feb 14;283(5748):673–676.
- [41] Kruse M, Hammond GR, Hille B. Regulation of voltage-gated potassium channels by PI(4,5)P2. *J Gen Physiol.* 2012 Aug;140(2):189–205.
- [42] Zaydman MA, Silva JR, Delaloye K, et al. Kv7.1 ion channels require a lipid to couple voltage sensing to pore opening. *Proc Natl Acad Sci U S A.* 2013 Aug 6;110(32):13180–13185.
- [43] Li Y, Gamper N, Shapiro MS. Single-channel analysis of KCNQ K<sup>+</sup> channels reveals the mechanism of augmentation by a cysteine-modifying reagent. *J Neurosci.* 2004 Jun 2;24(22):5079–5090.
- [44] Kruse M, Hille B. The phosphoinositide sensitivity of the K(v) channel family. *Channels (Austin).* 2013 Nov-Dec;7(6):530–536.
- [45] Falkenburger BH, Dickson EJ, Hille B. Quantitative properties and receptor reserve of the DAG and PKC branch of G(q)-coupled receptor signaling. *J Gen Physiol.* 2013 May;141(5):537–555.
- [46] Dickson EJ, Falkenburger BH, Hille B. Quantitative properties and receptor reserve of the IP(3) and calcium branch of G(q)-coupled receptor signaling. *J Gen Physiol.* 2013 May;141(5):521–535.
- [47] Lindner M, Leitner MG, Halaszovich CR, et al. Probing the regulation of TASK potassium channels by PI(4,5)P-2 with switchable phosphoinositide phosphatases. *J Physiol London.* 2011 JUL 1 2011;589(13):3149–3162.

- [48] Kosenko A, Kang S, Smith IM, et al. Coordinated signal integration at the M-type potassium channel upon muscarinic stimulation. *EMBO J.* 2012 May 29;31(14):3147–3156.
- [49] Wilke BU, Lindner M, Greifenberg L, et al. Diacylglycerol mediates regulation of TASK potassium channels by Gq-coupled receptors. *Nat Commun.* 2014;5:5540.
- [50] Gamper N, Li Y, Shapiro MS. Structural requirements for differential sensitivity of KCNQ K<sup>+</sup> channels to modulation by Ca<sup>2+</sup>/calmodulin. *Mol Biol Cell.* 2005 Aug;16(8):3538–3551.
- [51] Storch U, Forst AL, Pardatscher F, et al. Dynamic NHERF interaction with TRPC4/5 proteins is required for channel gating by diacylglycerol. *Proc Natl Acad Sci U S A.* 2017 Jan 3;114(1):E37–E46.
- [52] Hofmann T, Obukhov AG, Schaefer M, et al. Direct activation of human TRPC6 and TRPC3 channels by diacylglycerol. *Nature.* 1999 Jan 21;397(6716):259–263.
- [53] Chang A, Abderemane-Ali F, Hura GL, et al. A Calmodulin C-Lobe Ca(2+)-dependent switch governs Kv7 channel function. *Neuron.* 2018 Feb 21; 97(4):836–852 e6.
- [54] Decher N, Gonzalez T, Streit AK, et al. Structural determinants of Kvbeta1.3-induced channel inactivation: a hairpin modulated by PIP2. *EMBO J.* 2008 Dec 3;27 (23):3164–3174.
- [55] Oliver D, Lien CC, Soom M, et al. Functional conversion between A-type and delayed rectifier K<sup>+</sup> channels by membrane lipids. *Science.* 2004 Apr 9; 304(5668):265–270.
- [56] Leitner MG, Michel N, Behrendt M, et al. Direct modulation of TRPM4 and TRPM3 channels by the phospholipase C inhibitor U73122. *Br J Pharmacol.* 2016 Aug;173(16):2555–2569.
- [57] Leitner MG, Halaszovich CR, Oliver D. Aminoglycosides inhibit KCNQ4 channels in cochlear outer hair cells via depletion of phosphatidylinositol(4,5)bisphosphate. *Mol Pharmacol.* 2011 Jan;79(1)51–60.
- [58] Halaszovich CR, Leitner MG, Mavrantoni A, et al. A human phospholipid phosphatase activated by a transmembrane control module. *J Lipid Res.* 2012 Nov; 53(11):2266–2274.
- [59] Leitner MG, Feuer A, Ebers O, et al. Restoration of ion channel function in deafness-causing KCNQ4 mutants by synthetic channel openers. *Br J Pharmacol.* 2012 Apr;165(7):2244–2259.

## RESEARCH PAPER

# Histidine at position 462 determines the low quinine sensitivity of ether-à-go-go channel superfamily member K<sub>v</sub>12.1

Marlen Dierich<sup>1</sup> | Willem B. van Ham<sup>2,3</sup> | Anna Stary-Weinzinger<sup>3</sup> | Michael G. Leitner<sup>1,4</sup> 

<sup>1</sup>Department of Neurophysiology, Institute of Physiology and Pathophysiology, Philipps-University Marburg, Marburg, Germany

<sup>2</sup>Department of Medical Physiology, University Medical Center Utrecht, Utrecht, The Netherlands

<sup>3</sup>Department of Pharmacology and Toxicology, University of Vienna, Vienna, Austria

<sup>4</sup>Division of Physiology, Department of Physiology and Medical Physics, Medical University of Innsbruck, Innsbruck, Austria

**Correspondence**

Michael G. Leitner, Division of Physiology, Department of Physiology and Medical Physics, Medical University of Innsbruck, Schöpfstraße 41, Innsbruck, Austria.  
Email: michael.leitner@i-med.ac.at

**Funding information**

Deutsche Forschungsgemeinschaft, Grant/Award Number: LE 3600/1-1

**Background and Purpose:** The ether-à-go-go (Eag) K<sub>v</sub> superfamily comprises closely related K<sub>v</sub>10, K<sub>v</sub>11, and K<sub>v</sub>12 subunits. K<sub>v</sub>11.1 (termed hERG in humans) gained much attention, as drug-induced inhibition of these channels is a frequent cause of sudden death in humans. The exclusive drug sensitivity of K<sub>v</sub>11.1 can be explained by central drug-binding pockets that are absent in most other channels. Currently, it is unknown whether K<sub>v</sub>12 channels are equipped with an analogous drug-binding pocket and whether drug-binding properties are conserved in all Eag superfamily members.

**Experimental Approach:** We analysed sensitivity of recombinant K<sub>v</sub>12.1 channels to quinine, a substituted quinoline that blocks K<sub>v</sub>10.1 and K<sub>v</sub>11.1 at low micromolar concentrations.

**Key Results:** Quinine inhibited K<sub>v</sub>12.1, but its affinity was 10-fold lower than for K<sub>v</sub>11.1. Contrary to K<sub>v</sub>11.1, quinine inhibited K<sub>v</sub>12.1 in a largely voltage-independent manner and induced channel opening at more depolarised potentials. Low sensitivity of K<sub>v</sub>12.1 and characteristics of quinine-dependent inhibition were determined by histidine 462, as site-directed mutagenesis of this residue into the homologous tyrosine of K<sub>v</sub>11.1 conferred K<sub>v</sub>11.1-like quinine block to K<sub>v</sub>12.1(H462Y). Molecular modelling demonstrated that the low affinity of K<sub>v</sub>12.1 was determined by only weak interactions of residues in the central cavity with quinine. In contrast, more favourable interactions can explain the higher quinine sensitivity of K<sub>v</sub>12.1(H462Y) and K<sub>v</sub>11.1 channels.

**Conclusions and Implications:** The quinoline-binding “motif” is not conserved within the Eag superfamily, although the overall architecture of these channels is apparently similar. Our findings highlight functional and pharmacological diversity in this group of evolutionary-conserved channels.

**Abbreviations:** Eag, ether-à-go-go channel; Elk, ether-à-go-go-gene-like channel; hERG, human ether-à-go-go-related gene channel 1; Erg, ether-à-go-go-related gene channel; LQT, long QT; MD, molecular dynamics; RMSD, root-mean-square deviation

This is an open access article under the terms of the Creative Commons Attribution-NonCommercial License, which permits use, distribution and reproduction in any medium, provided the original work is properly cited and is not used for commercial purposes.

© 2019 The Authors. British Journal of Pharmacology published by John Wiley & Sons Ltd on behalf of British Pharmacological Society.

## 1 | INTRODUCTION

The ether-à-go-go (Eag) superfamily of  $K_v$  channels comprises the three conserved families of Eag ( $K_v10$ ), ether-à-go-go-related gene (Erg;  $K_v11$ ), and ether-à-go-go-gene-like (Elk;  $K_v12$ ) channels. These channels give rise to voltage-dependent  $K^+$  currents in many cell types (Bauer & Schwarz, 2001; Bauer & Schwarz, 2018). The best characterised member,  $K_v11.1$  (termed **hERG** for the human isoform), engenders rapidly activating  $K^+$  current  $I_{Kr}$  responsible for membrane repolarisation in cardiac myocytes (Sanguinetti, Jiang, Curran, & Keating, 1995). As  $I_{Kr}$  determines duration and end of heart action potentials, loss of  $K_v11.1$  function constitutes a frequent cause of cardiac dysfunction in humans (Curran et al., 1995; Keating & Sanguinetti, 2001; Mitcheson, Chen, Lin, Culberson, & Sanguinetti, 2000; Sanguinetti et al., 1995; Trudeau, Warmke, Ganetzky, & Robertson, 1995). Mutations in **KCNH2**, the gene encoding  $K_v11.1$ , cause congenital long QT (LQT) syndrome-2 characterised by a prolonged QT interval and polymorphic ventricular arrhythmias (torsade de pointes) that may lead to recurrent syncope or sudden death (Curran et al., 1995; Sanguinetti et al., 1995). More common, however, are acquired forms of LQT syndrome through drug-induced inhibition of  $K_v11.1$  (Keating & Sanguinetti, 2001; Roden, 1996; Sanguinetti et al., 1995).  $K_v11.1$  channels are extremely sensitive to a wide variety of drugs including substituted quinolines (**quinidine**, **quinine**, and **chloroquine**), antiarrhythmic agents (e.g., MK-499 and dofetilide), and many other substances (e.g., terfenadine, cisapride, and vesnarinone; Furutani et al., 2011; Kamiya, Mitcheson, Yasui, Kodama, & Sanguinetti, 2001; Lees-Miller, Duan, Teng, & Duff, 2000; Mitcheson et al., 2000; Mitcheson et al., 2005; Sanchez-Chapula, Ferrer, Navarro-Polanco, & Sanguinetti, 2003; Sanchez-Chapula, Navarro-Polanco, Culberson, Chen, & Sanguinetti, 2002). All of these substances may cause undesired prolongation of cardiac action potentials by inhibiting  $K_v11.1$  (Sanguinetti et al., 1995). The high susceptibility of human  $K_v11.1$  to these structurally divergent drugs is governed by amino acids facing the channel's central cavity to form hydrophobic-binding pockets (Wang & MacKinnon, 2017). Mutagenesis studies have shown that amino acids in the inner pore helix (threonine 623), selectivity filter (serine 624 and valine 625), and tyrosine 652/phenylalanine 656 of the sixth transmembrane segment (S6) determine the susceptibility of drug-induced inhibition in  $K_v11.1$  (Mitcheson et al., 2000; Sanchez-Chapula et al., 2002; Sanchez-Chapula et al., 2003; Wang & MacKinnon, 2017). Some of these residues are involved in drug binding (threonine 623, serine 624, tyrosine 652, and phenylalanine 656; Wang & MacKinnon, 2017), whereas others (e.g., valine 625 and also asparagine 588, serine 631, and serine 620) have been shown to control drug sensitivity through contributing to channel inactivation that is necessary for  $K_v11.1$  inhibition through many high-affinity blockers (Ficker, Jarolimek, & Brown, 2001; Ficker, Jarolimek, Kiehn, Baumann, & Brown, 1998; Kamiya, Niwa, Mitcheson, & Sanguinetti, 2006; Perrin, Kuchel, Campbell, & Vandenberg, 2008; Wu, Gardner, & Sanguinetti, 2015). Further, phenylalanine 557 located in the S5 helix is involved in binding of some drugs (Helliwell et al., 2018; Saxena et al., 2016). Most of these residues are conserved in  $K_v10$  channels, and

### What is already known

- Drug-induced inhibition of  $K_v11.1$  (hERG) is a frequent cause of sudden death in humans.
- It is not known whether closely related  $K_v12$  channels are also sensitive to drug-dependent inhibition.

### What this study adds

- Low quinine sensitivity, affinity, and characteristics of inhibition of  $K_v12.1$  channels are determined by H462.
- Drug sensitivity of  $K_v11.1$  and  $K_v12.1$  is different but determined by homologous amino acid positions.

### What is the clinical significance

- Drug-binding pockets are not conserved in Eag superfamily members, but channel architecture is similar.
- Our findings facilitate the understanding of the arrhythmogenic actions of quinine.

accordingly, the  **$K_v10.1$**  isoform exhibits similarly high sensitivity to some substances (Schonherr, Gessner, Lober, & Heinemann, 2002). However,  **$K_v10.2$**  is significantly less susceptible to drug-induced inhibition, indicating that additional motifs might contribute to drug binding in certain members of the superfamily (Chen, Seeböhm, & Sanguinetti, 2002; Gessner, Zacharias, Bechstedt, Schonherr, & Heinemann, 2004; Schonherr et al., 2002). In fact, it has been shown that high-affinity blockers of  $K_v11.1$  are less effective on  $K_v10$  channels, as these isoforms do not inactivate. This suggests that conformational reorientation of relevant residues associated with inactivation that are necessary for inhibition of  $K_v11.1$  is absent in  $K_v10$  channels (Chen et al., 2002; Ficker et al., 1998; Ficker et al., 2001).

In contrast to  $K_v10$  and  $K_v11$ , only little information is available on the three members of the  $K_v12$  (Elk) family predominantly expressed in neurons (Engeland, Neu, Ludwig, Roeper, & Pongs, 1998; Miyake, Mochizuki, Yokoi, Kohda, & Furuichi, 1999; Saganich, Machado, & Rudy, 2001; Shi et al., 1998; Trudeau, Titus, Branchaw, Ganetzky, & Robertson, 1999; Zou et al., 2003).  **$K_v12.2$**  regulates excitability of hippocampal neurons (Zhang et al., 2010), but no physiological role has been assigned to  **$K_v12.1$**  and  **$K_v12.3$**  channels yet. Recent studies provided significant insight into functional characteristics of  $K_v12.1$  (Dai & Zagotta, 2017; Dierich, Evers, Wilke, & Leitner, 2018; Dierich & Leitner, 2018; Kazmierczak et al., 2013; Li et al., 2015), but it is unknown whether  $K_v12$  channels are equipped with a high affinity drug-binding pocket as  $K_v10.1$  and  $K_v11.1$ .

We analysed the sensitivity of human  $K_v12.1$  to quinine, a substituted quinoline that blocks  $K_v11.1$  channels at low micromolar concentrations (Gessner et al., 2004; Mitcheson et al., 2000; Sanchez-Chapula et al., 2003; Schonherr et al., 2002). Quinine also inhibited recombinant  $K_v12.1$  channels, but their sensitivity was 10-fold lower than that of  $K_v11.1$ . Contrary to  $K_v11.1$ , quinine-dependent block of  $K_v12.1$  was largely voltage-independent and the substance

induced channel opening at more depolarised membrane potentials. Mutagenesis of histidine at position 462 (H462) into the homologous tyrosine (Y652) of  $K_v11.1$  conferred  $K_v11.1$ -like quinine sensitivity to  $K_v12.1$ (H462Y) channels. Molecular modelling analyses demonstrated that the low quinine sensitivity of  $K_v12.1$  was determined by only weak interactions of quinine with H462 in the central cavity, whereas more favourable interactions facilitated higher quinine sensitivity of  $K_v12.1$ (H462Y) and closely related  $K_v11.1$ . Our data showed that the drug-binding pocket in the central cavity is not conserved in the Eag superfamily, although the general architecture of these channels is apparently similar. Our findings highlight functional and pharmacological diversity within this group of evolutionary conserved  $K^+$  channels.

## 2 | METHODS

### 2.1 | Cell culture, transient transfection, and mutagenesis

CHO dhFR<sup>-</sup> cells (ATCC Cat# CRL-9096, RRID:CVCL\_1977) were maintained as previously reported (Leitner et al., 2016). In brief, cells were maintained in MEM alpha medium (with 10% fetal calf serum and 1% pen/strep; all Invitrogen GmbH, Darmstadt, Germany) at 5% CO<sub>2</sub> and 37°C in a humidified atmosphere. Transient transfection of cultured CHO cells was performed using jetPEI (Polyplus Transfection, Illkirch, France). The following vectors for ion channel expression were used:  $K_v11.1$  (Erg1)-pcDNA3.1 (gene: rat *Kcnh2*; UniProt accession number: O08962; UniProt, RRID:SCR\_002380),  $K_v12.1$  (Elk1)-pcDNA3.1-IRES-eGFP (human **KCNH8**; Q96L42), and pEGFP-C1 (transfection control; Addgene, Teddington, UK). An amino acid exchange (H462Y) was introduced into  $K_v12.1$  with the QuikChange XL site-directed mutagenesis kit (Stratagene, Santa Clara, CA). Site-directed mutagenesis was confirmed by sequencing prior to the experiments (Microsynth SEQLAB, Göttingen, Germany).

### 2.2 | Electrophysiological recordings

Whole-cell patch clamp recordings were performed at room temperature (22–25°C) with an HEKA EPC10 USB patch clamp amplifier controlled by PatchMaster software (HEKA, Lambrecht, Germany; Patchmaster, RRID:SCR\_000034). Voltage clamp recordings were low-pass filtered at 2 kHz and sampled at 5 kHz. The series resistance ( $R_s$ ) was kept below 6 MΩ, and  $R_s$  was compensated throughout the recordings (80–90%; Dierich & Leitner, 2018; Leitner, Halaszovich, & Oliver, 2011). All voltage protocols are indicated in the figures; dashed lines highlight zero current. Borosilicate glass patch pipettes (Sutter Instrument Company, Novato, CA) had an open-pipette resistance of 2–3 MΩ after backfilling with intracellular solution containing (in mM) 135 KCl, 2.41 CaCl<sub>2</sub> (100-nM free Ca<sup>2+</sup>), 3.5 MgCl<sub>2</sub>, 5 HEPES, 5 EGTA, 2.5 Na<sub>2</sub>ATP, and 0.1 Na<sub>3</sub>GTP, pH 7.3 (with KOH), 290–295 mOsm·kg<sup>-1</sup>. The extracellular solution contained (in mM) 144 NaCl, 5.8 KCl, 1.3 CaCl<sub>2</sub>, 0.9 MgCl<sub>2</sub>, 0.7 NaH<sub>2</sub>PO<sub>4</sub>, 10 HEPES, and

5.6 D-glucose, pH 7.4 (with NaOH), 305–310 mOsm·kg<sup>-1</sup>. Liquid junction potentials were not compensated (approximately -4 mV).

### 2.3 | Analysis of electrophysiological recordings

Patch clamp recordings were analysed with IgorPro (Wavemetrics, Lake Oswego, OR; IGOR Pro, RRID:SCR\_000325) and the PatchMaster (HEKA) software. Voltage-dependence of activation was derived from tail current amplitudes using voltage protocols indicated: Tail currents were fitted with a two-state Boltzmann function with  $I = I_{min} + (I_{max} - I_{min}) / (1 + \exp((V - V_h) / s))$ , where  $I$  is the current,  $V$  is the membrane voltage,  $V_h$  is the voltage at half-maximal activation, and  $s$  describes the slope of the curve ( $s$  is presented as positive values to describe the slope of voltage-dependent channel activation; Leitner et al., 2012). Results are shown as conductance–voltage curves, obtained by normalising to  $(I_{max} - I_{min})$ , obtained from fits to data of individual experiments. For dose–response relationships, currents were normalised to baseline and were fitted to a Hill equation with  $I = I_b + (I_{max} - I_b) / (1 + (IC_{50} / [S])^{n_H})$ , where  $I$  is the (normalised) current,  $I_b$  and  $I_{max}$  denote minimal and maximal currents, respectively,  $IC_{50}$  is the concentration at the half-maximal effect,  $[S]$  is the drug concentration, and  $n_H$  is the Hill coefficient. Time constants of activation were derived from mono-exponential fits to activating current components at indicated potentials ( $\tau$  activation; c.f. Figure 3e). For presentation, whole-cell currents were normalised to cell capacitance (current density; pA·pF<sup>-1</sup>) or to baseline current amplitudes ( $I/I_0$ ; normalised current).

### 2.4 | Data and statistical analysis

The data and statistical analysis comply with the recommendations of the *British Journal of Pharmacology* on experimental design and analysis in pharmacology (Curtis et al., 2018). Isolated cells under investigation were randomly assigned to different treatment groups. Data analysis for experiments presented was performed in a blinded manner. For some experiments, single recordings were normalised to baseline values individually to account for baseline variations between cells. Statistical analysis was performed using Student's two-tailed  $t$  test/Wilcoxon–Mann–Whitney test, and when appropriate comparisons between multiple groups were performed with ANOVA followed by Dunnett's test. Post hoc tests were run only if  $F$  achieved  $P < 0.05$  and there was no significant variance inhomogeneity. Significance was assigned at  $P \leq 0.05$  ( $*P \leq 0.05$ ). Data subjected to statistical analysis have  $n$  over 5 per group, and data are presented as mean  $\pm$  standard error of the means (SEM). In electrophysiological experiments,  $n$  represents the number of individual cells and accordingly the number of independent experiments (no pseudo-replication).

### 2.5 | Molecular modelling

A  $K_v12.1$  homology model of the pore module (residues S352–Y477) in the open/inactive conformation was built using the programme modeller 9v.17 (Webb & Sali, 2016, RRID:SCR\_008395) based on

the cryo-EM structure of the hERG (human  $K_v11.1$ ) channel (pdb identifier: 5VA1, 3.7 Å resolution; Wang & MacKinnon, 2017). The sequence identity between target and template is 61% (sequence similarity: 76%). Docking studies were carried out with the Genetic Optimization for Ligand Docking program, version 5.6.2 (GOLD, Jones, Willett, Glen, Leach, & Taylor, 1997). The “chemscore” fitness scoring function was used, and all residues within 12 Å of residue H462 in  $K_v12.1$  were defined as binding site. The Chemscore.DG scoring function was used to estimate free energies of binding. Side chains of residues H462 and F466 from all four domains were set as flexible. The pKa of H462 is calculated to be 3.13 (PROPKA; Olsson, Sondergaard, Rostkowski, & Jensen, 2011), indicating a hydrogen atom on the  $\delta$  nitrogen. The other two tautomers were considered in docking as well; however, similar binding modes/poses were obtained. For molecular dynamics (MD) system setups and ligand parametrisation (Vanommeslaeghe et al., 2010), the CHARMM-GUI (Jo, Kim, Iyer, & Im, 2008; CHARMM, RRID:SCR\_014892) was used. The quinine molecule was protonated at the tertiary N (pKa value of the quinolone group: 9.7, O’Neil, 2013). Protein–ligand complexes obtained from docking were embedded in a 1-palmitoyl-2-oleoyl-*sn*-glycero-3-phosphocholine bilayer and solvated with TIP3P waters.  $K^+$  ions were placed in the selectivity filter at sites S0, S2, and S4, with water molecules at sites S1 and S3 and 0.15-M KCl added to the simulation box. Energy minimisation, 20-ns equilibration, and three independent 50-ns production runs (with initial atom velocities assigned independently and randomly) were performed using GROMACS v.5.1.2 (GROMACS, RRID:SCR\_014565; Abraham et al., 2016) with the charmm36 force field for protein molecules (incorporating CMAP terms, Mackerell, Feig, & Brooks, 2004) and lipid molecules and salt ions (Best et al., 2012; Klauda et al., 2010; MacKerell et al., 1998). Electrostatics were modelled using particle mesh Ewald (Darden, York, & Pedersen, 1993), and LINCS was used to constrain covalent chemical bonds to hydrogens (Hess, Bekker, Berendsen, & Fraaije, 1997). Temperature was maintained at 310 K using velocity rescaling (*V*-rescale; Bussi, Donadio, & Parrinello, 2007), and semi-isotropic pressure coupling was accomplished using the Parrinello–Rahman barostat (Parrinello & Rahman, 1981). MD trajectories were analysed using VMD v.1.9.2 (VMD, RRID:SCR\_001820; Humphrey, Dalke, & Schulten, 1996) and GROMACS.

## 2.6 | Materials

Quinine was purchased from Tocris Bioscience (Bristol, UK) and was diluted in extracellular solution to concentrations indicated in Section 3. Quinine was applied locally via a glass capillary through a custom-made application system.

## 2.7 | Nomenclature of targets and ligands

Key protein targets and ligands in this article are hyperlinked to corresponding entries in <http://www.guidetopharmacology.org>, the common portal for data from the IUPHAR/BPS Guide to PHARMACOLOGY (Harding et al., 2018), and are permanently archived in the

Concise Guide to PHARMACOLOGY 2017/18 (Alexander et al., 2017).

## 3 | RESULTS

### 3.1 | Voltage-independent but mode shift-dependent inhibition of $K_v12.1$ channels through quinine at high concentrations

We started our pharmacological analyses by applying increasing concentrations of quinine to CHO cells transiently expressing human  $K_v12.1$ . When activating  $K_v12.1$  with 600-ms voltage steps to 0 mV from a holding potential of  $-60$  mV, quinine inhibited  $K_v12.1$  channels with an  $IC_{50}$  of 0.97 mM and a Hill coefficient of 1.0 (Figure 1a). At a concentration close to the  $IC_{50}$  (1 mM), this inhibition developed within seconds and was partially reversible after removal of the drug (Figure S1a,b). After having established the quinine sensitivity of  $K_v12.1$ , we set out to characterise effects of the substance on voltage-dependent activation of the channels. Noteworthy,  $K_v12.1$  channels exhibit a mode shift of activation (also termed pre-pulse facilitation or voltage-dependent potentiation; Dai & Zagotta, 2017; Dierich et al., 2018; Dierich & Leitner, 2018; Li et al., 2015), which designates stabilisation of the voltage-sensing domain in a “relaxed” open state after prolonged depolarisation of the membrane potential (Bezanilla, Taylor, & Fernandez, 1982; Villalba-Galea, Sandtner, Starace, & Bezanilla, 2008). Most prominently, mode shift manifests through a large shift of activation voltages to hyperpolarised potentials following membrane potential depolarisation (Dai & Zagotta, 2017; Dierich et al., 2018; Dierich & Leitner, 2018; Li et al., 2015). To induce mode shift, we applied conditioning potentials of  $-60$  or 0 mV (200 ms) before a series of voltage steps to activate  $K_v12.1$  (pulse potentials:  $-140$  to  $+20$  mV; 600 ms; Figure 1b,c; c.f. Dierich & Leitner, 2018; Dierich et al., 2018). Following the hyperpolarised conditioning potential ( $-60$  mV), half-maximal voltage ( $V_h$ ) and slope factor of  $K_v12.1$  channel activation were  $-30.0 \pm 2.0$  mV and  $14.9 \pm 1.1$  mV, respectively ( $n = 6$ ; Figure 1d–f). When we applied the conditioning potential of 0 mV,  $V_h$  was  $-75.9 \pm 1.7$  mV and  $s$  was  $10.6 \pm 0.5$  mV ( $n = 6$ ; Figure 1d–f). Depolarised conditioning potentials thus induced a large (and significant) shift of the voltages of activation of  $K_v12.1$  channels to hyperpolarised potentials by about  $-45$  mV, representing their mode shift of activation (Dai & Zagotta, 2017; Dierich et al., 2018; Dierich & Leitner, 2018; Li et al., 2015). Application of quinine (1 mM) shifted the voltage dependence of  $K_v12.1$  to depolarised voltages for both conditioning potentials. As this shift was more pronounced after the depolarised conditioning potential (0 mV; Figure 1d,e), the degree of mode shift was significantly attenuated to about  $-23$  mV in the presence of the substance (Figure 1e). Application of quinine (1 mM) inhibited both steady-state currents and tail currents through  $K_v12.1$  channels (Figure 1g,h). Following both conditioning potentials, quinine-induced inhibition of steady-state  $K_v12.1$  currents was the same for all activating voltages (Figure 1i;  $n = 6$ ; e.g., for conditioning potential  $-60$  mV: not significant



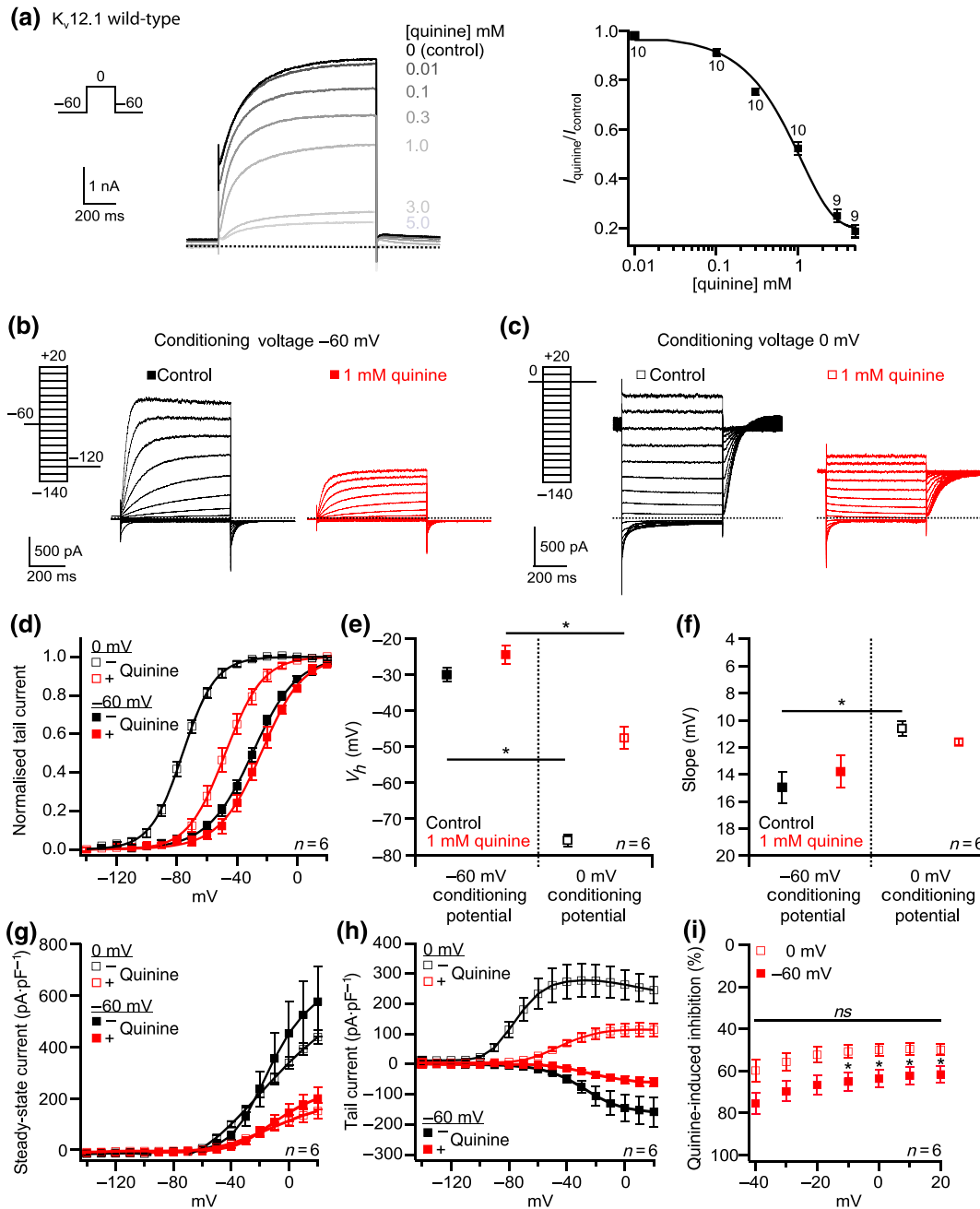


**FIGURE 1** Quinine inhibits human  $K_{v12.1}$  channels at high concentrations in a voltage-independent manner. (a) Dose-dependent inhibition of recombinant  $K_{v12.1}$  channels through extracellular application of quinine. The panel shows representative recordings of a CHO cell expressing human  $K_{v12.1}$  treated with increasing quinine concentrations (left) and the summarised quinine dose-response relationship (right;  $IC_{50}$  and Hill coefficient were calculated from a Hill fit to averaged recordings as shown in the left panel; solid line represents this fit). Scale bars, voltage protocol, quinine concentrations, and number of cells as indicated. (b–f) Quinine induced the activation of recombinant  $K_{v12.1}$  channels at more positive membrane potentials. Representative recordings of  $K_{v12.1}$  channels activated by voltage steps between  $-140$  and  $+20$  mV following 200-ms conditioning voltage steps to (b)  $-60$  mV or (c)  $0$  mV before (control) and at the end of quinine application (1 mM). (d) Summary of voltage-dependence of  $K_{v12.1}$  channels derived from Boltzmann fits to individual recordings as shown in (b, c); solid line represents Boltzmann fit to averaged data. (e) Mean  $V_h$  of channel activation and (f) summarised  $s$  factors of activation before and at the end of quinine treatment (1 mM; values derived from fits as shown in d). Quinine (1 mM) inhibited voltage-dependent (g) outward steady-state and (h) inward tail currents through recombinant  $K_{v12.1}$  channels (current amplitudes analysed from recordings as shown in b, c). (i) Quinine-induced inhibition of  $K_{v12.1}$  was voltage-independent (presented as % inhibition from data shown in (g); *ns*, no significant difference for quinine block between activating voltages of  $-40$  and  $20$  mV). Note that quinine block was significantly more pronounced, when  $K_{v12.1}$  channels were activated at membrane potentials more positive than  $-30$  mV. \*Significant difference of quinine block for both conditioning potentials

(*ns*) between  $-40$  mV and  $+20$  mV,  $P = 0.54$ ), that is, quinine inhibited  $K_v12.1$  channels in a voltage-independent manner. However, quinine-dependent block was significantly more pronounced following the hyperpolarised conditioning potential ( $-60$  mV) for activating voltages more positive than  $-30$  mV (indicated by “\*” in Figure 1i). These data demonstrated that to some extent,  $K_v12.1$  channels were more sensitive to quinine block after conditioning depolarisation of the membrane, and that accordingly, quinine block of  $K_v12.1$  channels depended on mode shift.

### 3.2 | Quinine is a voltage- and mode shift-dependent inhibitor of $K_v11.1$ channels

We then compared our findings on  $K_v12.1$  to quinine-dependent inhibition of closely related  $K_v11.1$ . In line with a previous study (Sanchez-Chapula et al., 2003), quinine inhibited recombinant  $K_v11.1$  channels with an  $IC_{50}$  of  $98$   $\mu$ M and a Hill coefficient of 1.3 (Figure 2a). Accordingly, the quinine affinity of  $K_v11.1$  channels was about 10 times higher than that of  $K_v12.1$  (c.f. Figure 1a). As for  $K_v12.1$ , quinine-dependent inhibition of  $K_v11.1$  developed in seconds and was partially reversible ( $50$ - $\mu$ M quinine; Figure S1c,d). By applying hyperpolarised ( $-60$  mV) and depolarised ( $+40$  mV) conditioning voltages before the activating pulse potentials, we then analysed effects of quinine on the voltage dependence of  $K_v11.1$  channels that also exhibit mode shift of activation (Figure 2b,c). As previously reported (Dierich et al., 2018; Tan, Perry, Ng, Vandenberg, & Hill, 2012), depolarised conditioning potentials ( $+40$  mV) significantly shifted the voltage dependence of  $K_v11.1$  channels by about  $-50$  mV compared with the hyperpolarised conditioning potential (Figure 2d-f). Following the hyperpolarised conditioning potential ( $-60$  mV), quinine ( $50$   $\mu$ M) significantly shifted the voltage dependence of  $K_v11.1$  channels by  $-13$  mV to more negative potentials (Figure 2d-f). As the voltage dependence of  $K_v11.1$  was not altered following the depolarised conditioning potential ( $+40$  mV), the degree of mode shift was attenuated in the presence of quinine ( $50$   $\mu$ M; Figure 2d,e). Quinine blocked both voltage-dependent outward and inward currents through  $K_v11.1$  (Figure 2g,h). After the conditioning potential of  $-60$  mV, the degree of this inhibition was significantly increased, when the channels were activated at more positive potentials (Figure 2i), that is, quinine block was voltage dependent following the hyperpolarised conditioning potential. In contrast, following the depolarised conditioning potential, quinine block of  $K_v11.1$  channels was completely voltage independent. Thus, for  $K_v11.1$  channels, quinine-induced inhibition depended on mode shift (c.f. quinidine; Furutani et al., 2011), but (in contrast to  $K_v12.1$ ) the  $K_v11.1$  channels apparently were more sensitive to quinine following the depolarised conditioning potential, when activated at negative membrane potentials.

### 3.3 | Functional characterisation of $K_v12.1$ (H462Y) channels

Sensitivity of human  $K_v11.1$  channels to several drugs has been attributed to the amino acids T623, V625, Y652, and F656, located

in the channels inner pore helix, selectivity filter, or sixth transmembrane segment (S6; Figure 3a; Lees-Miller et al., 2000; Mitcheson et al., 2000; Sanchez-Chapula et al., 2002; Sanchez-Chapula et al., 2003). As  $K_v12.1$  also carries threonine, valine, and phenylalanine at homologous positions (T433, V435, and F466 in  $K_v12.1$ ), we hypothesised that the amino acid exchange at position 462, where  $K_v12.1$  has a histidine instead of the tyrosine (Figure 3a), determined the low quinine sensitivity of  $K_v12.1$ . To elaborate this hypothesis, we mutated H462 in  $K_v12.1$  to the corresponding tyrosine (Y652) of  $K_v11.1$  and characterised the  $K_v12.1$ (H462Y) mutant in CHO cells. Recombinant  $K_v12.1$ (H462Y) channels produced robust voltage-dependent and outwardly rectifying  $K^+$  currents (Figure 3b,c). However,  $K_v12.1$ (H462Y)-mediated whole-cell currents were significantly smaller than for the wild-type channels (Figure 3b-d), and the mutant channels activated significantly faster than the wild-type, when activated through voltage steps between  $-40$  and  $0$  mV (Figure 3e). For conditioning voltages of  $-60$  and  $0$  mV,  $V_h$  was  $-38.0 \pm 1.8$  mV and  $-73.6 \pm 1.6$  mV, respectively, demonstrating that  $K_v12.1$ (H462Y) channels also exhibited a mode shift of activation (Figure 3f-h;  $n = 9$ ). However, in the mutant, mode shift was attenuated compared with wild-type to about  $-35$  mV ( $-45$  mV in wild-type; c.f. Figure 1), mainly because  $K_v12.1$ (H462Y) activated at significantly more negative membrane potentials after the hyperpolarised conditioning potential of  $-60$  mV (Figure 3f-h). The voltage dependence of wild-type and mutant channels was the same after the conditioning potential of  $0$  mV (Figure 3f-h).

### 3.4 | Histidine at position 462 determines the quinine sensitivity of human $K_v12.1$

When applying increasing quinine concentrations to CHO cells expressing  $K_v12.1$ (H462Y), we found that quinine inhibited this channel mutant with an  $IC_{50}$  of  $56$   $\mu$ M and a Hill coefficient of 1.1 (Figure 4a). Thus, the quinine affinity of  $K_v12.1$ (H462Y) was about 17-fold higher than that of the wild-type channels and accordingly more similar to  $K_v11.1$  (c.f. Figures 1a and 2a). As for  $K_v12.1$  wild-type, application of quinine ( $50$   $\mu$ M) blocked inward and outward currents through  $K_v12.1$ (H462Y) (Figure 4b-e), but in contrast to the wild-type channels, quinine-mediated inhibition of  $K_v12.1$ (H462Y) was rapidly reversible (Figure S1e,f). Noteworthy, we detected a transient increase of currents in the presence of quinine, when activating  $K_v12.1$ (H462Y) at membrane voltages more positive than  $0$  mV (following the hyperpolarised conditioning potential; Figure 4b). This observation indicated that channel opening may be required for quinine-dependent inhibition of  $K_v12.1$ (H462Y). In line, quinine-induced inhibition of  $K_v12.1$ (H462Y) was more pronounced, when the channels were activated at more positive membrane voltages, that is, quinine block of  $K_v12.1$ (H462Y) was voltage dependent following positive and negative conditioning potentials (Figure 4f). For  $K_v12.1$ (H462Y) channels, this voltage dependence of quinine block presumably also caused a reduction of tail currents at depolarised activating voltages after conditioning potential of  $0$  mV (Figure 4e,g). Of special note, in

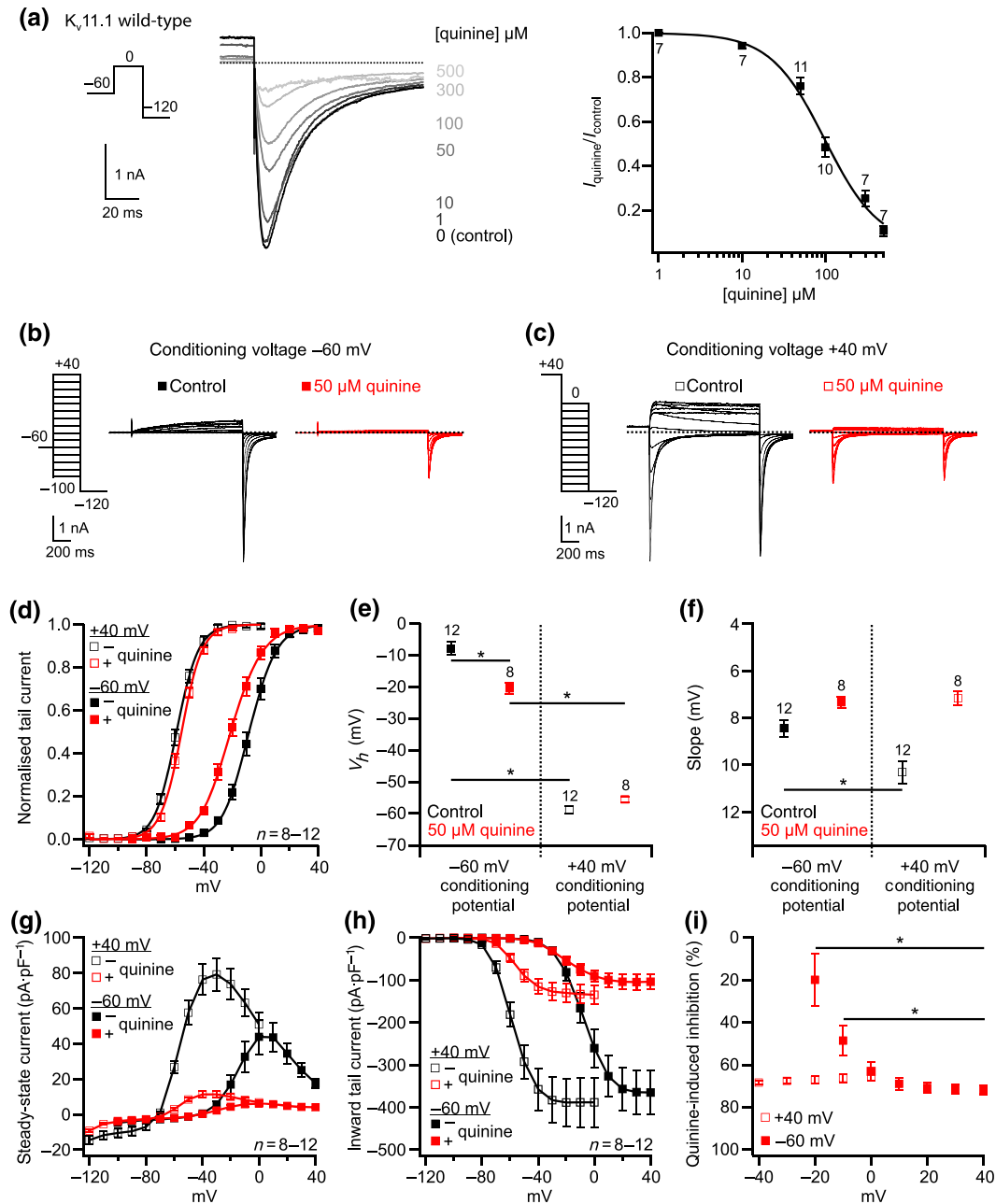


**FIGURE 2** Voltage-dependent inhibition of  $K_v11.1$  channels induced by quinine. (a) Quinine inhibited  $K_v11.1$  channels transiently expressed in CHO cells in a concentration-dependent manner. The left panel shows representative recordings of a CHO cell expressing  $K_v11.1$  treated with increasing quinine concentrations, the right panel depicts the summarised quinine dose–response relationship ( $IC_{50}$  and Hill coefficient calculated from a Hill fit to averaged data; solid line represents Hill fit). Scale bars, voltage protocol, quinine concentrations, and number of cells recorded as indicated. (b–f) After a conditioning potential of  $-60$  mV, quinine induced activation of recombinant  $K_v11.1$  channels at more negative membrane potentials. Representative recordings of  $K_v11.1$  channels activated with voltage steps (as indicated) after conditioning voltage steps to (b)  $-60$  mV or (c)  $+40$  mV before (control) and at the end of the application of quinine ( $50 \mu\text{M}$ ). (d) Summary of voltage-dependence of  $K_v11.1$  channels derived from Boltzmann fits to individual recordings as shown in (b, c); solid line represents Boltzmann fit to averaged data. (e) Mean  $V_h$  of channel activation and (f) summarised slope factors of activation before and at the end of quinine application ( $50 \mu\text{M}$ ; values derived from fits as shown in d). Quinine ( $1 \text{ mM}$ ) inhibited voltage-dependent (g) outward steady-state and (h) inward tail currents through recombinant  $K_v11.1$  channels (current amplitudes analysed from recordings as shown in b, c). (i) Quinine-induced inhibition of  $K_v11.1$  was voltage-dependent after conditioning potential of  $-60$  mV but not after the depolarised conditioning potential of  $+40$  mV (presented as % inhibition from data shown in g). \*denotes significant differences

contrast to  $K_v12.1$  wild-type channels, quinine block of  $K_v12.1(\text{H462Y})$  was the same following both conditioning potentials and thus was independent on mode shift. Contrary to  $K_v12.1$  wild-type, quinine

( $50 \mu\text{M}$ ) shifted the voltage dependence of  $K_v12.1(\text{H462Y})$  by  $-11$  mV and  $-10$  mV to hyperpolarised potentials after conditioning voltages of  $-60$  mV and  $0$  mV respectively (Figure 4g–i).

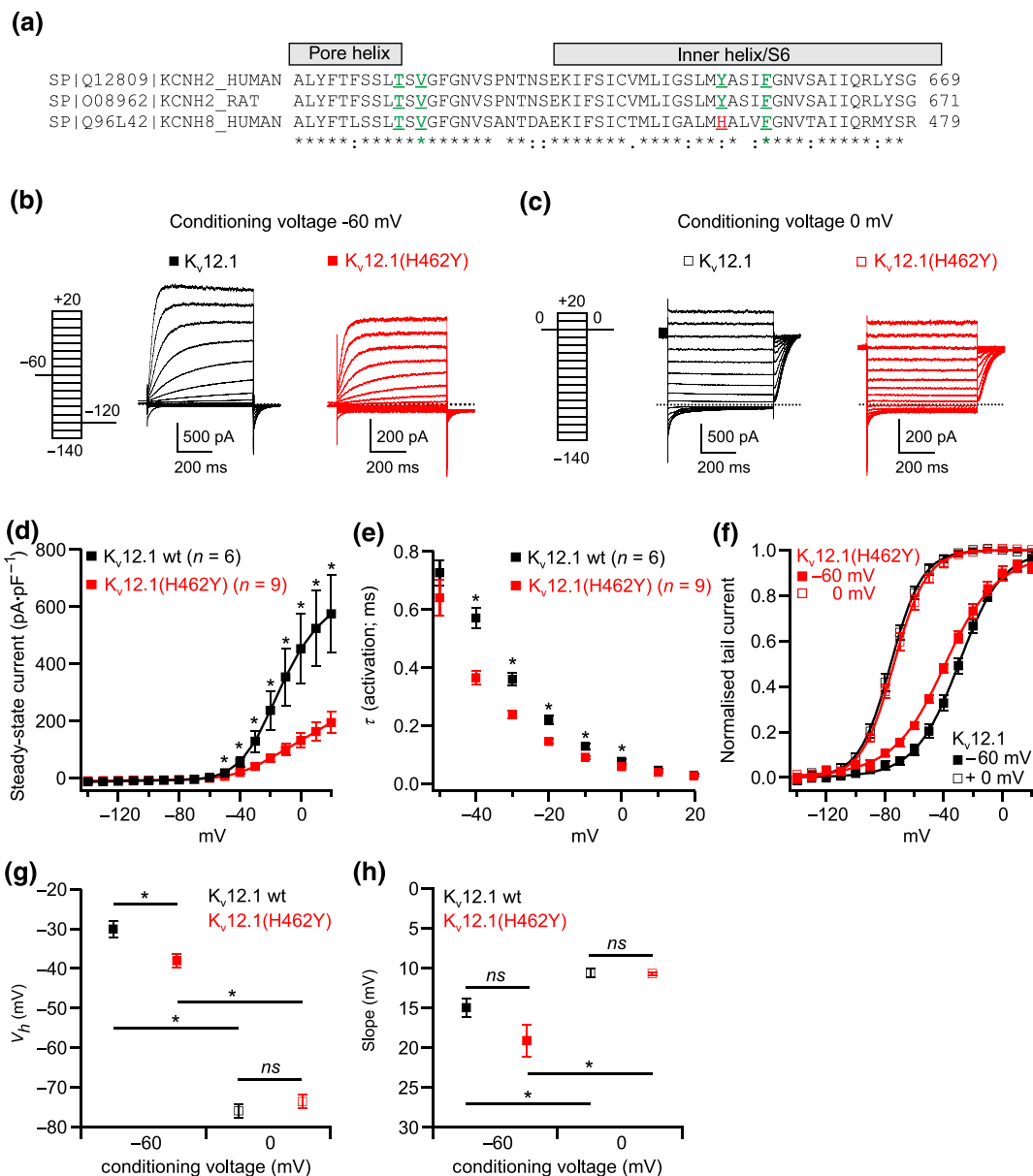


**FIGURE 3** Characteristics of the K<sub>v</sub>12.1(H462Y) channel mutant. (a) The panel shows an alignment of K<sub>v</sub>11.1 isoforms from humans and rats (encoded by the *KCNH2* gene) with human K<sub>v</sub>12.1 channels (*KCNH8* gene). Amino acids recently identified as important for quinoline-dependent inhibition of K<sub>v</sub>11.1 channels are highlighted in colour (green, identical amino acids; red, amino acid exchange in K<sub>v</sub>12.1; see text for details and references). Note that the quinine-binding “motif” of K<sub>v</sub>12.1 differs only at one position from K<sub>v</sub>11.1 channels. (b–h) Biophysical characteristics of K<sub>v</sub>12.1(H462Y; red) in comparison with K<sub>v</sub>12.1 wild-type channels (black). (b, c) Representative recordings of currents through K<sub>v</sub>12.1 wild-type (black) and K<sub>v</sub>12.1(H462Y; red) channels activated with the shown voltage protocols. (d) Steady-state outward currents through K<sub>v</sub>12.1(H462Y) were significantly smaller than through K<sub>v</sub>12.1 wild-type channels, and (e) K<sub>v</sub>12.1(H462Y) activated significantly faster than wild-type channels, when activated through voltage steps between -40 and 0 mV ( $\tau$  derived from monoexponential fits to activating current components in recordings shown in b, c). (f–h) K<sub>v</sub>12.1(H462Y) activated at significantly more negative membrane potentials than wild-type channels after conditioning potential of -60 mV. (f) Summary of voltage-dependence of K<sub>v</sub>12.1(H462Y) channels derived from Boltzmann fits to individual recordings as shown in (b, c); solid line represents Boltzmann fit to averaged data. (g) Mean V<sub>h</sub> of channel activation and (h) summarised slope factors of activation (data on K<sub>v</sub>12.1 wild-type channels are reproduced from Figure 1). \*denotes significant differences

### 3.5 | K<sub>v</sub>12.1(H462Y) channels exhibit K<sub>v</sub>11.1-like quinine sensitivity

In summary, K<sub>v</sub>12.1(H462Y) exhibited a 17 times higher quinine affinity than K<sub>v</sub>12.1 wild-type, that is, quinine sensitivity of K<sub>v</sub>12.1(H462Y)

was more similar to K<sub>v</sub>11.1 than to the wild-type channels (Figure 5a). Application of quinine induced opening of wild-type K<sub>v</sub>12.1 channels at more positive potentials but at more negative values for K<sub>v</sub>12.1(H462Y) and K<sub>v</sub>11.1 (Figure 5b). Quinine inhibited K<sub>v</sub>12.1 channels in a voltage-independent manner, but quinine block was

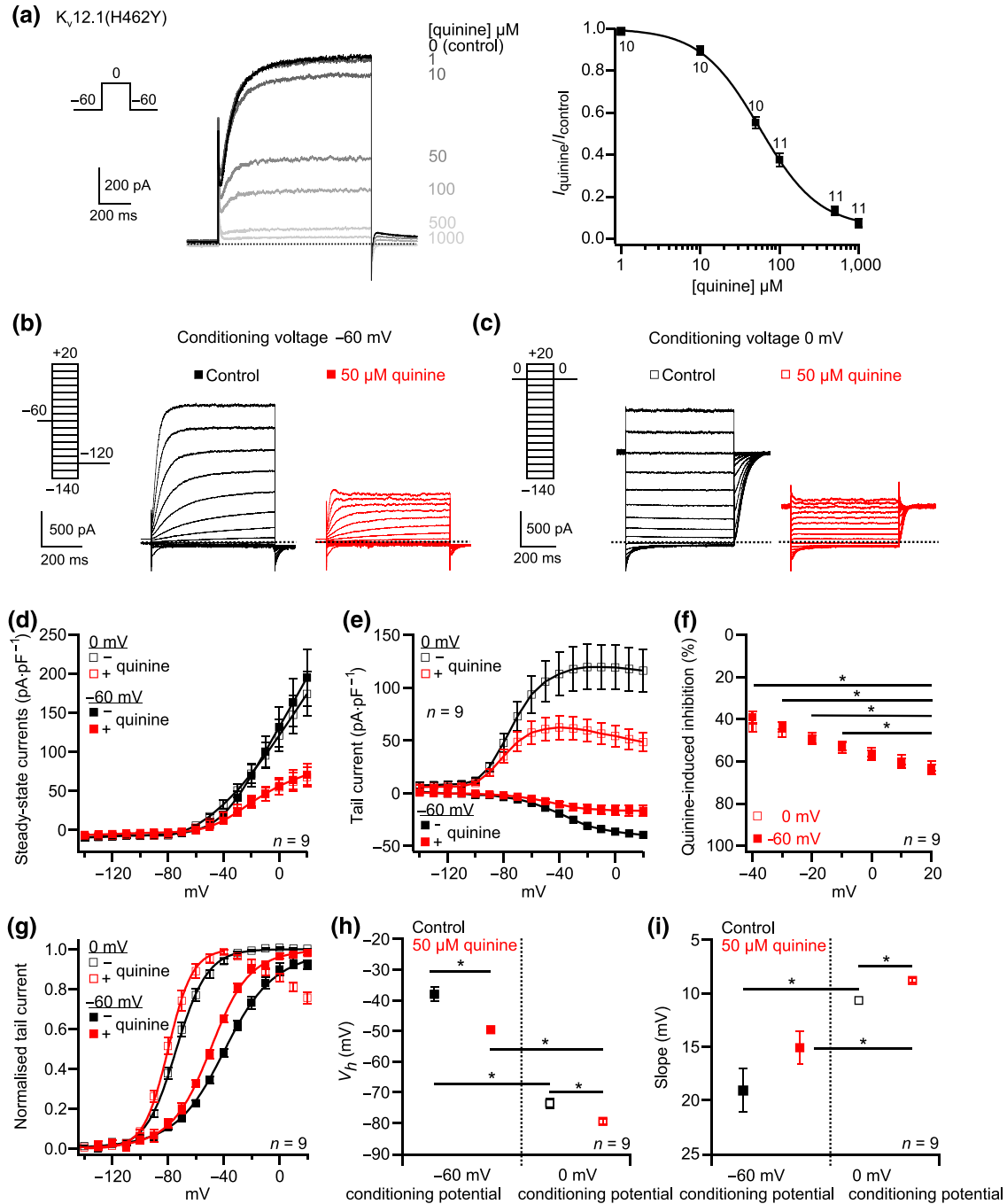


**FIGURE 4** Voltage-dependent inhibition of  $K_v12.1(H462Y)$  channels through quinine at low concentrations. (a) Extracellular application of quinine inhibited  $K_v12.1(H462Y)$  channels overexpressed in CHO cells. The panel shows representative recordings of a CHO cell expressing  $K_v12.1(H462Y)$  treated with increasing quinine concentrations (left) and the summarised dose-response relationship (right;  $IC_{50}$  and Hill coefficient were calculated from a Hill fit to averaged recordings as shown in the left panel; solid line represents Hill fit). Scale bars, voltage protocol, quinine concentrations, and number or cells recorded as indicated. (b–i) Quinine inhibited inward and outward currents through  $K_v12.1(H462Y)$  channels and induced channel activation at more negative membrane potentials. Representative recordings of recombinant  $K_v12.1$  channels activated by voltage steps between -140 and +20 mV following 200-ms conditioning voltage steps to (b) -60 mV or (c) 0 mV before (black) and at the end of quinine application (50  $\mu\text{M}$ ; red). Summarised voltage-dependent (d) steady-state currents and (e) inward tail currents through  $K_v12.1(H462Y)$  before (black) and at the end of quinine treatment (50  $\mu\text{M}$ ; current amplitudes analysed from recordings as shown in b, c). (f) Quinine-induced inhibition of  $K_v12.1(H462Y)$  was voltage-dependent (presented as % inhibition from data shown in d). (g–i) Summary of voltage-dependence of  $K_v12.1(H462Y)$  channels derived from Boltzmann fits to individual recordings as shown in (b, c); solid line represents Boltzmann fit to averaged data. (h) Mean  $V_{1/2}$  of channel activation and (i) summarised slope factors of activation before and at the end of treatment with quinine (50  $\mu\text{M}$ ; values derived from fits as shown in g). \*denotes significant differences

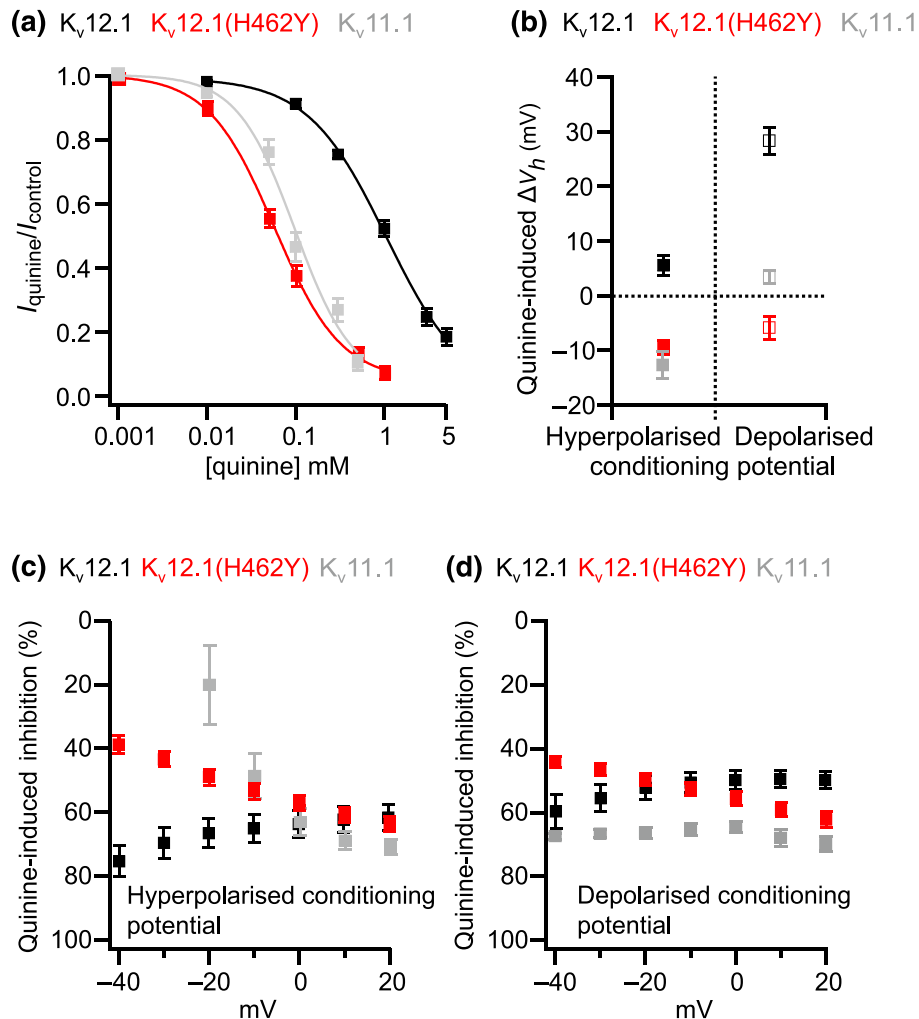


**FIGURE 5** The inhibition induced by quinine of  $K_v12.1(H462Y)$  channels shows  $K_v11.1$ -like characteristics. This figure summarises our findings on  $K_v12.1$  wild-type channels and H462Y mutant as well as on  $K_v11.1$  wild-type channels (data are reproduced from Figures 1–4). (a) The affinity of  $K_v12.1(H462Y)$  for quinine was 17-fold higher than that of the wild-type and accordingly very similar to  $K_v11.1$ . (b) Quinine induced activation of  $K_v12.1$  channels at more positive potentials following the hyperpolarised ( $-60$  mV) and the depolarised conditioning potential ( $0$  mV). In contrast,  $K_v12.1(H462Y)$  and  $K_v11.1$  channels activated at more negative membrane potentials in the presence of quinine following the hyperpolarised conditioning potential. Only slight changes of voltage-dependence of  $K_v12.1(H462Y)$  and  $K_v11.1$  channels were detected during application of quinine following the depolarised conditioning potential. (c, d) Quinine-mediated block was voltage-independent for  $K_v12.1$  but voltage-dependent for  $K_v12.1(H462Y)$ . Note that quinine inhibition of  $K_v11.1$  channels was voltage-dependent only following the hyperpolarised conditioning potential. Summaries of quinine-induced inhibition (% of controls) for (c) the hyperpolarised and for (d) the depolarised conditioning membrane potential. Quinine was applied at  $1$  mM for  $K_v12.1$  channels and at  $50$   $\mu$ M for  $K_v12.1(H462Y)$  and  $K_v11.1$ . Mode shift was induced through conditioning potentials of  $-60$  and  $0$  mV for  $K_v12.1$  isoforms and at  $-60$  and  $+40$  mV for  $K_v11.1$  channels

completely voltage dependent for  $K_v12.1(H462Y)$  and partially voltage dependent (after hyperpolarised conditioning potentials) for  $K_v11.1$  channels (Figure 5c,d). In contrast to  $K_v12.1(H462Y)$ ,  $K_v12.1$  wild-type channels apparently were more sensitive to quinine after conditioning hyperpolarisation of the membrane (c.f. Figure 1i), that is, for  $K_v12.1$  wild-type channels, quinine-induced inhibition depended on mode shift (just as for  $K_v11.1$  channels). Accordingly, closely related  $K_v12.1$  and  $K_v11.1$  channels exhibited markedly different quinine sensitivity and characteristics of inhibition, but introduction of the H462Y amino acid exchange conferred  $K_v11.1$ -

like quinine sensitivity to  $K_v12.1$  channels. Based on these findings, we conclude that H462 determines the low quinine sensitivity and the characteristics of quinine-dependent inhibition for  $K_v12.1$  channels and that the binding pocket for substituted quinolines in the central cavity is not completely conserved within the Eag superfamily of  $K_v$  channels. However, as the H462Y point mutation restored  $K_v11.1$ -like quinine sensitivity in  $K_v12.1$ , these findings demonstrated that the quinoline-binding pocket also exists in  $K_v12.1$  and that thus the overall architecture of the channels is similar.

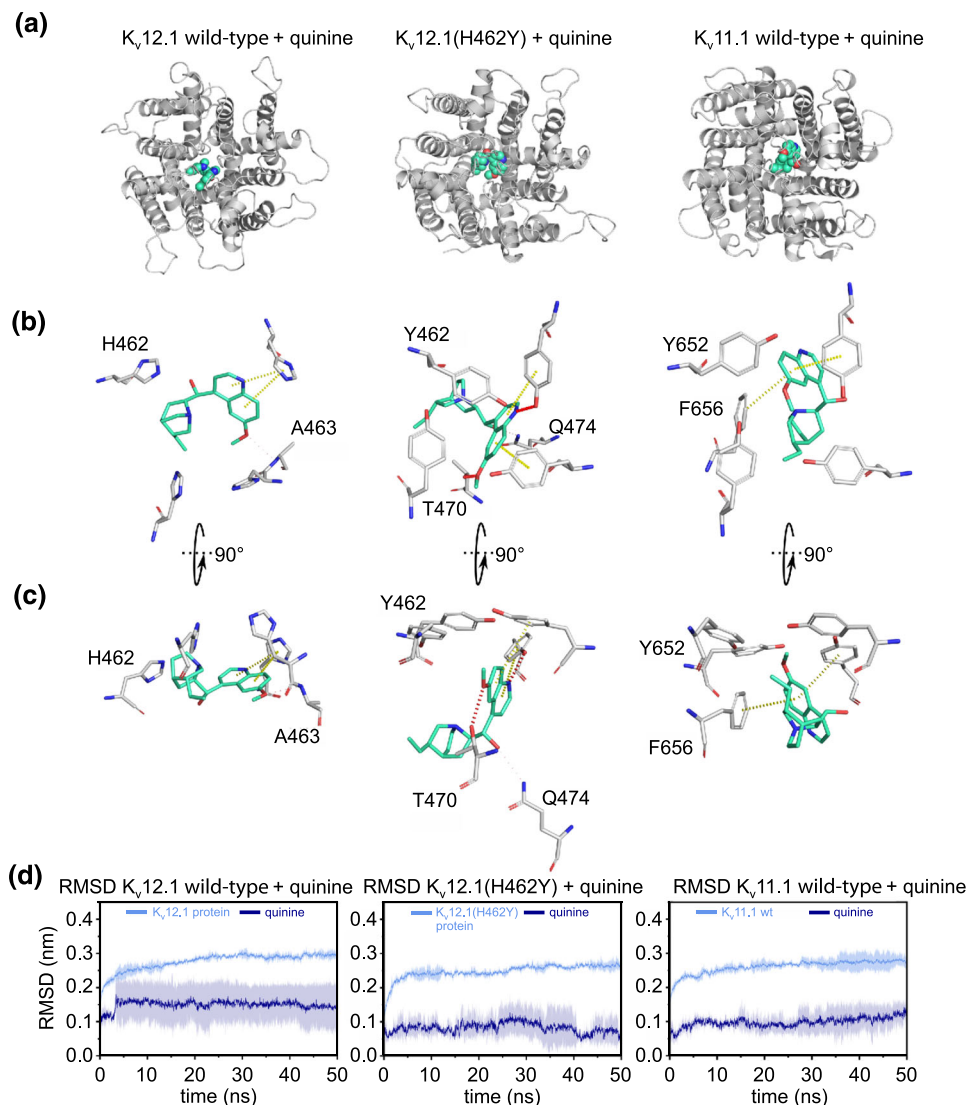


**FIGURE 6** Molecular interactions of quinine with  $K_v12.1$ ,  $K_v12.1(H462Y)$ , and  $K_v11.1$ . (a) Top-view representations of  $K_v12.1$  (left),  $K_v12.1(H462Y)$  (middle), and  $K_v11.1$  (right) channels with docked quinine (green-cyan spheres). (b) Top and (c) side view of the quinine-binding site after 50 ns of molecular dynamics simulations for  $K_v12.1$  (left),  $K_v12.1(H462Y)$  (middle), and  $K_v11.1$  (right). Directly interacting residues, as well as position 462 in  $K_v12.1$  isoforms (652 in  $K_v11.1$ ), are presented as sticks, with oxygen atoms coloured in red and nitrogen atoms coloured in blue. Yellow lines indicate  $\pi$ -stacking interactions, while red lines indicate H bonds. (d) Stability of the pore domains (excluding extracellular loops), measured as the root-mean-square deviation (RMSD) as a function of 50-ns simulation time

### 3.6 | H462 determines the low quinine affinity of human $K_v12.1$ channels

To elucidate the molecular principles of the low quinine affinity of  $K_v12.1$ , we performed molecular docking and subsequent MD analyses (Figure 6). Quinine binding to the pore helix/S6 domain (amino acids S353–Y477) of  $K_v12.1$  and  $K_v12.1(H462Y)$  channels was studied using homology models based on the cryo-EM structure of human  $K_v11.1$  (Wang & MacKinnon, 2017). We also utilised the available structural information to study quinine binding to  $K_v11.1$  channels. Molecular docking suggested that quinine binds below residue H462 into the central cavity of human  $K_v12.1$  (Figure 6a, left panel), with an estimated binding affinity (Chemscore.DG) of  $-20.5 \text{ kJ}\cdot\text{mol}^{-1}$ . To validate the stability and refine the binding pose

obtained from docking, we performed three independent 50-ns MD simulations of the highest scored docking pose. Overall, quinine remained stable in these MD simulations, as indicated by root-mean-square deviation (RMSD) below 2 Å (Figure 6d, left panel). Further,  $\pi$ - $\pi$  stacking between methoxyquinoline group and H462 from one subunit was maintained throughout 50 ns of MD simulation (Figure 6 b,c, left panel). Similar to wild-type channels, quinine docked into the central cavity of  $K_v12.1(H462Y)$  without any obvious interactions to the residues of the selectivity filter (Figure 6a–c, middle panel). In  $K_v12.1(H462Y)$ ,  $\pi$ - $\pi$  interactions with the methoxyquinoline moiety were also observed; however, in the mutant channel, these interactions are formed with mutated Y462 side chains from two adjacent subunits. Additionally, we observed a hydrogen bond between Y462 and quinoline moiety of quinine in the majority of docking poses that

remained stable throughout the 50-ns MD simulations. In agreement with our experimental findings, the estimated quinine-binding affinity of  $-31.1 \text{ kJ}\cdot\text{mol}^{-1}$  for  $K_v12.1(\text{H462Y})$  was considerably higher than for wild-type  $K_v12.1$  channels. In line, in the simulations, an additional hydrogen bond between the methoxy group of quinidine and the residue T470 formed in the mutant channels (Figure 6c, middle panel). As shown in Figure 6d, the binding pose of quinine was highly stable in MD simulations, with an RMSD of about  $1 \text{ \AA}$ . In the  $K_v11.1$  cryo-EM structure (Wang & MacKinnon, 2017), quinine was also predicted to bind slightly below Y652, in the central cavity, with favourable hydrophobic interactions with Y652 residues of all subunits and with F656 from only one subunit. Also, in line with our experimental findings, the estimated affinity of quinine binding to  $K_v11.1$  wild-type channels amounts to  $-33.9 \text{ kJ}\cdot\text{mol}^{-1}$  in our simulations and thus was similar to  $K_v12.1(\text{H462Y})$  and higher than that of wild-type  $K_v12.1$  channels. Further,  $\pi$ - $\pi$  interactions with Y652 and F656 residues in  $K_v11.1$  from opposite subunits were predicted by these simulations (Figure 6b,c, right panel), again leading to a very stable binding mode with RMSD values of  $\sim 1 \text{ \AA}$  (Figure 6d, right panel).

In summary, molecular modelling revealed that weak interactions between quinine and particularly H462 determined the low affinity and sensitivity of  $K_v12.1$  wild-type channels to quinine. The higher affinity of  $K_v12.1(\text{H462Y})$  channels and of the closely related  $K_v11.1$  can be explained by more favourable interactions with the drug, mainly at position Y462, and in the case of  $K_v11.1$  additionally with F656 from one subunit. Surprisingly, despite the conservation of this second aromatic side chain between  $K_v11$  and  $K_v12$  channels, interactions with this second aromatic residue are completely absent in the  $K_v12.1$  (Figure 6b, left panel vs. right panel). However, also in  $K_v11.1$  channels, these interactions are relatively weak due to a preferred orientation of the Y652/F656 side chains towards helix S5 (see Figure S2, for orientation of aromatic side chains at positions H462/F466 in  $K_v12.1$  wild-type and Y652/F656 in  $K_v11.1$  wild-type channels in simulations).

## 4 | DISCUSSION

Substituted quinolines are well-known antimalarial agents (quinine and chloroquine) and antiarrhythmic drugs (quinidine; Bozic, Uzelac, Kezic, & Bajcetic, 2018). As considerable side effect, these substances inhibit  $K_v11.1$  channels at low micromolar concentrations, which may result in acquired (drug-induced) LQT syndrome, syncope, and sudden death in humans (Mitcheson et al., 2005; Mitcheson et al., 2000; Sanguinetti & Tristani-Firouzi, 2006). Several mutagenesis studies have attributed the susceptibility of  $K_v11.1$  to drug-dependent block to amino acids in the pore domain of these channels, threonine 623 and valine 625 of inner pore helix and selectivity filter, respectively, as well as tyrosine 652 and phenylalanine 656 in the sixth transmembrane segment (S6; Mitcheson et al., 2000; Sanchez-Chapula et al., 2002; Sanchez-Chapula et al., 2003). On the one hand, valine 625 (together with other residues such as asparagine 588, serine 631, and serine 620) controls drug sensitivity of  $K_v11.1$

through its contribution to channel inactivation that has been shown to be necessary for channel inhibition by several high-affinity blockers (e.g., Kamiya et al., 2006; Perrin et al., 2008; Wu et al., 2015). On the other hand, some of these residues form hydrophobic pockets in combination with other amino acids at the inner surface of the small central cavity of  $K_v11.1$  channels (Wang & MacKinnon, 2017). These pockets are endowed with high electro-negative potentials and therefore favour binding of positively charged drugs (Wang & MacKinnon, 2017). The exclusive sensitivity of  $K_v11.1$  to a wide variety of drugs with diverging structures is explained by the absence of such binding pockets in other  $K^+$  channels (Wang & MacKinnon, 2017).

Closely related  $K_v10$  and  $K_v12$  channels share high similarity to  $K_v11.1$ , which suggests that these channels also possess analogous drug-binding pockets, similar drug sensitivity, and characteristics of inhibition (Bauer & Schwarz, 2018). Indeed, the respective amino acids determining the susceptibility of  $K_v11.1$  to quinoline block are conserved in  $K_v10$  channels. However, whereas  $K_v10.1$  displayed the same sensitivity to quinidine-dependent inhibition as  $K_v11.1$ , quinidine sensitivity of  $K_v10.2$  channels was 100-fold lower (Gessner et al., 2004; Lees-Miller et al., 2000; Sanchez-Chapula et al., 2003; Schonherr et al., 2002). The lower susceptibility of the  $K_v10$  isoforms to drug-induced inhibition is explained by their lack of inactivation, that is, conformational reorientations during inactivation necessary for high affinity drug block in  $K_v11.1$  do not occur in  $K_v10$  channels (Chen et al., 2002; Ficker et al., 1998; Ficker et al., 2001). Thus, the lower sensitivity of  $K_v10$  channels indicates that additional drug interaction sites outside the central binding motif might determine drug block in these channels (Gessner et al., 2004; Schonherr et al., 2002). We wondered whether  $K_v12.1$  channels possess a quinoline-binding pocket analogous to  $K_v10.1$  and  $K_v11.1$  channels despite an amino acid exchange at position 462. We found that quinine inhibited  $K_v12.1$  channels, but their sensitivity was 10 times lower than that of  $K_v11.1$  channels. Thus,  $K_v12.1$  constitutes a natural variant of Eag superfamily channels with low quinoline-binding affinity.

### 4.1 | H462 determines quinine sensitivity of $K_v12.1$

The quinoline-binding "motif" of  $K_v11.1$  is not completely conserved in the three members of the  $K_v12$  channel family that carry a histidine at the position homologous to tyrosine 652 in  $K_v11.1$  (H462 in  $K_v12.1$ ; c.f. Figure 3a). As in  $K_v11.1$ , this aromatic residue determines the quinoline-binding affinity (Lees-Miller et al., 2000; Sanchez-Chapula et al., 2003), we hypothesised that this small sequence difference explained the 10-fold lower quinine sensitivity of  $K_v12.1$ . Indeed, replacing this histidine in  $K_v12.1$  with the respective tyrosine of  $K_v11.1$  through site-directed mutagenesis dramatically increased the quinine affinity of  $K_v12.1(\text{H462Y})$ . In fact, quinine sensitivity of  $K_v12.1(\text{H462Y})$  was more similar to  $K_v11.1$  than to wild-type  $K_v12.1$ . Our findings are supported by earlier studies showing that mutating Y652 dramatically changes quinidine sensitivity of  $K_v11.1$  channels,



for example, introduction of an alanine at this position caused a threefold reduction of quinidine affinity in  $K_v11.1(Y652A)$  channels (Sanchez-Chapula et al., 2003). Utilising molecular modelling simulations, we found that the low sensitivity of  $K_v12.1$  channels may be explained by only weak interactions between quinine and amino acids in the central cavity (including H462). Noteworthy, in  $K_v12.1(H462Y)$  channels, more favourable interactions developed that most probably rendered this channel mutant more sensitive to quinine. In line with our experimental findings, docking analyses predicted considerably lower quinine affinities for  $K_v12.1$  ( $-20.5 \text{ kJ}\cdot\text{mol}^{-1}$ ), compared with the  $K_v12.1(H462Y)$  mutant ( $-31.1 \text{ kJ}\cdot\text{mol}^{-1}$ ) and  $K_v11.1$  wild-type channels ( $-33.9 \text{ kJ}\cdot\text{mol}^{-1}$ ). Our models predicted a key difference in the orientation and interactions of the first aromatic side chain, which limits hydrophobic and  $\pi$ - $\pi$  interactions in  $K_v12$ , while providing strong interactions in  $K_v11$  channels. Taking together, our findings are in good agreement with a hypothesis previously published by the Sanguinetti group (Chen et al., 2002). Thus, our modelling approach recapitulated experimental findings on  $K_v11.1$  (Sanchez-Chapula et al., 2003) and provided a ready and straightforward explanation for the higher quinine affinity of  $K_v11.1$  and  $K_v12.1(H462Y)$  compared with  $K_v12.1$  wild-type channels.

Yet, as mentioned above, drug sensitivity of  $K_v11.1$  channels is determined by channel inactivation (e.g., through V625, N588, S631, and S620; Ficker et al., 1998; Ficker et al., 2001; Kamiya et al., 2006; Perrin et al., 2008; Wu et al., 2015). As shown for  $K_v10$  channels (Chen et al., 2002; Ficker et al., 1998; Ficker et al., 2001), lack of inactivation might contribute to low drug sensitivity of  $K_v12.1$  channels. However, above-mentioned residues (except N588 where  $K_v12.1$  has an E) are conserved in  $K_v12.1$  channels, and the single amino acid exchange H462Y sufficed to significantly lower the quinine affinity of these channels (even slightly below that of  $K_v11.1$  channels; c.f. Figure 5a). We thus estimate that relevance of these amino acids for drug interactions is low in  $K_v12.1$ , but we cannot provide any evidence for this assumption at present. Thus, further work is needed to elucidate whether these residues also determine drug sensitivity in  $K_v12$  family members and whether the channel mutant inactivates at all (e.g., during prolonged depolarisations).

Importantly, our findings once again highlight that Y652 determines quinoline sensitivity in closely related  $K_v11.1$  channels (Lees-Miller et al., 2000; Macdonald, Kim, Kurata, & Fedida, 2018; Sanchez-Chapula et al., 2002; Sanchez-Chapula et al., 2003). Although indicated by an early report analysing binding of chloroquine to  $K_v11.1$  in silico (Sanchez-Chapula et al., 2002), we did not detect any cation- $\pi$  interactions between quinine and  $K_v11.1$ ,  $K_v12.1$ , or  $K_v12.1(H462Y)$  channels. Noteworthy, our simulations support a recent study that utilised unnatural amino acid incorporation to show that cation- $\pi$  interactions at position Y652 are not relevant for drug binding in  $K_v11.1$  channels (Macdonald et al., 2018). Based on these findings, we conclude that H462 determines the low quinine sensitivity of  $K_v12.1$  and that possibly no amino acid motifs outside the central cavity contribute to quinoline binding in  $K_v12.1$  channels (for  $K_v10$ , see Gessner et al., 2004; Schonherr et al., 2002). Thus, as far as quinoline sensitivity is concerned,

$K_v12$  channels are probably more similar to other  $K_v$  families that typically carry isoleucine or valine at this position than to closely related  $K_v11$  channels.

## 4.2 | H462 determines characteristics of quinine-dependent inhibition in $K_v12.1$

Our experiments showed that quinine-induced inhibition of  $K_v12.1$  channels was largely voltage independent and characterised by a shift of activation voltages to depolarised potentials. Although it has been shown that many inhibitors (including quinidine or chloroquine; Sanchez-Chapula et al., 2003; Sanchez-Chapula et al., 2002) preferentially block activated  $K_v11.1$  channels, we did not find any evidence for such quinine-dependent open channel block for  $K_v12.1$  wild-type channels. Transient activation of  $K_v12.1(H462Y)$  channels at depolarised membrane potentials in the presence of quinine (c.f. Figure 4b), however, might indicate such open channel block for the channel mutant, but we consider that further work including other inhibitors is needed to elucidate whether the amino acid position 462 indeed determines open channel block in  $K_v12.1$  channels.

As  $K_v12.1$  wild-type channels were more sensitive to quinine after conditioning hyperpolarisation of the membrane, quinine block depended on mode shift, in contrast to  $K_v12.1(H462Y)$  that were inhibited by quinine independent on conditioning potentials. Although we do not have any evidence for this assumption yet, conformational changes associated with establishment of mode shift might thus render  $K_v12.1$  channels less sensitive to quinine. Quinine inhibited  $K_v11.1$  more significantly, when the channels were activated at depolarised potentials, but only following the hyperpolarised conditioning potential. Thus, quinine block of  $K_v11.1$  also depended on mode shift, but the underlying mechanisms may be different between  $K_v11$  and  $K_v12$  channels. In contrast to  $K_v12.1$  wild-type channels, quinine induced  $K_v11.1$  channel opening at more negative membrane potentials in line with a previous report (Sanchez-Chapula et al., 2003). Interestingly, the H462Y amino acid exchange conferred  $K_v11.1$ -type characteristics of quinine-dependent inhibition to  $K_v12.1$  channels. Thus, H462 determines not only quinine sensitivity but also the characteristics of quinine-dependent inhibition in  $K_v12.1$  channels. Likewise, mutating the homologous tyrosine substantially changed the voltage dependence of quinoline block in  $K_v11.1$ , that is, voltage dependence was abolished in  $K_v11.1(Y652F)$ , but it was completely reversed in  $K_v11.1(Y652A)$  channels (Sanchez-Chapula et al., 2003). Yet the molecular mechanisms underlying such voltage-dependent inhibition remain elusive for the  $K_v12.1$  mutant, as well as for  $K_v11.1$  channels. It was hypothesised earlier for chloroquine-induced block of  $K_v11.1$  that Y652 might change position during voltage-dependent gating, thereby generating a depolarisation-induced binding pocket with higher affinity (Sanchez-Chapula et al., 2003). This may induce pronounced channel inhibition during channel activation at more depolarised membrane potentials. Accordingly, as proposed for  $K_v11.1$  carrying mutations at position 652 (Sanchez-Chapula et al., 2003), the low quinine affinity of  $K_v12.1$  wild-type

channels might prevent generation of an analogous binding site with higher affinity, which might account for lack of voltage dependence in these channels. Thus, similar molecular mechanisms may apply for  $K_v11.1$  and  $K_v12.1$  during drug-induced inhibition, but we cannot provide any evidence for such processes at present.

### 4.3 | Conclusion and significance

We showed that  $K_v12.1$  is a natural variant of Eag superfamily channels with low quinine sensitivity. Thus, the drug-binding pocket in the central cavity is not completely conserved in the Eag superfamily of  $K_v$  channels, which highlights functional and pharmacological diversity within this group of evolutionary conserved ion channels. However, our work also demonstrated that the drug-binding pocket exists in  $K_v12.1$  and that thus the overall architecture of the channels is similar. Further work is needed to elucidate whether  $K_v12.1$  channels are also endowed with lower sensitivity to the many more drugs that block closely related  $K_v11.1$ .

### ACKNOWLEDGEMENTS

The authors gratefully acknowledge the kind gift of plasmids for  $K_v12.1$  from Dr T. Jegla and for  $K_v11.1$  from Dr. C.K. Bauer. We thank Olga Ebers for superb technical assistance.

This work was funded by the Deutsche Forschungsgemeinschaft (DFG Priority Program 1608: "Ultrafast and temporally precise information processing: Normal and dysfunctional hearing," [LE 3600/1-1 to M.G.L.]).

W.B.V.H. was supported by an internship from the Graduate School of Life Sciences from the University of Utrecht and a travel grant from the Dutch Heart Foundation.

The computational results presented have been achieved in part using the Vienna Scientific Cluster (VSC).

### CONFLICT OF INTEREST

The authors declare no conflict of interest.

### AUTHOR CONTRIBUTIONS

M.D., A.S.-W., and M.G.L. participated in the research design; M.D., W.B.V.H., A.S.-W., and M.G.L. conducted the experiments and performed the data analysis; M.D., A.S.-W., and M.G.L. wrote or contributed to the writing of the manuscript; and all authors approved the final version of the manuscript.

### DECLARATION OF TRANSPARENCY AND SCIENTIFIC RIGOUR

This Declaration acknowledges that this paper adheres to the principles for transparent reporting and scientific rigour of preclinical research as stated in the *BJP* guidelines for [Design & Analysis](#) and as recommended by funding agencies, publishers, and other organisations engaged with supporting research.

### ORCID

Michael G. Leitner  <https://orcid.org/0000-0002-3259-6481>

### REFERENCES

- Abraham, M. J., van der Spoel, D., Lindahl, E., Hess, B., & team atGd (2016). GROMACS user manual version 5.1.2, [www.gromacs.org](http://www.gromacs.org).
- Alexander, S. P., Striessnig, J., Kelly, E., Marrion, N. V., Peters, J. A., Faccenda, E., ... CGTP Collaborators. (2017). The Concise Guide to PHARMACOLOGY 2017/18: Voltage-gated ion channels. *British Journal of Pharmacology*, 174(Suppl 1), S160–S194. <https://doi.org/10.1111/bph.13884>
- Bauer, C. K., & Schwarz, J. R. (2001). Physiology of EAG  $K^+$  channels. *The Journal of Membrane Biology*, 182, 1–15. <https://doi.org/10.1007/s00232-001-0031-3>
- Bauer, C. K., & Schwarz, J. R. (2018). Ether-a-go-go  $K^+$  channels: Effective modulators of neuronal excitability. *The Journal of Physiology*, 596, 769–783. <https://doi.org/10.1113/JP275477>
- Best, R. B., Zhu, X., Shim, J., Lopes, P. E., Mittal, J., Feig, M., & MacKerell, A. D. Jr. (2012). Optimization of the additive CHARMM all-atom protein force field targeting improved sampling of the backbone  $\phi$ ,  $\psi$  and side-chain  $\chi_1$  and  $\chi_2$  dihedral angles. *Journal of Chemical Theory and Computation*, 8, 3257–3273. <https://doi.org/10.1021/ct300400x>
- Bezanilla, F., Taylor, R. E., & Fernandez, J. M. (1982). Distribution and kinetics of membrane dielectric polarization. 1. Long-term inactivation of gating currents. *The Journal of General Physiology*, 79, 21–40. <https://doi.org/10.1085/jgp.79.1.21>
- Bozic, B., Uzelac, T. V., Kezic, A., & Bajcetic, M. (2018). The role of quinidine in the pharmacological therapy of ventricular arrhythmias 'quinidine'. *Mini Reviews in Medicinal Chemistry*, 18, 468–475. <https://doi.org/10.2174/1389557517666170707110450>
- Bussi, G., Donadio, D., & Parrinello, M. (2007). Canonical sampling through velocity rescaling. *The Journal of Chemical Physics*, 126, 014101. <https://doi.org/10.1063/1.2408420>
- Chen, J., Seebohm, G., & Sanguinetti, M. C. (2002). Position of aromatic residues in the S6 domain, not inactivation, dictates cisapride sensitivity of HERG and eag potassium channels. *Proceedings of the National Academy of Sciences of the United States of America*, 99, 12461–12466. <https://doi.org/10.1073/pnas.192367299>
- Curran, M. E., Splawski, I., Timothy, K. W., Vincent, G. M., Green, E. D., & Keating, M. T. (1995). A molecular basis for cardiac arrhythmia: HERG mutations cause long QT syndrome. *Cell*, 80, 795–803. [https://doi.org/10.1016/0092-8674\(95\)90358-5](https://doi.org/10.1016/0092-8674(95)90358-5)
- Curtis, M. J., Alexander, S., Cirino, G., Docherty, J. R., George, C. H., Giembycz, M. A., ... Ahluwalia, A. (2018). Experimental design and analysis and their reporting II: updated and simplified guidance for authors and peer reviewers. *British Journal of Pharmacology*, 175, 987–993. <https://doi.org/10.1111/bph.14153>
- Dai, G., & Zagotta, W. N. (2017). Molecular mechanism of voltage-dependent potentiation of KCNH potassium channels. *eLife*, 6. <https://doi.org/10.7554/eLife.26355>
- Darden, T., York, D., & Pedersen, L. (1993). Particle mesh Ewald: An  $N\log(N)$  method for Ewald sums in large systems. *The Journal of Chemical Physics*, 98, 10089–10092. <https://doi.org/10.1063/1.464397>
- Dierich, M., Evers, S., Wilke, B. U., & Leitner, M. G. (2018). Inverse modulation of neuronal  $K_v12.1$  and  $K_v11.1$  channels by 4-aminopyridine and NS1643. *Frontiers in Molecular Neuroscience*, 11, 11. <https://doi.org/10.3389/fnmol.2018.00011>
- Dierich, M., & Leitner, M. G. (2018).  $K_v12.1$  channels are not sensitive to  $G_q$ PCR-triggered activation of phospholipase C $\beta$ . *Channels (Austin, Tex.)*, 12, 228–239. <https://doi.org/10.1080/19336950.2018.1475783>

- Engeland, B., Neu, A., Ludwig, J., Roeper, J., & Pongs, O. (1998). Cloning and functional expression of rat ether-a-go-go-like K<sup>+</sup> channel genes. *The Journal of Physiology*, 513 (Pt 3), 647–654. <https://doi.org/10.1111/j.1469-7793.1998.647ba.x>
- Ficker, E., Jarolimek, W., & Brown, A. M. (2001). Molecular determinants of inactivation and dofetilide block in ether a-go-go (EAG) channels and EAG-related K<sup>+</sup> channels. *Molecular Pharmacology*, 60, 1343–1348. <https://doi.org/10.1124/mol.60.6.1343>
- Ficker, E., Jarolimek, W., Kiehn, J., Baumann, A., & Brown, A. M. (1998). Molecular determinants of dofetilide block of HERG K<sup>+</sup> channels. *Circulation Research*, 82, 386–395. <https://doi.org/10.1161/01.RES.82.3.386>
- Furutani, K., Yamakawa, Y., Inanobe, A., Iwata, M., Ohno, Y., & Kurachi, Y. (2011). A mechanism underlying compound-induced voltage shift in the current activation of hERG by antiarrhythmic agents. *Biochemical and Biophysical Research Communications*, 415, 141–146. <https://doi.org/10.1016/j.bbrc.2011.10.034>
- Gessner, G., Zacharias, M., Bechstedt, S., Schonherr, R., & Heinemann, S. H. (2004). Molecular determinants for high-affinity block of human EAG potassium channels by antiarrhythmic agents. *Molecular Pharmacology*, 65, 1120–1129. <https://doi.org/10.1124/mol.65.5.1120>
- Harding, S. D., Sharman, J. L., Faccenda, E., Southan, C., Pawson, A. J., Ireland, S., ... NC-IUPHAR (2018). The IUPHAR/BPS Guide to PHARMACOLOGY in 2018: Updates and expansion to encompass the new guide to IMMUNOPHARMACOLOGY. *Nucleic Acids Research*, 46, D1091–D1106. <https://doi.org/10.1093/nar/gkx1121>
- Helliwell, M. V., Zhang, Y., El Harchi, A., Du, C., Hancox, J. C., & Dempsey, C. E. (2018). Structural implications of hERG K<sup>+</sup> channel block by a high-affinity minimally structured blocker. *Journal of Biological Chemistry*, 293, 7040–7057. <https://doi.org/10.1074/jbc.RA117.000363>
- Hess, B., Bekker, H., Berendsen, H. J. C., & Fraaije, J. (1997). LINC: A linear constraint solver for molecular simulations. *Journal of Computational Chemistry*, 18, 1463–1472. [https://doi.org/10.1002/\(SICI\)1096-987X\(199709\)18:12<1463::AID-JCC4>3.0.CO;2-H](https://doi.org/10.1002/(SICI)1096-987X(199709)18:12<1463::AID-JCC4>3.0.CO;2-H)
- Humphrey, W., Dalke, A., & Schulten, K. (1996). VMD: Visual molecular dynamics. *Journal of Molecular Graphics & Modelling*, 14, 33–38. [https://doi.org/10.1016/0263-7855\(96\)00018-5](https://doi.org/10.1016/0263-7855(96)00018-5)
- Jo, S., Kim, T., Iyer, V. G., & Im, W. (2008). CHARMM-GUI: A web-based graphical user interface for CHARMM. *Journal of Computational Chemistry*, 29, 1859–1865. <https://doi.org/10.1002/jcc.20945>
- Jones, G., Willett, P., Glen, R. C., Leach, A. R., & Taylor, R. (1997). Development and validation of a genetic algorithm for flexible docking. *Journal of Molecular Biology*, 267, 727–748. <https://doi.org/10.1006/jmbi.1996.0897>
- Kamiya, K., Mitcheson, J. S., Yasui, K., Kodama, I., & Sanguinetti, M. C. (2001). Open channel block of HERG K<sup>+</sup> channels by vesnarinone. *Molecular Pharmacology*, 60, 244–253. <https://doi.org/10.1124/mol.60.2.244>
- Kamiya, K., Niwa, R., Mitcheson, J. S., & Sanguinetti, M. C. (2006). Molecular determinants of HERG channel block. *Molecular Pharmacology*, 69, 1709–1716. <https://doi.org/10.1124/mol.105.020990>
- Kazmierczak, M., Zhang, X., Chen, B., Mulkey, D. K., Shi, Y., Wagner, P. G., ... Jegla, T. (2013). External pH modulates EAG superfamily K<sup>+</sup> channels through EAG-specific acidic residues in the voltage sensor. *The Journal of General Physiology*, 141, 721–735. <https://doi.org/10.1085/jgp.201210938>
- Keating, M. T., & Sanguinetti, M. C. (2001). Molecular and cellular mechanisms of cardiac arrhythmias. *Cell*, 104, 569–580. [https://doi.org/10.1016/S0092-8674\(01\)00243-4](https://doi.org/10.1016/S0092-8674(01)00243-4)
- Klauda, J. B., Venable, R. M., Freites, J. A., O'Connor, J. W., Tobias, D. J., Mondragon-Ramirez, C., ... Pastor, R. W. (2010). Update of the CHARMM all-atom additive force field for lipids: Validation on six lipid types. *The Journal of Physical Chemistry. B*, 114, 7830–7843. <https://doi.org/10.1021/jp101759q>
- Lees-Miller, J. P., Duan, Y., Teng, G. Q., & Duff, H. J. (2000). Molecular determinant of high-affinity dofetilide binding to HERG1 expressed in *Xenopus* oocytes: Involvement of S6 sites. *Molecular Pharmacology*, 57, 367–374.
- Leitner, M. G., Feuer, A., Ebers, O., Schreiber, D. N., Halaszovich, C. R., & Oliver, D. (2012). Restoration of ion channel function in deafness-causing KCNQ4 mutants by synthetic channel openers. *British Journal of Pharmacology*, 165, 2244–2259. <https://doi.org/10.1111/j.1476-5381.2011.01697.x>
- Leitner, M. G., Halaszovich, C. R., & Oliver, D. (2011). Aminoglycosides inhibit KCNQ4 channels in cochlear outer hair cells via depletion of phosphatidylinositol(4,5)bisphosphate. *Molecular Pharmacology*, 79, 51–60. <https://doi.org/10.1124/mol.110.068130>
- Leitner, M. G., Michel, N., Behrendt, M., Dierich, M., Dembla, S., Wilke, B. U., ... Oliver, D. (2016). Direct modulation of TRPM4 and TRPM3 channels by the phospholipase C inhibitor U73122. *British Journal of Pharmacology*, 173, 2555–2569. <https://doi.org/10.1111/bph.13538>
- Li, X., Anishkin, A., Liu, H., van Rossum, D. B., Chintapalli, S. V., Sassic, J. K., ... Jegla, T. (2015). Bimodal regulation of an Elk subfamily K<sup>+</sup> channel by phosphatidylinositol 4,5-bisphosphate. *The Journal of General Physiology*, 146, 357–374. <https://doi.org/10.1085/jgp.201511491>
- Macdonald, L. C., Kim, R. Y., Kurata, H. T., & Fedida, D. (2018). Probing the molecular basis of hERG drug block with unnatural amino acids. *Scientific Reports*, 8, 289. <https://doi.org/10.1038/s41598-017-18448-x>
- MacKerell, A. D., Bashford, D., Bellott, M., Dunbrack, R. L., Evanseck, J. D., Field, M. J., ... Karplus, M. (1998). All-atom empirical potential for molecular modeling and dynamics studies of proteins. *The Journal of Physical Chemistry. B*, 102, 3586–3616. <https://doi.org/10.1021/jp973084f>
- Mackerell, A. D. Jr., Feig, M., & Brooks, C. L. 3rd (2004). Extending the treatment of backbone energetics in protein force fields: Limitations of gas-phase quantum mechanics in reproducing protein conformational distributions in molecular dynamics simulations. *Journal of Computational Chemistry*, 25, 1400–1415. <https://doi.org/10.1002/jcc.20065>
- Mitcheson, J., Perry, M., Stansfeld, P., Sanguinetti, M. C., Witchel, H., & Hancox, J. (2005). Structural determinants for high-affinity block of hERG potassium channels. *Novartis Foundation Symposium*, 266, 136–150. discussion 150-138
- Mitcheson, J. S., Chen, J., Lin, M., Culberson, C., & Sanguinetti, M. C. (2000). A structural basis for drug-induced long QT syndrome. *Proceedings of the National Academy of Sciences of the United States of America*, 97, 12329–12333. <https://doi.org/10.1073/pnas.210244497>
- Miyake, A., Mochizuki, S., Yokoi, H., Kohda, M., & Furuichi, K. (1999). New ether-a-go-go K<sup>+</sup> channel family members localized in human telencephalon. *The Journal of Biological Chemistry*, 274, 25018–25025. <https://doi.org/10.1074/jbc.274.35.25018>
- Olsson, M. H., Sondergaard, C. R., Rostkowski, M., & Jensen, J. H. (2011). PROPKA3: Consistent treatment of internal and surface residues in empirical pKa predictions. *Journal of Chemical Theory and Computation*, 7, 525–537. <https://doi.org/10.1021/ct100578z>
- O'Neil, M. J. (2013). *The Merck index—An encyclopedia of chemicals, drugs, and biologicals* 15th edition edn. Cambridge, UK: Royal Society of Chemistry.

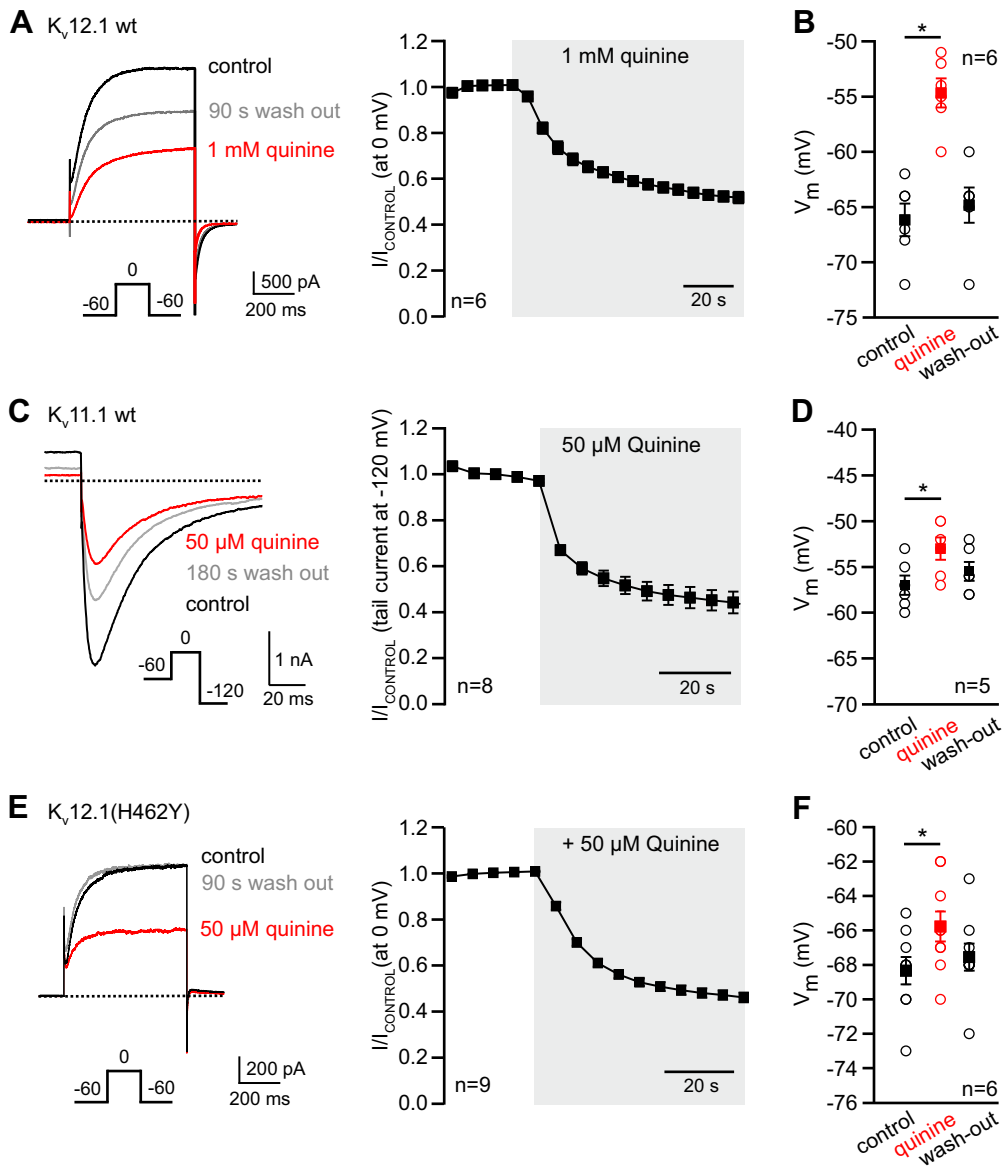
- Parrinello, M., & Rahman, A. (1981). Polymorphic transitions in single-crystals—A new molecular dynamics method. *Journal of Applied Physics*, 52, 7182–7190. <https://doi.org/10.1063/1.328693>
- Perrin, M. J., Kuchel, P. W., Campbell, T. J., & Vandenberg, J. I. (2008). Drug binding to the inactivated state is necessary but not sufficient for high-affinity binding to human ether-a-go-go-related gene channels. *Molecular Pharmacology*, 74, 1443–1452. <https://doi.org/10.1124/mol.108.049056>
- Roden, D. M. (1996). Ionic mechanisms for prolongation of refractoriness and their proarrhythmic and antiarrhythmic correlates. *The American Journal of Cardiology*, 78, 12–16. [https://doi.org/10.1016/S0002-9149\(96\)00448-1](https://doi.org/10.1016/S0002-9149(96)00448-1)
- Saganich, M. J., Machado, E., & Rudy, B. (2001). Differential expression of genes encoding subthreshold-operating voltage-gated K<sup>+</sup> channels in brain. *The Journal of Neuroscience*, 21, 4609–4624. <https://doi.org/10.1523/JNEUROSCI.21-13-04609.2001>
- Sanchez-Chapula, J. A., Ferrer, T., Navarro-Polanco, R. A., & Sanguinetti, M. C. (2003). Voltage-dependent profile of human ether-a-go-go-related gene channel block is influenced by a single residue in the S6 transmembrane domain. *Molecular Pharmacology*, 63, 1051–1058. <https://doi.org/10.1124/mol.63.5.1051>
- Sanchez-Chapula, J. A., Navarro-Polanco, R. A., Culberson, C., Chen, J., & Sanguinetti, M. C. (2002). Molecular determinants of voltage-dependent human ether-a-go-go related gene (HERG) K<sup>+</sup> channel block. *The Journal of Biological Chemistry*, 277, 23587–23595. <https://doi.org/10.1074/jbc.M200448200>
- Sanguinetti, M. C., Jiang, C., Curran, M. E., & Keating, M. T. (1995). A mechanistic link between an inherited and an acquired cardiac arrhythmia: HERG encodes the IKr potassium channel. *Cell*, 81, 299–307. [https://doi.org/10.1016/0092-8674\(95\)90340-2](https://doi.org/10.1016/0092-8674(95)90340-2)
- Sanguinetti, M. C., & Tristani-Firouzi, M. (2006). hERG potassium channels and cardiac arrhythmia. *Nature*, 440, 463–469. <https://doi.org/10.1038/nature04710>
- Saxena, P., Zangerl-Plessl, E. M., Linder, T., Windisch, A., Hohaus, A., Timin, E., ... Stary-Weinzinger, A. (2016). New potential binding determinant for hERG channel inhibitors. *Scientific Reports*, 6, 24182. <https://doi.org/10.1038/srep24182>
- Schönherr, R., Gessner, G., Lober, K., & Heinemann, S. H. (2002). Functional distinction of human EAG1 and EAG2 potassium channels. *FEBS Letters*, 514, 204–208. [https://doi.org/10.1016/S0014-5793\(02\)02365-7](https://doi.org/10.1016/S0014-5793(02)02365-7)
- Shi, W., Wang, H. S., Pan, Z., Wymore, R. S., Cohen, I. S., McKinnon, D., & Dixon, J. E. (1998). Cloning of a mammalian elk potassium channel gene and EAG mRNA distribution in rat sympathetic ganglia. *The Journal of Physiology*, 511 (Pt 3), 675–682. <https://doi.org/10.1111/j.1469-7793.1998.675bg.x>
- Tan, P. S., Perry, M. D., Ng, C. A., Vandenberg, J. I., & Hill, A. P. (2012). Voltage-sensing domain mode shift is coupled to the activation gate by the N-terminal tail of hERG channels. *The Journal of General Physiology*, 140, 293–306. <https://doi.org/10.1085/jgp.201110761>
- Trudeau, M. C., Titus, S. A., Branchaw, J. L., Ganetzky, B., & Robertson, G. A. (1999). Functional analysis of a mouse brain Elk-type K<sup>+</sup> channel. *The Journal of Neuroscience*, 19, 2906–2918. <https://doi.org/10.1523/JNEUROSCI.19-08-02906.1999>
- Trudeau, M. C., Warmke, J. W., Ganetzky, B., & Robertson, G. A. (1995). HERG, a human inward rectifier in the voltage-gated potassium channel family. *Science*, 269, 92–95. <https://doi.org/10.1126/science.7604285>
- Vanommeslaeghe, K., Hatcher, E., Acharya, C., Kundu, S., Zhong, S., Shim, J., ... Mackerell AD Jr (2010). CHARMM general force field: A force field for drug-like molecules compatible with the CHARMM all-atom additive biological force fields. *Journal of Computational Chemistry*, 31, 671–690. <https://doi.org/10.1002/jcc.21367>
- Villalba-Galea, C. A., Sandtner, W., Starace, D. M., & Bezannilla, F. (2008). S4-based voltage sensors have three major conformations. *Proceedings of the National Academy of Sciences of the United States of America*, 105, 17600–17607. <https://doi.org/10.1073/pnas.0807387105>
- Wang, W., & MacKinnon, R. (2017). Cryo-EM structure of the open human ether-a-go-go-related K<sup>+</sup> channel hERG. *Cell*, 169, 422–430 e410. <https://doi.org/10.1016/j.cell.2017.03.048>
- Webb, B., & Sali, A. (2016). Comparative Protein Structure Modeling Using Modeller. *Current Protocols in Bioinformatics*, 54, 5.6.1–5.6.37. John Wiley & Sons, Inc.
- Wu, W., Gardner, A., & Sanguinetti, M. C. (2015). The link between inactivation and high-affinity block of hERG1 channels. *Molecular Pharmacology*, 87, 1042–1050. <https://doi.org/10.1124/mol.115.098111>
- Zhang, X., Bertaso, F., Yoo, J. W., Baumgartel, K., Clancy, S. M., Lee, V., ... Jegla, T. (2010). Deletion of the potassium channel K<sub>v</sub>12.2 causes hippocampal hyperexcitability and epilepsy. *Nature Neuroscience*, 13, 1056–1058. <https://doi.org/10.1038/nn.2610>
- Zou, A., Lin, Z., Humble, M., Creech, C. D., Wagoner, P. K., Krafte, D., ... Wickenden, A. D. (2003). Distribution and functional properties of human KCNH8 (Elk1) potassium channels. *American Journal of Physiology. Cell Physiology*, 285, C1356–C1366. <https://doi.org/10.1152/ajpcell.00179.2003>

## SUPPORTING INFORMATION

Additional supporting information may be found online in the Supporting Information section at the end of the article.

**How to cite this article:** Dierich M, van Ham WB, Stary-Weinzinger A, Leitner MG. Histidine at position 462 determines the low quinine sensitivity of ether-à-go-go channel superfamily member K<sub>v</sub>12.1. *Br J Pharmacol*. 2019;176: 2708–2723. <https://doi.org/10.1111/bph.14693>

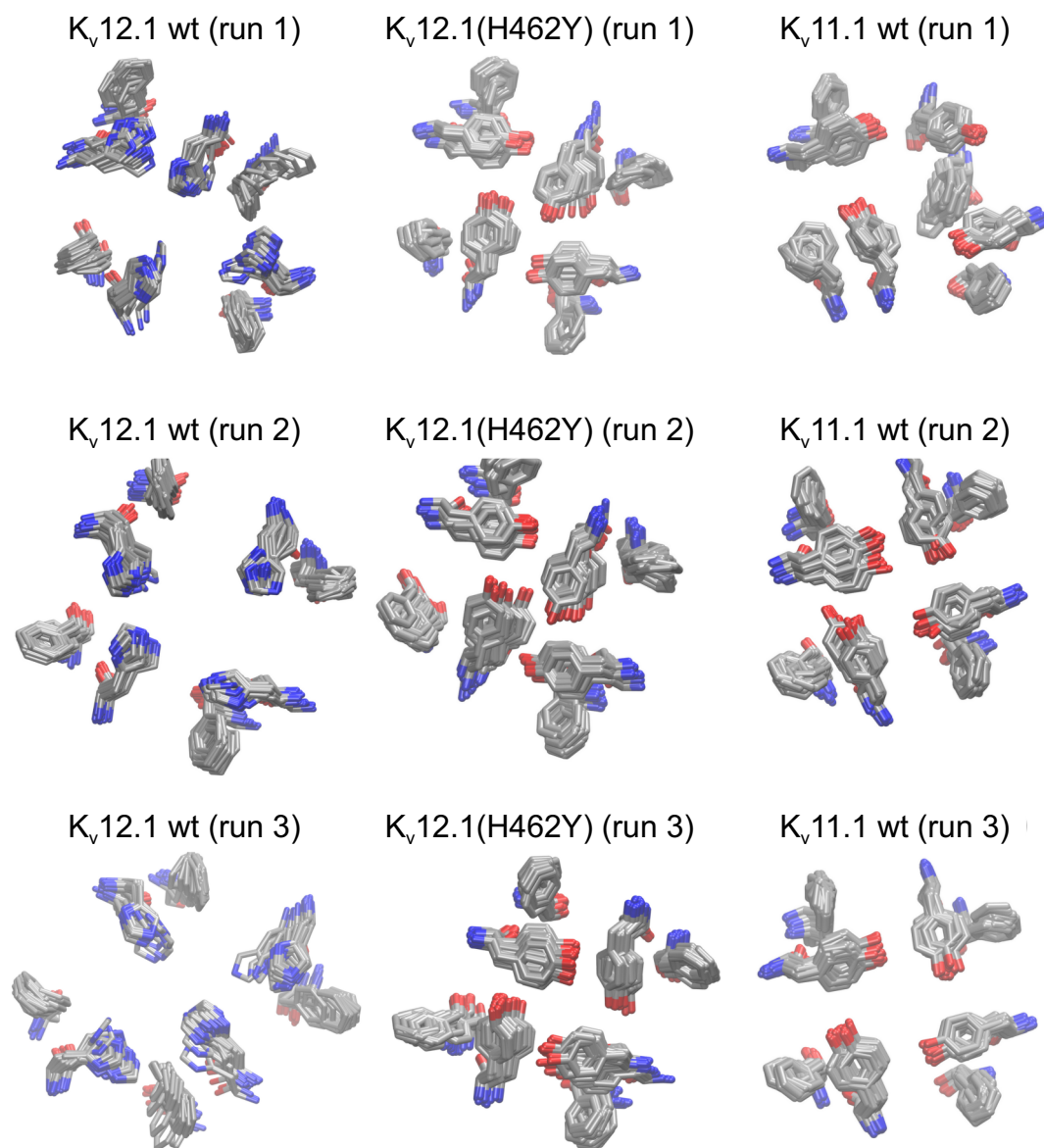
Dierich M et al., Figure S1



**Supplementary Figure 1. Rapid inhibition of recombinant  $K_v12.1$ ,  $K_v11.1$  and  $K_v12.1$ (H462Y) channels through quinine.**

(A,C,E) Within seconds, application of quinine inhibited currents through (A)  $K_v12.1$ , (C)  $K_v11.1$  and (E)  $K_v12.1$ (H462Y) channels transiently overexpressed in CHO cells. The left panels show representative recordings of CHO cells expressing these channel subunits before application of quinine (control; *black*), at the end of quinine treatment (*red*) and several minutes after wash-out of the substance (*grey*). The right panels show analyses of the time course of current amplitudes recorded in these experiments upon application of quinine. Data are presented as normalised to base line current amplitudes ( $I/I_{\text{CONTROL}}$ ). (B,D,F) In the same cells, application of quinine induced reversible depolarisation of the membrane potential. All voltage-protocols, scale bars, quinine concentrations and time points after wash-out as indicated.

Dierich M et al., Figure S2

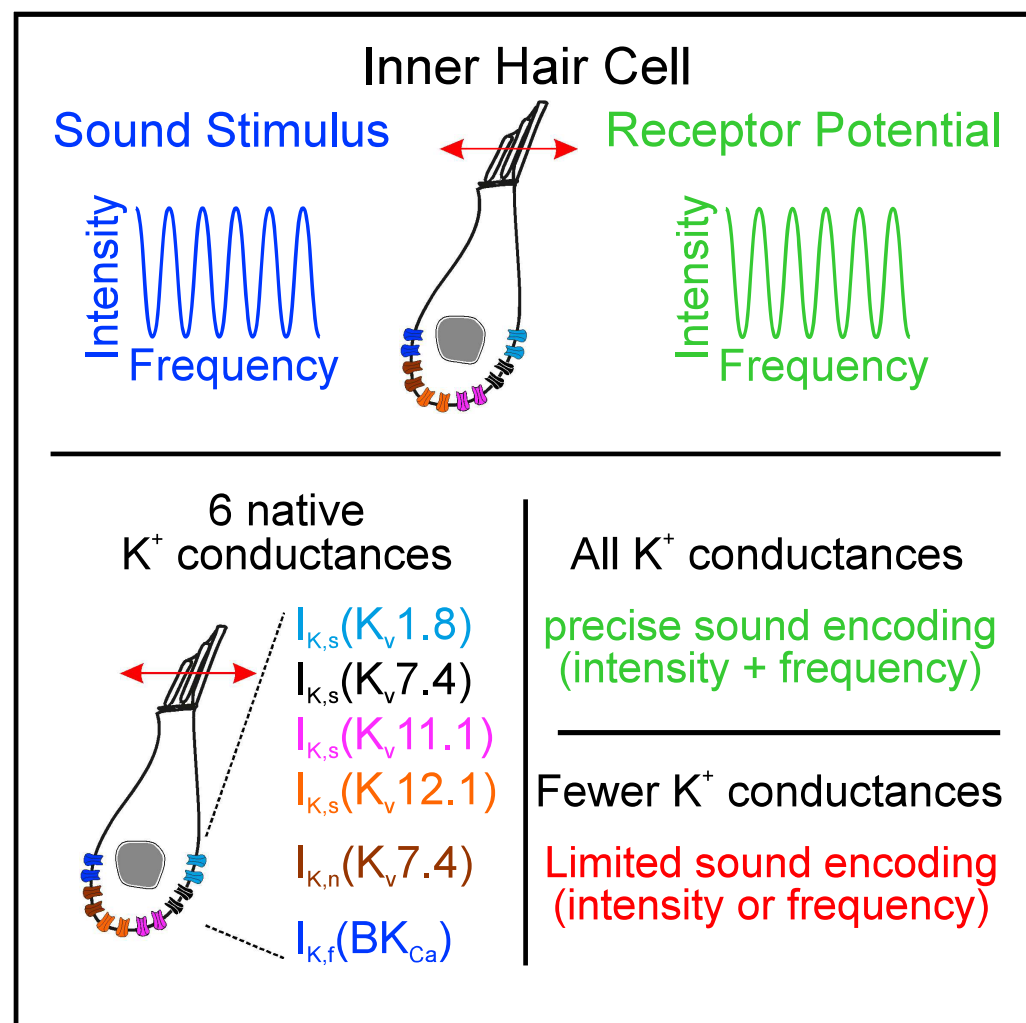


**Supplementary Figure 2. Molecular dynamics of residues H462/F466 in (K<sub>v</sub>12.1 and K<sub>v</sub>12.1(H462Y)) and Y652/F656 (in K<sub>v</sub>11.1).**

Top view of superposed snapshots from 3 independent 50 ns molecular dynamics simulations of residues H462/F466 in K<sub>v</sub>12.1 wt (*left column*) and K<sub>v</sub>12.1(H462Y) (*middle column*) and of corresponding residues Y652/F656 in K<sub>v</sub>11.1 wt channels (*right column*).

# Optimized Tuning of Auditory Inner Hair Cells to Encode Complex Sound through Synergistic Activity of Six Independent $K^+$ Current Entities

## Graphical Abstract



## Authors

Marlen Dierich, Alessandro Altoè, Julia Koppelman, ..., Sarah Verhulst, Dominik Oliver, Michael G. Leitner

## Correspondence

michael.leitner@i-med.ac.at

## In Brief

Dierich et al. show that  $K_v1.8$ ,  $K_v11.1$ ,  $K_v12.1$ ,  $K_v7.4$ , and  $BK_{Ca}$  channels give rise to six  $K^+$  conductances in auditory inner hair cells. The combined activity of all of the channels synergistically improves frequency and intensity coding. This channel repertoire constitutes an evolutionary adaptation to encode complex sound through multifaceted receptor potentials.

## Highlights

- $K_v1.8$ ,  $K_v7.4$ ,  $K_v11.1$ ,  $K_v12.1$ , and  $BK_{Ca}$  provide six  $K^+$  conductances in inner hair cells
- These conductances shape receptor potentials during sound stimulation
- Combined activity of all channels improves hair cell frequency and intensity coding
- The channel repertoire is an evolutionary adaptation to encode complex sound precisely



## Article

# Optimized Tuning of Auditory Inner Hair Cells to Encode Complex Sound through Synergistic Activity of Six Independent K<sup>+</sup> Current Entities

Marlen Dierich,<sup>1,9</sup> Alessandro Altoè,<sup>2,9</sup> Julia Koppelman,<sup>1,10</sup> Saskia Evers,<sup>1</sup> Vijay Renigunta,<sup>1</sup> Martin K. Schäfer,<sup>3,4</sup> Ronald Naumann,<sup>5</sup> Sarah Verhulst,<sup>6</sup> Dominik Oliver,<sup>1,4,7</sup> and Michael G. Leitner<sup>8,11,\*</sup>

<sup>1</sup>Department of Neurophysiology, Institute of Physiology and Pathophysiology, Philipps-University Marburg, 35037 Marburg, Germany

<sup>2</sup>Caruso Department of Otolaryngology, University of Southern California, Los Angeles, 90033 CA, USA

<sup>3</sup>Institute of Anatomy and Cell Biology, Philipps-University Marburg, 35037 Marburg, Germany

<sup>4</sup>Center for Mind, Brain, and Behavior (CMBB), Universities of Marburg and Giessen, Marburg and Giessen, Germany

<sup>5</sup>Max-Planck-Institute of Molecular Cell Biology and Genetics, 01307 Dresden, Germany

<sup>6</sup>Hearing Technology at WAVES, Department of Information Technology, Ghent University, Technologiepark 126, 9052 Zwijnaarde, Belgium

<sup>7</sup>DFG Research Training Group, Membrane Plasticity in Tissue Development and Remodelling, GRK 2213, Philipps University, Marburg, Germany

<sup>8</sup>Institute of Physiology, Department of Physiology and Medical Physics, Medical University of Innsbruck, 6020 Innsbruck, Austria

<sup>9</sup>These authors contributed equally

<sup>10</sup>Present address: Experimental Neuroimmunology, German Centre for Neurodegenerative Disease (DZNE), 72076 Tübingen, Germany

<sup>11</sup>Lead Contact

\*Correspondence: [michael.leitner@i-med.ac.at](mailto:michael.leitner@i-med.ac.at)

<https://doi.org/10.1016/j.celrep.2020.107869>

## SUMMARY

Auditory inner hair cells (IHCs) convert sound vibrations into receptor potentials that drive synaptic transmission. For the precise encoding of sound qualities, receptor potentials are shaped by K<sup>+</sup> conductances tuning the properties of the IHC membrane. Using patch-clamp and computational modeling, we unravel this membrane specialization showing that IHCs express an exclusive repertoire of six voltage-dependent K<sup>+</sup> conductances mediated by K<sub>v</sub>1.8, K<sub>v</sub>7.4, K<sub>v</sub>11.1, K<sub>v</sub>12.1, and BK<sub>Ca</sub> channels. All channels are active at rest but are triggered differentially during sound stimulation. This enables non-saturating tuning over a far larger potential range than in IHCs expressing fewer current entities. Each conductance contributes to optimizing responses, but the combined activity of all channels synergistically improves phase locking and the dynamic range of intensities that IHCs can encode. Conversely, hypothetical simpler IHCs appear limited to encode only certain aspects (frequency or intensity). The exclusive channel repertoire of IHCs thus constitutes an evolutionary adaptation to encode complex sound through multifaceted receptor potentials.

## INTRODUCTION

The mammalian inner ear processes sound over a wide range of frequencies and intensities. This high performance is realized through the conversion of a tonotopic sound-frequency map along the basilar membrane into electrical signals in inner hair cells (IHCs) and outer hair cells (OHCs) (Robles and Ruggero, 2001; Schwander et al., 2010). In these cells, sound-induced deflection of actin-based stereocilia (hair bundle) controls the activity of mechano-electrical transduction (MET) channels (Beurg et al., 2009; Pan et al., 2018; Ricci et al., 2006). This gives rise to depolarizing and hyperpolarizing receptor potentials (Schwander et al., 2010) that in OHCs drive somatic length changes thought to provide cochlear amplification associated with high sensitivity and sharp frequency selectivity in mammals (Dallos et al., 2008; Liberman et al., 2002; Zheng et al., 2000). In IHCs, depolarization activates voltage-gated Ca<sup>2+</sup> channels that control neurotrans-

mitter release triggering action potential firing in auditory neurons (Platzer et al., 2000).

Receptor potential characteristics vary significantly along the cochlear axis. In apical (low-frequency) IHCs, they exhibit a phasic (AC) component following sound frequency precisely up to few kilohertz (Dallos, 1985a, 1985b; Johnson, 2015; Russell and Sellick, 1978). In high-frequency basal IHCs, the AC component is attenuated and receptor potentials show predominant sustained (DC) potentials proportional in size to sound intensity (Johnson, 2015; Russell and Sellick, 1978). In the gerbil, the IHC membrane is intrinsically tuned to efficiently encode sound phase (frequency following) or intensity (intensity following) in the cochlear apex and base, respectively (Johnson, 2015). This is achieved through tonotopically graded activity of MET channels and accordingly depolarized resting potentials, larger resting conductance, and faster membrane time constants, enabling more precise AC potentials in apical IHCs (Johnson, 2015). IHCs along the tonotopic axis are characterized by graded combinations of three basolateral





voltage-dependent  $K^+$  currents classified into fast-activating  $I_{K,f}$ , slowly activating  $I_{K,s}$ , and negatively activating  $I_{K,n}$  based on their characteristics (Kros and Crawford, 1990; Kros et al., 1998; Oliver et al., 2003). These currents determine electrical IHC membrane properties, thereby controlling the shape and amplitude of the receptor potentials (Johnson, 2015; Kros and Crawford, 1990; Kros et al., 1998; Marcotti et al., 2003). Amplitudes of the basolateral currents vary gradually along the tonotopic axis (Johnson, 2015; Marcotti et al., 2003), which may be critical for intrinsic tuning of the IHC membrane to encode complex sound (Johnson, 2015). It is unknown whether such gradual amplitude changes are a general mechanism for intrinsic membrane tuning across species, although there is evidence for such tonotopic gradients in mice (Marcotti et al., 2003).

$I_{K,n}$  and  $I_{K,f}$  are mediated by  $K_v7.4$  and  $BK_{Ca}$  subunits, respectively (Kharkovets et al., 2006; Rüttiger et al., 2004), but the molecular identity of the channels mediating  $I_{K,s}$  is unknown. It remains elusive whether the expression of the different  $K^+$  currents provides physiological advantages to encode sound. We identified the  $K^+$  channels underlying  $I_{K,s}$  in mature IHCs and implemented all  $K^+$  channels into an extended biophysical model to unravel their physiological relevance. We show that mature IHCs express at least six independent  $K^+$  current entities with distinct biophysical properties that synergistically optimize the encoding of complex sound in the cochlea.

## RESULTS

### Pharmacological Isolation of $I_{K,s}$

In mice, IHC  $K^+$  conductances are fully developed at the end of the third postnatal week (Marcotti et al., 2003). We analyzed IHCs in the last cochlear turn of C57BL/6J mice (either sex) between 19 and 21 days after birth and refer to these as mature IHCs. As shown earlier (Kros and Crawford, 1990; Kros et al., 1998; Marcotti et al., 2003, 2004; Oliver et al., 2003), depolarizing voltage steps elicited large outwardly rectifying  $K^+$  currents in these IHCs (Figure 1A). To identify the underlying channels, we isolated  $I_{K,s}$  by inhibiting  $I_{K,f}$  and  $I_{K,n}$ .

We inhibited  $I_{K,f}$  through the extracellular application of the  $BK_{Ca}$  antagonist iberiotoxin (IbTX; 100 nM) (Lingle et al., 2019; Marcotti et al., 2003, 2004) or with the unspecific  $K^+$  channel blocker tetraethylammonium (TEA) (5 mM) (Oliver et al., 2003; Thurm et al., 2005). Both inhibited  $K^+$  currents with the same characteristics and amplitudes (at 0 mV: IbTX sensitive  $\sim 32\%$ , TEA sensitive  $\sim 34\%$  of control currents; Figures 1A, 1B, S1A, and S1B). IbTX and TEA did not depolarize IHC resting membrane potentials (IbTX:  $n = 9$ ; TEA:  $n = 10$ ; Figure 1C; Oliver et al., 2003) and thus did not affect non- $I_{K,f}$  currents (Kimitsuki et al., 2010; Oliver et al., 2003). Due to the faster time course (Figure S1A), we used TEA (5 mM) for  $I_{K,f}$  inhibition in further experiments.

We inhibited  $I_{K,n}$  with the specific  $K_v7$  antagonist XE991 (10  $\mu M$ ; Figures 1D and S1C) (Kharkovets et al., 2006; Oliver et al., 2003), which depolarized the resting membrane potential of untreated IHCs by  $\sim +8$  mV ( $n = 8$ ; Figure 1E, black). This was the same, when XE991 was applied after TEA (5 mM;  $n = 6$ ; Figure 1E, red), demonstrating TEA insensitivity of  $I_{K,n}$  (Kimitsuki et al., 2010; Oliver et al., 2003). We calculated XE991-sensitive currents by subtracting currents after the application

of XE991 from controls (Figures 1F and 1G). The XE991-sensitive currents consisted of two fractions: a small component activated at negative membrane potentials ( $V_h = -85.5 \pm 5.1$  mV;  $n = 5$ ) and a larger component activated at more depolarized potentials ( $V_h = -17.8 \pm 3.2$  mV;  $n = 5$ ; Figure 1F).

After the inhibition of  $I_{K,f}$  and  $I_{K,n}$ , the IHC resting membrane potential was close to  $-65$  mV (Figure 1E), and large outward currents remained (Figures 1H and S1D) that are generally referred to as  $I_{K,s}$  (Johnson, 2015; Marcotti et al., 2003, 2004).

### Identification of $K_v$ Subunits Underlying $I_{K,s}$

We screened datasets provided by the SHIELD database for mRNA transcripts of voltage-gated  $K^+$  ( $K_v$ ) channels (Liu et al., 2014; Scheffer et al., 2015; Shen et al., 2015). Taking  $K_v7.4$ , which mediates  $I_{K,n}$  as a reasonable expression threshold (Kharkovets et al., 2006), we considered levels of  $K_v1.8$ ,  $K_v3.3$ ,  $K_v11.1$ , and  $K_v12.1$  in a single-cell transcriptome analysis of mature IHCs as indicative of their presence in IHCs (Figure S2; Liu et al., 2014). We therefore asked whether these channels contribute to  $I_{K,s}$  in IHCs.

### $K_v11.1$ Channels Are Active at Rest in IHCs

We started with analyzing the expression of  $K_v11$  channels ( $K_v11.1$ – $K_v11.3$ ) with reverse-transcriptase PCR (RT-PCR) and detected mRNA transcripts of  $K_v11.1$ ,  $K_v11.2$ , and  $K_v11.3$  in cochlear lysates of wild-type (WT) mice (Figure 2A). Confocal microscopy demonstrated strong anti- $K_v11.1$  immunosignals in the IHC membrane (Figure 2B) that were completely absent in mice carrying hair cell-specific deletion of the *Kcnh2* gene encoding  $K_v11.1$  (*Kcnh2<sup>Hc-/-</sup>*). We did not detect any immunosignals against  $K_v11.2$  or  $K_v11.3$  in IHCs (Figure S3A), although the primary antibodies reliably detected recombinant subunits (Figure S3B). Supporting our initial screen (Figure S2),  $K_v11.1$  thus is the exclusive  $K_v11$  family member in IHCs. In untreated IHCs, the specific  $K_v11$  antagonist E-4031 (20  $\mu M$ ) (Ishii et al., 2003; Trudeau et al., 1995) inhibited substantial  $K_v$  currents ( $n = 10$ ; Figures 2C and S3C) and significantly depolarized the resting membrane potential by  $\sim +7$  mV ( $n = 10$ ;  $p \leq 0.05$ ; Figure 2E). E-4031-sensitive currents and depolarization were completely absent in IHCs from *Kcnh2<sup>Hc-/-</sup>* mice, demonstrating that  $K_v11.1$  channels are functional in IHCs (Figures 2D, 2E, S3D, and S3F). To elucidate whether  $K_v11.1$  channels mediate  $I_{K,s}$ , we applied E-4031 (20  $\mu M$ ) after the inhibition of  $I_{K,f}$  and  $I_{K,n}$ . In these cells, E-4031 inhibited  $\sim 20\%$  of the remaining currents at 0 mV (i.e., E-4031-sensitive currents accounted for one-fifth of the total  $I_{K,s}$ ; Figures 2F, 2G, and S3E). The E-4031-sensitive currents had a  $V_h$  and slope factors of activation of  $-12.8 \pm 1.4$  mV and  $12.5 \pm 0.5$  mV, respectively ( $n = 7$ ; Figures 2H and 2I). These data showed that  $K_v11.1$  channels mediate a significant component of  $I_{K,s}$  in mature IHCs.

### $K_v11.1$ and $K_v1.8$ Channels Mediate the 4-AP-Sensitive Component of $I_{K,s}$

Large outward currents remained in mature IHCs even after the inhibition of  $I_{K,n}$  ( $K_v7.4$ ),  $I_{K,f}$  ( $BK_{Ca}$ ), and  $I_{K,s}$  ( $K_v11.1$ ), demonstrating that additional channels contribute to  $I_{K,s}$ . In line,  $I_{K,s}$  comprises at least two components, of which only one is inhibited by 4-aminopyridine (4-AP) (Marcotti et al., 2003). We thus hypothesized that the candidate channels  $K_v11.1$ ,  $K_v1.8$ , and  $K_v3.3$  known to be

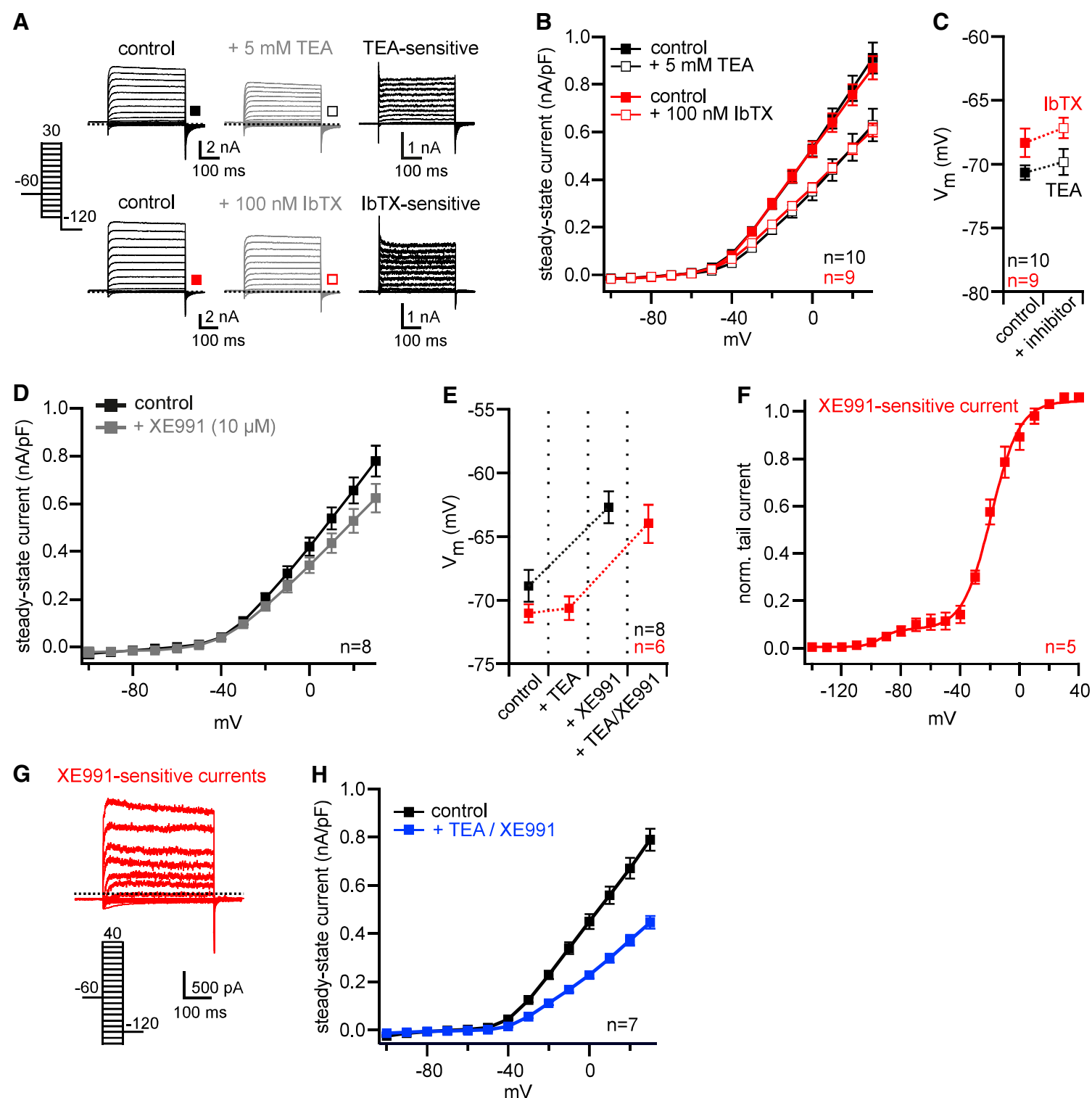


### Figure 1. Pharmacological Isolation of $I_{K,s}$ in Mature IHCs

(A) Representative currents in IHCs before (left) and after (center) application of TEA (5 mM; upper panel) or IbTX (100 nM; lower panel). TEA- and IbTX-sensitive currents (right) were obtained by current subtraction from recordings shown in (A).

(B) Summary of steady-state currents analyzed from recordings shown in (A).

(C) Inhibition of  $I_{K,f}$  with TEA (5 mM; red) or IbTX (100 nM; black) did not depolarize the IHC resting membrane potential.

(D) Summary of IHC steady-state currents before and after application of XE991 (10  $\mu$ M).

(E) XE991 depolarized the resting membrane potential of untreated IHCs (black) and after application of TEA (5 mM; red).

(F and G) XE991-sensitive currents comprised two components.

(F) Double-Boltzmann fit-to-average XE991-sensitive currents as shown in (G) (solid line represents fit).

(G) XE991-sensitive currents obtained by current subtraction.

(H) Summary of steady-state currents before (black) and after application of TEA (5 mM) with XE991 (10  $\mu$ M) (blue).

In (A) and (G), voltage protocols and scale bars, as indicated. For absolute steady-state current amplitudes of recordings shown in (B), (D), and (H) see [Figures S1B–S1D](#). Sample sizes (n) are given in (B)–(F) and (H). Data are presented as means  $\pm$  SEMs.

inhibited by 4-AP ([Figure S2](#)) ([Dierich et al., 2018](#); [Lang et al., 2000](#); [Tian et al., 2002](#)) mediate the 4-AP-sensitive  $I_{K,s}$  component. Extracellular 4-AP (5 mM) rapidly inhibited outwardly rectifying currents in IHCs that accounted for 26% of controls (at 0 mV; [Figures 3A, 3B, S4A, and S5A](#)). Given the insensitivity of  $I_{K,f}$  and

$I_{K,n}$  ([Kimitsuki et al., 2010](#); [Marcotti et al., 2003](#); [Oliver et al., 2003](#); [Thurm et al., 2005](#)), these currents represented 4-AP-sensitive  $I_{K,s}$ . 4-AP blocked significantly fewer currents (19% of controls;  $p \leq 0.05$ ) when applied after pharmacological inhibition of  $I_{K,s}$  ( $K_{v11.1}$ ) (together with  $I_{K,n}$  and  $I_{K,f}$ ) ([Figures 3C–3E and S4B](#)).

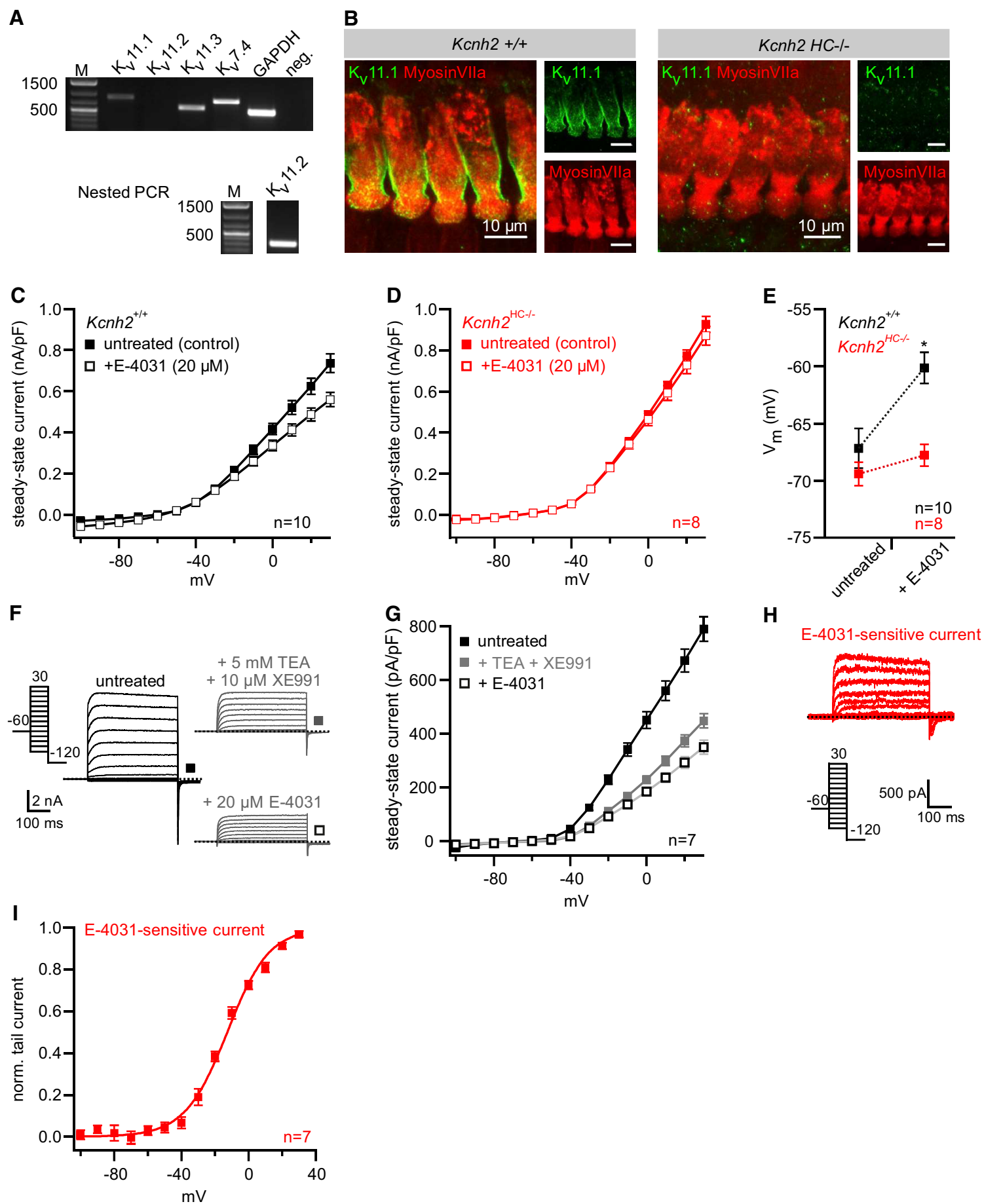


**Figure 2.  $K_v11.1$  Channels Are Functional in Mature IHCs**

(A) RT-PCR showed the expression of  $K_v11.1$ ,  $K_v11.2$ , and  $K_v11.3$  mRNA in cochlear lysates (M, nucleotide marker with size;  $K_v7.4$  + glyceraldehyde 3-phosphate dehydrogenase [GAPDH], positive controls; neg., negative control without cDNA). The lower panel shows a second PCR with nested primers for  $K_v11.2$  transcripts.

(B) Immunohistochemistry revealed strong anti- $K_v11.1$  immunosignals in WT IHCs ( $Kcnh2^{+/+}$ ; left) that were absent in  $Kcnh2^{HC-/-}$  mice (right). Maximum intensity projections of confocal z stacks in apical turns of the organ of Corti (myosin VIIa, hair cell marker; all scale bars represent 10  $\mu\text{m}$ ). For the evaluation of antibodies and anti- $K_v11.2$ /anti- $K_v11.3$  stainings, see Figures S3A and S3B.

(C and D) E-4031 (20  $\mu\text{M}$ ) inhibited  $K^+$  currents in IHCs in (C)  $Kcnh2^{+/+}$  (WT), but not (D)  $Kcnh2^{HC-/-}$  mice.

(E) E-4031 (20  $\mu\text{M}$ ) did not depolarize the IHC resting potential in  $Kcnh2^{HC-/-}$  (red) mice (\* $p \leq 0.05$ ).

(F) Representative recordings of an untreated IHC and after application of the indicated substances.

(legend continued on next page)

These results showed that  $K_v11.1$  channels contribute to the 4-AP-sensitive component of  $I_{K,s}$ .

4-AP still blocked significant currents even after the inhibition of  $K_v11.1$ , demonstrating that other channels must contribute to 4-AP-sensitive  $I_{K,s}$ . To identify these channels, we isolated the remaining 4-AP-sensitive component by current subtraction early after application of the substance (Figures 3E and S5A). We found that these currents activated in a voltage-dependent manner ( $V_h$ :  $-2.2 \pm 0.4$  mV; slope:  $13.3 \pm 1.1$  mV;  $n = 8$ ) and did not inactivate (Figures 3E–3H). To evaluate whether these currents were mediated by  $K_v1.8$ , we used RT-PCR and indeed detected  $K_v1.8$  mRNA transcripts in the cochlea (Figure 3I). After cloning cDNA-encoding  $K_v1.8$  from the same cochlear lysates, we characterized recombinant  $K_v1.8$  channels in Chinese hamster ovary (CHO) cells. Recombinant  $K_v1.8$  channels did not inactivate, and their voltage dependence was indistinguishable from the respective 4-AP-sensitive IHC current ( $V_h$ :  $0.9 \pm 0.9$  mV; slope:  $11.1 \pm 0.5$  mV;  $n = 31$ ; Figures 3F–3H). Of note, the native IHC currents activated significantly faster than the recombinant  $K_v1.8$  channels (see scale bars in Figure 3E), just as the hair cell current recombinant  $K_v1.8$  channels were completely inhibited by extracellular 4-AP (5 mM), but were largely insensitive to TEA (5 mM), E-4031 (20  $\mu$ M), and XE991 (10  $\mu$ M) (Figures S4C–S4I).

The properties of a second 4-AP-sensitive IHC component were consistent with recombinant  $K_v1.8$  channels. As  $K_v1.8$  mRNA transcripts are expressed in mature IHCs (Liu et al., 2014),  $K_v1.8$  channels mediate 4-AP-sensitive  $I_{K,s}$  together with  $K_v11.1$ .

#### 4-AP Potentiates $K^+$ Currents in Mature IHCs

Extracellular 4-AP (5 mM) inhibited certain IHC currents very rapidly (Figure S5A), but it also induced a significant (and slow) hyperpolarisation of the membrane potential ( $\sim -7$  mV) in the same IHCs ( $n = 6$ ;  $p \leq 0.001$ ; Figure 4A). After the inhibition of  $I_{K,f}$ ,  $I_{K,n}$ , and  $I_{K,s}(K_v11.1)$ , 4-AP (5 mM) still significantly hyperpolarized the IHC membrane potential ( $n = 7$ ;  $p \leq 0.001$ ; Figure 4B), indicating that 4-AP activated  $K^+$  currents. Whereas 4-AP inhibited IHC currents within seconds, it significantly potentiated outward currents at hyperpolarized potentials slowly (e.g., at  $-60$  mV:  $n = 7$ ;  $p \leq 0.001$ ; Figures 4C and S5A). These different time courses made possible pharmacological separation of two current components with differential 4-AP sensitivity (Figure S5A). Longer 4-AP (5 mM) application induced the activation of the remaining IHC currents at significantly more negative membrane potentials, as is evident by a change of  $V_h$  by  $\sim -15$  mV ( $n = 7$ ;  $p \leq 0.001$ ; Figures 4D, 4E, and S5B) and by associated changes of the slope factors ( $n = 7$ ;  $p \leq 0.01$ ; Figure 4F).

#### IHC Currents Share Distinct Pharmacological Properties with $K_v12.1$

The 4-AP-activated IHC current showed striking similarities to the  $I_{K,s}$  candidate channel  $K_v12.1$ : 4-AP potentiated currents through

recombinant  $K_v12.1$  channels and induced channel activation at hyperpolarized potentials (Figures S5C–S5K) (Dierich et al., 2018). We thus probed the expression of  $K_v12.1$  subunits in IHCs. Available antibodies did not detect recombinant  $K_v12.1$  channels reliably (Figure S5L), precluding the direct analysis of channel abundance with immunohistochemistry. However, we detected mRNA transcripts for  $K_v12.1$  and its close relative  $K_v12.3$  with RT-PCR in cochlear lysates (Figure 4G). Considering the SHIELD datasets (Liu et al., 2014; Shen et al., 2015), we conclude that  $K_v12.1$  is the exclusive family member expressed in IHCs.

Due to a lack of specific antagonists, we probed  $K_v12.1$  activity in IHCs with NS1643, which inhibits recombinant  $K_v12.1$  (Figures S5G and S5H; Dierich et al., 2018). As NS1643 is a known activator of  $K_v11$  channels (Casis et al., 2006), we applied NS1643 after inhibiting  $K_v11.1$  with E-4031 (and after inhibition of  $I_{K,f}$  and  $I_{K,n}$ ). Extracellular NS1643 (30  $\mu$ M) substantially reduced the remaining  $I_{K,s}$  (Figures S6A–S6C). However, as NS1643 (30  $\mu$ M) also inhibited recombinant  $K_v1.8$  channels (Figures S4G and S4I), the substance was not suited for demonstrating the expression of  $K_v12.1$  in IHCs unequivocally. It is noteworthy that NS1643-sensitive currents in IHCs displayed biphasic activating kinetics: the activation kinetics of the slower component (e.g.,  $\tau(-30$  mV):  $32 \pm 0.2$  ms,  $n = 9$ ) were the same as for the  $K_v1.8$  currents in IHCs (e.g.,  $\tau(-30$  mV):  $33 \pm 0.4$  ms,  $n = 8$ ), and the kinetics of the faster component were comparable to the currents remaining after the inhibition of  $I_{K,f}$ ,  $I_{K,n}$ , and  $I_{K,s}(K_v11.1, K_v1.8)$  ( $\tau(-30$  mV):  $\sim 24$  ms). Thus, the kinetics of the latter component were similar to those potentially mediated by  $K_v12.1$ . These data indicated that two current components in IHCs were sensitive to NS1643 in IHCs that were potentially mediated by  $K_v1.8$  and  $K_v12.1$  channels.

#### Voltage-Dependent Mode Shift of Activation in Mature IHCs

We then probed  $K_v12.1$  currents in IHCs by means of the mode shift of activation (Villalba-Galea, 2017); this manifests through a shift of activating voltages to hyperpolarized potentials following conditioning depolarization of the membrane (Dai and Zagotta, 2017; Dierich et al., 2018; Dierich and Leitner, 2018; Li et al., 2015). Voltage protocols were designed to maximize mode shift as determined for recombinant  $K_v12.1$  (Dierich et al., 2018, 2019b) and consisted of a 200-ms conditioning pre-pulse (hyperpolarized:  $-60$  mV; depolarized: 0 mV), followed by 600-ms voltage steps for channel activation (Figure 5A). The depolarized conditioning potential (0 mV) induced a large shift in the voltage dependence of recombinant  $K_v12.1$  channels by  $\sim -50$  mV (Figures 5A–5C;  $n = 10$ ;  $p \leq 0.001$ ; Dierich et al., 2018). To examine whether the currents in IHCs also exhibited mode shift, we applied the same voltage protocols after the pharmacological inhibition of  $I_{K,f}$ ,  $I_{K,n}$ , and  $I_{K,s}(K_v1.8 + K_v11.1)$ . The remaining currents exhibited a

(G) Summarized steady-state currents from recordings shown in (F).

(H and I) Voltage dependence of E-4031-sensitive currents in IHCs.

(H) Representative E-4031-sensitive currents; obtained by current subtraction from recordings shown in (F).

(I) Summarized Boltzmann fits (solid line) to averaged recordings, as shown in (H).

In (F) and (H), voltage protocols and scale bars, as indicated. For absolute steady-state current amplitudes of recordings shown in (C), (D), and (G), see Figures S3C–S3F. Sample sizes ( $n$ ) are given in (C)–(E), (G), and (I). Data are presented as means  $\pm$  SEMs.

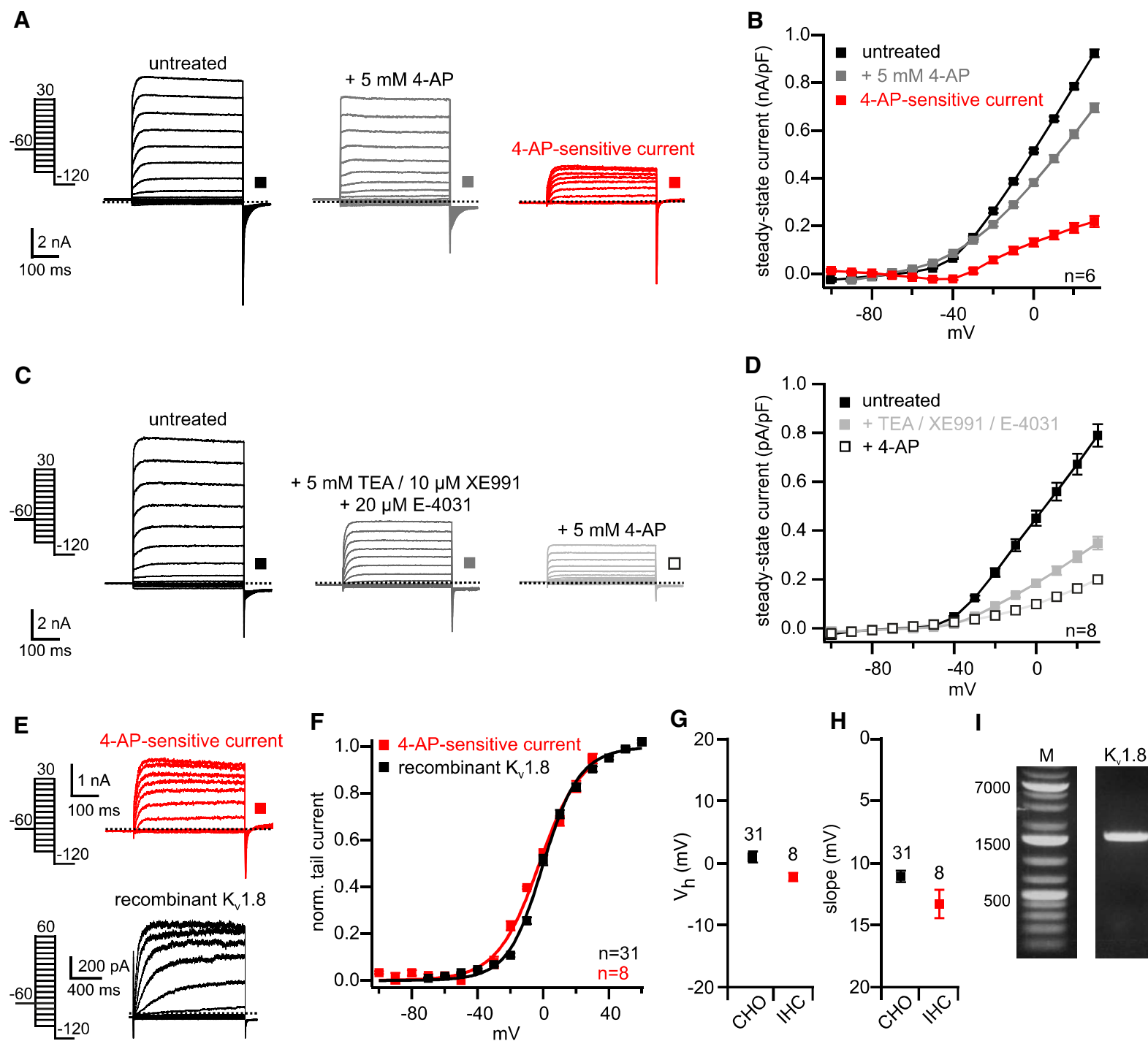


**Figure 3.  $K_v1.8$  Channels Mediate a 4-AP-Sensitive Current Component in IHCs**

(A) Representative recordings of an IHC before (left) and after (center) application of 4-AP (5 mM). 4-AP-sensitive currents (right) were obtained by current subtraction.

(B) Averaged steady-state currents analyzed from recordings, as shown in (A).

(C–H) 4-AP-sensitive currents after the inhibition of  $K_v11.1$  channels in IHCs.

(C) Representative recordings of an IHC under control conditions (untreated; left) and after application of the indicated substances.

(D) Summary of recordings as shown in (C). For absolute steady-state current amplitudes of recordings shown in (B) and (D), see [Figures S4A](#) and [S4B](#).

(E) Representative 4-AP-sensitive IHC currents (red) derived from recordings shown in (C) and through recombinant  $K_v1.8$  channels (black). Note the different activation kinetics.

(F) Voltage dependence of the 4-AP-sensitive IHC currents (red) and recombinant  $K_v1.8$  channels (black). The solid lines represent Boltzmann fits to averaged data from recordings as shown in (C) and (E).

(G) Mean  $V_h$  (left) and slope factor (right) of activation for recombinant  $K_v1.8$  channels and 4-AP-sensitive currents in IHCs derived from analysis shown in (F).

(H) Expression of  $K_v1.8$  mRNA transcripts in cochlear lysates. All voltage protocols and scale bars are as indicated.

For pharmacological characterization of recombinant  $K_v1.8$  channels, see [Figures S4C–S4I](#); for time course of 4-AP effects in IHCs, see [Figure S5A](#). Sample sizes (n) are given in (B), (D), and (F)–(H). Data are presented as means  $\pm$  SEMs.

significant mode shift, as is evident by an  $-20$ -mV shift of the activation voltages after the depolarized conditioning potential ( $n = 5$ ;  $p \leq 0.01$ ; [Figures 5D](#) and [5E](#)).

IHC currents share striking properties with recombinant  $K_v12.1$  channels (4-AP/NS1643 sensitivity; mode shift). Mode shift of the native currents was attenuated compared to recom-

binant  $K_v12.1$  channels, which is consistent with the reduced mode shift of recombinant  $K_v12.1$  channels after potentiation through 4-AP ([Dierich et al., 2018](#)) also present in the IHC recording solution. Based on these unique characteristics and expression of mRNA transcripts in IHCs, we conclude that  $K_v12.1$  channels are functional in IHCs.

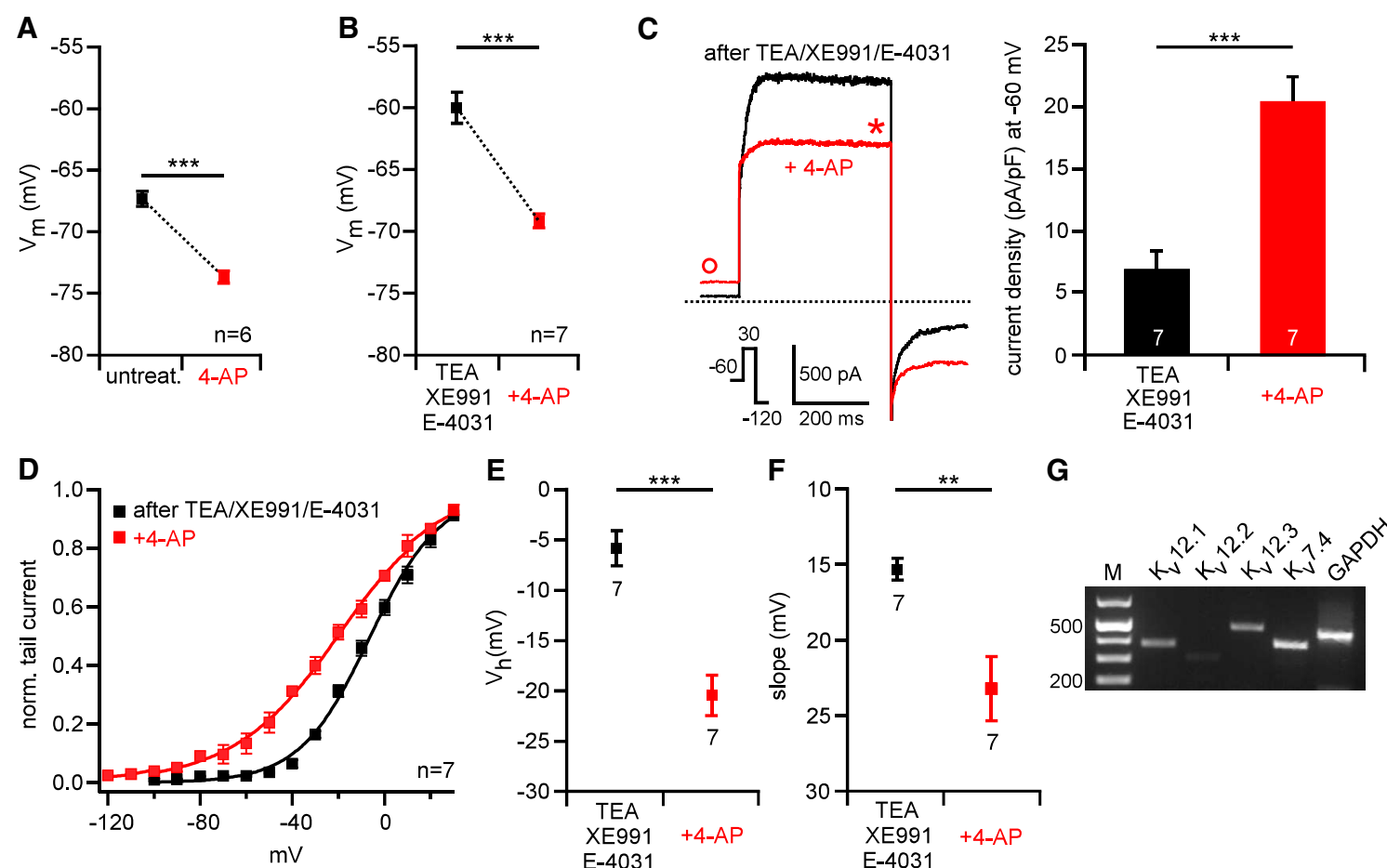


**Figure 4. 4-AP Potentiates K<sup>+</sup> Currents at Negative Membrane Potentials in IHCs**

(A and B) Application of 4-AP (5 mM) induced a hyperpolarization of the membrane potential (A) in control IHC and (B) in IHCs treated with TEA, XE991, and E-4031. (C) Representative recordings of IHC currents elicited with the indicated voltage steps before and after 1 min of extracellular 4-AP (after TEA, XE991, and E-4031). 4-AP inhibited currents at +30 mV (indicated by asterisk), but potentiated currents at -60 mV (indicated by open circle). For the time course of 4-AP effects, see Figure S5A.

(D–F) 4-AP induced a hyperpolarizing shift in the voltage dependence of currents (after TEA, XE991, and E-4031).

(D) Boltzmann fits to averaged recordings before (black) and after (red) application of 4-AP in IHCs.

(E and F) Mean  $V_h$  (E) and slope factors (F) of activation derived from analysis shown in (D). For absolute current amplitudes of recordings shown in (D), see Figure S5B.

(G) RT-PCR detected mRNA for  $K_v12.1$ ,  $K_v12.2$ , and  $K_v12.3$  channels in cochlear lysates (M, nucleotide marker with size; positive controls:  $K_v7.4$  and GAPDH). \*\* $p \leq 0.01$ ; \*\*\* $p \leq 0.001$ .

Concentrations of applied substances: 4-AP (5 mM), TEA (5 mM), XE991 (10  $\mu$ M), and E-4031 (20  $\mu$ M). Sample sizes (n) are given in (A)–(F). Data are presented as means  $\pm$  SEMs.

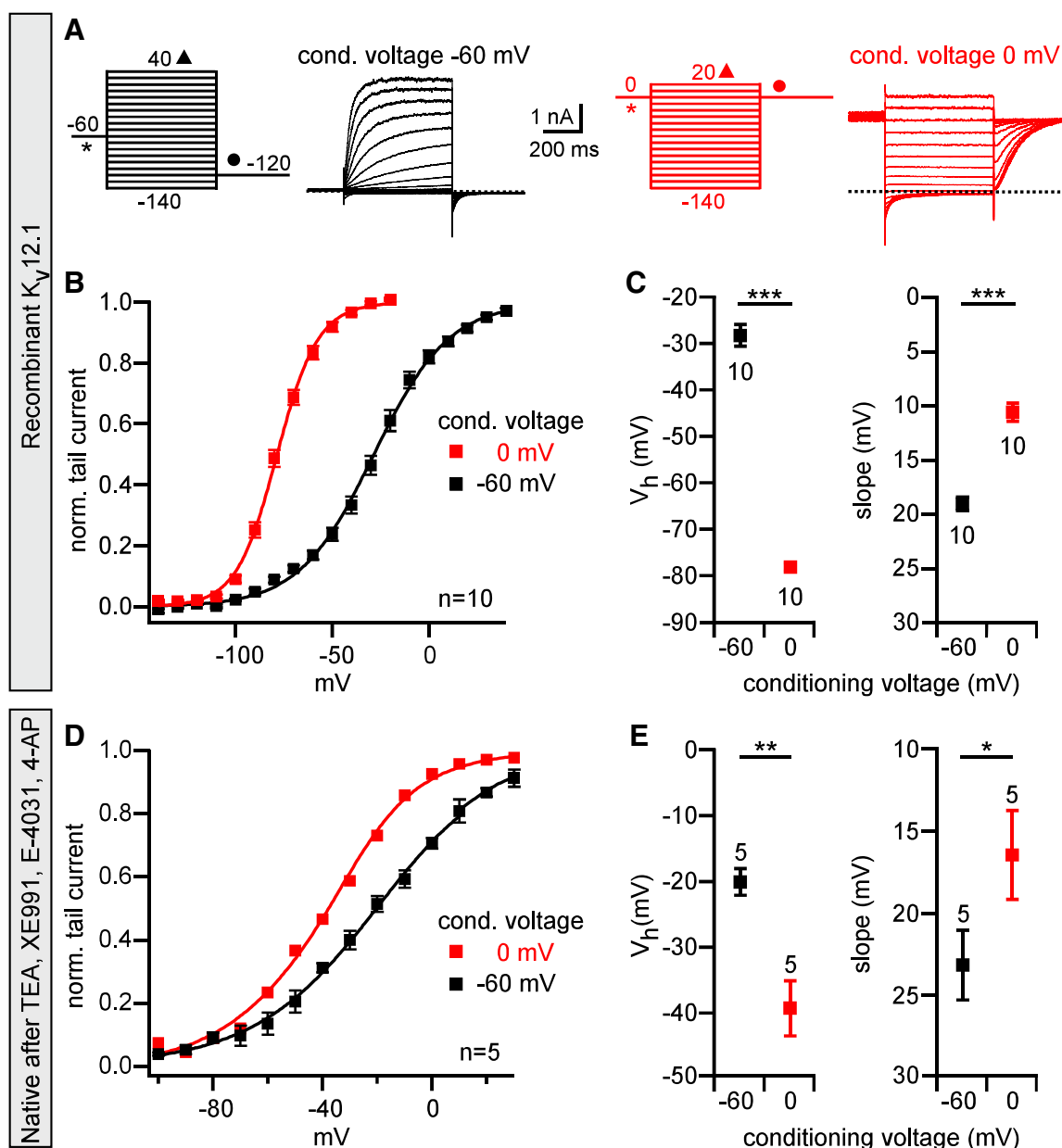
### Mature IHCs Express Six Independent K<sup>+</sup> Currents

Mature apical IHCs of mice express at least five K<sup>+</sup> channel populations giving rise to six different K<sup>+</sup> currents (Figures S6D and S6E).  $I_{K,f}$ (BK<sub>Ca</sub>) and  $K_v7.4$  currents together account for ~49% ( $I_{K,f}$ : 34%;  $K_v7.4$ : 15%) of controls at 0 mV.  $K_v7.4$  subunits mediate two components: small negatively activating currents resemble  $I_{K,n}$  found in IHCs earlier (Marcotti et al., 2003; Oliver et al., 2003), and a larger fraction activates at more positive potentials resembling the currents described in apical IHCs of the gerbil (Johnson, 2015).  $I_{K,s}$  accounts for ~51% of control currents (at 0 mV) and is mediated by  $K_v1.8$ ,  $K_v11.1$ , and  $K_v12.1$ . At 0 mV,  $K_v1.8$  accounts for ~19% and  $K_v11.1$  for ~10% of control currents. The component remaining after the inhibition of  $I_{K,f}$ (BK<sub>Ca</sub>),  $K_v7.4$ ,  $K_v1.8$ , and  $K_v11.1$  is probably mediated by  $K_v12.1$  channels and accounts for ~22% of controls (at 0 mV).

### Assessing the Functional Relevance of the IHC K<sup>+</sup> Currents

To elucidate the physiological relevance of the IHC K<sup>+</sup> currents, we refined a recently published computational model of apical

IHCs (Altoè et al., 2018) by implementing all six K<sup>+</sup> conductances (native model; Figures 6A and S7A) (for the properties of  $I_{K,f}$ , see Kros and Crawford, 1990; the properties of  $I_{K,s}$  and of  $I_{K,n}$  over the whole voltage range were implemented into the model, as recorded in our study). The model input is sinusoidal stereocilia deflection controlling the activity of the MET channels (Figures 6A and S7B) (Altoè et al., 2018). The model outputs are IHC K<sup>+</sup> currents and conductances (Figure 6) and membrane (receptor) potentials (Figures 7, S7C, and S7D). We extrapolated from the recordings the individual activation time constants close to the resting membrane potential and included them in the model (Figure S7A; for calculation see Method Details). The kinetics of  $K_v1.8$ ,  $K_v11.1$ , and  $K_v12.1$  currents and positively activating  $K_v7.4$  are significantly slower than those of  $I_{K,f}$  (Figure S7A). Furthermore, due to full activation,  $I_{K,n}$  provides a constant K<sup>+</sup> conductance at rest in the simulations. Hence, following the established nomenclature of basolateral K<sup>+</sup> conductances in IHCs (Marcotti et al., 2003), we discriminate between  $I_{K,f}$  and  $I_{K,n}$  and assign currents through  $K_v1.8$ ,  $K_v11.1$ ,  $K_v12.1$ , and  $K_v7.4$  (positive fraction) to  $I_{K,s}$  (Figure 6A).



The native IHC model (all  $K^+$  conductances) predicts a resting potential of  $-53$  mV and a membrane resistance-capacitance (RC) time constant ( $\tau_m$ ) of 0.24 ms, in good agreement with published recordings (Johnson, 2015; Johnson et al., 2011). This model further shows that all  $K^+$  channels are active at rest and during (sound) stimulation (Figures 6B–6F). Whole-cell currents (and conductances) at rest are dominated by  $I_{K,f}$  (followed by the sum of  $I_{K,s}$  components; Figures 6C and 6D), and  $I_{K,n}$  is only small in apical IHCs (Figures 1F and 1G; Johnson, 2015; Marcotti et al., 2003; Oliver et al., 2003). At rest, of the  $I_{K,s}$  components,  $K_v1.8$  and  $K_v7.4$  provide the most conductance followed by  $K_v11.1$  channels, whereas the contribution of  $K_v12.1$  is only small ( $K_v1.8 > K_v7.4 > K_v11.1 > K_v12.1$ ; Figures 6B and 6E). Furthermore, the channels differentially activate during membrane potential depolarization (i.e., sound stimulation; Figures 6B, 6C, and 6F).

### The Six $K^+$ Conductances Optimize IHC Responses to Encode Complex Sound

To assess physiological relevance of the  $K^+$  channels, we compared the “native model” (see above) with other simulations. In the “voltage-independent (conductances)” model, all of the  $K^+$  currents were made voltage insensitive by imposing constant

resting conductance. In others, only individual channels (or channel combinations) were implemented as voltage dependent (indicated in Figure 7), allowing for analysis of the relevance of the respective components. This *in silico* approach allows the evaluation of the physiological relevance of the  $K^+$  conductances (Altoè et al., 2018) without affecting the IHC resting properties (resting potential, RC time constant). For comprehensive visualization, some panels of Figure 7 show  $I_{K,s}$  as a single component, although the underlying channels were modeled independently in all of the simulations.

First, we found that in the native IHC model the simulated receptor potentials as reported (Johnson, 2015) show characteristic onset and offset relaxations (e.g., depolarization and hyperpolarization sags) and are characterized by distinct AC and DC components (Figure 7A). Due to the slow activation kinetics, the  $I_{K,s}$  components ( $K_v1.8$ ,  $K_v7.4$ ,  $K_v11.1$ , and  $K_v12.1$ ) largely determine these onset and offset responses.

Second, we analyzed the AC component of the IHC receptor potential (Figure 7A, insert) by simulating the amplitudes of the oscillating receptor potentials as a function of stimulus frequency. These data are normalized to maximal receptor potential amplitudes at low frequencies to visualize membrane low-pass filtering (Figures 7B and 7C). The simulations show that

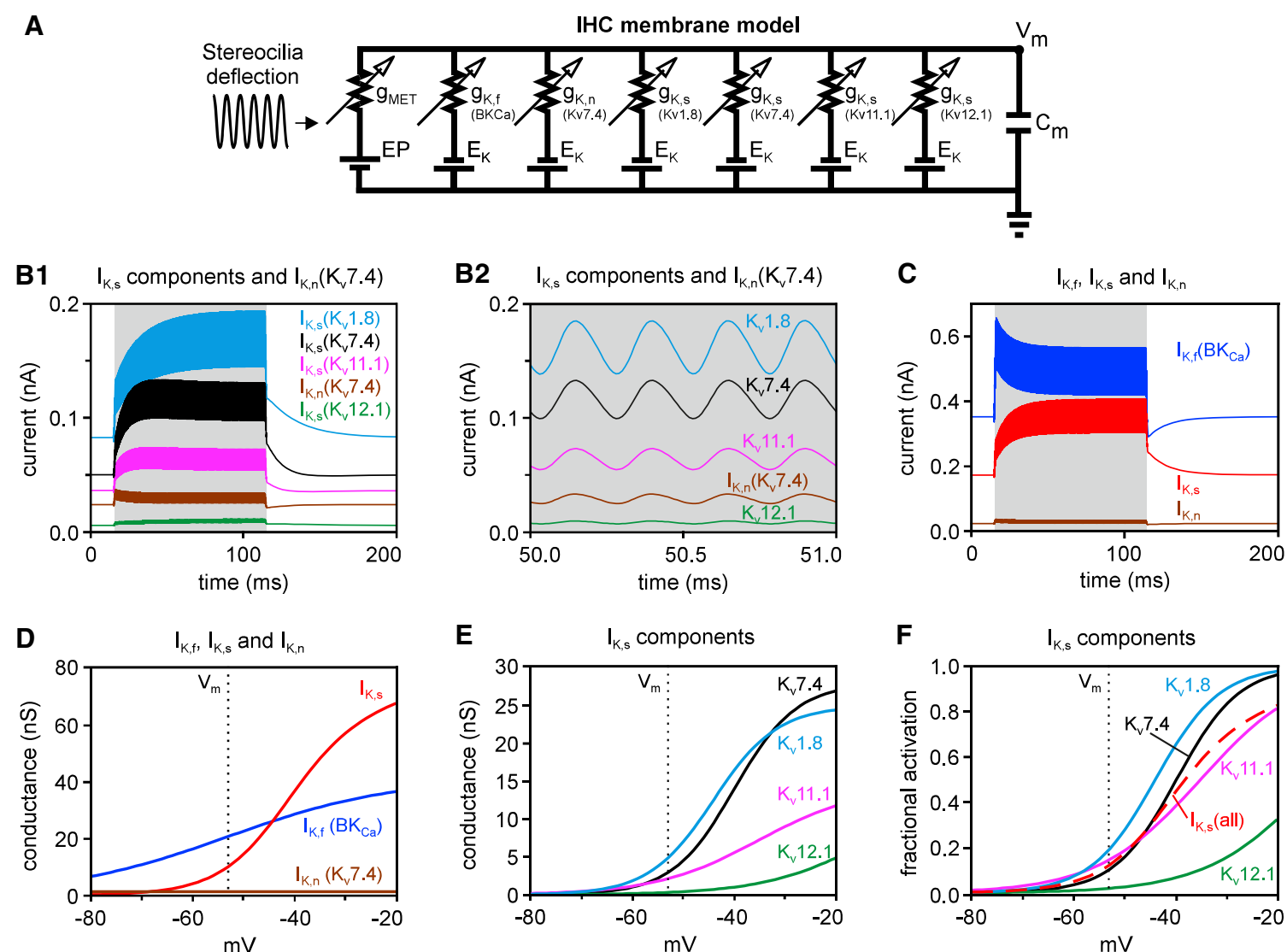


**Figure 6. All K<sup>+</sup> Current Entities Are Active at Rest and during Sound Stimulation**

(A) Extended computational model of IHCs implementing all K<sup>+</sup> currents.

(B and C) At rest and during sound stimulation, all identified K<sup>+</sup> currents are active (B) and whole-cell currents are dominated by I<sub>K,f</sub>(BK<sub>Ca</sub>) (C) (4-kHz and 40-nm hair bundle deflections, gray inset). (B2) shows currents from (B1) on an expanded timescale.

(D–F) Simulated conductance-voltage curves for IHC K<sup>+</sup> currents. (D) At rest (dashed line; V<sub>m</sub>), the whole-cell conductance is dominated by I<sub>K,f</sub> (followed by the sum of the I<sub>K,s</sub> components), and (E) all channels mediating I<sub>K,s</sub> are active (K<sub>v</sub>1.8, K<sub>v</sub>7.4, and K<sub>v</sub>11.1 provide the largest conductance). (F) shows the fractional (normalized) voltage-dependent activation of I<sub>K,s</sub> components. For simulated conductance-stereocilia vibration (i.e., intensity) curves, see Figure 7F.

the native K<sup>+</sup> channel repertoire dramatically increases the upper cutoff frequency of the AC response. The cutoff frequency of the IHC membrane is approximately one octave higher in the native model (black) than in the voltage-independent model (gray; Figure 7B). More importantly, an increase in the cutoff frequency may be achieved by the expression of either I<sub>K,f</sub> (blue) or I<sub>K,s</sub> (red) (Figure 7B). Concerning the I<sub>K,s</sub> components, the improvement in AC responses is mainly mediated by the voltage-dependent activity of K<sub>v</sub>1.8 or K<sub>v</sub>7.4, with smaller contributions of K<sub>v</sub>11.1 and K<sub>v</sub>12.1 (Figure 7C). Voltage-dependent activation of the channels mediating I<sub>K,s</sub> produces an effective increase in basolateral conductance over stimulus presentation, hence leading to a significant decrease in the effective membrane time constant. Fast voltage-dependent activation of I<sub>K,f</sub> produces “phase-locked” fluctuation of the IHC conductance, thus increasing the membrane cutoff frequency beyond that predicted by the effective membrane time constant (see also Altoè et al., 2018). The increase in the cutoff frequency is always most pronounced in the native model.

We then analyzed the relevance of the K<sup>+</sup> channels for the DC response of IHCs and plotted the DC component of receptor po-

tentials in the different models as a function of the amplitude of stereocilia vibrations (i.e., stimulus intensity; Figures 7D and 7E). This showed that the exclusive presence of all of the I<sub>K,s</sub> components (red) dramatically compresses the DC potential (Figure 7D). I<sub>K,f</sub> (blue) alone also considerably compresses the DC component of the receptor potentials, but sole inclusion of I<sub>K,n</sub>(K<sub>v</sub>7.4) does not affect the DC response (Figure 7D). The combination of all of the currents causes an even stronger compression of the DC component, leading to a dramatic reduction in the steepest slope of the curve from 0.21 mV/nm without voltage-activated channels (gray) to 0.08 mV/nm in the native model (black) (slope with all I<sub>K,s</sub> = 0.09 mV/nm, red; slope with I<sub>K,f</sub> = 0.16 mV/nm, blue) (Figure 7D). This curve slope difference highlights that in native IHCs, the largest range of stereocilia vibration amplitudes (greater than a factor of 2) can be encoded within the same receptor potential range. Assuming that mechanical responses of the cochlea increase by ~0.3 dB for a 1-dB sound level increase (compressive growth of mechanical responses at a rate of 0.3 dB/dB sound level; Robles and Ruggero, 2001), a factor 2 of deflection amplitudes corresponds to 20 dB for sound pressure levels. Our simulations hence point out that the



native  $K^+$  conductance repertoire extends by  $\sim 20$  dB the range of sound levels that an individual IHC can encode within the same range of receptor potentials. This significant effect of the  $K^+$  currents on the dynamic range is dominated by the activation of the channels mediating  $I_{K,s}$  (Figure 7D), with most substantial contribution from either  $K_v7.4$ ,  $K_v1.8$ , or  $K_v11.1$  (Figure 7E). More important, due to their heterogeneous voltage dependence, these channels activate and saturate at different membrane potentials, with  $K_v1.8$  providing the most conductance at the resting membrane potential, followed by  $K_v7.4$ ,  $K_v11.1$ , and  $K_v12.1$  (Figure 6E). Accordingly, they activate and saturate at different levels of stereocilia vibrations (i.e., depolarization) and thus stimulus level (Figure 7F). The individual components of  $I_{K,s}$  compress the IHC DC response over an individually exclusive range of stereocilia displacements (Figure 7E). The individual activation curves of the channels sum up to an overall conductance (Figure 7F, red) that increases over a wide range of stereocilia vibration amplitudes (red; Figures 6E, 6F, and 7E); in other words, the combination of all “slow” components allows for sensitive conductance changes with stereocilia deflection over a far larger range of intensities. This overall  $I_{K,s}$  conductance does not saturate completely for stereocilia vibrations up to  $1 \mu m$  (Figure 7F), which enables compressive growth of the DC potential over a larger range of stimulus intensities in IHCs expressing all  $I_{K,s}$  channel components (Figures 7D and 7E).

We further plotted simulated AC:DC ratios as a function of stimulus frequency (Figure 7G), which are a metric tailored for continuous signals conceptually equivalent to vector strength (or synchronization index) used to characterize phase locking in spiking neurons (Palmer and Russell, 1986). Thus, higher AC:DC ratios indicate more efficient phase locking. Compared to the voltage-independent conductances model, the frequency limit for phase locking increases dramatically with active  $I_{K,f}$  or  $I_{K,s}$  (Figure 7G). The native combination increases AC:DC ratios at all frequencies and intensities more significantly than the individual contributions. This improvement in AC:DC ratios is achieved mainly by the pronounced compression of the DC component through the channels mediating  $I_{K,s}$  (Figures 7D and 7E) and, to a lesser extent, by the increase of the cutoff frequency associated with the IHC low-pass filtering (Figures 7B and 7C). In particular, the compression of the DC potential through the slow currents accounts for the significant increase in AC:DC ratios at low frequencies (Figure 7G).

### The $I_{K,n}$ -to- $I_{K,s}$ Relation Largely Determines the Tonotopic Response Properties of IHCs

In the models,  $I_{K,n}$  as the exclusive  $K_v$  current does not significantly alter AC and DC responses of IHCs compared to the voltage-independent conductance model (Figures 7B, 7D, and 7G). This is caused by the fact that due to complete activation at rest,  $I_{K,n}$  can be considered a voltage-independent  $K^+$  conductance. However, we wondered about the physiological relevance of  $I_{K,n}$  in IHCs. Recently, it was shown in the gerbil that  $I_{K,n}$  amplitudes were large in basal IHCs, whereas, in line with our results, apical IHCs express larger  $K_v7$ -type currents activating at more positive potentials (Figures 1F and 1G; Johnson, 2015). Apical and basal IHCs are specialized for the precise encoding of sound frequency and intensity, respectively (Johnson, 2015). We thus

hypothesized that the  $I_{K,n}$ -to- $I_{K,s}$  relation determines the tonotopic response characteristics of IHCs. We compared two models (implementing  $I_{K,f}$  and  $I_{K,s}$ ), in which the entire  $K_v7.4$ -mediated conductance was assigned either to  $I_{K,n}$  (extreme basal IHC) or to the  $K_v7.4$ -like fraction (extreme apical IHC), thereby varying the relative contribution of  $I_{K,n}$  to the whole-cell conductance. In these simulations, apical IHCs exhibit more depolarized resting membrane potentials than basal IHCs in full agreement with recordings (Johnson, 2015). However, in contrast to the recordings (Johnson, 2015), modeled apical IHCs display a slower membrane time constant, as the depolarization of the membrane potential is caused by a decrease in the total  $K^+$  conductance at rest (i.e., increased membrane resistance). This automatically increases the membrane time constant and highlights the importance of tonotopically graded activity of the MET channels for intrinsic tuning of the time constants in living IHCs (Johnson, 2015). Of note, graded MET channel activity was not included in the model, as this hampers analysis of the relevance of basolateral  $K^+$  channels. Furthermore, we found that apical IHCs exhibit more pronounced compression of DC responses, as the depolarized resting potential renders the  $K^+$  channels more sensitive to voltage changes (i.e., the channels retain an effectively larger activation range over stimulus presentation). This results in strikingly higher AC:DC ratios (especially at low frequencies) for apical than for basal IHCs (Figure 7H). Accordingly, this apical IHC model shows a more compressed DC response and more precise phase locking than the basal, just as shown for living IHCs (Johnson, 2015). Accordingly, these simulations suggest that the relative contribution of  $I_{K,n}$  to the whole-cell conductance (i.e.,  $I_{K,n}:I_{K,s}$  ratio) largely determines the tonotopic response characteristics of IHCs.

### Physiological Advantages of the Native $K^+$ Current Repertoire

Our simulations showed that the native channel repertoire clearly optimizes IHC receptor potentials to encode complex sound. However, we wondered whether a similar improvement in receptor potentials may also be achieved through the expression of fewer  $K_v$  populations. We therefore performed additional simulations in which the entire conductance size provided by the native  $K_v$  ensemble (Figures 6D and 6E:  $I_{K,s} + I_{K,n}$ ) is assigned to either of the channels mediating  $I_{K,s}$  or  $I_{K,n}$  ( $K_v7.4$ ) exclusively: These simulations considered only  $I_{K,f}$  and one  $K_v$  isoform and thus only two  $K^+$  current entities. As quality measures, IHC phase locking (i.e., AC:DC ratios versus frequency or intensity; Figures 7I and 7J) and characteristics of receptor potential DC components (compression, dynamic range, sensitivity) were assessed. These simulations show that assigning all of the  $K_v$  conductance to  $I_{K,n}$  ( $K_v7.4$ ),  $I_{K,s}$  ( $K_v11.1$ ), or  $I_{K,s}$  ( $K_v12.1$ ) substantially reduces the efficacy of phase locking (i.e., frequency coding) compared to native IHCs (Figures 7I and 7J). Whereas sensitivity is not altered for  $I_{K,n}$  ( $K_v7.4$ ) or  $I_{K,s}$  ( $K_v11.1$ ), assigning all of the  $K_v$  conductance to  $I_{K,s}$  ( $K_v12.1$ ) renders IHC receptor potentials more sensitive to low sound intensities by 5.5 dB (of stereocilia vibration) as compared to native IHCs (Figures 7K, S7C and S7D). Thus, expressing  $K_v12.1$  as the only  $K_v$  subunit optimizes receptor potentials to detect faint sounds, but deteriorates phase locking. Conversely, assigning all of the  $K_v$  conductance to either

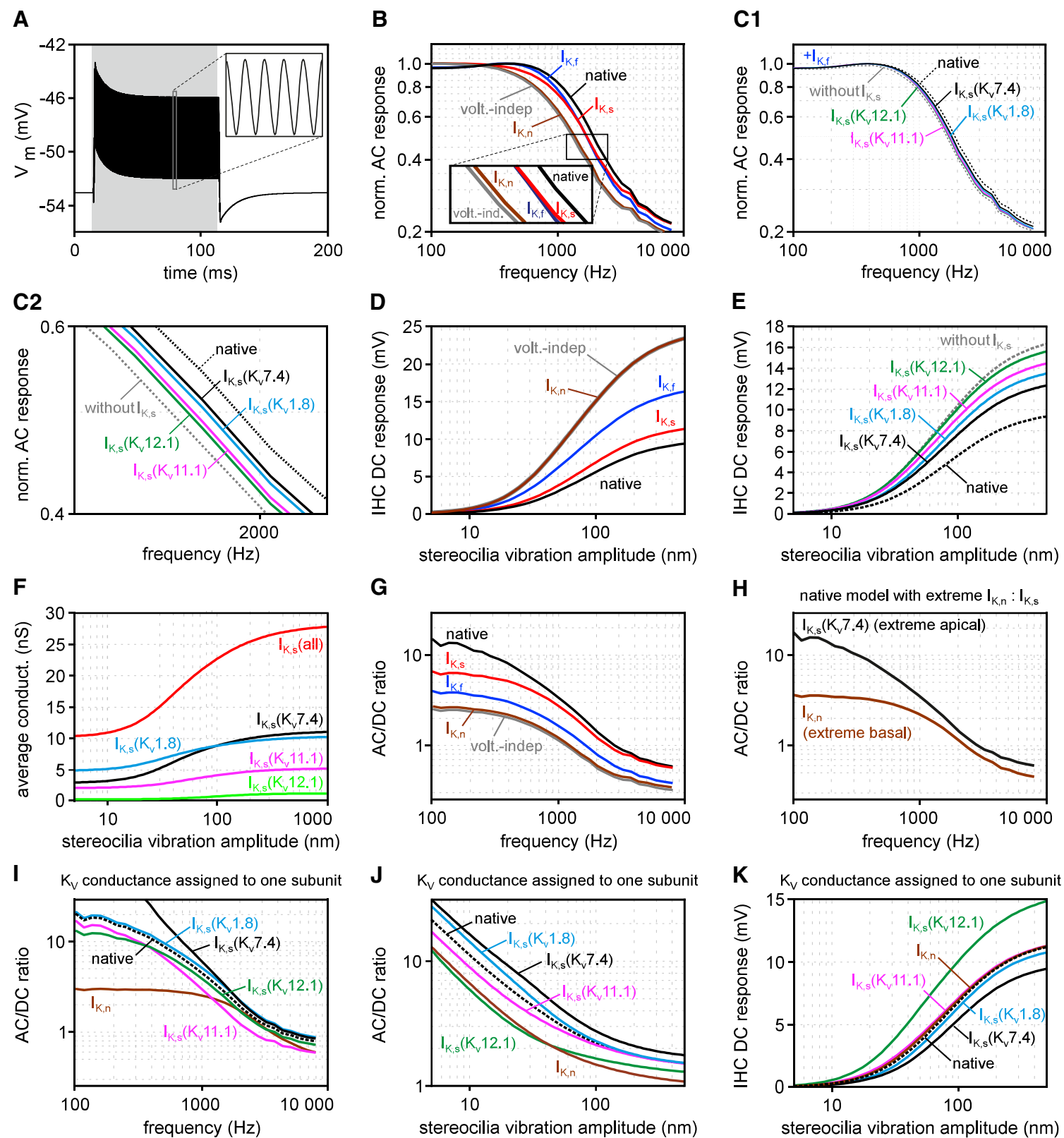


**Figure 7. Six  $K^+$  Current Entities Optimize IHC Receptor Potentials to Encode Complex Sound**

(A) Simulated IHC receptor potentials during stereocilia deflections exhibit sustained DC and oscillating AC potentials (stereocilia vibration 40 nm at 4 kHz; gray inset). (B–G) Comparison of different IHC models that consider only voltage-dependent activation of the conductances highlighted in the graph (all others are voltage insensitive; see text and Method Details for description). Differences represent the contributions of the individual components. (B and C) Amplitude of the oscillating AC component as a function of stimulus frequency (normalized to maximum values at low frequencies) in the different models. (C1) Simulated AC responses for frequencies between 100 and 10 kHz. (C2) highlights a smaller frequency sector (close to 2 kHz) of simulations shown in (C1). (D and E) Simulated DC response in IHCs presented as a function of stereocilia deflection amplitude (stimulation at 1 kHz). (F) Channel conductances as function of stereocilia vibration amplitude: IHC  $K^+$  channels activate at different levels of vibrations, and their maximal conductances saturate at different sound intensities. (G) AC:DC ratios (versus frequency) as measure of phase-locking efficiency (60 nm stereocilia deflection, 300 ms) in different models. (H) AC:DC ratios in two models in which all of the  $K_v 7.4$ -mediated conductance is either assigned to  $I_{K,n}$  (extreme basal model) or to the current fraction that activated at more positive membrane potentials (extreme apical model). All of the other conductances were implemented with their native properties. (I–K) Simulations in which all of the native  $K_v$  conductance ( $I_{K,s}$  and  $I_{K,n}$ ) is assigned only to the one  $K_v$  subunit indicated in the panels. (I and J) AC:DC ratios as function of (I) frequency or (J) stereocilia vibration amplitude. (K) DC response as function of stereocilia vibration amplitude (stimulation at 1 kHz; see also Figure S7C for a logarithmic presentation of the same data). See text for details.

$I_{K,s}(K_v7.4)$  or  $I_{K,s}(K_v1.8)$  improves the phase locking of IHC potentials but reduces the sensitivity at low sound intensity by  $\sim 3$  dB (Figures 7K, S7C, and S7D). Thus, scaling-up  $I_{K,s}(K_v7.4)$  or  $I_{K,s}(K_v1.8)$  currents improves temporal precision at the expense of sensitivity. These simulations show that the combined activity of all of the  $K_v$  channels is beneficial for IHCs to fine-tune the membrane electrical properties in terms of sensitivity to low-level sounds, temporal precision, and dynamic range.

## DISCUSSION

### $K_v1.8$ , $K_v11.1$ , and $K_v12.1$ Contribute to $I_{K,s}$ in IHCs

Our study was motivated by a single-cell transcriptome analysis of mature IHCs (Liu et al., 2014; Shen et al., 2015). Taking the  $K_v7.4$  expression as the threshold,  $K_v1.8$ ,  $K_v3.3$ ,  $K_v11.1$ , and  $K_v12.1$  were the only  $K_v$  subunits in IHCs. Experiments with a specific  $K_v11$  antagonist and in mice with hair cell-specific *Kcnh2* deletion (Gutman et al., 2005; Ishii et al., 2003) demonstrated the functional expression of  $K_v11.1$  in IHCs, and 4-AP inhibited a current with properties consistent with recombinant  $K_v1.8$ . As no other  $K_v1$  and  $K_v11$  subunits are expressed in IHCs, this demonstrated the expression of  $K_v1.8$  and  $K_v11.1$ . Recent studies indicated the expression of  $K_v1.8$  and  $K_v11.1$  protein in hair cells (Lee et al., 2013; Nie et al., 2005), and *Kcna10* (encoding  $K_v1.8$ ) knockout mice displayed mild auditory deficits (Lee et al., 2013).

Due to the lack of specific tools, the identification of native  $K_v12.1$  currents depends on unique channel properties. Similarly, closely related  $K_v10$  and  $K_v11$  were functionally identified in tissues by exploiting their distinct characteristics (see, for example, Hardman and Forsythe, 2009; Hirdes et al., 2005, 2009; Meyer and Heinemann, 1998). Recently, we identified 4-AP (a known  $K^+$  channel inhibitor) as a potent activator (Dierich et al., 2018) and NS1643 (a  $K_v11$  agonist) as an inhibitor of  $K_v12.1$  (Casis et al., 2006; Dierich et al., 2018; Hansen et al., 2006).  $K_v12.1$  channels exhibit a mode shift of activation that manifests as a shift of activation to hyperpolarized potentials after membrane depolarization (Dai and Zagotta, 2017; Dierich et al., 2018; Dierich and Leitner, 2018; Li et al., 2015). Here, we identified IHC  $K^+$  currents that reproduce the exclusive combination of these distinct  $K_v12.1$  characteristics, providing very strong evidence for the abundance of  $K_v12.1$ . With the same strategy, we recently identified  $K_v12.1$  activity in cells heterologously expressing  $K_v$  combinations, including  $K_v11.1$  and  $K_v7$  (Dierich et al., 2018). Hence,  $K_v1.8$ ,  $K_v11.1$ , and  $K_v12.1$  channels are functional in IHCs and collectively mediate the IHC current  $I_{K,s}$  (Kros and Crawford, 1990; Marcotti et al., 2003). This is supported by their pharmacological characteristics completely reproducing these of  $I_{K,s}$  (Marcotti et al., 2003).

### Are $K_v3.3$ Channels Expressed in IHCs?

Although it was suggested by our database screen, we did not find any evidence for  $K_v3$  currents in IHCs: (1) we did not detect currents with fast voltage-dependent inactivation, a hallmark of  $K_v3.3$  (Fernandez et al., 2003; Vega-Saenz de Miera et al., 1992; Zhang et al., 2016); (2)  $K_v3.3$  channels are highly TEA sensitive (Fernandez et al., 2003; Vega-Saenz de Miera et al., 1992), but TEA and  $BK_{Ca}$  inhibitor IbTX blocked exactly the same IHC

currents; and (3)  $K_v3.3$  channels are sensitive to 4-AP, but 4-AP-sensitive IHC currents were TEA insensitive and activated more negatively than  $K_v3.3$  (Vega-Saenz de Miera et al., 1992; Zhang et al., 2016). We thus consider the expression of  $K_v3.3$  channels in IHCs unlikely.

### $K_v7.4$ Mediates Two Components in IHCs

$K_v7.4$  subunits mediate the current  $I_{K,n}$  in both hair cell types, which is small in IHCs but predominant in OHCs (Housley and Ashmore, 1992; Kharkovets et al., 2006; Leitner et al., 2011; Marcotti and Kros, 1999; Oliver et al., 2003). However, recombinant  $K_v7.4$  channels activate at 60 mV more positive potentials ( $V_h \sim -20$  mV) than  $I_{K,n}$  ( $V_h \sim -80$  mV) (Kubisch et al., 1999; Leitner et al., 2011, 2012), suggesting that unknown hair cell-specific interaction partners determine the properties of  $K_v7.4$  in these cells. In mature IHCs of mice,  $K_v7.4$  channels mediate a small  $I_{K,n}$ -like and a larger  $K_v7.4$ -like component (Kubisch et al., 1999; Leitner et al., 2011, 2012). As amplitudes of these two fractions vary reciprocally along the cochlear axis (e.g., in the gerbil; Johnson, 2015), this hair cell-specific modulation could be regulated tonotopically. As the proportion of  $I_{K,n}$  to the whole-cell conductance determines the tonotopic differences in receptor potentials, this may constitute a physiological adaptation of IHCs to encode complex sound.

### The $K^+$ Channel Repertoire Optimizes the Encoding of Complex Sound

Exquisite sensitivity, dynamic range, and temporal precision of hearing impose certain IHC specifications; detection of faint sounds requires sensitivity to small stereocilia vibrations, whereas encoding of a large range of sound intensities necessitates low sensitivity at high levels. Especially at low frequencies ( $< 2$  kHz), temporal precision needs to be high to encode temporal sound information in the auditory nerve precisely. These contrasting demands require the nonlinear regulation of IHC sensitivity. This level-dependent sensitivity of IHCs is greatly determined by asymmetric Boltzmann-type nonlinearity of MET channel activation (Cheatham and Dallos, 2000). However, if this was the exclusive mechanism, temporal precision would rapidly degrade with increasing sound levels due to the faster growth of DC components compared to AC components (see, for example, Shamma et al., 1986). We found that the  $K^+$  channel repertoire plays a fundamental role in regulating the nonlinear sensitivity of IHCs and in improving temporal precision. As discussed earlier (Altoè et al., 2018), we found that nonlinear activation of the  $K_v$  and  $BK_{Ca}$  channels produces a nonlinear increase in outward membrane conductance over continuous stimulus presentation, simultaneously reducing effective membrane time constant and electrical excitability. Thus, IHC  $K^+$  currents act as compressive nonlinearity for receptor potentials and significantly increase the dynamic range of sound levels that a single IHC and consequently nerve fibers can encode (Altoè et al., 2018; Kros and Crawford, 1990; Lopez-Poveda and Eustaquio-Martín, 2006). The slow kinetics of the  $K_v$  channels prevent that their conductance fluctuates at stimulus frequency, thereby producing a larger compression of the DC than of the AC component of receptor potentials. This increases temporal precision at all frequencies and opposes the degradation of AC:DC ratios

with increasing stimulus levels. In contrast, fast BK<sub>Ca</sub> channels allow for phase-locked fluctuations of the membrane conductance, which substantially increases the membrane cutoff frequency, rendering membrane potential oscillations effectively faster than those determined by the effective RC time constant (Figure 7B; Altoè et al., 2018). The combined activity of BK<sub>Ca</sub> and K<sub>v</sub> channels synergistically optimizes AC and DC responses more significantly than predicted from individual contributions. We conclude that the expression of K<sub>v</sub> channels constitutes an important evolutionary adaptation to improve the dynamic range and temporal precision of IHC responses.

### Expression of Various K<sup>+</sup> Channels Is an Evolutionary Advantage

Our models show why the expression of various K<sup>+</sup> channels is advantageous to IHCs: (1) Combined activity of the K<sup>+</sup> channels leads to more pronounced improvement in the dynamic range and phase locking than expected from individual contributions. This is an advantage of multi-component systems. (2) Activation of the K<sub>v</sub> channels (with limited individual sensitivity) sums up into a high-order Boltzmann nonlinearity, with steep sensitivity near rest that does not saturate over the entire range of physiological potentials. (3) As suggested earlier (Johnson, 2015), the I<sub>K,n</sub>:I<sub>K,s</sub> ratio essentially determines and optimizes tonotopic responses, which is clearly beneficial for sound encoding. (4) Expression of the channel repertoire optimizes receptor potentials to encode multiple modalities of complex sound, as each conductance contributes to the improvement of a different aspect. They individually optimize frequency responses (I<sub>K,f</sub> and I<sub>K,s</sub>(K<sub>v</sub>1.8, K<sub>v</sub>7.4)) or improve phase locking (I<sub>K,n</sub>-to-I<sub>K,s</sub> relation). At the same time, I<sub>K,s</sub>(K<sub>v</sub>1.8, K<sub>v</sub>7.4, K<sub>v</sub>11.1) dramatically increases the range of sound levels that can be encoded. Supporting this, a study in gerbils showed that receptor potentials in apical IHCs with relatively large I<sub>K,f</sub> and I<sub>K,s</sub> more precisely follow sound frequency (Johnson, 2015). Our data demonstrate that the expression of multiple K<sup>+</sup> channel entities provides clear functional advantages for IHCs.

Could comparably precise encoding of complex sound be achieved by expressing fewer K<sup>+</sup> channel entities? We addressed this *in silico* in cells in which all of the native K<sub>v</sub> conductance was assigned to a single K<sub>v</sub> entity. These simulations revealed that the native channel repertoire allows for an effective trade-off between the requirements of (1) high IHC sensitivity at low stimulus levels, (2) dynamic range compression, and (3) high temporal precision. Assigning all K<sub>v</sub> conductance to individual K<sub>v</sub> subunits either deteriorates the encoding of sound frequency and intensity or improves the encoding of one sound quality at the expense of another. Thus, expressing the native channel repertoire and the observed separation of physiological functions of the components constitutes an evolutionary adaptation to encode complex sound through multifaceted receptor potentials. “Simpler” IHCs may be limited to encoding only certain aspects (frequency or intensity) of sound.

### Physiological Roles of K<sub>v</sub>1.8, K<sub>v</sub>11.1, and K<sub>v</sub>12.1

We provided evidence for the relevance of K<sub>v</sub>12.1 and K<sub>v</sub>1.8 channels, as well as for homomeric K<sub>v</sub>11.1 channels that have been shown mainly in cardiac muscle. We found that K<sub>v</sub>12.1 currents in IHCs exhibited a significant mode shift, but our results

cannot provide evidence for the relevance of this phenomenon for sound encoding. It is tempting to speculate that biophysical properties of IHCs may be adjusted to continuous sound stimulation or pathological depolarization through such a mode shift, adding supplementary specialization to intrinsic IHC membrane tuning. However, further work is needed to unravel whether mode shift can be important for sound processing in hair cells.

### STAR★METHODS

Detailed methods are provided in the online version of this paper and include the following:

- KEY RESOURCES TABLE
- RESOURCE AVAILABILITY
  - Lead Contact
  - Materials Availability
  - Data and Code Availability
- EXPERIMENTAL MODEL AND SUBJECT DETAILS
  - Animal handling and animal experimentation
  - Mouse lines analyzed in this study
  - Hair cell-specific Kcnh2 (K<sub>v</sub>11.1) knock-out mice
  - Cell line
- METHOD DETAILS
  - Transient transfection
  - RNA isolation and reverse transcription PCR
  - Cloning of K<sub>v</sub>1.8 channels
  - Immunohistochemistry
  - Confocal Imaging
  - Electrophysiological Recordings
  - Reagents
  - Computational Model of Receptor Potentials
- QUANTIFICATION AND STATISTICAL ANALYSIS

### SUPPLEMENTAL INFORMATION

Supplemental Information can be found online at <https://doi.org/10.1016/j.celrep.2020.107869>.

### ACKNOWLEDGMENTS

The authors gratefully acknowledge the kind gift of plasmids for K<sub>v</sub>12.1 from Dr. Jegla, and for K<sub>v</sub>11.1, K<sub>v</sub>11.2, and K<sub>v</sub>11.3 (Erg) from Dr. Bauer. We thank Dr. Zuo and Dr. Engel for providing Prestin-Cre mice, and Olga Ebers for superb technical assistance. This work was funded by the German Research Foundation (DFG Priority Program 1608: “Ultrafast and Temporally Precise Information Processing: Normal and Dysfunctional Hearing” [LE 3600/1-1 to M.G.L., VE 924/1-1 to S.V., and OL 240/4-2 to D.O.]), by research grants from the University Medical Center Giessen und Marburg to M.G.L. (UKGM 17/2013 and UKGM 13/2016), Tiroler Wissenschaftsförderung (TWF GZ UNI-0404/2381 to M.G.L.), the Caruso Department of Otolaryngology (University of Southern California, to A.A.), and by NIH/NIDCD grant no. R01 DC003687 (CAS; to A.A.).

### AUTHOR CONTRIBUTIONS

M.D., A.A., S.V., D.O., and M.G.L. designed the research; M.D., J.K., S.E., V.R., M.K.S., R.N., and M.G.L. conducted the experiments; A.A. did the modeling; R.N. generated the mouse line; M.D., J.K., S.E., V.R., and M.G.L. performed the analysis; and M.D., A.A., D.O., and M.G.L. wrote the manuscript.

## DECLARATION OF INTERESTS

The authors declare no competing interests.

Received: January 8, 2020

Revised: April 8, 2020

Accepted: June 16, 2020

Published: July 7, 2020

## REFERENCES

- Altoè, A., Pulkki, V., and Verhulst, S. (2018). The effects of the activation of the inner-hair-cell basolateral  $K^+$  channels on auditory nerve responses. *Hear. Res.* 364, 68–80.
- Beurg, M., Fettiplace, R., Nam, J.H., and Ricci, A.J. (2009). Localization of inner hair cell mechanotransducer channels using high-speed calcium imaging. *Nat. Neurosci.* 12, 553–558.
- Casis, O., Olesen, S.P., and Sanguinetti, M.C. (2006). Mechanism of action of a novel human ether-a-go-go-related gene channel activator. *Mol. Pharmacol.* 69, 658–665.
- Cheatham, M.A., and Dallos, P. (2000). The dynamic range of inner hair cell and organ of Corti responses. *J. Acoust. Soc. Am.* 107, 1508–1520.
- Cox, B.C., Liu, Z., Lagarde, M.M., and Zuo, J. (2012). Conditional gene expression in the mouse inner ear using Cre-loxP. *J. Assoc. Res. Otolaryngol.* 13, 295–322.
- Dai, G., and Zagotta, W.N. (2017). Molecular mechanism of voltage-dependent potentiation of KCNH potassium channels. *eLife* 6, e26355.
- Dallos, P. (1985a). Membrane potential and response changes in mammalian cochlear hair cells during intracellular recording. *J. Neurosci.* 5, 1609–1615.
- Dallos, P. (1985b). Response characteristics of mammalian cochlear hair cells. *J. Neurosci.* 5, 1591–1608.
- Dallos, P., Wu, X., Cheatham, M.A., Gao, J., Zheng, J., Anderson, C.T., Jia, S., Wang, X., Cheng, W.H., Sengupta, S., et al. (2008). Prestin-based outer hair cell motility is necessary for mammalian cochlear amplification. *Neuron* 58, 333–339.
- Dickinson, M.E., Flenniken, A.M., Ji, X., Teboul, L., Wong, M.D., White, J.K., Meehan, T.F., Wengler, W.J., Westerberg, H., Adissu, H., et al.; International Mouse Phenotyping Consortium; Jackson Laboratory; Infrastructure Nationale PHENOMIN, Institut Clinique de la Souris (ICS); Charles River Laboratories; MRC Harwell; Toronto Centre for Phenogenomics; Wellcome Trust Sanger Institute; RIKEN BioResource Center (2016). High-throughput discovery of novel developmental phenotypes. *Nature* 537, 508–514.
- Dierich, M., and Leitner, M.G. (2018).  $K_v12.1$  channels are not sensitive to  $G_q$ PCR-triggered activation of phospholipase  $C\beta$ . *Channels (Austin)* 12, 228–239.
- Dierich, M., Evers, S., Wilke, B.U., and Leitner, M.G. (2018). Inverse modulation of neuronal  $K_v12.1$  and  $K_v11.1$  channels by 4-aminopyridine and NS1643. *Front. Mol. Neurosci.* 11, 11.
- Dierich, M., Hartmann, S., Dietrich, N., Moeser, P., Brede, F., Johnson Chacko, L., Tziridis, K., Schilling, A., Krauss, P., Hessler, S., et al. (2019a).  $\beta$ -Secretase BACE1 Is Required for Normal Cochlear Function. *J. Neurosci.* 39, 9013–9027.
- Dierich, M., van Ham, W.B., Stary-Weinzinger, A., and Leitner, M.G. (2019b). Histidine at position 462 determines the low quinine sensitivity of ether-a-go-go channel superfamily member  $K_v12.1$ . *Br. J. Pharmacol.* 176, 2708–2723.
- Fernandez, F.R., Morales, E., Rashid, A.J., Dunn, R.J., and Turner, R.W. (2003). Inactivation of  $K_v3.3$  potassium channels in heterologous expression systems. *J. Biol. Chem.* 278, 40890–40898.
- Gutman, G.A., Chandy, K.G., Grissmer, S., Lazdunski, M., McKinnon, D., Pardo, L.A., Robertson, G.A., Rudy, B., Sanguinetti, M.C., Stühmer, W., and Wang, X. (2005). International Union of Pharmacology. LIII. Nomenclature and molecular relationships of voltage-gated potassium channels. *Pharmacol. Rev.* 57, 473–508.
- Hansen, R.S., Diness, T.G., Christ, T., Demnitz, J., Ravens, U., Olesen, S.P., and Grunnet, M. (2006). Activation of human ether-a-go-go-related gene potassium channels by the diphenylurea 1,3-bis-(2-hydroxy-5-trifluoromethylphenyl)-urea (NS1643). *Mol. Pharmacol.* 69, 266–277.
- Hardman, R.M., and Forsythe, I.D. (2009). Ether-a-go-go-related gene  $K^+$  channels contribute to threshold excitability of mouse auditory brainstem neurons. *J. Physiol.* 587, 2487–2497.
- Hirdes, W., Schweizer, M., Schuricht, K.S., Guddat, S.S., Wulfsen, I., Bauer, C.K., and Schwarz, J.R. (2005). Fast erg  $K^+$  currents in rat embryonic serotonergic neurones. *J. Physiol.* 564, 33–49.
- Hirdes, W., Napp, N., Wulfsen, I., Schweizer, M., Schwarz, J.R., and Bauer, C.K. (2009). Erg  $K^+$  currents modulate excitability in mouse mitral/tufted neurons. *Pflugers Arch.* 459, 55–70.
- Housley, G.D., and Ashmore, J.F. (1992). Ionic currents of outer hair cells isolated from the guinea-pig cochlea. *J. Physiol.* 448, 73–98.
- Ishii, K., Nagai, M., Takahashi, M., and Endoh, M. (2003). Dissociation of E-4031 from the HERG channel caused by mutations of an amino acid results in greater block at high stimulation frequency. *Cardiovasc. Res.* 57, 651–659.
- Johnson, S.L. (2015). Membrane properties specialize mammalian inner hair cells for frequency or intensity encoding. *eLife* 4, e08177.
- Johnson, S.L., Beurg, M., Marcotti, W., and Fettiplace, R. (2011). Prestin-driven cochlear amplification is not limited by the outer hair cell membrane time constant. *Neuron* 70, 1143–1154.
- Kharkovets, T., Dedek, K., Maier, H., Schweizer, M., Khimich, D., Nouvian, R., Vardanyan, V., Leuwer, R., Moser, T., and Jentsch, T.J. (2006). Mice with altered KCNQ4  $K^+$  channels implicate sensory outer hair cells in human progressive deafness. *EMBO J.* 25, 642–652.
- Kimitsuki, T., and Komune, S. (2013). Temperature enhances activation and inactivation kinetics of potassium currents in inner hair cells isolated from Guinea-pig cochlea. *Clin. Exp. Otorhinolaryngol.* 6, 140–145.
- Kimitsuki, T., Komune, N., Noda, T., Takaiwa, K., Ohashi, M., and Komune, S. (2010). Property of  $I(K)_n$  in inner hair cells isolated from guinea-pig cochlea. *Hear. Res.* 261, 57–62.
- Koch, C. (2004). *Biophysics of Computation: Information Processing in Single Neurons* (Computational Neuroscience Series) (Oxford University Press).
- Kranz, A., Fu, J., Duerschke, K., Weidlich, S., Naumann, R., Stewart, A.F., and Anastassiadis, K. (2010). An improved Flp deleter mouse in C57Bl/6 based on Flpo recombinase. *Genesis* 48, 512–520.
- Kros, C.J., and Crawford, A.C. (1990). Potassium currents in inner hair cells isolated from the guinea-pig cochlea. *J. Physiol.* 421, 263–291.
- Kros, C.J., Ruppersberg, J.P., and Rüscher, A. (1998). Expression of a potassium current in inner hair cells during development of hearing in mice. *Nature* 394, 281–284.
- Kubisch, C., Schroeder, B.C., Friedrich, T., Lutjohann, B., El-Amraoui, A., Marlin, S., Petit, C., and Jentsch, T.J. (1999). KCNQ4, a novel potassium channel expressed in sensory outer hair cells, is mutated in dominant deafness. *Cell* 96, 437–446.
- Lang, R., Lee, G., Liu, W., Tian, S., Rafi, H., Orias, M., Segal, A.S., and Desir, G.V. (2000). KCNA10: a novel ion channel functionally related to both voltage-gated potassium and CNG cation channels. *Am. J. Physiol. Renal Physiol.* 278, F1013–F1021.
- Lee, S.I., Conrad, T., Jones, S.M., Lagziel, A., Starost, M.F., Belyantseva, I.A., Friedman, T.B., and Morell, R.J. (2013). A null mutation of mouse *Kcna10* causes significant vestibular and mild hearing dysfunction. *Hear. Res.* 300, 1–9.
- Leitner, M.G., Halaszovich, C.R., and Oliver, D. (2011). Aminoglycosides inhibit KCNQ4 channels in cochlear outer hair cells via depletion of phosphatidylinositol(4,5)bisphosphate. *Mol. Pharmacol.* 79, 51–60.
- Leitner, M.G., Feuer, A., Ebers, O., Schreiber, D.N., Halaszovich, C.R., and Oliver, D. (2012). Restoration of ion channel function in deafness-causing KCNQ4 mutants by synthetic channel openers. *Br. J. Pharmacol.* 165, 2244–2259.

- Leitner, M.G., Michel, N., Behrendt, M., Dierich, M., Dembla, S., Wilke, B.U., Konrad, M., Lindner, M., Oberwinkler, J., and Oliver, D. (2016). Direct modulation of TRPM4 and TRPM3 channels by the phospholipase C inhibitor U73122. *Br. J. Pharmacol.* *173*, 2555–2569.
- Leitner, M.G., Hobiger, K., Mavrantoni, A., Feuer, A., Oberwinkler, J., Oliver, D., and Halaszovich, C.R. (2018). A126 in the active site and T1167/168 in the TI loop are essential determinants of the substrate specificity of PTEN. *Cell. Mol. Life Sci.* *75*, 4235–4250.
- Li, X., Anishkin, A., Liu, H., van Rossum, D.B., Chintapalli, S.V., Sassic, J.K., Gallegos, D., Pivaroff-Ward, K., and Jegla, T. (2015). Bimodal regulation of an Elk subfamily K<sup>+</sup> channel by phosphatidylinositol 4,5-bisphosphate. *J. Gen. Physiol.* *146*, 357–374.
- Lieberman, M.C., Gao, J., He, D.Z., Wu, X., Jia, S., and Zuo, J. (2002). Prestin is required for electromotility of the outer hair cell and for the cochlear amplifier. *Nature* *419*, 300–304.
- Lingle, C.J., Martinez-Espinosa, P.L., Yang-Hood, A., Boero, L.E., Payne, S., Persic, D., V-Ghaffari, B., Xiao, M., Zhou, Y., Xia, X.-M., et al. (2019). LRRC52 regulates BK channel function and localization in mouse cochlear inner hair cells. *Proc. Natl. Acad. Sci. USA* *116*, 18397–18403.
- Liu, H., Pecka, J.L., Zhang, Q., Soukup, G.A., Beisel, K.W., and He, D.Z. (2014). Characterization of transcriptomes of cochlear inner and outer hair cells. *J. Neurosci.* *34*, 11085–11095.
- Lopez-Poveda, E.A., and Eustaquio-Marín, A. (2006). A biophysical model of the inner hair cell: the contribution of potassium currents to peripheral auditory compression. *J. Assoc. Res. Otolaryngol.* *7*, 218–235.
- Marcotti, W., and Kros, C.J. (1999). Developmental expression of the potassium current I<sub>K,n</sub> contributes to maturation of mouse outer hair cells. *J. Physiol.* *520* (Pt 3), 653–660.
- Marcotti, W., Johnson, S.L., Holley, M.C., and Kros, C.J. (2003). Developmental changes in the expression of potassium currents of embryonic, neonatal and mature mouse inner hair cells. *J. Physiol.* *548*, 383–400.
- Marcotti, W., Johnson, S.L., and Kros, C.J. (2004). Effects of intracellular stores and extracellular Ca<sup>2+</sup> on Ca<sup>2+</sup>-activated K<sup>+</sup> currents in mature mouse inner hair cells. *J. Physiol.* *557*, 613–633.
- Mavrantoni, A., Thallmair, V., Leitner, M.G., Schreiber, D.N., Oliver, D., and Halaszovich, C.R. (2015). A method to control phosphoinositides and to analyze PTEN function in living cells using voltage sensitive phosphatases. *Front. Pharmacol.* *6*, 68.
- Meyer, R., and Heinemann, S.H. (1998). Characterization of an eag-like potassium channel in human neuroblastoma cells. *J. Physiol.* *508*, 49–56.
- Nie, L., Gratton, M.A., Mu, K.J., Dinglasan, J.N., Feng, W., and Yamoah, E.N. (2005). Expression and functional phenotype of mouse ERG K<sup>+</sup> channels in the inner ear: potential role in K<sup>+</sup> regulation in the inner ear. *J. Neurosci.* *25*, 8671–8679.
- Oliver, D., Knipper, M., Derst, C., and Fakler, B. (2003). Resting potential and submembrane calcium concentration of inner hair cells in the isolated mouse cochlea are set by KCNQ-type potassium channels. *J. Neurosci.* *23*, 2141–2149.
- Palmer, A.R., and Russell, I.J. (1986). Phase-locking in the cochlear nerve of the guinea-pig and its relation to the receptor potential of inner hair-cells. *Hear. Res.* *24*, 1–15.
- Pan, B., Akyuz, N., Liu, X.P., Asai, Y., Nist-Lund, C., Kurima, K., Derfler, B.H., Gyorgy, B., Limapichat, W., Walujkar, S., et al. (2018). TMC1 Forms the Pore of Mechanosensory Transduction Channels in Vertebrate Inner Ear Hair Cells. *Neuron* *99*, 736–753.e6.
- Platzer, J., Engel, J., Schrott-Fischer, A., Stephan, K., Bova, S., Chen, H., Zheng, H., and Striessnig, J. (2000). Congenital deafness and sinoatrial node dysfunction in mice lacking class D L-type Ca<sup>2+</sup> channels. *Cell* *102*, 89–97.
- Poueymirou, W.T., Auerbach, W., Frenthewey, D., Hickey, J.F., Escaravage, J.M., Esau, L., Doré, A.T., Stevens, S., Adams, N.C., Dominguez, M.G., et al. (2007). F0 generation mice fully derived from gene-targeted embryonic stem cells allowing immediate phenotypic analyses. *Nat. Biotechnol.* *25*, 91–99.
- Ricci, A.J., Kachar, B., Gale, J., and Van Netten, S.M. (2006). Mechano-electrical transduction: new insights into old ideas. *J. Membr. Biol.* *209*, 71–88.
- Robles, L., and Ruggero, M.A. (2001). Mechanics of the mammalian cochlea. *Physiol. Rev.* *81*, 1305–1352.
- Russell, I.J., and Sellick, P.M. (1978). Intracellular studies of hair cells in the mammalian cochlea. *J. Physiol.* *284*, 261–290.
- Rüttiger, L., Sausbier, M., Zimmermann, U., Winter, H., Braig, C., Engel, J., Knirsch, M., Arntz, C., Langer, P., Hirt, B., et al. (2004). Deletion of the Ca<sup>2+</sup>-activated potassium (BK) alpha-subunit but not the BKbeta1-subunit leads to progressive hearing loss. *Proc. Natl. Acad. Sci. USA* *101*, 12922–12927.
- Scheffer, D.I., Shen, J., Corey, D.P., and Chen, Z.Y. (2015). Gene Expression by Mouse Inner Ear Hair Cells during Development. *J. Neurosci.* *35*, 6366–6380.
- Schwander, M., Kachar, B., and Müller, U. (2010). The cell biology of hearing. *J. Cell. Biol.* *190*, 9–20.
- Shamma, S.A., Chadwick, R.S., Wilbur, W.J., Morrish, K.A., and Rinzell, J. (1986). A biophysical model of cochlear processing: intensity dependence of pure tone responses. *J. Acoust. Soc. Am.* *80*, 133–145.
- Shen, J., Scheffer, D.I., Kwan, K.Y., and Corey, D.P. (2015). SHIELD: an integrative gene expression database for inner ear research. *Database* (Oxford) *2015*, bav071.
- Skarnes, W.C., Rosen, B., West, A.P., Koutourakis, M., Bushell, W., Iyer, V., Mujica, A.O., Thomas, M., Harrow, J., Cox, T., et al. (2011). A conditional knockout resource for the genome-wide study of mouse gene function. *Nature* *474*, 337–342.
- Thurm, H., Fakler, B., and Oliver, D. (2005). Ca<sup>2+</sup>-independent activation of BKCa channels at negative potentials in mammalian inner hair cells. *J. Physiol.* *569*, 137–151.
- Tian, S., Liu, W., Wu, Y., Rafi, H., Segal, A.S., and Desir, G.V. (2002). Regulation of the voltage-gated K<sup>+</sup> channel KCNA10 by KCNA4B, a novel beta-subunit. *Am. J. Physiol. Renal Physiol.* *283*, F142–F149.
- Tian, Y., Li, M., Fritsch, B., and Zuo, J. (2004). Creation of a transgenic mouse for hair-cell gene targeting by using a modified bacterial artificial chromosome containing Prestin. *Dev. Dyn.* *231*, 199–203.
- Trudeau, M.C., Warmke, J.W., Ganetzky, B., and Robertson, G.A. (1995). HERG, a human inward rectifier in the voltage-gated potassium channel family. *Science* *269*, 92–95.
- Vega-Saenz de Miera, E., Moreno, H., Fruhling, D., Kentros, C., and Rudy, B. (1992). Cloning of Shlll (Shaw-like) cDNAs encoding a novel high-voltage-activating, TEA-sensitive, type-A K<sup>+</sup> channel. *Proc. Biol. Sci.* *248*, 9–18.
- Villalba-Galea, C.A. (2017). Hysteresis in voltage-gated channels. *Channels (Austin)* *11*, 140–155.
- Vogl, C., Butola, T., Haag, N., Hausrat, T.J., Leitner, M.G., Moutschen, M., Lefebvre, P.P., Speckmann, C., Garrett, L., Becker, L., et al. (2017). The BEACH protein LRBA is required for hair bundle maintenance in cochlear hair cells and for hearing. *EMBO Rep.* *18*, 2015–2029.
- Zhang, Y., Zhang, X.F., Fleming, M.R., Amiri, A., El-Hassar, L., Surguchev, A.A., Hyland, C., Jenkins, D.P., Desai, R., Brown, M.R., et al. (2016). Kv3.3 Channels Bind Hax-1 and Arp2/3 to Assemble a Stable Local Actin Network that Regulates Channel Gating. *Cell* *165*, 434–448.
- Zheng, J., Shen, W., He, D.Z., Long, K.B., Madison, L.D., and Dallos, P. (2000). Prestin is the motor protein of cochlear outer hair cells. *Nature* *405*, 149–155.

## STAR★METHODS

### KEY RESOURCES TABLE

REAGENT or RESOURCE	SOURCE	IDENTIFIER
<b>Antibodies</b>		
Rabbit polyclonal anti-K <sub>v</sub> 11.1	Alomone Labs	Cat #: APC-016
Rabbit polyclonal anti-K <sub>v</sub> 11.2	Alomone Labs	Cat #: APC-114
Rabbit polyclonal anti-K <sub>v</sub> 11.3	Enzo Life Sciences	Cat #: ALX-215-053-R100
Rabbit polyclonal anti-K <sub>v</sub> 12.1	Alomone Labs	Cat #: APC-113
Mouse monoclonal anti-MyosinVIIa	Santa Cruz Biotechnology	Cat #: sc-74516
Goat anti-Rabbit IgG (H+L) Cross-Adsorbed Secondary Antibody, Alexa Fluor 488	Thermo Fischer	Cat #: A11008
Goat anti-Mouse IgG (H+L) Cross-Adsorbed Secondary Antibody, Alexa Fluor 633	Thermo Fischer	Cat #: A21050
<b>Chemicals, Peptides, and Recombinant Proteins</b>		
Tetraethylammonium chloride	Tocris	Cat #: 3068
Iberiotoxin	Tocris	Cat #: 1086
XE991 dihydrochloride	Tocris	Cat #: 2000
E-4031 dihydrochloride	Tocris	Cat #: 1808
4-AP	Tocris	Cat #: 0940
NS1643	Tocris	Cat #: 3062
<b>Experimental Models: Cell Lines</b>		
Chinese hamster ovary (CHO) dhFR <sup>-</sup> cells	ATCC	CRL-9096
<b>Experimental Models: Organisms/Strains</b>		
C57BL/6NCrl mice	Charles River	Strain Code 027
C57Bl6/NJ mice	The Jackson Laboratory	Stock No: 005304
<i>Kcnh2</i> <sup>tm1a(EUCOMM)Wtsi</sup> KO first allele ES cells	European Conditional Mouse Mutagenesis Program (EUCOMM)	MGI ID MGI:1341722
Prestin-Cre (BAC transgenic) mice	<a href="#">Tian et al., 2004</a>	N/A
<b>Oligonucleotides</b>		
Primers for RT-PCR, see <a href="#">Table S1</a> (last page of supplementary pdf)	This Paper	N/A
<b>Recombinant DNA</b>		
K <sub>v</sub> 1.8-pRFP-N1	This paper	Uniprot: B2RQA1
K <sub>v</sub> 11.1a-pcDNA3.1	Dr. CK Bauer	Uniprot: O08962
K <sub>v</sub> 11.2-pcDNA3.1	Dr. CK Bauer	Uniprot: O54853
K <sub>v</sub> 11.3-pcDNA3.1	Dr. CK Bauer	Uniprot: O54852
K <sub>v</sub> 12.1-pcDNA3.1-IRES-eGFP	Dr. T Jegla	Uniprot: Q96L42
Lyn11-GFP-pcDNA3.1	Dr. D. Oliver	Uniprot: P07948
<b>Software and Algorithms</b>		
PatchMaster (HEKA)	HEKA Elektronik	<a href="https://www.heka.com/downloads/">https://www.heka.com/downloads/</a>
IgorPro	Wavemetrics	<a href="https://www.wavemetrics.com/downloads/current">https://www.wavemetrics.com/downloads/current</a>
<b>Other</b>		
Inner hair cell biophysical model codes	This Paper	<a href="https://www.mechanicsofhearing.org/apg/">https://www.mechanicsofhearing.org/apg/</a>
DAPI	Sigma-Aldrich	Cat #: D9542

## RESOURCE AVAILABILITY

### Lead Contact

Further information and requests for resources and reagents should be directed to and will be fulfilled by the Lead Contact, Michael G. Leitner ([Michael.Leitner@i-med.ac.at](mailto:Michael.Leitner@i-med.ac.at)).

### Materials Availability

Plasmids encoding cloned  $K_v1.8$  channel subunits will be provided upon request by the Lead contact, Michael G. Leitner ([Michael.Leitner@i-med.ac.at](mailto:Michael.Leitner@i-med.ac.at)).

### Data and Code Availability

The code generated during this study is available at: <https://www.mechanicsofhearing.org/apg/>

## EXPERIMENTAL MODEL AND SUBJECT DETAILS

### Animal handling and animal experimentation

Mice were kept and treated according to German law and institutional guidelines at Philipps-University Marburg (Germany). All procedures complied to 3R principles and were approved by research ethics committee (Tierschutzkommission) at Regierungspräsidium Gießen (Germany).

### Mouse lines analyzed in this study

This study was performed on wild-type C57BL/6 mice and on mice with hair cell-specific deletion of the *Kcnh2* gene (see below) of either sex between 18 and 23 days after birth.

### Hair cell-specific *Kcnh2* ( $K_v11.1$ ) knock-out mice

*Kcnh2*<sup>tm1a(EUCOMM)Wtsi</sup> KO first allele (reporter-tagged insertion with conditional potential) embryonic stem (ES) cells were obtained from the European Conditional Mouse Mutagenesis Program (EUCOMM) (Dickinson et al., 2016; Skarnes et al., 2011) and were injected into C57BL/6NClr 8-cell embryos (Poueymirou et al., 2007). The resulting chimeras were mated to C57BL/6NClr mice, and progeny were screened to confirm germline transmission. Following the establishment of germline transmitting progeny, heterozygotes were crossed with C57BL/6NClr wild-type (WT) mice to produce a heterozygous mouse population. Mice heterozygous for the desired insert were then mated with Flp-O(N) deleter mice for removal of the neomycin-reporter cassette (Kranz et al., 2010), and resulting heterozygous mice were intercrossed to produce mice with homozygous insertion of two loxP sites in the *Kcnh2* gene (*Kcnh2*<sup>loxP/loxP</sup>). *Kcnh2*<sup>loxP/loxP</sup> mice were crossed with Prestin-Cre (BAC transgenic) mice (Cox et al., 2012; Tian et al., 2004) to obtain mice carrying loxP insertions together with Prestin-Cre (BAC transgenic). These mice were then crossed with *Kcnh2*<sup>loxP/loxP</sup> mice to obtain *Kcnh2*<sup>loxP/loxP</sup> mice with Prestin-Cre (BAC transgenic) that were then used for the experiments. These hair-cell specific knock-out mice are denoted as *Kcnh2*<sup>HC-/-</sup> to differentiate from WT (*Kcnh2*<sup>+/+</sup>) mice.

### Cell line

Chinese hamster ovary (CHO) dhFR<sup>-</sup> cells (ATCC: CRL-9096) were utilized for transient overexpression of proteins (see below). Chinese hamster ovary (CHO) dhFR<sup>-</sup> cells were maintained as previously reported (Leitner et al., 2016). In brief, cells were kept in MEM Alpha Medium supplemented with 10% fetal calf serum (FCS) and 1% penicillin/streptomycin (pen/strep) (Invitrogen GmbH, Darmstadt, Germany) in a humidified atmosphere at 5% CO<sub>2</sub> and 37°C

## METHOD DETAILS

### Transient transfection

CHO cells were transiently transfected with jetPEI transfection reagent (Polyplus Transfection, Illkirch, France). All experiments were performed 48 h after transfection at room temperature (22°C-25°C). The expression vectors used were:  $K_v11.1$ a-pcDNA3.1 (rat *Kcnh2*; isoform 1a; Uniprot: O08962),  $K_v11.2$ -pcDNA3.1 (rat *Kcnh6*; O54853),  $K_v11.3$ -pcDNA3.1 (rat *Kcnh7*; O54852),  $K_v12.1$ -pcDNA3.1-IRESegFP (human *KCNH8*; Q96L42);  $K_v1.8$ -pRFP-N1 (mouse *Kcna10*; B2RQA1), and Lyn11-GFP-pcDNA3.1 (transfection control; P07948).

### RNA isolation and reverse transcription PCR

For isolation of RNA, the two inner ears were isolated from a C57BL/6J mouse, as previously reported (Leitner et al., 2011) and the cochleae were separated from the vestibular organ. The two cochleae were homogenized in 400  $\mu$ l lysis buffer on ice three times for 10 s, and total RNA was isolated using the peqGOLD Total RNA Kit (peqlab/ VWR Life Science, Radnor/USA). RNA purity was evaluated by NanoDrop One<sup>C</sup> (Thermo Fisher Scientific, Waltham, USA). For RT-PCR, 1  $\mu$ g total RNA was reverse transcribed using random hexamer primers for Superscript II Reverse Transcriptase Kit (Invitrogen, Carlsbad, CA) or gene-specific primers for



QIAGEN OneStep RT-PCR Kit (QIAGEN, Hilden, Germany). AmpliTaq Gold DNA Polymerase (Thermo Fisher Scientific, Waltham, USA) and HotStarTaq DNA Polymerase (QIAGEN OneStep RT-PCR Kit) was used together with one of the gene-specific primer pairs listed in [Table S1](#) for amplification of the cDNA of interest (last page of supplementary pdf). RT-PCR reactions comprised 35–40 cycles with annealing temperatures adjusted to the employed primer pair (typically between 55–58 °C for 30–40 s) and template extension at 72 °C for 40–60 s. All PCR products were separated with standard gel-electrophoreses and verified by sequencing (Seqlab GmbH, Göttingen, Germany). For identification of  $K_{v}11.2$  transcripts in cochlear lysates nested PCR was performed.

### Cloning of $K_{v}1.8$ channels

Total RNA was extracted from the cochlea of P20–P23 mice using peqGOLD Total RNA Kit (peqlab/ VWR Life Science, Radnor/ USA), and cDNA synthesis (QIAGEN OneStep RT-PCR Kit) was performed with gene-specific primers for  $K_{v}1.8$ . The full-length RT-PCR product was separated with standard gel-electrophoreses and purified using QIAquick Gel Extraction Kit (QIAGEN, Hilden, Germany). This 1826 bp fragment was cloned into a pGEM<sup>®</sup>-T Easy Vector (Promega, USA) by taking advantage of 3' terminal deoxyadenosine overhangs of the PCR product and the 3'-deoxythymidine terminals of the vector. The coding region was excised with a single restriction digestion (*NotI*), and was inserted into a pRFP-N1 (TakaraBio Europe) expression vector dephosphorylated with FastAP Thermosensitive Alkaline Phosphatase (Thermo Fisher Scientific). For the ligation reactions, we used a T4 DNA Ligase (Thermo Fisher Scientific, Waltham, USA) and incubated vector and insert in a ratio of 1:8 overnight at 4 °C. The transformation was done in XL-10 gold *E. coli* cells.

### Immunohistochemistry

Immunohistochemistry was performed on formaldehyde-fixed whole-mount preparations of the apical turn of the organ of Corti of C57BL/6J mice (between P19 and P21), as previously reported ([Vogl et al., 2017](#)). In brief, cochleae were removed from the temporal bone and after introduction of a small hole were placed in 2% paraformaldehyde for 2 h at 4 °C. The apical turn of the organ of Corti was then dissected from the cochlea and separated from modiolus, stria vascularis and tectorial membrane. Samples were blocked and permeabilized for 1 h at room temperature in a buffer containing 10% normal goat serum (NGS), 0.3% Triton X-100, 20 mM PB, and 450 mM NaCl. Immunostaining was performed overnight at 4 °C with commercially available primary antibodies detecting  $K_{v}11.1$  (1:400; Alomone labs: #APC-016; for  $K_{v}11.2$  and  $K_{v}11.2$  see [Key Resources Table](#)) and Myosin VIIa (1:200; Santa Cruz: sc-74516) and  $K_{v}12.1$  (1:400; Alomone labs; #APC-113). Alexa 488- and Alexa-633-conjugated secondary IgG antibodies (1:200; life technologies: A11008 and A21050) were used for detection. Nuclei were stained with 2  $\mu$ g/ml 4',6-Diamidino-2'-phenylindole dihydrochloride (DAPI, Sigma-Aldrich, Hamburg, Germany, D9542). For imaging, tissue was mounted on Superfrost microscope slides (Thermo Scientific; 4951PLUS4). Specificity of all primary antibodies was assessed on not transfected CHO cells and on CHO cells transiently expressing  $K^{+}$  channel subunits, and for the anti- $K_{v}11.1$  antibody also on organ of Corti preparations isolated from hair cell-specific *Kcnh2* knock-out mice (see above). As commercially available antibody against  $K_{v}12.1$  (available at Alomone labs; #APC-113) produced unspecific immunosignals in not transfected CHO cells, we did not utilize this antibody for expression analyses in cochlear tissue. For  $K_{v}1.8$  channels there are no commercial antibodies available.

### Confocal Imaging

Confocal imaging was performed with an upright LSM 710 Axio Examiner microscope using W-Plan-Apochromat 63x 1,0 VIS-IR water immersion objective (Carl Zeiss, Jena, Germany) ([Leitner et al., 2018](#); [Mavrantoni et al., 2015](#)). Alexa 488 was excited at 488 nm with an argon laser and fluorescence emission was recorded at 493–597 nm, and Alexa-633 was excited at 633 nm with a HeNe633 laser (Zeiss) and fluorescence emission was sampled at 640–740 nm. All images are presented as maximum intensity projections of confocal z stacks (step size 1  $\mu$ m).

### Electrophysiological Recordings

Whole-cell recordings were performed on acutely isolated IHCs (in a whole mount organ of Corti preparation) and transfected CHO cells in culture, as previously reported ([Leitner et al., 2011, 2018](#)). In brief, apical turns of the organ of Corti of C57BL/6J mice (P19–P21) were isolated in extracellular solution containing (in mM): 144 NaCl, 5.8 KCl, 1.3 CaCl<sub>2</sub>, 0.7 Na<sub>2</sub>HPO<sub>4</sub>, 0.9 MgCl<sub>2</sub>, 5.6 glucose, 10 HEPES, pH adjusted to 7.4 (NaOH) (305–310 mOsm/kg). For recordings, the tissue was transferred into an experimental chamber and continuously perfused with the same extracellular solution. Outer hair cells and supporting cells were removed carefully by gentle suction through a cleaning pipette to obtain access to the basal cell pole of IHCs ([Dierich et al., 2019a](#)). Whole-cell patch clamp recordings were performed at room temperature (22–24 °C) with an HEKA EPC10 USB patch clamp amplifier controlled by PatchMaster software (HEKA, Lambrecht, Germany). Voltage clamp recordings were low-pass filtered at 2.5 kHz and sampled at 5 kHz. Recordings were excluded from analyses, when the series resistance ( $R_s$ ) was  $\geq 6$  M $\Omega$ , and  $R_s$  was compensated through-out the recordings (80%–90%).  $R_s$  typically was  $\sim 4$  M $\Omega$  and consequently remaining  $R_s$  was about 0.4 M $\Omega$  (90% compensation) to 0.8 M $\Omega$  (80% compensation) in the majority of recordings. We did not correct for voltage errors (accordingly max. 3 – 6 mV at largest control currents of about 7.5 nA recorded at +30 mV) caused by this remaining  $R_s$ . Steady-state current amplitudes are presented as normalized to cell capacitance (current density: pA/pF; main text) and as absolute current amplitudes ([Supplemental Figures](#)). Membrane potentials shown were not corrected for liquid junction potentials (approx. –4 mV). Patch pipettes were pulled from borosilicate glass (Sutter Instrument Company, Novato, CA, USA) and had a resistance of 2–3.5 M $\Omega$  after filling with intracellular solution containing (mM): 135 KCl, 3.5 MgCl<sub>2</sub>, 2.4 CaCl<sub>2</sub> (0.1 free Ca<sup>2+</sup>), 5 EGTA, 5 HEPES and 2.5 Na<sub>2</sub>-ATP (pH adjusted with KOH to 7.3; 290–295 mOsm/kg).

## Reagents

Tetraethylammonium (TEA; Tocris: Cat. 3068), iberiotoxin (IbTX; Tocris: Cat. 1086), 10,10-bis(4-Pyridinylmethyl)-9(10H)-anthracene dihydrochloride (XE991; Tocris: Cat. 2000), N-[4-[[1-[2-(6-Methyl-2-pyridinyl)ethyl]-4-piperidinyl]carbonyl]phenyl]methanesulfonamide dihydrochloride (E-4031, Tocris: Cat. 1808), 4-aminopyridine (4-AP; Tocris: Cat. 0940), 1,3-Bis-(2-hydroxy-5-trifluoromethyl-phenyl)-urea (NS1643, Tocris: Cat. 3062), were diluted in extracellular solution to concentrations indicated in [Results](#). All substances were applied locally to the cell under investigation via a glass capillary through a custom-made application system. “Control currents” signify currents recorded in untreated IHCs through-out the manuscript.

## Computational Model of Receptor Potentials

We extended a previously published computational model of IHCs ([Altoè et al., 2018](#)) by implementing six voltage-dependent  $K^+$  current components in IHCs ( $I_{K,f}$ ,  $I_{K,n}$  and the components of  $I_{K,s}$  in this study:  $I_{K,s}(K_v1.8)$ ,  $I_{K,s}(K_v7.4)$ ,  $I_{K,s}(K_v11.1)$ ,  $I_{K,s}(K_v12.1)$ ) together with a shunt IHC membrane capacitance (set to 9.8 pF in good agreement to our recordings,  $9.8 \pm 1.2$  pF,  $n = 38$  IHCs) and activity of mechano-electrical transduction (MET) channels (see [Figure 7A](#) for model details). Note that the individual current (conductance) voltage curves for the  $K^+$  current components  $I_{K,s}$  and  $I_{K,n}$  were implemented into the models over the whole membrane potential range as recorded. The model input is the sinusoidal deflection of the IHC hair bundle, which controls the activation of the MET channels (detailed description in Appendix A of [Altoè et al., 2018](#); for activation curves of the MET channels see [Figure S7B](#)). The outputs of the model were the IHC receptor potentials and whole cell  $K^+$  currents modeled at 37 °C. Voltage-dependent activation of the IHC  $K^+$  channels is expressed by the following equations:

$$I(t) = g * (V_m - E_K), \quad g(t) = m * G_{max}, \quad m + \tau \frac{dm}{dt} = m_i, \quad m_i = \left[ 1 + \exp\left(-\frac{Vm - v_{0.5}}{s}\right) \right]^{-1},$$

where  $V_m$  is the IHC membrane potential,  $E_K$  the reversal potential for  $K^+$ ,  $G_{max}$  the maximal conductance,  $v_{0.5}$  and  $s$  voltages of half-activation and sensitivity of the  $K^+$  conductance, respectively.  $m_i$  describes the steady fraction of open channels at a specific membrane potential, and  $\tau$ , the activation time constant, describes the kinetics of the variation in open versus close channels with membrane potential changes ( $\tau$  does not model the kinetics of single channels). Thus,  $m_i$  and  $\tau$  are determined by the opening versus closing rates of the individual channels at a given membrane potential (see Chapter 6 in [Koch, 2004](#)).  $G_{max}$ ,  $v_{0.5}$  and  $s$  were extrapolated from tail current recordings using least-square fits in *MATLAB* (MathWorks, Natick, MA) while imposing  $E_K$  to match recorded reversal potentials. The simulated currents and activation curves of the inner hair cell conductances are shown in [Figures 6B–6D](#). For the numerical simulations,  $E_K$  was set to  $-70$  mV in line with our recordings and an earlier report ([Marcotti et al., 2003](#)). For simplicity,  $\tau$  was considered voltage-independent and set to values obtained near the IHC resting potential of about  $-53$  mV in the model. Reliable recording of  $\tau$  close to the resting membrane potential was virtually impossible due to small current amplitudes. We thus extrapolated the value of  $\tau$  at the resting potential from Boltzmann fits to the time constants (derived from mono- or double exponential fits) recorded at more depolarised membrane potentials (more depolarised than  $-40$  mV) for  $I_{K,n}$  and the individual components of  $I_{K,s}$ . Note that the NS1643-sensitive current consisted of two components, of which the faster component was considered to be mediated by  $K_v12.1$  channels (see Results for details). All  $\tau$  values were corrected for temperature by utilizing a  $Q_{10}$  factor of 2, following a previous report on temperature sensitivity of IHC  $K^+$  currents ( $Q_{10}$  between 1.83 - 3 in [Kimitsuki and Komune, 2013](#)). The time constant of activation of  $I_{K,f}$  was set to 0.3 ms based on Figure 12 of [Kros and Crawford \(1990\)](#). By means of various manipulations of the model parameters, computational simulations were utilized to elucidate the physiological relevance of the IHC currents. These manipulations (i.e., the different employed models) are comprehensively described in the Results section.

## QUANTIFICATION AND STATISTICAL ANALYSIS

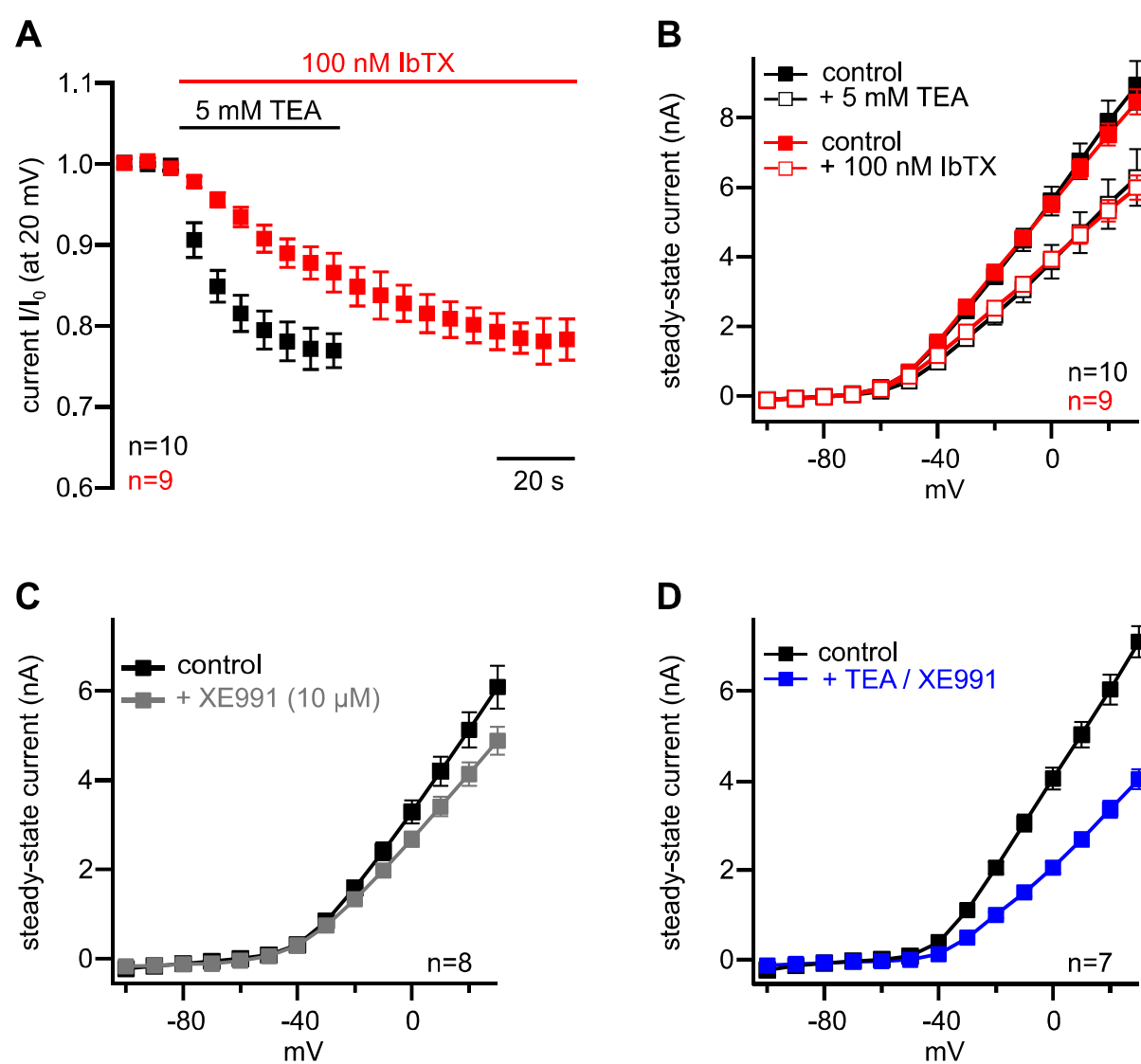
Patch clamp recordings were analyzed with PatchMaster (HEKA) and IgorPro (Wavemetrics, Lake Oswego, OR). Voltage dependence of activation was derived from tail current amplitudes using voltage protocols indicated: Maximal amplitudes of tail currents (quantified approx. 0.2-0.4 ms after the test potential) were fit with a two-state Boltzmann function with  $I = I_{min} + (I_{max} - I_{min}) / (1 + \exp((V - V_h) / s))$ , where  $I$  is current,  $V$  is the membrane voltage,  $V_h$  is the voltage at half maximal activation, and  $s$  describes the steepness of the curve. Tail currents of XE991-sensitive currents were fitted with a double (sum of two) Boltzmann functions considering two  $V_h$  and  $s$  parameters ([Figures 1F and 1G](#))  $(I_{min} + I_{max1} / (1 + \exp((V - V_{h1}) / s1)) + I_{max2} / (1 + \exp((V - V_{h2}) / s2)))$ .  $s$  is presented as positive values to describe the slope of voltage-dependent channel activation. Results on voltage dependence are shown as normalized tail current (conductance)-voltage curves, obtained by normalizing to  $(I_{max} - I_{min})$ , obtained from fits to data of individual experiments. Time constants of activation were derived from mono- or double-exponential fits to activating current components at indicated potentials ([Dierich et al., 2018](#)). Statistical analysis was performed with two-tailed Student's, Wilcoxon signed, Dunnett or Scheffé test. Statistical significance was assigned at  $p \leq 0.05$  (\*  $p \leq 0.05$ , \*\*  $p \leq 0.01$ , \*\*\*  $p \leq 0.001$ ). All data are presented as mean  $\pm$  SEM. In electrophysiological experiments,  $n$  represents the number of individual cells recorded from at least three independent experiments (independent transfections or independent tissue, i.e., biological replicates).

**Cell Reports, Volume 32**

**Supplemental Information**

**Optimized Tuning of Auditory Inner Hair Cells  
to Encode Complex Sound through Synergistic  
Activity of Six Independent K<sup>+</sup> Current Entities**

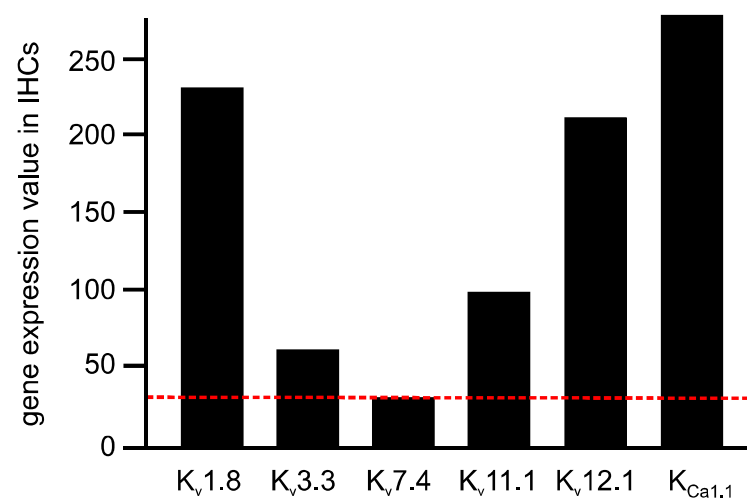
**Marlen Dierich, Alessandro Altoè, Julia Koppelman, Saskia Evers, Vijay Renigunta, Martin K. Schäfer, Ronald Naumann, Sarah Verhulst, Dominik Oliver, and Michael G. Leitner**



**Supplementary Figure 1. Pharmacological isolation of  $I_{K_s}$  in mature IHCs. Related to Figure 1.**

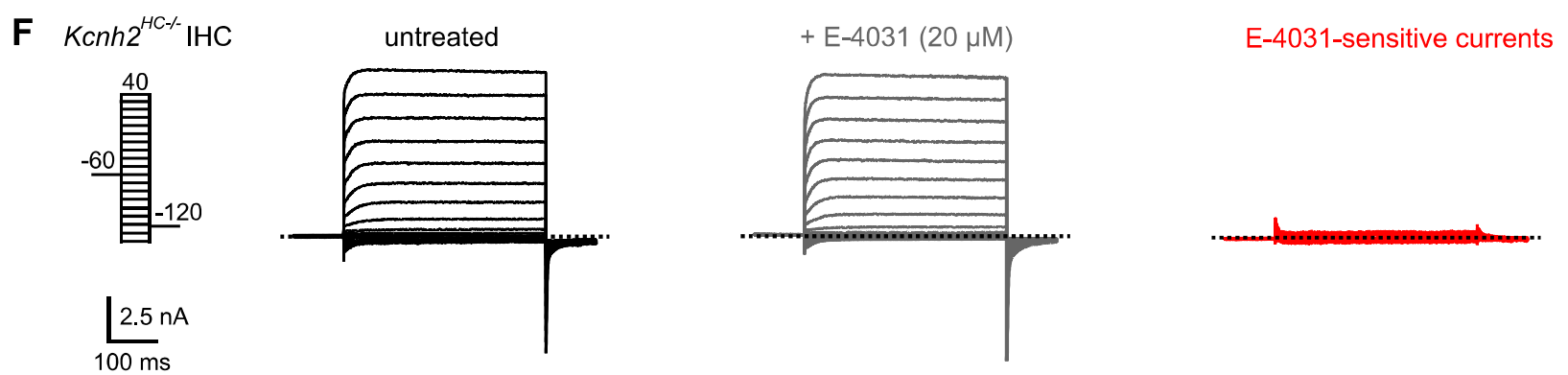
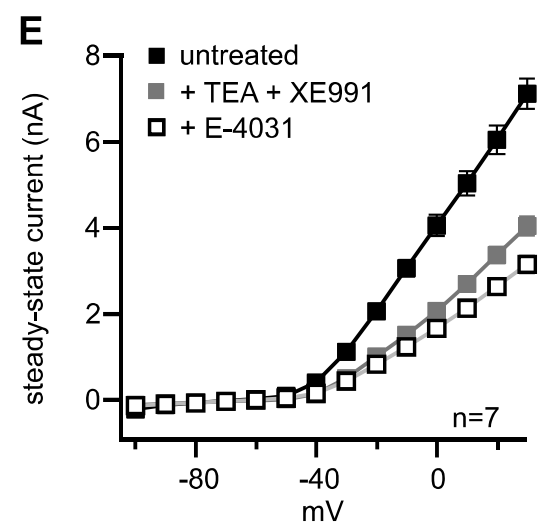
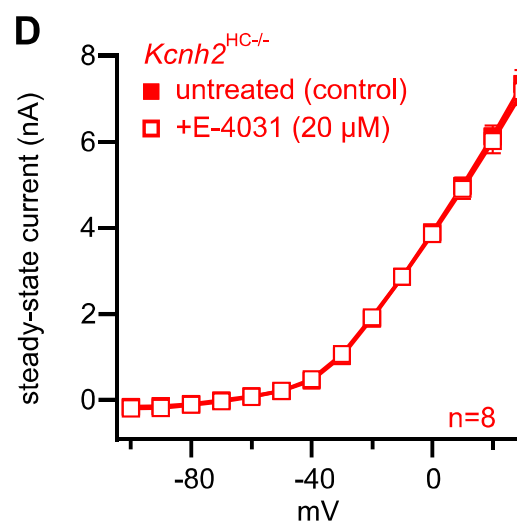
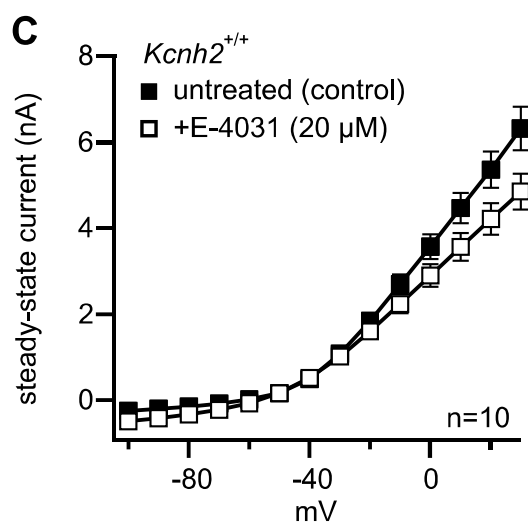
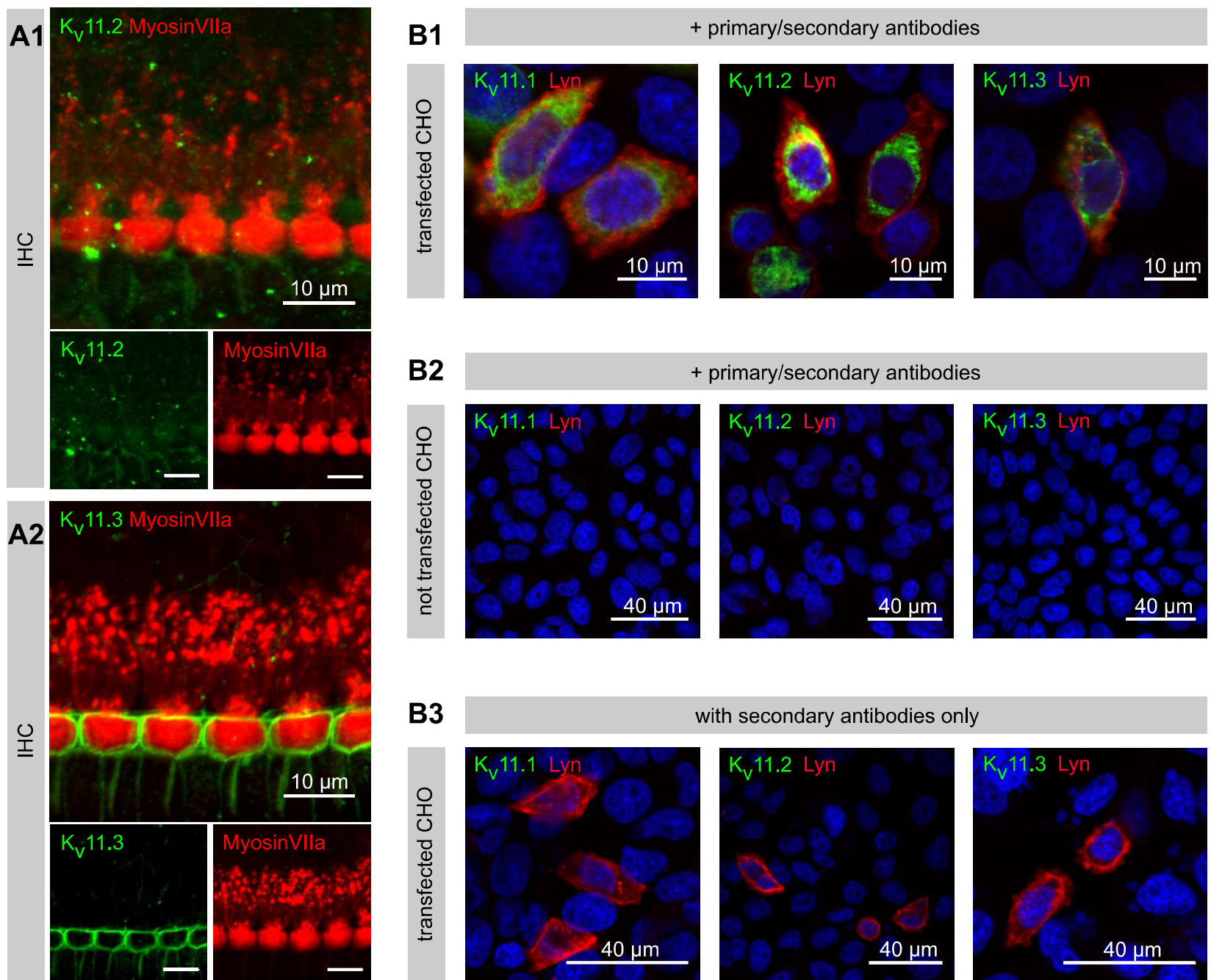
(A) Time course of inhibition of  $I_{K_f}$  in mature IHCs of the apical turn of the organ of Corti upon application of 100 nM IbTX (red) or 5 mM TEA (black). Note that TEA inhibited the  $K^+$  currents markedly faster than IbTX. Current amplitudes were quantified at the end of a 400 ms voltage step to +20 mV from the holding potential of -60 mV (c.f. Figure 1A+B of the main text). Data were normalised to baseline for visualisation ( $I/I_0$ ). (B)-(D) Absolute voltage-dependent steady-state current amplitudes recorded in mature IHCs under control conditions (*untreated*) and after pharmacological inhibition of (B)  $I_{K_f}$  (with 100 nM IbTX or 5 mM TEA), (C)  $I_{K_n}$  (with 10  $\mu$ M XE991) and (D)  $I_{K_f}$  and  $I_{K_n}$  together. These recordings correspond to current densities presented in Figure 1 of the main text: (B) corresponds to data shown in Figure 1B, (C) corresponds to data in Figure 1D and (D) corresponds to data in Figure 1H. (A-D) Sample sizes ( $n$ ) are given in the figure. Data presented as mean  $\pm$  SEM.

Dierich M, Altoè A et al., Figure S2



**Supplementary Figure 2. Identifying candidate K<sub>v</sub> channels in mature IHCs. Related to Figures 1-7.**

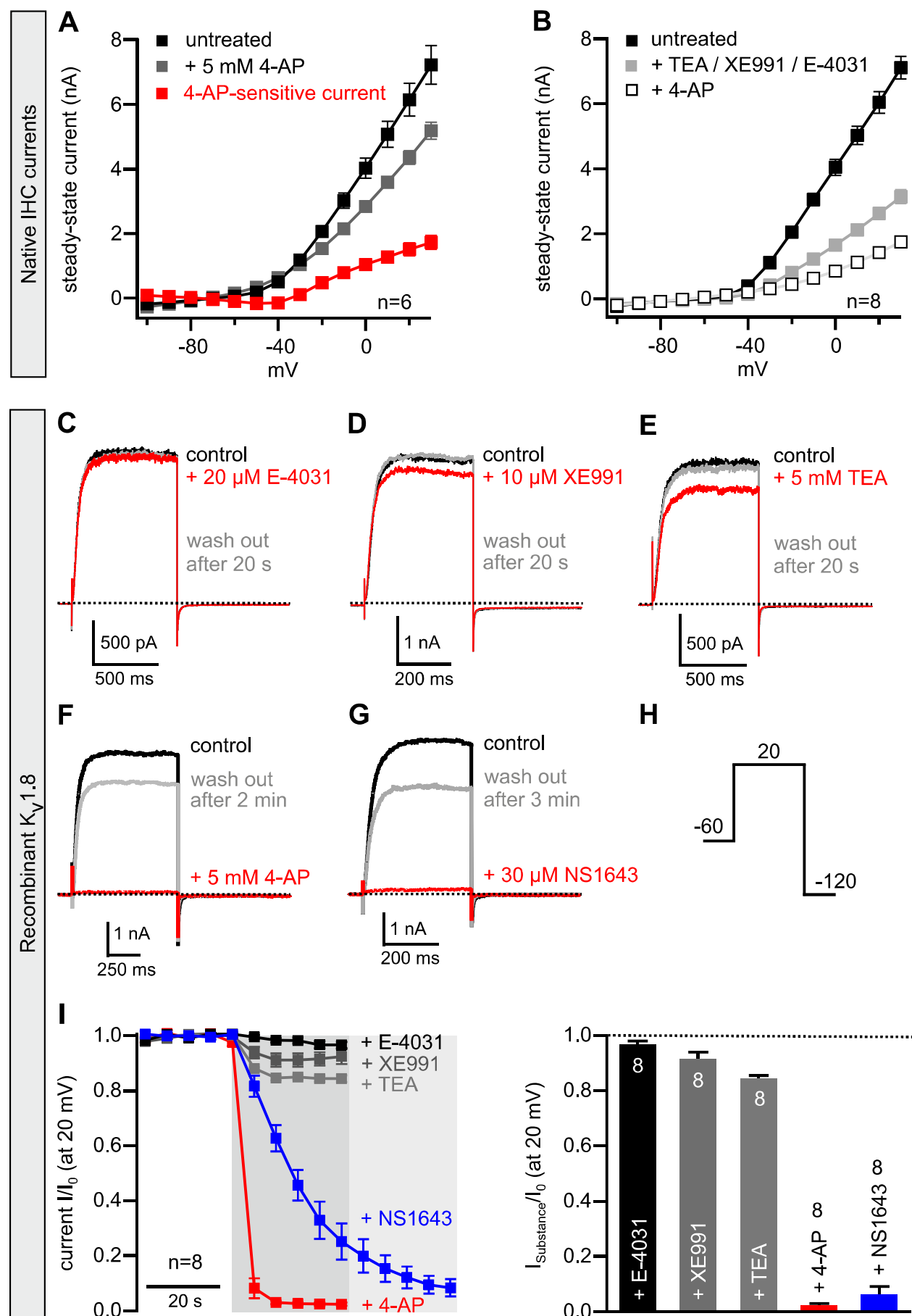
We screened a single cell transcriptome analysis performed by the laboratory of Dr. He (Liu et al., 2014) and provided by the SHIELD database (Shen et al., 2015) for candidate K<sub>v</sub> channels expressed in mature IHCs. Taking K<sub>v</sub>7.4 as reasonable threshold (*red dashed line*), we considered expression levels of K<sub>v</sub>1.8, K<sub>v</sub>3.3, K<sub>v</sub>11.1 and K<sub>v</sub>12.1 as indicative for abundance of these channels in IHCs. Expression values represent raw data as provided by (Liu et al., 2014). Note that K<sub>v</sub>7.4 and K<sub>Ca</sub>1.1 (BK<sub>Ca</sub>) mediate I<sub>K,n</sub> and I<sub>K,f</sub> in IHCs (Kharkovets et al., 2006; Ruttiger et al., 2004), respectively.



Supplementary Figure 3. Expression analyses of  $K_v11$  channels. Related to Figure 2.

### Supplementary Figure 3. Expression analyses of K<sub>v</sub>11 channels. Related to Figure 2.

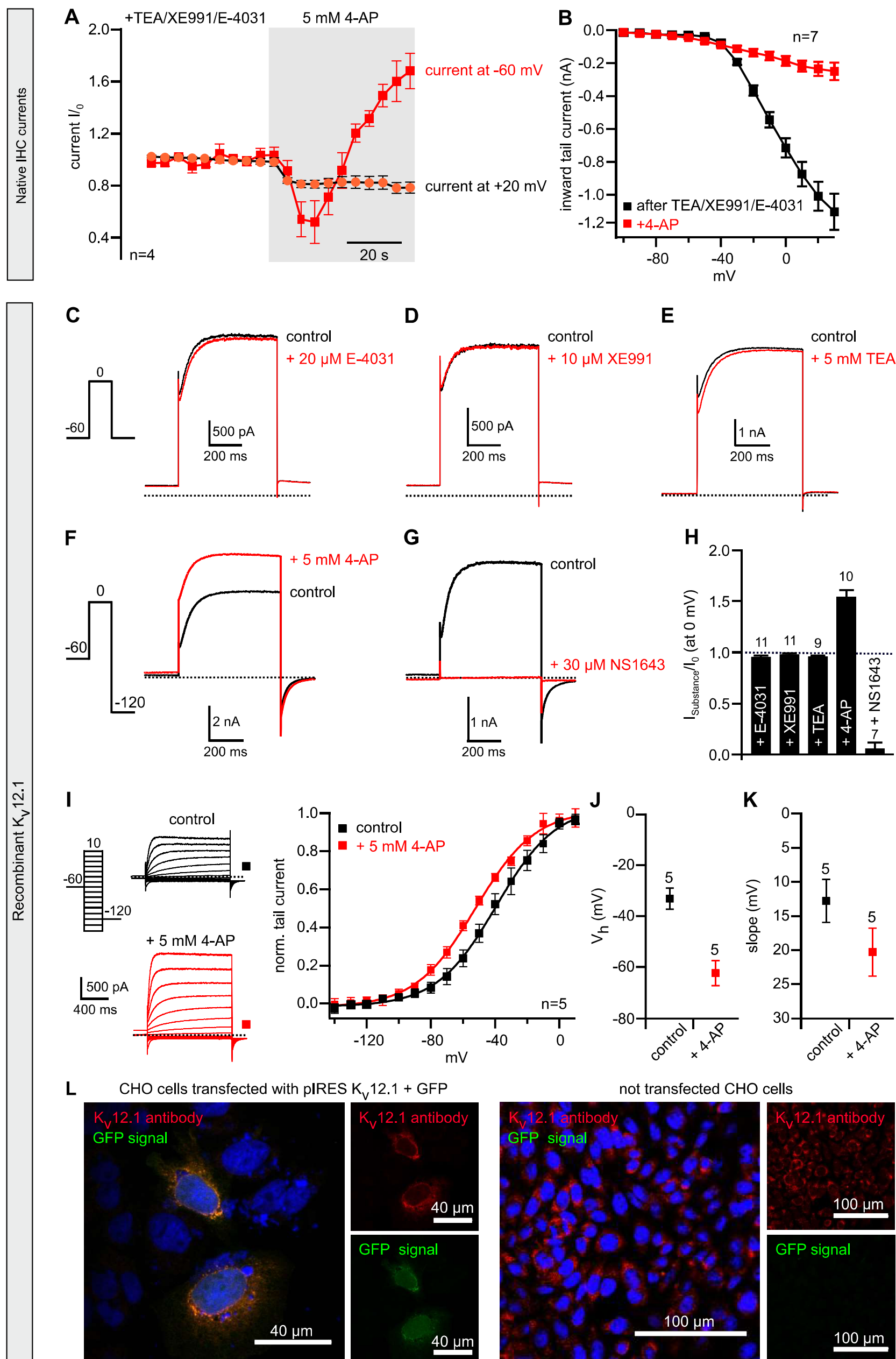
**(A+B)** Immunohistochemistry with antibodies targeting K<sub>v</sub>11 channels in (A) acutely isolated apical turns of the organ of Corti and (B) Chinese hamster ovary (CHO) cells. The panels show maximum intensity projections of confocal z-stacks of cells/tissue stained with the indicated antibodies. **(A)** We did not detect any immuno-positive signals in IHCs, when employing antibodies targeting K<sub>v</sub>11.2 (*left*) and K<sub>v</sub>11.3 (*right*). Note that IHCs were highlighted by staining with antibodies targeting MyosinVIIa (*red*). In these experiments, we detected anti-K<sub>v</sub>11.3 immunosignals in supporting cells close to IHCs (all scale bars represent 10 μm). **(B)** highlights control experiments in CHO cells performed to evaluate specificity of the employed antibodies (cells were co-stained with DAPI to visualise nuclei, and co-transfected with Lyn11-RFP as transfection marker). **(B1)** depicts CHO cells transfected with K<sub>v</sub>11.1 (*left*), K<sub>v</sub>11.2 (*middle*) or K<sub>v</sub>11.3 (*right*) treated with primary antibodies targeting the respective channels and the appropriate secondary antibodies (*positive control*). **(B2)** shows not transfected CHO cells treated with primary and secondary antibodies (*negative control*). **(B3)** shows CHO cells transfected with K<sub>v</sub>11.1 (*left*), K<sub>v</sub>11.2 (*middle*) or K<sub>v</sub>11.3 (*right*) (together with Lyn11-RFP) treated with only secondary antibodies (*secondary antibody control*). As we did not detect any immuno-positive signals (B2) in not transfected CHO cells and (B3) in absence of primary antibodies, we conclude that the employed antibodies specifically recognise K<sub>v</sub>11 channels (scale bars in B1 represent 10 μm, in B2+B3 40 μm). **(C-E)** Absolute voltage-dependent steady-state current amplitudes recorded in mature IHCs under control conditions (*untreated*) and after application of E-4031 (20 μM) to (C) *Kcnh2*<sup>+/+</sup> mice (WT) or (D) *Kcnh2*<sup>HC/-</sup> mice and (E) after application of TEA (5 mM), XE991 (10 μM) and E-4031 (20 μM) in WT mice. Note that these recordings correspond to current densities presented in Figure 2 of the main text: (C) corresponds to data shown in Figure 2C, (D) corresponds to data in Figure 2D and (E) corresponds to data in Figure 2G. **(F)** Representative whole cell currents recorded in an IHC isolated from a *Kchn2*<sup>HC/-</sup> mouse under control conditions (*untreated, left*), and after extracellular application of E-4031 (20 μM, *middle*). E-4031-sensitive currents (*red, right*) were obtained by subtracting currents after application of E-4031 from control currents. Note that E-4031 did not inhibit relevant currents in this IHCs from a *Kchn2*<sup>HC/-</sup> mouse (voltage protocol and scale bars as indicated). (C-E) Sample sizes (n) are given in the figure. Data presented as mean ± SEM.



**Supplementary Figure 4. 4-AP-sensitive currents in IHCs and pharmacological properties of recombinant  $K_v1.8$  channels. Related to Figure 3.**

(A+B) Absolute voltage-dependent steady-state current amplitudes recorded in mature IHCs under control conditions (*untreated*) and after application of (A) 4-AP (5 mM) and (B) TEA (5 mM), XE991 (10  $\mu$ M), E-4031 (20  $\mu$ M) and 4-AP (5 mM). Note that these recordings correspond to current densities presented in Figure 3 of the main text: (A) corresponds to data shown in Figure 3B and (B) corresponds to data in Figure 3D. (C-G) Representative whole-cell currents recorded from CHO cells transiently expressing mouse  $K_v1.8$  before (*black*), at the end of extracellular application (*red*) of (C) 20  $\mu$ M E-4031, (D) 10  $\mu$ M XE991, (E) 5 mM TEA, (F) 5 mM 4-AP or (G) 30  $\mu$ M NS1643 and after wash-out of the substances (*grey*; scale bars as indicated). Note that NS1643- and 4-AP-dependent inhibition was rapidly reversible. (H) shows the voltage protocol for recordings as shown in (C-G). (I) Averaged time course of  $K_v1.8$ -mediated currents upon application of the indicated substances (*left*) and summarized steady-state current amplitudes at the end of the application (*right*; n=8 for all substances). Current amplitudes were quantified at +20 mV from experiments shown in (C-H) and were normalised to baseline ( $I_{\text{Substance}}/I_0$ ). (A, B, I) Sample sizes (n) are given in the figure. Data presented as mean  $\pm$  SEM.

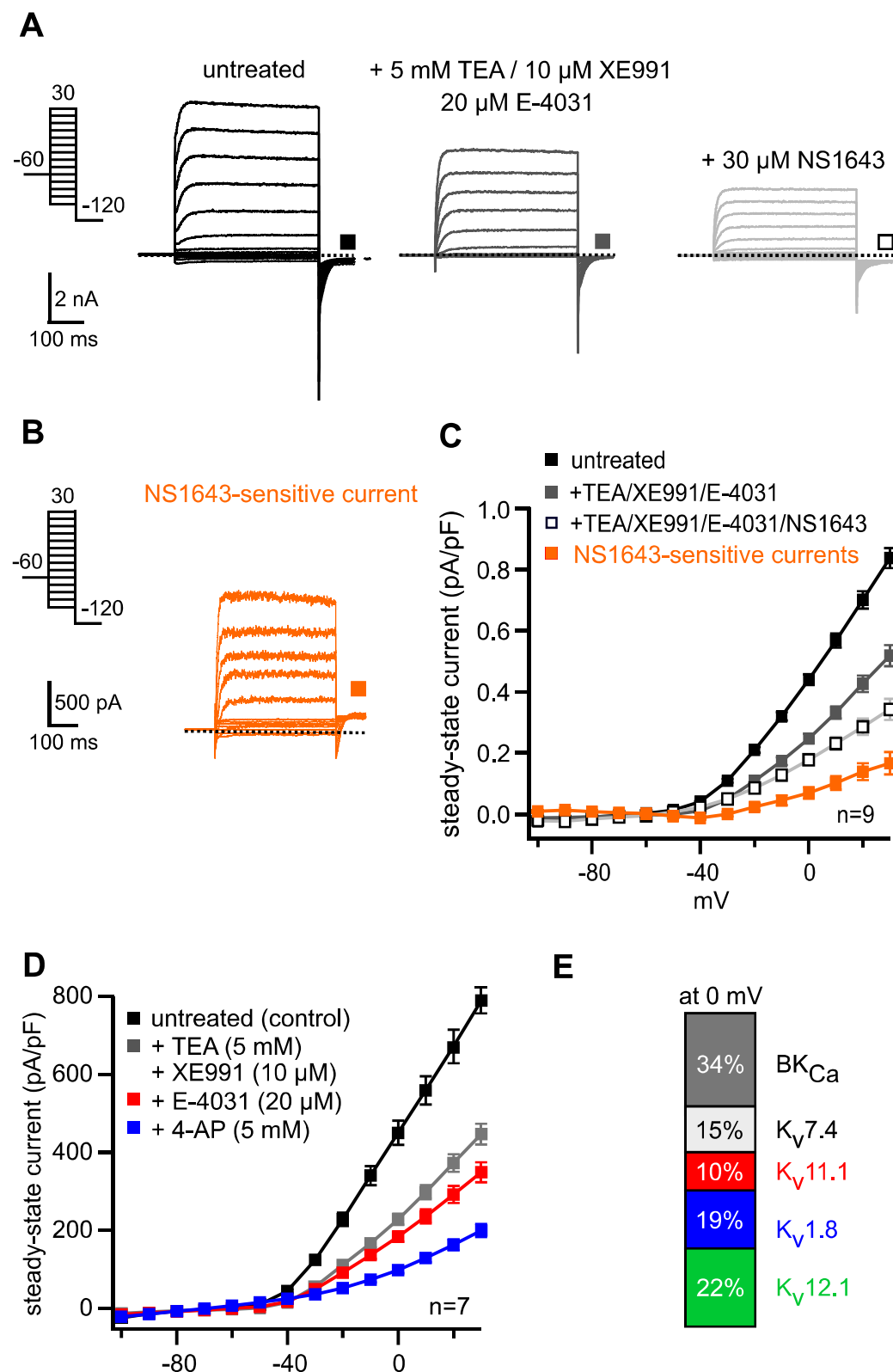




Supplementary Figure 5. Effects of 4-AP in IHCs and characteristics of recombinant  $K_v12.1$  channels. Related to Figures 4 and 5.

**Supplementary Figure 5. Effects of 4-AP in IHCs and characteristics of recombinant K<sub>v</sub>12.1 channels. Related to Figures 4 and 5.**

This figure summarises experiments in **(A+B)** mature IHCs of mice and **(C-L)** CHO cells heterologously expressing K<sub>v</sub>12.1 (+GFP in pIRES vector). **(A)** Time course of effects of 4-AP (5 mM): Application of 4-AP (in cells treated with 5 mM TEA, 10 μM XE991 and 20 μM E-4031, i.e. to inhibit I<sub>K,f</sub>, I<sub>K,n</sub> and K<sub>v</sub>11.1) caused a rapid inhibition of currents at positive potentials and a slow potentiation of currents at hyperpolarised potentials. These different time courses allowed for pharmacological separation of the two current components. Steady-state currents were quantified at +20 mV and at -60 mV in recordings as shown in Figure 4C, and are presented as normalised to base line (current I/I<sub>0</sub>). **(B)** Absolute tail current amplitudes (elicited at -120 mV after activating pulses between -100 mV and +30 mV; 10 mV increments) in IHCs treated with TEA (5 mM), XE991 (10 μM), and E-4031 (20 μM) (*black*) and in the same cells after additional application of 4-AP (5 mM; *red*). Note that these recordings correspond to normalised tail currents presented in Figure 4D of the main text. **(C-H)** Representative whole-cell currents recorded from CHO cells transiently transfected with human K<sub>v</sub>12.1, before (*black*) and at the end of extracellular application (*red*) of (C) 20 μM E-4031, (D) 10 μM XE991, (E) 5 mM TEA, (F) 5 mM 4-AP or (G) 30 μM NS1643 (voltage command and scale bars as indicated). Note (F) 4-AP-dependent potentiation and (G) NS1643-dependent inhibition of K<sub>v</sub>12.1-mediated currents (c.f. Dierich et al., 2018). **(H)** Summarized steady-state current amplitudes at the end of application of the indicated substances. Currents were quantified at 0 mV from recordings as shown in (C-G) and normalised to baseline (I<sub>Substance</sub>/I<sub>0</sub>). **(I-K)** As previously reported (c.f. Dierich et al., 2018), 4-AP potentiated K<sub>v</sub>12.1-mediated currents and induced a shift of voltage-dependent activation of human K<sub>v</sub>12.1 channels to hyperpolarised potentials. (G) Representative patch clamp recordings (*left*) of a CHO cell transiently transfected with human K<sub>v</sub>12.1 subunits before (*black*) and after (*red*) application of 5 mM 4-AP. The right panel shows Boltzmann fits (solid line) to averaged data derived from experiments shown on the left. (H) displays averaged V<sub>h</sub> and (I) shows the slope factor of activation from fits shown in (G) before (*black*) and after (*red*) application of 4-AP (5 mM) (values derived from Boltzmann fits to data as shown in (G)). **(L)** Commercially available anti-K<sub>v</sub>12.1 antibodies did not detect recombinant K<sub>v</sub>12.1 in CHO cells reliably. The left panel shows CHO cells transiently transfected with a pIRES plasmid containing genetic information for GFP and K<sub>v</sub>12.1 stained with an anti-K<sub>v</sub>12.1 antibody. The right panel shows analogous stainings in not transfected CHO cells. Note that in not transfected CHO cells treatment with anti-K<sub>v</sub>12.1 antibody showed strong immune-positive signals. (L) shows maximum intensity projections of confocal z-stacks. Scale bars in left panel indicate 40 μm in right panel 100 μm. (A, B, H, I-K) Sample sizes (n) are given in the figure. Data presented as mean ± SEM.



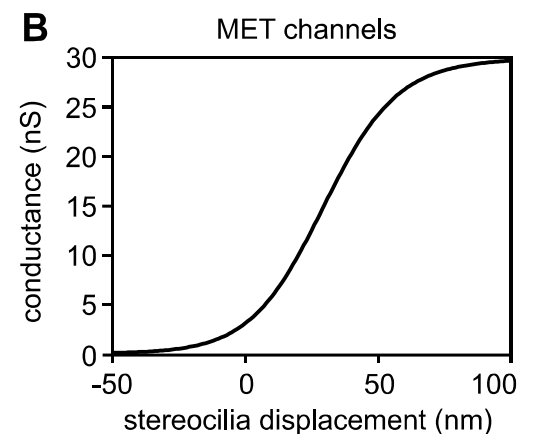
**Supplementary Figure 6. NS1643 inhibits K<sup>+</sup> currents in mature IHCs and summary of IHC K<sup>+</sup> currents. Related to Figures 1-7.**

(A) Representative recordings of an IHC under control conditions (*untreated*, left), after application of 5 mM TEA, 10  $\mu$ M XE991 and 20  $\mu$ M E-4301 (*middle*) and after additional application of 30  $\mu$ M NS1643 (*right*). Note that NS1643 is an agonist of K<sub>v</sub>11 channels and thus was applied after inhibition of these channels with E-4031. (B) NS1643-sensitive currents (*left panel*, orange) obtained by current subtraction in recordings shown in (A). (C) summarized steady-state currents analysed from recordings depicted in (A). (D+E) Mature IHCs in the apical turn of the organ of Corti express five independent K<sup>+</sup> channel populations (BK<sub>Ca</sub>, K<sub>v</sub>1.8, K<sub>v</sub>7.4, K<sub>v</sub>11.1, K<sub>v</sub>12.1) that give rise to six K<sup>+</sup> current entities with different biophysical properties (note that K<sub>v</sub>7.4 channels mediate two components with different voltage-dependent activation in IHCs; see main text for details). (D) shows summarised steady-state currents in mature IHCs under control conditions (*untreated*) and for the same cells after successive application of TEA (5 mM) with XE991 (10  $\mu$ M), of E-4031 (20  $\mu$ M) and of 4-AP (5 mM). (E) presents the relative contribution of the currents through the individual K<sup>+</sup> channels to whole cell control currents at 0 mV (in %). (A+C) Sample size (n) is given in the figure. Data presented as mean  $\pm$  SEM.

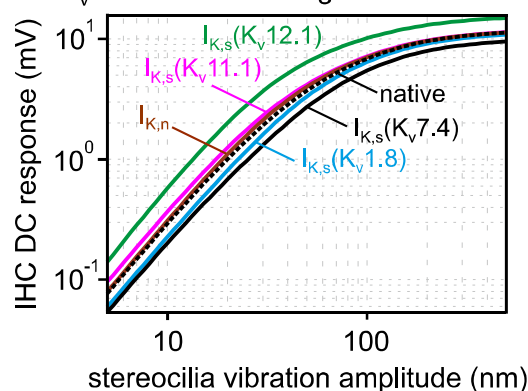
**A** Parameters of the refined computational IHC model.

	$G_{\max}$ (nS)	$V_{0.5}$ (mV)	$s$ (mV)	$\tau$ (ms)
$I_{K,t}(BK)$	42	-53	16.4	0.3
$I_{K,n}(K_v7.4)$	1.4	-107	1.5	instant.
$I_{K,s}(K_v11.1)$	14.3	-35.3	10	11
$I_{K,s}(K_v12.1)$	14.7	-12.7	10.5	38
$I_{K,s}(K_v1.8)$	25	-44	6.3	23.4
$I_{K,s}(K_v7.4)$	28	-40	6.5	11.2

$G_{\max}$ , max. conductance;  $V_{0.5}$ , half-activation voltage of conductance;  $s$ , sensitivity;  $\tau$ , time constant of activation at rest



**C**  $K_v$  conductance assigned to one subunit



**D** Results of models assigning all  $K_v$  conductance to one  $K_v$  subunit

	$V_m$ mV	AC/DC 1 kHz* 10 nm**	AC/DC 1 kHz* 60 nm**	AC/DC 1 kHz* 200 nm**	AC -3 dB corner frequency Hz	DC sensitivity 10 nm** mV/nm	DC sensitivity dB vs. native
<b>Native</b>	-53	10	3	1.8	1 300	0.030	0
$I_{K,n}(K_v7.4)$	-64	6.5	1.8	1.2	1 950	0.030	0
$I_{K,s}(K_v11.1)$	-53	9	2.7	1.7	1 280	0.036	+1.5
$I_{K,s}(K_v12.1)$	-49	6	2	1.5	1 100	0.057	+5.5
$I_{K,s}(K_v1.8)$	-54	14	3.3	1.8	1 380	0.022	-3
$I_{K,s}(K_v7.4)$	-52	16	4	2	1 340	0.020	-3

$V_m$ , resting membrane potential; \* stimulus frequency; \*\* stereocilia vibration amplitude

**Supplementary Figure 7. Parameters of the refined computational model, activation curves of the MET channels and models assigning all  $K_v$  conductance to a single  $K_v$  subunit. Related to Figures 6 and 7.**

(A) Parameters of the refined computational model (temperature: 37°C; membrane capacitance: 9.8 pF; endocochlear potential: +90 mV;  $K^+$  reversal potential (Marcotti et al., 2003): -70 mV). MET channel parameters (see Altoè et al., 2008 for parameter determination and Kennedy et al., 2003 for activation time constant):  $G_{\max} = 30$  nS; half-activation stereocilia displacement = 20 nm; mechanical sensitivity = 16 nm;  $\tau = 50$   $\mu$ s. (B) Simulated activation curves of IHC MET channels (see *Material and Methods* and *text* for details). (C+D) Results of models assigning all  $K_v$  conductance to a single  $K_v$  subunit. (C) shows IHC DC responses as function of stereocilia vibration amplitudes in models in which all  $K_v$  conductance is assigned to single  $K_v$  subunit (indicated in the graph labelling). These data correspond to the data also presented in Figure 7K. Note log-log scaling to visualise  $K_v$ -subunit-dependent DC responses at faint stereocilia vibrations and compression of DC responses. (D) Summarised results of models assigning all  $K_v$  conductance to one  $K_v$  subunit (see main *text* for details).

**Supplemental Table S1. Sequences of primers used for RT-PCR. Related to STAR Methods**

gene [accession number]	gene-specific primer	sequence
<b><i>Kcnh2</i></b> [NM_013569.2]	K <sub>v</sub> 11.1 for	GAAGGTCACCCAGGTCCTGTCCTTG
	K <sub>v</sub> 11.1 rev	GAAGATCTTTTCTGAGTTGGTGTG
<b><i>Kcnh6</i></b> [NM_053937.1]	K <sub>v</sub> 11.2 for	TCTCCAGTCAACACCCCGAC
	K <sub>v</sub> 11.2 rev	CTCTGGAACTCTAGCTGCTT
	K <sub>v</sub> 11.2 nested for	CCAGATGAACAGACTGGAG
	K <sub>v</sub> 11.2 nested ref	GCTGCTCTTGTCTGAGGAC
<b><i>Kcnh7</i></b> [NM_133207.2]	K <sub>v</sub> 11.3 for	CCTCAGGACTTCAGAGAGC
	K <sub>v</sub> 11.3 rev	GCCTATGGAGACCCAAGATCCC
<b><i>Kcna10</i></b> [NM_001081140.1]	K <sub>v</sub> 1.8 for	ATGGATGTGTGTAGCTGGAAAGAAATGGAG
	K <sub>v</sub> 1.8 rev	TCACTTCCTGGACTTCTCTGCAGAGCA
<b><i>Kcnh8</i></b> [NM_001031811.2]	K <sub>v</sub> 12.1 for	TCACATCTCAGGACACCTTCAA
	K <sub>v</sub> 12.1 rev	ATGCAAATGGATCTCGCTTCAA
<b><i>Kcnh3</i></b> [NM_010601.3]	K <sub>v</sub> 12.2 for	GTGTCTCCTGGATGTGATACCT
	K <sub>v</sub> 12.2 rev	GCAGCGACTTTATATTCAGGCA
<b><i>Kcnh4</i></b> [NM_001081194.2]	K <sub>v</sub> 12.3 for	AAGACTCCAGTAACACAGCTGA
	K <sub>v</sub> 12.3 rev	AGAGATGCATGGTAGTCTCTGG
<b><i>Kcnq4</i></b> [NM_001081142.2]	K <sub>v</sub> 7.4 for	CCCACCTCGCCAAGCAGTGAGCAGGTG
	K <sub>v</sub> 7.4 rev	TCAGTCCATGTTGGTGCTGACTGAGCG
<b><i>Gapdh</i></b> [NM_001289726.1]	GAPDH for	AACTTTGGCATTGTGGAAGG
	GAPDH rev	CCCTGTTGCTGTAGCCGTAT

## 6.2 Lebenslauf

### Persönliche Daten

Name: Marlen Dierich  
Geburtstag: 18.01.1988  
Nationalität: Deutsch

### Berufserfahrung

- Seit 06/2019 **Wissenschaftliche Außendienstmitarbeiterin bei AstraZeneca**
- 10/2013-12/2018 **Wissenschaftliche Mitarbeiterin an der Universität zu Marburg**
- Institut für Physiologie und Pathophysiologie (Prof. Dr. D. Oliver)
  - Forschung: K<sup>+</sup>-Kanäle in nativen auditorischen Haarsinneszellen
- 4/2012-2/2013: **Studentische Hilfskraft an der Universität zu Potsdam**
- AG: Vergleichende Sinnes- und Neurobiologie (Prof. Dr. M. Vater)
  - Praktikumsbegleitung für Bachelorstudiengänge
  - Methoden: Funktionelle Histologie
- 10/2008-09/2010 **Selbstständige Tätigkeit**
- Promotion/Verkauf für Textilfabrik Wiehler
  - Rostocker Weihnachtsmarkt/Hanse Sail

### Ausbildung

- 10/2013 - heute: **Universität Marburg**
- Kumulative Dissertation
- 10/2010-03/2013: **Universität Potsdam**
- Master of Science in Molekularbiologie und Biochemie (Note: 1,5)
  - Master Thesis: Untersuchung hyperpolarisationsabhängiger Ströme von Neuronen des auditorischen Kortex der Maus (Note: 1,3)
- 10/2007-09/2010: **Universität Rostock**
- Bachelor of Science in Biowissenschaften (Note: 2,1)
  - Bachelor Thesis: Development of standard operation procedures (SOPs) for blood serum analysis with biosensor Ssens K5 (Note: 1,1)
- 2000-2007: **Gymnasium Wittstock**
- Abitur (Note: 1,8)
-

### **6.3 Verzeichnis der akademischen Lehrer/-innen**

Meine akademischen Lehrenden waren...

... in Rostock:

Hubert Johannes Bahl, Stefan Forster, Goldammer, Dethardt Götze, Renate Horn, Thomas Hübener, Birgit Piechulla, Stefan Porembski, Reinhard Schröder...

... in Potsdam:

Andreas Abraham, Salma Balazadeh, Silke Leimkühler, Ingo Scheffler, Ralph Tiedemann, Marianne Vater, Ulla Wollenberger...

---

## 6.4 Danksagung

Ohne die Unterstützung zahlreicher Personen und Institutionen hätte diese Dissertation mit fünf Erstautoren Publikationen in dieser Form nicht realisiert werden können. Für die vielfältig erfahrene Hilfe möchte ich mich an dieser Stelle sehr herzlich bedanken. An erster Stelle möchte ich mich bei Prof. Dr. Oliver bedanken für die freundliche Aufnahme in seinen Arbeitskreis, für die Unterstützung und hilfreichen Diskussionen während der gesamten Zeit und schlussendlich für das Korrekturlesen meiner Arbeit.

Ein spezieller Dank geht an meinen Doktorvater Michael, dem von der ersten Stunde an, kein Weg zu weit und keine Erläuterung auch noch so komplexer Fragestellungen zu viel gewesen ist. Du hattest immer ein offenes Ohr für mich, egal ob es sich um fachliche oder private Dinge handelte. Du bist für mich einer der zielstrebigsten, kreativsten und kompetentesten Wissenschaftler, den ich kennengelernt habe. Ich erinnere mich auch gerne an unsere gemeinsamen Abende mit Bettina zurück, wo es das ein oder andere Glas Wein (angeblich 20 Mini-Gläser) gab. Ihr wart mehr als nur „Chef“ und Kollegin, denn ihr seid über die Jahre zu richtig guten Freunden geworden und dafür möchte ich einmal Danke sagen, ohne euch wäre das nie möglich gewesen.

Allen aktuellen und ehemaligen Mitarbeitern der Arbeitsgruppe Oliver danke ich für die angenehme Arbeitsatmosphäre und die immense Unterstützung während der Arbeit. Vor allem natürlich Olga für die hervorragende Zellkulturarbeit und Sigrid und Nesli für die Hilfe bei den echt nervigen Genotypisierungen der Mäuse. Meinen wissenschaftlichen Kollegen Florian und Chris H. danke ich für die immer zielführenden Diskussionen bei einem Feierabend Bier/Weinchen und für die kurzweiligen Pausen im Institut. Auch wenn es im Endeffekt leider nicht ganz funktioniert hat, möchte ich mich bei Prof. Dr. Schäfer, sowie dessen Mitarbeiter, für die Einarbeitung in die Technik der In-situ-Hybridisierung bedanken.

Für die immense Unterstützung bei den gemeinsamen Publikationen bedanke ich mich einerseits bei Tobias Huth und Philipp Moeser für die Hörtests bei den BACE1 Mäusen und andererseits bei Dr. Alexandro Altoè für die Computersimulationen zu meinen elektrophysiologischen Messungen an Haarsinneszellen.

Meiner Familie danke ich für die immer wiederkehrende Frage: „Wann bist du denn jetzt endlich fertig?“ Ich: „Dieses Jahr noch“. Familie: „Das sagst du schon seit 2 Jahren.“ Vielen Dank, dass ihr trotzdem immer an mich geglaubt habt und mir das Studium ermöglichen konntet ;)

Abschließend möchte ich mich noch bei meinem AstraZeneca-Arbeitskollegen Marcel, meiner zukünftigen Schwägerin Janni und bei Bettina bedanken, die meiner schriftlichen Arbeit den letzten Schliff verpasst haben. Nicht zu vergessen ist natürlich mein Freund Jan, der mich gerade im letzten Jahr immer wieder motiviert hat, mich an den Schreibtisch zu setzen, um diese Dissertation zu Ende zu bringen und währenddessen den Haushalt geschmissen und sich um mein leibliches Wohl gekümmert hat, Danke.

DANKE EUCH ALLEN

---